Faculty of Science and Engineering
Department of Imaging and Applied Physics

Non-Gaussian and non-homogeneous Poisson models of snapping shrimp noise

Matthew W. Legg

This thesis is presented for the Degree of
Doctor of Philosophy
of
Curtin University of Technology

February 2010

Declaration

To the best of my knowledge and belief this thesis contains no material previously published by any other person except where due acknowledgment has been made. This thesis contains no material which has been accepted for the award of any other degree or diploma in any university.

_____ _____

Signature Date

Abstract

The problem of sonar detection and underwater communication in the presence of impulsive snapping shrimp noise is considered. Non-Gaussian amplitude and non-homogeneous Poisson temporal statistical models of shrimp noise are investigated from the perspective of a single hydrophone immersed in shallow waters. New statistical models of the noise are devised and used to both challenge the superiority of existing models, and to provide alternative insights into the underlying physical processes.

A heuristic amplitude statistical model of snapping shrimp noise is derived from first principles and compared with the Symmetric-α-stable model. The models are shown to have similar variability through the body of the amplitude probability density functions of real shrimp noise, however the new model is shown to have a superior fit to the extreme tails. Narrow-band detection using locally optimum detectors derived from these models show that the Symmetric-α-stable detector retains it's superiority, despite providing a poorer overall fit to the amplitude probability density functions. The results also confirm the superiority of the Symmetric-α-stable detector for detection of narrow-band signals in shrimp noise from Australian waters.

The temporal nature of snapping from a field of shrimp is investigated by considering the snapping as a point process in time. Point process analysis techniques are drawn from the fields of optics, neuro-physics, molecular biology, finance and computer science, and applied to the problem of snapping shrimp noise. It is concluded that the snapping is not consistent with a homogeneous Poisson process and that correlations

exist in the point process on three different time scales. The cause of short time correlations is identified as surface reflected replicas, and models of medium time correlations are investigated. It is shown that a Cox-Ingersoll-Ross driven doubly-stochastic Poisson model is able to describe the medium time correlations observed from the counting process, but a k^{th}-order interval analysis reveals that there is more information contained within the snapping than can be described by the model. Analysis of shrimp snap times over a full day provides evidence of correlation between snap events on long time scales. Simulation of ocean noise is conducted to illustrate the use of such temporal models, and implications for their use in detection algorithms are discussed.

Acknowledgements

I would first and foremost like to thank my wife Tracy and my children Sarah and Jacob for all of the evenings and weekends that they allowed me to use for this study.

Special thanks go to my official supervisors Dr Alec Duncan, Prof. Tony Zaknich and Dr Mike Greening for their guidance and support, and for simultaneously allowing me the time to explore in shady corners and for not allowing me to be lost forever in complete darkness. Special thanks also go to my unofficial supervisors Dr Derek Bertilone and Dr Dave Matthews, who bore the brunt of my immediate questions and continually encouraged me to get the thesis completed.

Thanks go to Dr Dave Matthews, Dr Rod MacLeod, Damien Killeen, Paul Moses and Mark Savage for their assistance with field work, and to Dr Doug Cato, Dr Rob McCauley, Dr Brian Ferguson and Jane Cleary for providing (respectively) data from the Spencer Gulf, Feather Reef and Sydney Harbour. Special thanks go to Dr Dave Matthews for providing Seal Island, Seal Cave, Exmouth Jetty and Pyrmont data.

I would also like to thank the many people who helped with reviewing, proofreading and grammatical editing of this thesis. Special thanks go to Dr Derek Bertilone for an in-depth review of the mathematical derivation in this thesis. Also to my sister Caz for her continued tutoring and guidance in grammar and writing style. I would like to thank the examiners for the time and effort they have expended to ensure this thesis is of a high standard.

Support and resources were provided by the Department of Imaging and Applied Physics and the Centre for Marine Science and Technology (CMST) at Curtin University, and the Defence Science and Technology Organisation (DSTO). I extend my gratitude to the people who have helped with administration within these two organisations.

Contents

1 Introduction **1**

1.1 Thesis aims 2

1.2 Research methodology 3

1.3 Supporting field work 4

1.4 Thesis format and outline 6

2 Snapping shrimp noise **8**

2.1 Snapping shrimp 9

2.2 Acoustic characteristics of individual shrimp snaps 10

2.3 Snapping shrimp and ambient noise 11

2.4 Shrimp noise analyses and applications 18

2.5 Summary of snapping shrimp noise 21

3 Amplitude models **23**

3.1 Models of snapping shrimp noise 24

3.1.1 The Gaussian distribution 24

3.1.2 The Gaussian-Gaussian mixture distribution 26

3.1.3 The α-stable distribution 29

3.2 A heuristic model of snapping shrimp noise 34

3.2.1 Derivation of the density function 36

3.2.2 Derivation of the distribution function 45

3.3 Ambient noise: a Gaussian-Garnele mixture model 46

3.3.1 Parameter estimation for the Gaussian-Garnele distribution . . . 47

3.4 Comparison of SαS and Gaussian-Garnele models 50

3.5 Frequency dependence of the pressure amplitude pdf 61

3.6 Experimental investigation of pdf asymmetry in real shrimp noise 65

3.7 Summary of amplitude models 72

4 Temporal models **74**

4.1 Random point processes 75

4.2 Homogeneous Poisson model 77

4.3 Event detection 78

4.3.1 Pre-detection filtering 79

4.3.2 Threshold detection with dead-time 81

4.3.3 Consequences of threshold detection 83

4.4 Inter-snap interval histogram analysis 83

4.4.1 The uniform conditional test 87

4.5 K^{th} order interval analysis 89

4.6 Intensity function analysis 99

4.7 Fano-factor analysis 106

4.8 The cause of short time effects 124

4.9 Modelling medium and long time effects 125

4.9.1 Doubly-stochastic Poisson models 126

4.9.2 The Ornstein-Uhlenbeck model 128

4.9.3 The Cox-Ingersoll-Ross model 132

4.9.4 Asymptote for infinite counting time 140

4.9.5 A 24 hour time-series 140

4.10 Summary of temporal models 144

5 Application to simulation and detection 148

5.1 Simulated ocean ambient noise 148

5.2 Detection in snapping shrimp noise 156

5.3 Summary of applications 160

6 Discussion 161

6.1 Discussion of amplitude probability density function models 162

6.2 Emerging knowledge of the temporal nature of snapping shrimp noise . 164

6.3 Implications for sonar detection and communications 167

7 Conclusions 169

7.1 Thesis conclusions 169

7.2 Recommendations for further work 171

A Field Measurements 173

A.1 AWharf (AW) 173

A.2 Busselton Jetty (BUWO) 176

A.3 Cockburn Sound measurements 178

A.3.1 10 March 2008 (CS-A,CS-D) 178

A.3.2 1 December 2005 (CS-B) 181

A.3.3 25 November 2005 (CS-C) 184

A.4 Nornalup-Walpole Estuary (WP) 187

A.5 24 hour recording at the AWharf (AW24) 189

B Field data sets **193**

B.1 Seal Island 193

B.1.1 Seal Island Cave (SEAL-A and SEAL-B) 193

B.1.2 Seal Island (SEAL-C) 196

B.2 Feather Reef (FR) 196

B.3 Spencer Gulf (SG) 199

B.4 Sydney Harbour (SYD-A and SYD-B) 201

C Logarithmic smoothing algorithm **203**

List of Figures

2.1 Top and side views of a snapping shrimp 13

2.2 Sketches of shrimp claw closure 14

2.3 Detail of an individual shrimp snap 15

2.4 Shallow water ambient noise spectrum 16

2.5 Shrimp noise spectra at various locations 17

2.6 An empirical probability density function of real shrimp noise compared with a Gaussian fit 18

3.1 Probability density function of real shrimp noise and a Gaussian fit. . . 27

3.2 Probability density function of real shrimp noise and a Gaussian-Gaussian mixture fit 29

3.3 Probability density of real shrimp noise and a SαS fit 34

3.4 SαS parameter α estimated for shrimp noise from various locations around Australian shores. 35

3.5 Simulated locations of shrimp uniformly distributed in a circular field on the seabed 40

3.6 Propagation environment assumed for the Garnele distribution 42

3.7 A pictorial description of the difference between switching and additive combination of random variables 48

3.8 SαS and Gaussian-Garnele models fitted to AWharf noise. 52

3.9 Relative difference between SαS and Gaussian-Garnele models and the pdf of AWharf noise. 53

3.10 SαS and Gaussian-Garnele models fitted to Cockburn Sound noise. . . . 54

3.11 Relative difference between SαS and Gaussian-Garnele models and the pdf of Cockburn Sound (CS-B) noise. 55

3.12 SαS and Gaussian-Garnele models fitted to Busselton Jetty noise. . . . 57

3.13 Relative difference between SαS and Gaussian-Garnele models and the pdf of Busselton Jetty noise. 58

3.14 SαS and Gaussian-Garnele models fitted to Nornalup-Walpole estuary noise. 59

3.15 Relative difference between SαS and Gaussian-Garnele models and the pdf of Nornalup-Walpole Estuary noise. 60

3.16 Frequency response of the receiver used to measure shrimp noise used for down-sampling analysis 63

3.17 Split-log plot of probability density versus pressure amplitude for down-sampled real shrimp noise 64

3.18 Hydrophone setup used for the pdf asymmetry experiment 66

3.19 Asymmetry between positive and negative pressure probability densities observed in real shrimp noise 67

3.20 Shrimp noise amplitude pdf asymmetry function 68

3.21 Amplitude pdf asymmetry for wide bandwidth data from Cockburn Sound 70

3.22 Amplitude pdf asymmetry for low sample rate data from Cockburn Sound 71

4.1 Example point process showing how counts and intervals are computed . 76

4.2 Effect of the pre-detection filter on a single shrimp snap 79

4.3 Spectrum of shrimp noise before and after pre-detection filtering 80

4.4 SnapDetection 81

4.5 Inter-event interval probability density functions 86

4.6 Anderson-Darling statistic summary 87

4.7 Uniform conditional test summary 89

4.8 K^{th}-order intervals for the homogeneous Poisson control 93

4.9 K^{th}-order intervals for Spencer Gulf 94

4.10 K^{th}-order intervals for Cockburn Sound 95

4.11 K^{th}-order intervals for the Nornalup-Walpole Estuary 96

4.12 K^{th}-order intervals for Seal Island 97

4.13 K^{th}-order intervals for Feather Reef 98

4.14 Real shrimp noise snapping intensity as a function of time 101

4.15 Intensity estimated from simulated homogeneous Poisson events 102

4.16 Gaussian representation of rate distribution as a function of window size. 103

4.17 Snapping intensity variance as a function of window size (simulated snaps).104

4.18 Normalised intensity variance as a function of window size (real shrimp noise) 105

4.19 Method used to compute Fano-factors for different counting times . . . 108

4.20 Dead-time and regularity corrections for the Fano-factor. 110

4.21 Combined dead-time and regularity corrected Fano-factor curve. 111

4.22 Fano-factor guide levels for homogeneous Poisson events 113

4.23 Fano-factor results for homogeneous Poisson control data 115

4.24 Fano-factor results for Spencer Gulf data 116

4.25 Fano-factor results for Cockburn Sound data 117

4.26 Fano-factor results for Nornalup-Walpole Estuary data 118

4.27 Fano-factor results for Seal Island cave data 119

4.28 Fano-factor results for Feather Reef data 120

4.29 Percentage of Fano-factor values outside the guide levels 121

4.30 Short-time features of shrimp noise Fano-factor curves 122

4.31 Medium and long-time features of shrimp noise Fano-factor curves . . . 123

4.32 Fano-factor short time rise and plateau from Cockburn Sound data . . . 125

4.33 Fano-factor short time results with surface reflections manually removed 126

4.34 A sample of Ornstein-Uhlenbeck noise and corresponding (coloured) power spectral density 129

4.35 Gaussian fits to intensity distributions of real shrimp noise 131

4.36 Gamma fits to intensity distributions of real shrimp noise 133

4.37 Fano-factor variability of simulated CIR doubly-stochastic Poisson data. 135

4.38 Comparison of Fano-factors between the CIR model and real shrimp noise 139

4.39 Snap rates as a function of time for the 24 hour data 143

4.40 Snap rate probability density function for 24 hour data 144

4.41 Fano-factor as a function of counting time for the 24 hour data 145

5.1 A section of simulated ocean ambient noise time-series 150

5.2 Spectral density of simulated ocean ambient noise 151

5.3 Probability density function of simulated ocean ambient noise 152

5.4 Relative difference between SαS and Gaussian-Garnele models for simulated ocean ambient noise. 153

5.5 K^{th}-order intervals of simulated ocean ambient noise 154

5.6 CIR driven doubly-stochastic Poisson fit to the Fano-factor of simulated ocean ambient noise 155

5.7 ROC curves for SαS, Gaussian-Garnele, Gaussian-Gaussian mixture and Periodogram detectors. 158

5.8 Probability density function of shrimp noise amplitudes with SαS and Gaussian-Garnele model fits. 159

A.1 Hydrophone sensitivity and recorder response used to measure the AWharf (AW) data 175

A.2 Hydrophone sensitivity and recorder response curves used to measure the Busselton (BUWO) data 177

A.3 Hydrophone sensitivity and recorder response used to measure the Cockburn Sound (CS-A and CS-D) data 180

A.4 Hydrophone sensitivity and recorder response used to measure the CS-B data 182

A.5 Vertical and horizontal hydrophone directivity at 100 kHz 183

A.6 Combined hydrophone and recorder response used to measure the CS-C data 185

A.7 Vertical and horizontal hydrophone directivity at 100 kHz 186

A.8 Nominal hydrophone sensitivity and recorder response used to measure the Walpole (WP) data 188

A.9 Local wind record for the day of the 24 hour measurement 190

A.10 Rigging used to hold the hydrophone for the 24 hour measurement . . . 191

A.11 Hydrophone sensitivity and recorder response used to measure the 24 hour data 192

B.1 Nominal hydrophone sensitivity and recorder response used to measure the Seal Island (SEAL-A and SEAL-B) data 195

B.2 Nominal hydrophone sensitivity and recorder response used to measure the Feather Reef (FR) data 198

B.3 Nominal hydrophone sensitivity and recorder response used to measure the Spencer Gulf data 200

B.4 Hydrophone sensitivity and recorder response used to measure the Sydney Harbour (SYD-A and SYD-B) data 202

List of Abbreviations

Symbol	Meaning
A^2	Anderson-Darling
AR	autoregressive
ARMA	autoregressive moving average
BWF	Broadcast Wave Format
°C	degrees Celsius
cdf	cumulative distribution function
CFAR	constant false alarm rate
CIR	Cox-Ingersoll-Ross (process)
CS	Cockburn Sound
D	Kolmogorov-Smirnov (statistic)
DAT	digital audio tape
dB	decibel
DSPP	doubly-stochastic Poisson process
DTMP	dead-time modified Poisson (process)
epdf	empirical probability density function
ENBW	equivalent noise bandwidth
EWMA	exponentially weighted moving average

Symbol	Meaning
FF	Fano-factor (or index of dispersion of counts)
FFT	fast Fourier transform
FR	Feather Reef
GG-mix	Gaussian-Gaussian mixture
HPSIM	homogeneous Poisson simulated (data)
IIH	inter-snap interval histogram
MA	moving average
NFFT	Number of FFT points
OU	Ornstein-Uhlenbeck (process)
pdf	probability density function
PVC	polyvinylchloride
QE	Quasi-equivalent
ROC	receiver operating characteristic
SαS	Symmetric-α-stable
SEAL	Seal Island
SG	Spencer Gulf
SL	source level
SNR	signal to noise ratio
SYD	Sydney (Pyrmont)
UCDWR	University of California's Division of War Research
UK	United Kingdom
W^2	Cramér-von Mises (statistic)
WP	Nornalup-Walpole Estuary

Chapter 1

Introduction

Olla hiljaa, niin saada kaloja
Be quiet and we'll catch some fish
(Finnish saying)

The problem of detecting signals in noise is fundamental. There are many different types of noise in the oceans, some are produced by natural phenomena such as seismic activity, surface agitation (due to the wind) and rain. Others have biological or man-made origins. Some of these noises are fairly constant such as distant shipping noise, others are infrequent but may last for an extended period of time, for example air-gun noise from seismic surveys. Many of the noises in the ocean combine so that the distribution of pressure amplitudes is approximately Gaussian, and consequently an additive Gaussian noise model is often chosen for use in underwater acoustic signal processing algorithms (Chitre et al. 2008). In warm, shallow waters the acoustic activity of snapping shrimp introduces a sustained, impulsive (and therefore non-Gaussian) noise into the ocean. Scientists from the University of California Division of War Research were among the first to identify snapping shrimp noise as a serious concern for sonar (Inman 2003). In general the performance of linear correlation receivers are degraded in the presence of impulsive noise (Aazhang & Poor 1987) and this is true for

such receivers operating in snapping shrimp noise (Chitre et al. 2006). Snapping shrimp noise will also degrade the performance of conventional sonar (Bertilone & Killeen 2001) and traditional communication techniques (Chitre 2007, Aazhang & Poor 1987) when operated using the acoustic frequency band where shrimp noise is dominant.

1.1 Thesis aims

The aim of this thesis is to further understand the impulsive noise produced by fields of snapping shrimp, with a view to improving sonar detection and communication in such noise. Justification for expending effort on understanding the statistical properties of snapping shrimp noise, not just because snapping shrimp are interesting, but also for improving signal processing is provided by Middleton's general rule (Middleton 1995):

> *...the more relevant information regarding both the signal and noise that is properly used, the better the performance.*

The following research activities were chosen for their relevance to fundamental understanding of shrimp noise, and their potential for improving signal processing algorithms used in sonar and underwater communication systems:

1. Review non-Gaussian amplitude models of snapping shrimp noise
2. Derive a phenomenological amplitude model of noise received at a hydrophone
3. Initiate a study of snapping shrimp noise as a point process in time
4. Apply amplitude and temporal statistics to a simulation of ocean acoustic noise
5. Investigate the use of non-Gaussian models applied to a fundamental detection problem.

The first three aims were to investigate shrimp noise from a fundamental point of view and to provide new statistical information about the shrimp noise. The last two aims were intended to both demonstrate and investigate the application of this knowledge to practical problems.

1.2 Research methodology

Amplitude and temporal models of shrimp noise are investigated. The analysis is conducted from the point of view of a single hydrophone placed in the water, and so the models are appropriate for received pressure levels of shrimp noise combined with all other sources of ambient noise. Established or commonly assumed models of the temporal and amplitude statistics are investigated and some new models are developed. Where possible the models are explained from a physical point of view and comparisons are made using real ambient noise.

Amplitude models were considered in terms of first order probability density functions of the instantaneous pressure amplitudes at a receiving hydrophone. Candidate models were drawn from the existing body of knowledge, and a new heuristic model was derived from first principles as a dedicated model of shrimp noise with an analytic probability density function. The models were tested for goodness of fit to real ambient plus shrimp noise using visual comparison of probability density functions, aided by plots showing the relative difference between theoretical and empirical results.

Temporal analysis techniques were sourced from scientific fields such as optics and neuro-physics, and applied to the problem of snapping shrimp noise. Two of the techniques were based on first order statistics and all subsequent techniques made use of higher order statistics. All of the temporal analyses were conducted using real snapping shrimp noise with simulated data used only in a secondary confirming (rather than establishing) role. Conclusions were supported by formal statistical testing, most often using the Anderson Darling A^2 statistic because of important information in the tails of

the relevant distributions. One of the analysis methods (Fano-factor analysis) did not admit a formal statistical test because the required distributions were not known. In place of a formal test, a pseudo-test was applied using guide levels and containment (the percentage of points residing within a set of guide levels). All tests (and pseudo-tests) were conducted at the 95% confidence (or 95% containment) level. Visual comparisons were used when formal statistical tests could not be applied.

To demonstrate a practical application of the amplitude and temporal statistical models, a simulated pressure time-series was produced and some of the analysis used in the amplitude and temporal sections were applied to the simulated data. Visual judgement was used to compare results from simulated data with similar results from real shrimp noise. A check of parameter consistency was conducted by comparing the parameters used to produce the simulated noise with parameters obtained from the analysis techniques. The parameters were found to be consistent.

Amplitude models were used to produce locally optimum detectors. The locally optimum detectors were applied to the problem of detecting narrow-band signals in real shrimp noise. Receiver operating characteristic (ROC) curves were produced by adding synthetic signals (with pre-determined signal to noise ratio) into a representative set of real shrimp noise. Detector performance is defined using the detection threshold (the signal-to-noise ratio giving a probability of detection of one half) and the results are discussed.

1.3 Supporting field work

The project was intended to use real shrimp noise for all analyses; a large amount of effort was expended gaining expertise in wide-band underwater acoustic measurement. The following lists itemise the field measurements and data sets used for this project:

1. Ambient noise measurement at the AWharf jetty, Western Australia (AW).

2. Ambient noise measurement at the Busselton jetty, Geographe Bay, Western Australia (BUWO).

3. Several field measurements from a set of pontoons in Cockburn Sound, Western Australia (CS-A to CS-D).

4. An exploratory measurement from the Rest Point jetty in the Nornalup-Walpole Estuary, Western Australia (WP).

5. A field experiment to investigate an asymmetry in the pressure amplitude distribution.

6. A 24 hour measurement at the AWharf to investigate long counting time effects (AW-24).

In addition to field measurements, several sets of data were sourced from measurements made by other people:

1. Ambient noise data from Seal Island, Western Australia (SEAL-A to SEAL-C) provided by Dr Dave Matthews.

2. Ambient noise data from Feather Reef, Queensland, Australia (FR) provided by Dr Rob McCauley.

3. Ambient noise data from Spencer Gulf, South Australia (SG) provided by Dr Doug Cato.

4. Ambient noise data from Sydney Harbour, New South Wales, Australia (SYD-A and SYD-B) provided by Dr Dave Matthews.

Careful review of the data was conducted to ensure that the field data were of high quality and suitable for the analysis presented in this thesis. Details of field measurements are given in Appendix A and the available details of data sets from other people are in Appendix B.

1.4 Thesis format and outline

The format of the thesis is based on large individual chapters, with each chapter containing discussion and a summary. Introductory material is presented at the beginning of the thesis before splitting into two separate topics: amplitude statistics and temporal statistics. An application chapter is used to rejoin the concepts from both topics, followed by some selected discussion and the thesis conclusions.

Thesis chapters are organised as follows:

Chapter 1 (this chapter) outlines the motivations, aims, and research methodologies used for the thesis.

Chapter 2 provides background information on underwater acoustic noise and snapping shrimp.

Chapter 3 reviews non-Gaussian amplitude models of snapping shrimp noise, then proceeds with a theoretical derivation of a heuristic model of snapping shrimp noise received at a hydrophone. Goodness of fit of the amplitude models to selected real ambient plus shrimp noise are conducted and the results discussed. The issue of probability density function asymmetry (between positive and negative pressure amplitudes) is addressed, and some conclusions are drawn from the results of a field experiment.

Chapter 4 initiates a study of the temporal nature of snapping shrimp noise. A number of candidate analysis methods are drawn from other scientific fields and applied to the problem of snapping shrimp noise. A threshold event detection method (and associated data processing) is described and some of the consequences discussed. Analysis of the shrimp snap events, as a point process, proceeds with techniques based on interval and count distributions. The relative strengths of the techniques for analysing shrimp noise are discussed and the most promising analysis techniques identified. Short time effects are discovered and the cause identified. Other medium and long time effects

are investigated using some doubly-stochastic Poisson models, but the origins of these effects remain unidentified.

Chapter 5 contains applications of the amplitude and temporal models to simulation of ocean acoustic noise. A simulated time-series of pressure received by a hydrophone is generated using only a series of random number generators. Some of the analysis presented in the thesis is applied to the simulated noise to show how well the properties of the real noise are reflected in the simulation. Finally an investigation of locally optimum detectors (based on the amplitude models) was conducted using a fundamental detection problem. Results are shown using receiver operating characteristic curves.

Chapter 6 discusses some selected aspects of the amplitude and temporal models arising from, and relating to, their use in practical applications. Implications of new results for sonar detection and communication are also discussed and some potential applications identified.

Chapter 7 presents the thesis contributions and conclusions, followed by a summary of topics for further investigation.

Chapter 2

Snapping shrimp noise

In shallow water, one of the dominant and persistent noise sources is the snapping shrimp (Cato & Bell 1992). The noise caused by snapping shrimp has long been observed and studied, with an early reference to an unknown "crackling" sound in the water reported by Hulbert (1943). Hulbert points out that fishermen had observed the noise, and presumed the noise was caused by toadfish gnashing their teeth. This theory on the origin of the noise was considered by Hulbert, although he admits to not knowing if toadfish have any teeth. The noise from snapping shrimp had also been observed by naval personnel as cited in a 1946 report by the University of California's Division of War Research (UCDWR) (University of California Division of War Research 1946). The report also describes the shrimp species and their snapping mechanism, the geographical distribution of shrimp throughout the world, characteristics of shrimp fields including transmission from shrimp beds, depth dependence, diurnal variations and masking of signals by the noise produced by shrimp fields. A related publication by Everest et al. (1948) also describes the acoustical characteristics of noise produced by snapping shrimp. In their paper they discuss ambient noise over shrimp beds, diurnal and seasonal variations in shrimp spectra, and include an oscillogram of an individual shrimp snap. The oscillogram contains detailed acoustic information about the shrimp snap. This acoustic information has only recently been understood (Versluis et al.

2000).

In this chapter some background information on snapping shrimp is provided, including where they are found, how they snap and how the snapping of groups of shrimp contributes to the ambient noise of the ocean.

2.1 Snapping shrimp

Snapping shrimp (also called pistol shrimp) are small shrimp, usually only a few centimetres long. The distinguishing physical feature of the shrimp is a single enlarged claw, as can be seen in Figure 2.1. The claw is used to produce a loud impulsive snapping sound. Snapping shrimp belong to the family *Alpheidae* of which the genera *Alpheus* and *Synalpheus* are reported to snap vigorously (Cato & Bell 1992, Potter et al. 1997b, Readhead 1997).

Typical habitat for snapping shrimp are warm shallow waters where debris or structures exist that allow the shrimp to hide. Shrimp are commonly found in waters warmer than 11°C, which corresponds roughly with 40 degrees of latitude (see for example University of California Division of War Research (1946) and Cato & Bell (1992)). Shrimp are rarely observed in water depths greater than 60 m, however shrimp have been found in 450 m depths (Cato & Bell 1992). Shrimp tend to favour debris covered sea floors and reefs or other structures that provide a place to hide, such as piers, wharfs and rock walls.

Snapping shrimp use their snaps for self defence and for stunning or killing prey (Versluis et al. 2000). The snapping sound is caused by a cavitation bubble (described in Section 2.2) that is also highly destructive and can cause damage to attackers or prey. It is difficult to imagine that these purposes alone would result in the persistent snapping observed through both day and night. There is some speculation about other uses for the snaps, including communication. In close encounters shrimp respond to snaps from

other shrimp and have the potential to analyse the snap using hydrodynamic receptors on the snapping claw (Herberholz & Schmitz 1998).

2.2 Acoustic characteristics of individual shrimp snaps

It was discovered (Versluis et al. 2000) that the noise produced by snapping shrimp was not due to the claw banging closed, but by the collapse and rebound of a cavitation bubble. The evolution of a shrimp snap is illustrated in Figure 2.2 with an accompanying example acoustic time-series in Figure 2.3. The sketches shown in Figure 2.2 were based on high speed (approx. 2000 frames-per-second) video footage from http://stilton.tnw.utwente.nl/shrimp/video.html. To produce a cavitation bubble, shrimp start with their enlarged claw open Figure 2.2(a), then the claw is snapped closed and a plunger shoots a high speed jet of water into the surrounding water (b-c). The action of the jet of water creates a cavitation bubble (d) that grows, collapses (e-f) and then rebounds (f-g). The term rebound is used here to describe the point of total collapse of the cavitation bubble and coincides with an intense positive acoustic pressure pulse. Rebound is followed by rapid destruction of the bubble (h) due to Rayleigh-Taylor type instability (Versluis et al. 2000). Bubble destruction occurs before any secondary oscillations.

Shrimp snaps produce a highly impulsive acoustic signal. Peak-to-peak source levels can be as high as 189 dB re 1 μPa at 1 m (Ferguson & Cleary 2001). The bandwidth of a shrimp snap is among the widest of any biological source. The upper frequency limit of the snap extends beyond 250 kHz (Cato & Bell 1992), with theoretical models (Versluis et al. 2000) predicting pulse widths as small as 100 ps, or an upper frequency limit of 10 GHz. In practice the observed upper frequency limit will be less than the theoretical prediction due to the low-pass filtering effect of the ocean (Chitre et al. 2003).

2.3 Snapping shrimp and ambient noise

Ambient noise in the ocean is defined as the persistent noise that is independent of the method used to observe it (Urick 1986). Dominant sources contributing to the sustained ambient noise in the ocean are seismic and turbulence activity, distant shipping, surface agitation, and thermal noise due to molecular agitation. Noise levels observed in deep and shallow waters differ and are frequency dependent.

Empirical deep water noise curves taken from Wenz (1962) and Coates (1990) are shown in Figure 2.4, along with the results of a field measurement conducted at the AWharf site (a Jetty located near 32°10′36.3″S, 115°40′42.7″E). In deep water, seismic activity and hydrostatic effects are mainly responsible for noise below 10 Hz. Distant shipping noise dominates the spectrum between 10 Hz and 100 Hz. In this region the noise levels can be expected between 75 dB and 95 dB relative to $1\mu\text{Pa}^2/\text{Hz}$ at 10 Hz reducing in trend by 7 dB per octave (approx. 23 dB per decade), and broadening slightly, to give an expected range from 50 dB to 75 dB at 100 Hz. Sea surface activity due to wind and rain becomes the dominant noise source from 100 Hz up to 100 kHz. Noise spectrum levels over this relatively wide band are correlated with sea state. A 5 dB per octave (approx. 17 dB per decade) decrease in noise levels is shown between 1 kHz and 10 kHz, steepening slightly to 6 dB per octave between 10 kHz and 100 kHz. At higher frequencies thermal noise reverses the trend and noise levels increase with increasing frequency. In deep water the frequency of intersection of these two slopes will depend primarily on sea state.

Ambient noise in shallow waters differs from that in deep water. The propagation of sound through shallow water tends to reduce the contribution from distant shipping, to the point that surface agitation may become the dominant source at these frequencies as well as higher frequencies (Urick 1986). In addition to propagation effects in

shallow waters, there are additional noise sources that may provide persistent or periodic contributions to the noise in shallow waters, depending on location. These noise sources tend to be either biological or man-made, some examples are: fish choruses in tropical waters, near-shipping noise in or around harbours and ports, and snapping shrimp noise in tropical and temperate waters. The AWharf was a shallow water site, with local shipping noise causing relatively high noise levels below 300 Hz. At 300 Hz the AWharf noise agreed with the expected noise for the sea state 1 conditions under which the measurements were taken. The noise levels rise significantly for frequencies greater than 300 Hz due to a local field of snapping shrimp. At 4 kHz the AWharf snapping shrimp noise levels peak at 70 dB re $1\mu\text{Pa}^2/\text{Hz}$, which is 23 dB greater than the expected (sea state 1) noise level.

At locations where snapping shrimp are acoustically active, the noise produced by fields of shrimp will persistently contribute to the local ambient noise. The noise levels produced by fields of shrimp are location dependent, with factors such as the number of shrimp in the field and snapping activity of the shrimp affecting the overall noise levels. In Figure 2.5 several spectra from different locations are presented on the same plot to illustrate the differences in shrimp noise. Colour groups have been used in the figure to indicate locations that are in the same region. Locations that are not part of a region group are plotted using black lines. The blue line region is the north-east of Australia and here shrimp noise levels vary by as much as 15 dB. The green plot region is near San Diego and showed variation up to 12 dB. The greatest overall difference in noise level is 35 dB at 10 kHz, between the locations of Kaneohe Bay and San Diego Harbour. These spectra show that large variations can be expected in snapping shrimp noise levels, both between locations that are in the same region as well as between locations that have large geographic separation.

Figure 2.1: Images of a snapping shrimp taken from above and from the side. The shrimp has a single enlarged claw (chela) that is used for snapping. (Major scale markers are centimetres)

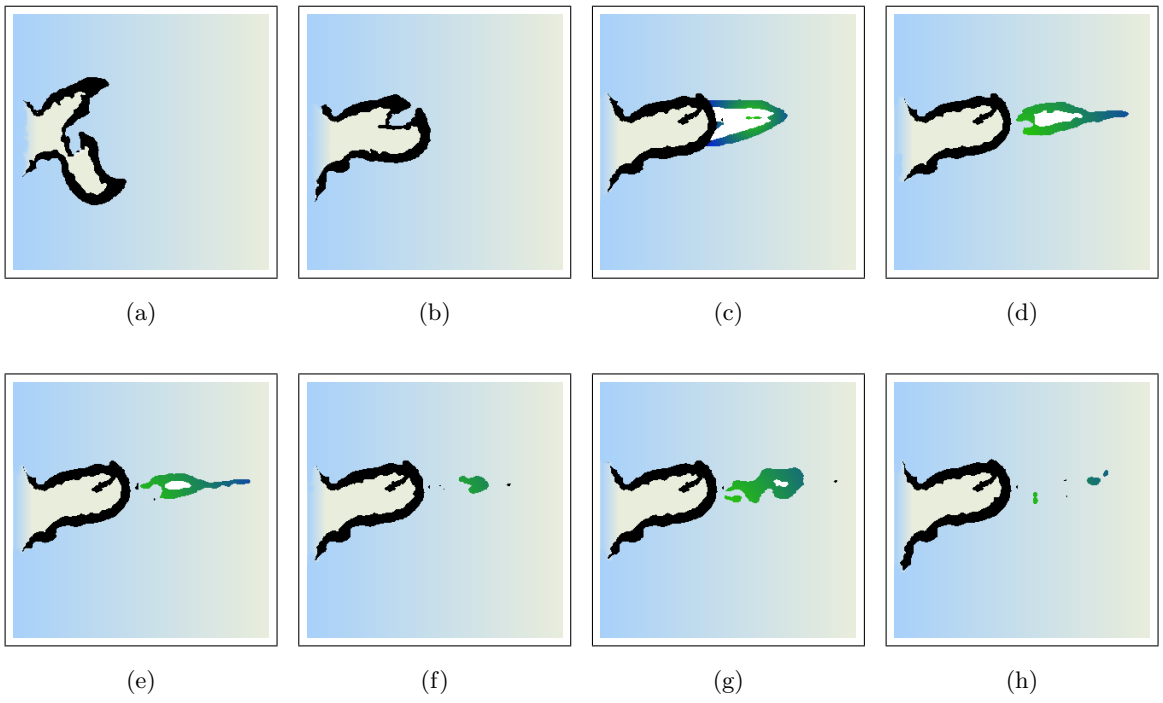

Figure 2.2: Sketches showing shrimp claw closure and bubble development. The shrimp starts with its claw open (a) then rapidly closes the claw (b), which activates a plunger that shoots a high-speed jet of water out from the claw (c). A cavitation bubble is created by the jet of water shooting into the surrounding water (d). (Sketches based on high speed video footage from URL http://stilton.tnw.utwente.nl/shrimp/video.html)

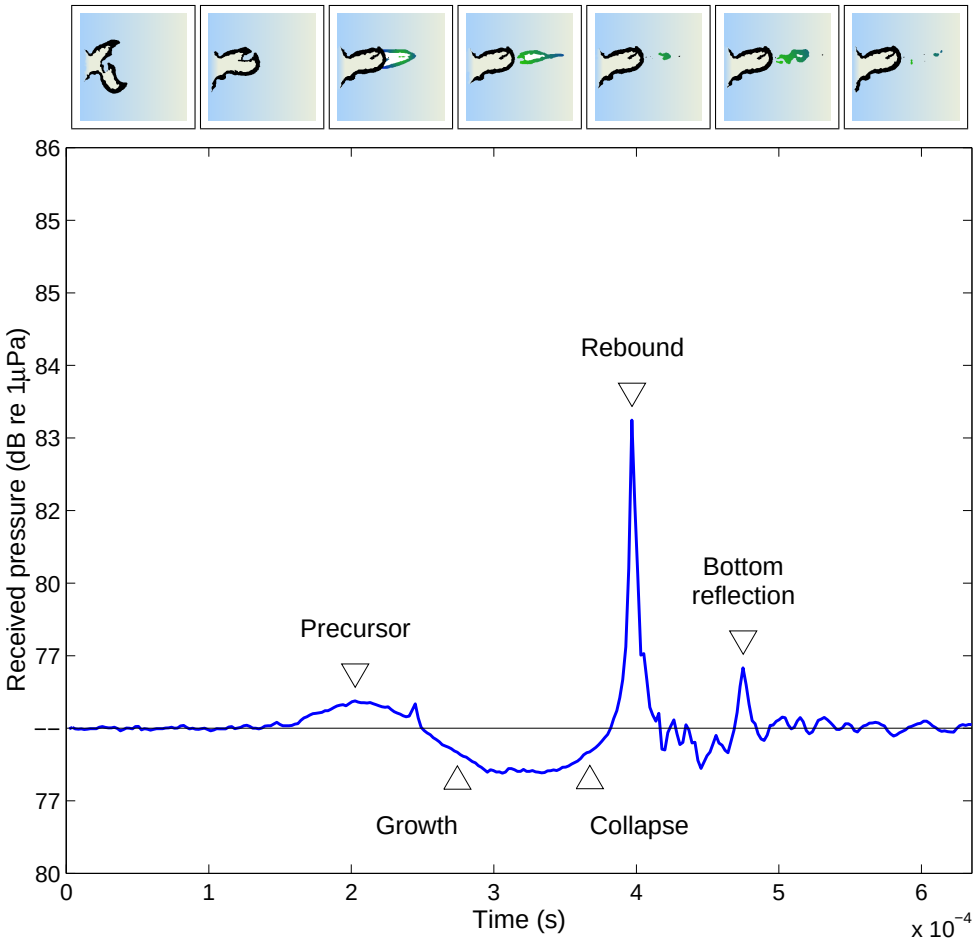

Figure 2.3: The acoustic signature of an individual shrimp snap. The snap starts with a precursor pulse caused by the claw closure, then the cavitation bubble develops, collapses and rebounds to give a high positive pressure peak.

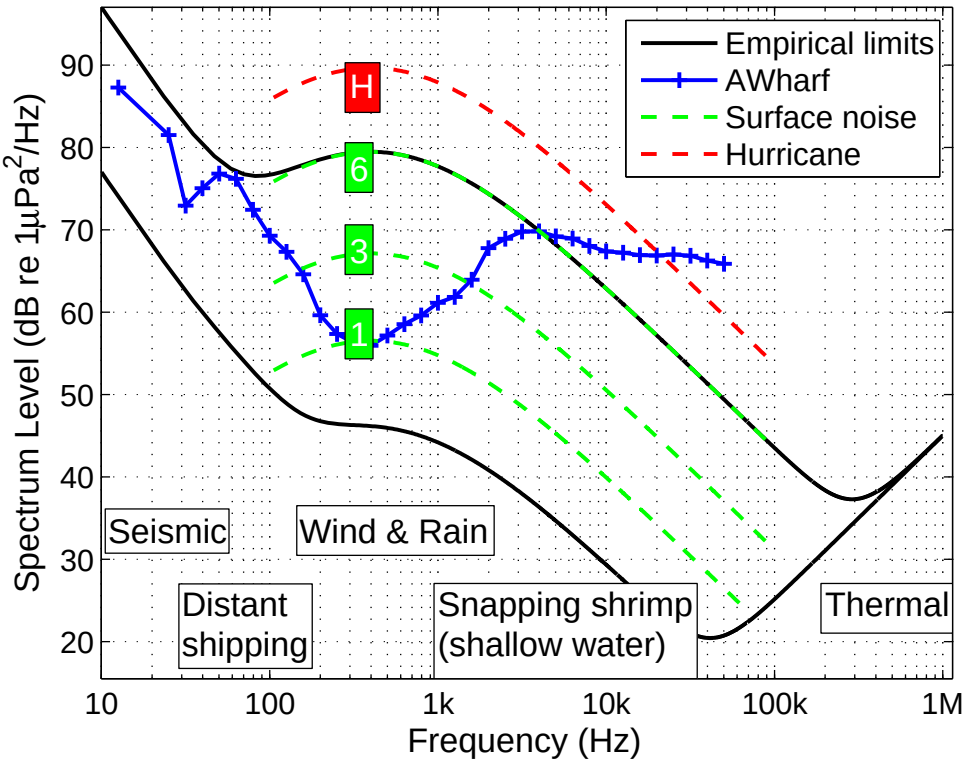

Figure 2.4: Ambient noise in the ocean. Typical dominant noise sources are listed at the bottom of the figure near the frequency band they influence. Empirical limit curves from Coates (1990) show nominal maximum and minimum noise levels (solid black lines) along with nominal noise levels at sea states 1, 3 and 6 (green dashed lines) and the extreme case of a hurricane (red dashed line). A noise spectrum, averaged over 1/3 octaves, from measurements at the AWharf site (solid blue crossed line) is shown. The increase in noise level for the AWharf spectrum beyond 1 kHz is due to snapping shrimp.

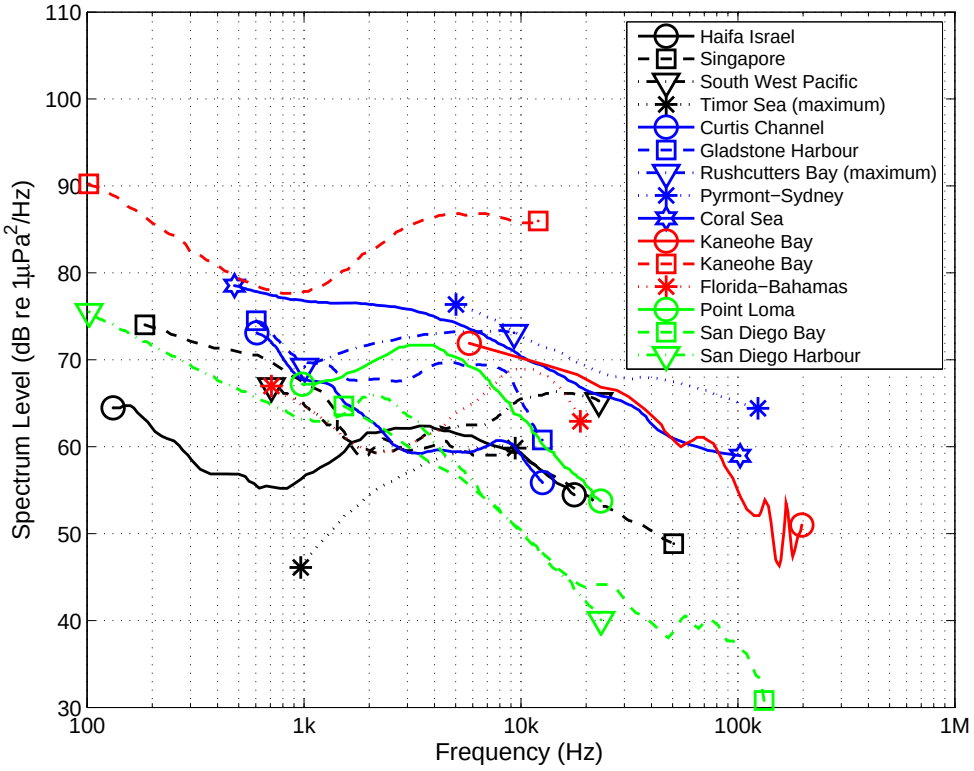

Figure 2.5: Shrimp noise spectra at various locations around the world. The colouring is a rough grouping of spectra by region. There seems to be little consistency between spectra; the shrimp noise is location dependent. The curves are hand interpretations of results from Au & Banks (1998), Bardyshev (2007), Cato & Bell (1992), Everest et al. (1948), Potter et al. (1997a), Readhead (1997, 1994) and Widener (1967).

In addition to increasing the ambient noise levels at frequencies beyond 1 kHz, snapping shrimp noise also makes the distribution of pressure amplitudes non-Gaussian. The snaps produce many more high pressure amplitude values than would be expected for a Gaussian distribution. A probability density function (pdf) of pressure amplitudes taken from real ambient noise (that contains shrimp noise) is shown in Figure 2.6. The blue markers are empirical pdf values computed from the ambient noise, and the red line shows the pdf of a Gaussian fit to the data. As the pressure amplitudes increase in both positive and negative directions, the probability density of the ambient noise is higher than the Gaussian. In this case, the ambient noise distribution is said to have a *heavy tail* because the extreme values have a higher probability than expected

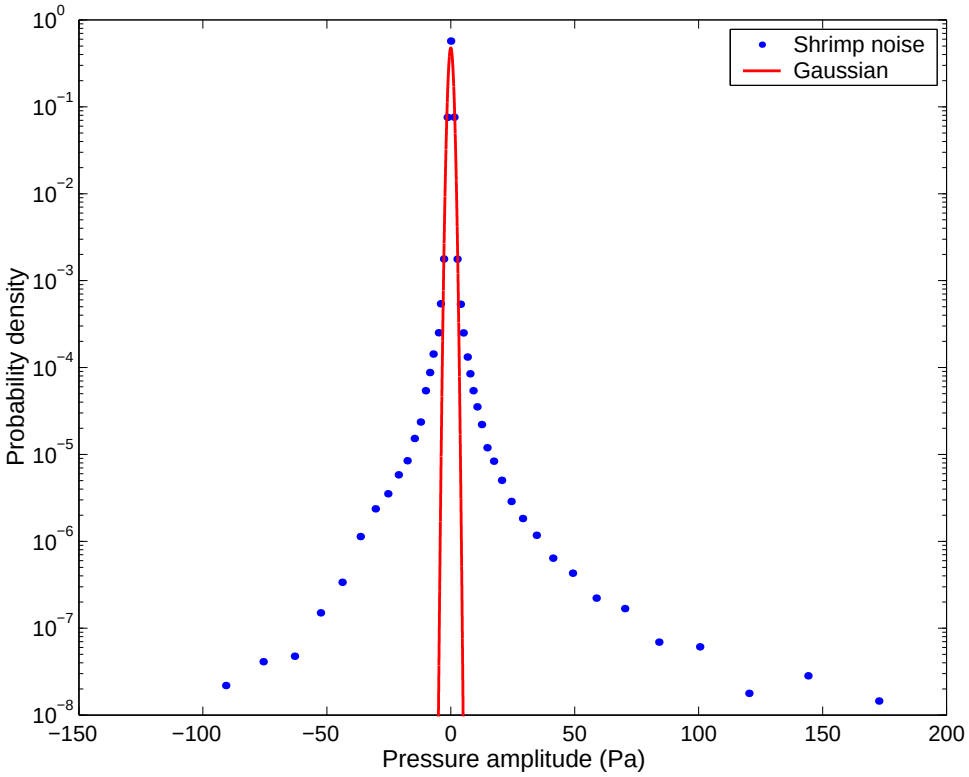

Figure 2.6: An empirical probability density function of real shrimp noise from field measurements in Cockburn Sound (blue dot markers). Also shown is a Gaussian fit to the data (red solid line).

for a Gaussian. Detection algorithms that make decisions based on an assumption of Gaussian distributed noise will experience a high rate of false alarms in such heavy tailed noise (Bertilone & Killeen 2000). It is therefore important that more appropriate non-Gaussian noise models of shrimp noise be developed. Detection algorithms using these non-Gaussian noise models will suffer fewer false alarms when operating in areas where shrimp noise is prevalent.

2.4 Shrimp noise analyses and applications

Acoustic characteristics of snapping shrimp have been measured using several different techniques and in various locations. Each measurement seeks to explore one or more

of the amplitude, spatial or temporal characteristics of the noise. Shrimp noise can be analysed on different scales, for example, the acoustic signal of an individual snap is quite different from the noise produced by a group of shrimp. The term *micro-scale* refers to individual shrimp, such as the individual's location or the acoustics of an individual snap. *Macro-scale* refers to a group of shrimp, such as a cluster of shrimp around a wharf or pier, or the acoustic noise produced by a shrimp field or across a region containing many shrimp fields.

Amplitude measurements of snapping shrimp are typically taken using a pressure transducer (hydrophone) and analysed to give a noise power level spectrum (noise levels as a function of frequency). For some of these measurements the aim is to present the snapping shrimp spectrum for a specific location against snapping shrimp spectra from other locations, (see for example Readhead 1997), while others compare with dominant contributions to the persistent ambient noise spectrum, such as wind noise (Cato & Bell 1992), and shipping and rain (Potter et al. 1997a). Motivation for making such measurements include using ambient noise to mask other sounds, such as engine noises from a vessel, or to gain some *a priori* knowledge of the noise environment against which a piece of equipment must operate, such as an underwater communication device. Fewer, more specialised experiments have been conducted to estimate snap source levels, either from a field of shrimp, or from an individual shrimp in an acoustic tank. Experiments of this type require more sophisticated equipment and analysis to obtain additional information such as shrimp location, or to exclude unwanted reflections from tank walls. Examples of systems used for estimating snap source levels are the wavefront curvature technique using a linear hydrophone array used by Ferguson & Cleary (2001), and the tetrahedral array used by Beng et al. (2003). Measurements of individual shrimp snaps in acoustic tanks have been conducted by Au & Banks (1998) and Versluis et al. (2000) to discover both individual source levels and micro-scale detail in the acoustic signature. These measurements use high speed data acquisition systems to allow the detail in the snaps to be seen over the impulse response of the acquisition system, and to allow separation of direct path signals from other spurious signals such as reflections from tank walls.

Spatial analyses seek to discover the location or distribution of shrimp in fields or as individuals. Such analyses allow correlations between shrimp fields and ambient noise levels, or other ocean environment factors such as bottom type. Higher shrimp noise levels tend to occur when the sea-floor contains rocky and coral outcrops or where debris covers the floor. Lower shrimp noise levels occur over mud or sand (Cato & Bell 1992). The spatial distribution of shrimp is also very important if the shrimp noise is to be used as a noise source, such as for the *acoustic daylight* project (Buckingham et al. 1992). Studies of spatial distributions of shrimp for this purpose using parabolic mirror hydrophones, a tetrahedral hydrophone array, and a sophisticated ambient noise imaging array can be found in Potter & Koay (2000), Beng et al. (2003), Chitre et al. (2003) and Venugopalan et al. (2003). These studies showed that spatial anisotropy variations of ± 2 to ± 3 dB about the mean can be expected.

Locating the position of individual shrimp is also useful for estimating snap source levels. Ferguson & Cleary (2001) used a wavefront curvature technique to locate individual shrimp to within a few centimetres. The study was conducted near a wharf in Sydney harbour and showed that shrimp were clustered about the wharf pylons, presumably using the growth on the pylons for shelter. Both macro and micro scale spatial analyses indicate that shrimp can be expected to be spatially clustered, favouring areas that contain growth or debris. This has implications for non-stationary acoustic systems, for example a sonar being towed, because the noise levels of the shrimp may change rapidly over relatively small distances.

Another important characteristic of shrimp noise is how the snapping varies with time. Temporal variations can include the change in noise intensity from a field of shrimp over days or years (macro-scale), or the detailed analysis of a single snap and how they develop and collapse with time (micro-scale).

Macro-scale observations are reported for measurement sites in San Diego, Kaneohe Bay, Midway Island (Everest et al. 1948), and the Timor Sea (Cato 1980, Cato & Bell 1992). Diurnal observations in all locations except the Timor Sea report consistently

elevated shrimp noise just before sunrise and just after sunset. No consistent diurnal variations were reported for the Timor Sea. Longer term measurements were taken in the Timor Sea and revealed average levels lower in October than July and April, but only by a few decibels. General observations of snapping shrimp noise suggest that the temporal variation in the ensemble noise levels are not likely to exceed 10 dB over short or long timescales.

Micro-scale studies include comparisons between acoustic and video footage to investigate the relationship between cavitation bubble activity and the acoustic signature of individual snaps (Versluis et al. 2000), and identifying bottom reflected and surface reflected replicas of the snap (Chitre et al. 2003).

There is an additional medium-time scale (seconds to minutes) that resides between the extremes of the macro and micro scales described - these are the times at which individual snaps occur relative to each other. Relatively few studies appear to have been conducted regarding this time scale. A Monte-Carlo simulation of interdependent snapping was used by Potter et al. (1997a) to show that interdependence can produce the expected lognormal distribution of received energy, but this was also true for a spatial clustering model. Both spatial and temporal distributions of shrimp noise need to be described statistically, in order to exploit the snaps for ambient noise imaging or for optimising detection algorithms (Potter & Koay 2000). Significant progress has been made in understanding the spatial distribution of shrimp (see for example Chitre et al. 2003), however, more medium-time temporal analysis of shrimp noise is required to complement these spatial distribution studies. Medium-time temporal analyses were conducted as part of this thesis.

2.5 Summary of snapping shrimp noise

This chapter provided some background information on ocean acoustic noise and the impulsive noise created by snapping shrimp. Locations where shrimp noise is likely to

be encountered were described on a macro-scale and micro-scale showing the shrimps' preference for rocky or debris covered sea-floors where rocks, coral and other debris provide opportunities for seclusion. Acoustic characteristics of individual shrimp snaps were described along with the physical mechanism used to produce the snap. The noise produced by fields of snapping shrimp, and how the noise contributes to the ambient noise in warm shallow oceans, was described. Shrimp noise spectra from different locations were plotted on a single figure to illustrate the diversity of noise levels around the world. A probability density function of ambient noise pressure amplitudes was plotted along with a Gaussian fit to illustrate that snapping shrimp noise is non-Gaussian. The current state of knowledge was discussed for amplitude, spatial and temporal characteristics and current best practice was identified for each of these areas.

Chapter 3

Amplitude models

The persistent ambient noise in the ocean is usually due to the combined effect of many individual noise sources spread over a large area, such as surface wave noise, distant shipping noise, and rain. The central limit theorem suggests that the ensemble statistics of such sources should tend to be Gaussian (McDonough & Whalen 1995, Chapter 4). However, analysis of experimental data has shown that the statistics of persistent ambient noise in the ocean is Gaussian only for the deep water case when it contains no shipping noise, and is only stationary for a few minutes (Arase & Arase 1968).

Non-Gaussian noise modelling is a very broad topic. Many naturally occurring processes are non-Gaussian, from the apparent magnitude of stars (Neyman & Scott 1952) to the intensity of solar flares (Newman 2005). An important subclass of non-Gaussian noise is impulsive noise, common in electromagnetic and communication applications and relatively common in underwater (particularly shallow water) acoustics. Models of impulsive noise can be loosely grouped into two types: those that are based on mathematical abstractions (statistical models), such as the Cauchy distribution; and those that are based on the underlying physics of the noise process (physical-statistical models), such as the Middleton Class A and Class B models. Physically based models

provide the benefit of links between parameter values and measurable quantities, but are often overly complicated. Simpler approximations can be used in their place, for example Middleton's ClassA model can be approximated by a Gaussian-Gaussian mixture (see for example Aazhang & Poor 1987, Poor & Tanda 2002). Middleton's Class A and Class B models have not been considered, instead the related Gaussian-Gaussian mixture and α-stable models are considered (Middleton 1999).

In this chapter, the Gaussian, Gaussian-Gaussian mixture, and Symmetric-α-stable models of snapping shrimp noise are discussed. Each model is described by a characteristic function or probability density function, and suitable methods for estimating model parameters (from real data) are outlined. A new model of shrimp noise is derived from first principles, using a physical-statistical approach with some assumptions that are fundamentally different from those used to derive the Symmetric-α-stable model. The Symmetric-α-stable model is compared with the new model using shrimp noise from field measurements at different locations around Western Australian shores. Similarities and differences between the models are discussed.

3.1 Models of snapping shrimp noise

3.1.1 The Gaussian distribution

The Gaussian distribution is often the first candidate for any model of noise. The fundamental motivation for the Gaussian distribution arises from the Central Limit Theorem, which states that a large number of random variables added together under certain conditions will converge to a Gaussian distribution as the number of contributing variables tends to infinity.

Gaussian probability density (pdf) and distribution (also called the cumulative distri-

bution) (cdf) functions are respectively

$$f(x) = \frac{1}{\sqrt{2\pi}\sigma} \exp\left(-\frac{x^2}{2\sigma^2}\right) \tag{3.1}$$

and

$$F(x) = \frac{1}{2}\left(1 + \operatorname{erf}\left[\frac{x}{\sqrt{2}\sigma}\right]\right) \tag{3.2}$$

where x is the dependent variable defined between negative and positive infinity, and σ is the standard deviation. The expected value (or mean) has been omitted because when x represents a pressure fluctuation value, the expected value is zero. The notation $\exp(\cdot)$ and $\operatorname{erf}[\cdot]$ are used for the exponential and error functions respectively.

The standard deviation parameter σ can be estimated for real data using any parameter estimation technique. A commonly used estimator $\hat{\sigma}$ is

$$\hat{\sigma}^2 = \frac{1}{N-1}\sum_{k=1}^{N}(x_k - \mu)^2 \tag{3.3}$$

where μ is the expected value (as mentioned, this is assumed to be zero for acoustic pressure fluctuations), and N is the number of sample values used to compute the estimate.

In certain cases the Gaussian distribution is not an appropriate model for noise. Impulsive noise is typically dominated by a few nearby sources with very loud source levels, transmitting for a very short period of time. Such impulsive noise (from nearby sources) usually does not provide a large enough number of impulse events that overlap at each instant in time, so that the required conditions for the Central Limit Theorem are not met, and the resulting noise is non-Gaussian. This is the case for the impulsive noise caused by snapping shrimp.

Figure 3.1 shows the probability density function of real shrimp noise from a field measurement at the AWharf site (blue dot markers) and a Gaussian fit (red solid line). The probability density function of real shrimp noise was estimated using a scaled quantization level histogram, a histogram with bin width equal to one quantization level of the digital data. Logarithmically spaced bin smoothing was applied to the histogram

estimate to improve the estimates in the tails of the distribution, where count numbers are low (see Appendix C for details of the smoothing algorithm). Probability densities are plotted as a function of pressure amplitude using two log-log plots so that the body and the tails of the distribution can be observed (in sufficient detail) concurrently. The log-log plots are split at the pressure origin to avoid the singularity at zero. Negative pressure values proceed to the left of the origin and positive pressure values to the right, both on a logarithmic scale. This type of plot will be referred to as a *split-log* plot.

The body of the density function (Figure 3.1) shows that the Gaussian fit under-estimates the probability near the mean (zero value), then over-estimates between 0.5 and 2 standard deviations either side of the mean. Permanent deviation occurs beyond 3 standard deviations where the Gaussian fit significantly under-estimates the probability of higher amplitude events. The Gaussian model provides a poor fit to almost all of the observed noise probability densities, which is a typical result for ocean acoustic noise that has impulses from snapping shrimp.

3.1.2 The Gaussian-Gaussian mixture distribution

The Gaussian-Gaussian mixture model (also called other names such as the ϵ-mixture model (Aazhang & Poor 1987), or the contamination model (Martin & Thomson 1982)) arises from a simplification of Middleton's ClassA model (Blum et al. 1999). In this model a relative fraction of two Gaussian distributions are combined together as in Equation 3.4. The relative fraction is determined using a *mixing parameter*, ϵ. Valid values for ϵ are between 0 and 1, to ensure that the probability density is properly scaled (integrates to unity). The probability density function for this distribution is

$$f(x) = \frac{1-\epsilon}{\sqrt{2\pi}\sigma_1} \exp\left(-\frac{x^2}{2\sigma_1^2}\right) + \frac{\epsilon}{\sqrt{2\pi}\sigma_2} \exp\left(-\frac{x^2}{2\sigma_2^2}\right) \tag{3.4}$$

where x is the dependent variable, σ_1 and σ_2 are the standard deviation of each respective Gaussian component. The mean value of each Gaussian is assumed to be zero because x represents pressure fluctuation. The Gaussian-Gaussian mixture model assumes that the background and impulsive noise components "switch" between each

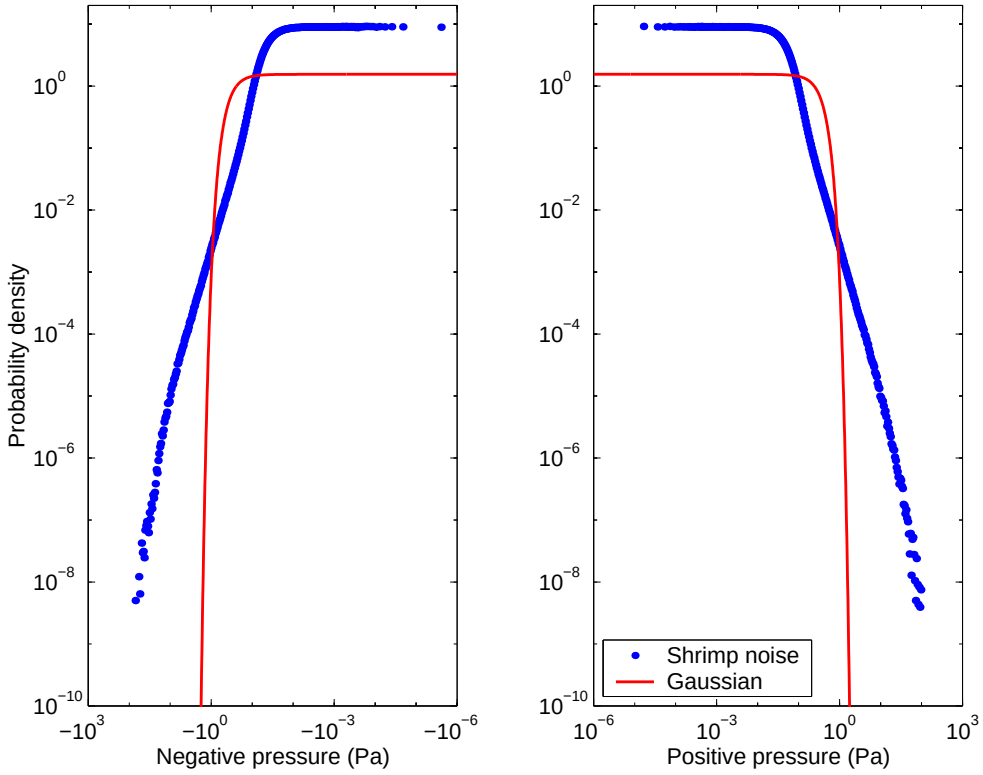

Figure 3.1: Probability density function of real shrimp noise (blue dot markers) from field measurements at the AWharf site. A Gaussian fit (red solid line) provides a poor model of the observed noise distribution.

other, rather than being additive. The variance of the impulsive noise is typically much higher than the variance of the background noise, with factors of 10 to 100 being common (Aazhang & Poor 1988) and factors of up to 1×10^4 considered reasonable (Vastola 1984).

Parameter estimates were obtained for this distribution using the method of moments. The odd moments do not exist for this distribution, since it is a linear combination of two Gaussians that also have no odd moments. The first three even sample moments

(M_2,M_4 and M_6) were computed using

$$M_n(x) = \int_{-\infty}^{\infty} x^n \mathrm{d}\, x \tag{3.5}$$

$$\approx \frac{1}{N} \sum_{k=1}^{N} x_k^n. \tag{3.6}$$

Defining values α, β and γ according to

$$\alpha = M_2^2 - \frac{M_4}{3} \tag{3.7a}$$

$$\beta = \frac{M_6}{15} - \frac{M_2 M_4}{3} \tag{3.7b}$$

$$\gamma = \frac{M_4^2}{9} - \frac{M_2 M_6}{15} \tag{3.7c}$$

$$\tag{3.7d}$$

allows the final moment-based parameter estimates to be expressed as

$$\sigma_1 = \sqrt{\frac{-\beta + \sqrt{\beta^2 - 4\alpha\gamma}}{2\alpha}} \tag{3.8a}$$

$$\sigma_2 = \sqrt{\frac{\frac{M_4}{3} - M_2\sigma_1^2}{M_2 - \sigma_1^2}} \tag{3.8b}$$

$$\epsilon = \left(\frac{M_2 - \sigma_1^2}{\sigma_2^2 - \sigma_1^2} \right) \tag{3.8c}$$

The Gaussian-Gaussian mixture model provides an important benchmark since it is used, or referred to, extensively in non-Gaussian noise modelling. An important characteristic of this distribution is the relative variance of the two Gaussians (Vastola 1984). In this model one of the Gaussians fits the body, while the other fits the tail of the distribution and the transition between the two is abrupt. Figure 3.2 shows a Gaussian-Gaussian mixture fit to real ambient noise data. The abrupt transition (in the mixture model) can be seen near pressure magnitudes of 1 Pa, but is not evident in the shrimp noise; there is a smooth transition between the body and tail of the shrimp noise distribution.

Modelling shrimp noise with a Gaussian-Gaussian mixture cannot be expected to give excellent results, since it is a simplification of Middleton's Class A model. The Class

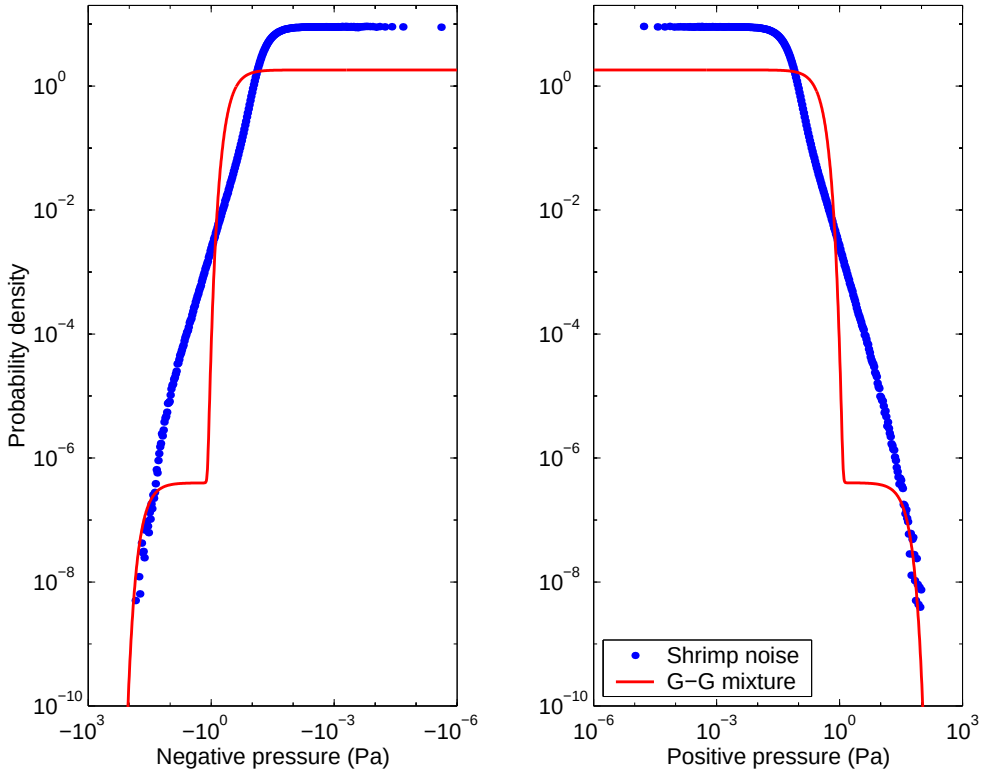

Figure 3.2: Probability density of real shrimp noise and a Gaussian-Gaussian mixture fit, plotted on logarithmic scales. The mixture model uses one Gaussian to fit the body of the density function, and another Gaussian (of significantly higher variance) to fit the heavy tails.

A model was designed specifically for deliberate or "intelligent" impulsive noises, such as interference from other communication signalling, rather than for natural "non-intelligent" noise sources, such as the snapping shrimp.

3.1.3 The α-stable distribution

A family of distributions known as the α-stable distributions have been shown to provide a suitable model for snapping shrimp noise (Chitre 2006, Chapter 3). These distributions are defined, not in terms of their probability density or distribution functions for which there is no analytic expression, but rather their characteristic functions,

that have the general form (Nikias & Shao 1995, Chapter 2)

$$\varphi(t) = \exp\left(i\,at - \gamma\,|t|^{\alpha}\left[1 + i\,\mathrm{sgn}\,(t)\,\beta\,\omega(t,\alpha)\right]\right) \tag{3.9}$$

$$\omega(t,\alpha) = \begin{cases} \frac{2}{\pi}\log|t| & \alpha = 1 \\ \tan\left(\frac{\pi\alpha}{2}\right) & \alpha \neq 1 \end{cases}$$

where a is a location parameter defined on $-\infty < a < \infty$, β is a symmetry parameter between -1 and 1, and γ is a scale parameter greater than zero. Parameter α is called the characteristic exponent and is defined on $0 < \alpha \leq 2$. The value of α measures the thickness (or heaviness) of the tails of the distribution. Small values of α indicate highly impulsive (or heavy tailed) noise, and as the value of α increases the heaviness of the tails reduces until the point when $\alpha = 2$ and the distribution reduces to a Gaussian. When considering acoustic pressure fluctuation the distribution will be expected to be located at zero pressure, so $a = 0$. It may also be assumed under certain circumstances that the distribution will be symmetric, so that $\beta = 0$, however there is evidence to suggest that this is not the case for shrimp noise. Asymmetry in the shrimp noise is investigated further in later sections of this chapter. Estimation of parameters γ and α using the sample quantile method is outlined later in this section.

A few special cases exist where an analytic solution for the pdf can be found; when $\alpha = 2$ the pdf is a Gaussian, when $\alpha = 1$ and $\beta = 0$ the pdf is that of a Cauchy distribution, and when $\alpha = 0.5$ and $\beta = 1$ the pdf reduces to that of a Pearson (or Lévy) distribution. In all other cases the pdf must be evaluated numerically. When $\beta = a = 0$ the α-stable distributions reduce to an important subclass: the *Symmetric-*α-stable (SαS) distributions. Substituting $\beta = a = 0$ into Equation 3.9 gives the characteristic function of the SαS distribution

$$\varphi(t)_{S\alpha S} = \exp\left(-\,|\gamma t|^{\alpha}\right). \tag{3.10}$$

Although the SαS characteristic function provides a substantial reduction in complexity as compared to the general α-stables, the density function still has no analytic solution except for the Gaussian and Cauchy cases mentioned previously.

Several methods exist for numerical evaluation of the SαS pdf. Direct methods use numerical inverse Fourier transformation of the characteristic function, that is, evaluating

$$f_\alpha(x) = \frac{1}{\pi}\int_0^\infty \exp\left(-|\gamma t|^\alpha\right) cos(xt)\,\mathrm{d}t. \tag{3.11}$$

A method (referred to as the Zolotarev method) uses a transformation so that the integral is evaluated on the interval [0, $\pi/2$], however the technique suffers from numerical difficulties when α is close to 1 or 2, and when x is (very) large or small (McCulloch 1998). Power series expansions and asymptotic expressions are available for both small and large x (Nikias & Shao 1995) but joining the results to give a pdf over a full range of x values can introduce discontinuities.

To overcome these numerical difficulties the method of McCulloch (McCulloch 1998) was suggested (M Chitre 2008, per. Comm., 26 September). McCulloch's method transforms x onto the interval [0,1] and defines the complementary (symmetric) stable distribution function (S^c) in terms of the complementary distribution function of the Cauchy (C^c) and Gaussian (G^c) plus a small residual term R, giving

$$S^\mathrm{c} = (2-\alpha)C^\mathrm{c}(x_1) + (\alpha-1)G^\mathrm{c}(x_2) + R(z) \tag{3.12}$$

where x_1 and x_2 are original x transformed to z using α, then inverse transformed using $\alpha = 1$ (i.e. a Cauchy assumption) for x_1 and $\alpha = 2$ (a Gaussian assumption) for x_2. It can be seen that when the Cauchy ($\alpha = 1$) or Gaussian ($\alpha = 2$) assumptions are true, the other term vanishes and the residual will (necessarily) be zero. When α equals a value other than 1 or 2, then Cauchy and Gaussian contributions are combined, and the residual becomes the important function that reconciles the Cauchy-Gaussian combination with the true value of the SαS. The residual function $R(z)$ is fit by a quintic spline in z using spline coefficients from McCulloch (1998). The probability density function is the analytical derivative of Equation 3.12

$$s(x) = \left[(2-\alpha)c(x_1)x_1'(z) + (\alpha-1)g(x_2)x_2'(z) - R'(z)\right] z'(x) \tag{3.13}$$

where $c(x)$ and $g(x)$ are respectively the Cauchy and Gaussian probability density functions, and a dashed notation is used to indicate a derivative with respect to the

argument. The (relative) precision of the density function estimated using McCulloch's method is less than 1×10^{-6} for values of α likely to be encountered with shrimp noise (α between 1 and 2), sufficient for all subsequent evaluations of the SαS probability density function in this thesis. The density function in Equation 3.13 is standardised therefore a scaling operation was conducted to give non-standardised pdf values. To evaluate a SαS pdf with characteristic function from Equation 3.10 the following scaling operations were performed

$$f(x) = \zeta s(x\zeta) \tag{3.14}$$

where

$$\zeta = \frac{1}{\gamma^{\frac{1}{\alpha}}} \tag{3.15}$$

and γ and α are the scale and characteristic exponent parameters described previously.

Several methods exist for computing the parameters of SαS distributions. Maximum likelihood, sample fractile (or sample quantile), sample characteristic function, and negative-order moment methods are outlined in Nikias & Shao (1995). From these methods the sample fractile method was chosen, as suggested by Chitre (2006), and implemented as described in Nikias & Shao (1995). The method computes an interim value v_α using

$$v_\alpha = \frac{q_{0.95} - q_{0.05}}{q_{0.75} - q_{0.25}} \tag{3.16}$$

where the q are quantiles obtained from the samples using

$$q_f = \begin{cases} Q_{(1)}, & i = 0 \\ Q_{(i)} + \left(Q_{(i+1)} - Q_{(i)}\right) \frac{f - \zeta(i)}{\zeta(i+1) - \zeta(i)}, & 0 < i < N \\ Q_{(N)}, & i = N \end{cases} \tag{3.17}$$

with f being a value greater than 0 and less than 1, the Q are order statistics between 1 and N: $Q_{(1)}, ..., Q_{(N)}$, the function ζ defined as

$$\zeta(k) = \frac{2k - 1}{2N} \tag{3.18}$$

and i is an integer computed using

$$i = \lfloor fN + 0.5 \rfloor \tag{3.19}$$

where $\lfloor \cdot \rfloor$ represents the nearest integer less than the argument. Parameter estimates for α and γ are then found by interpolating tables; a table for obtaining α directly given v_α, and a table providing v_c given α from which γ can be computed using

$$\gamma = \left(\frac{q_{0.75} - q_{0.25}}{v_c} \right)^{\alpha}. \tag{3.20}$$

Sample quantiles were estimated using the Exponentially Weighted Moving Average (EWMA) incremental estimator (Chen et al. 2000). Given N blocks of data of length M then the incremental estimator for the f^{th} quantile at the k^{th} of N iterations is

$$q_{(k)(f)} = (1 - w) q_{(k-1)(f)} + (w) \hat{q}_f \tag{3.21}$$

where $\hat{q}_f$ is the f^{th} quantile estimate for the current iteration (k) computed using Equation 3.17 on the M available points, and $0 < w < 1$ is a fixed "aging" parameter, with values typically between 0.01 and 0.1. When $k = 1$ (i.e. the first iteration) then $q_{(k)(f)} = \hat{q}_f$.

An example of the SαS fit to the amplitude probability density of real shrimp noise from the AWharf (AW) is shown in Figure 3.3. The SαS provides a very good fit to the data through both the body and the tails of the density function, consistent with similar comparisons in Chitre et al. (2006) and Chitre (2006). Some very minor variations of the real noise about the SαS fit are evident, including a downward turn of the extreme tails of the real noise.

The α parameter of the SαS, which gives an indication of the heaviness of the tails, was estimated using the above parameter estimation technique (and in all cases using the EWMA quantile estimator) for a number of snapping shrimp noise data sets from locations around Australia. The results are shown in Figure 3.4. Values of α (cross markers) range between 1.3 and 1.8, which are slightly lower than those quoted for Singapore waters (between 1.6 and 1.9) (Chitre et al. 2006). An outlier at $\alpha = 2$ (circle marker in Figure 3.4) was obtained for noise from the Nornalup-Walpole Estuary. The outlier suggests that the sample fractile estimator was not an appropriate estimation method for this data. A value of $\alpha = 1.5$ was found to give a reasonable fit to the

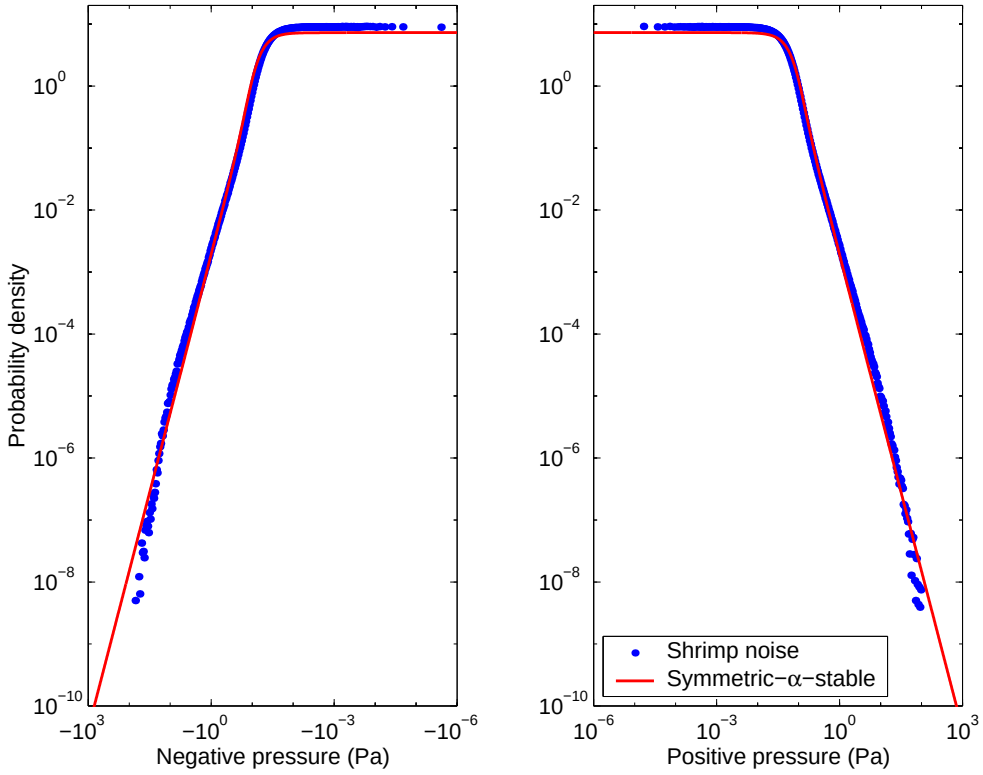

Figure 3.3: Probability density of real shrimp noise with a SαS fit, plotted on logarithmic scales. The SαS provides a very good fit to the data through both the body and the tails of the distribution. Some very minor variations of the real noise about the SαS fit are evident.

data pdf. There does not appear to be any consistent relationship between the type of location where the data was gathered and the level of ambient noise or the value of α for the SαS fit.

3.2 A heuristic model of snapping shrimp noise

In the following section a new heuristic model of the amplitude distribution of snapping shrimp noise is derived. The model is heuristic in the sense that many simplifications have been used to keep the model mathematically amenable - the objective being to

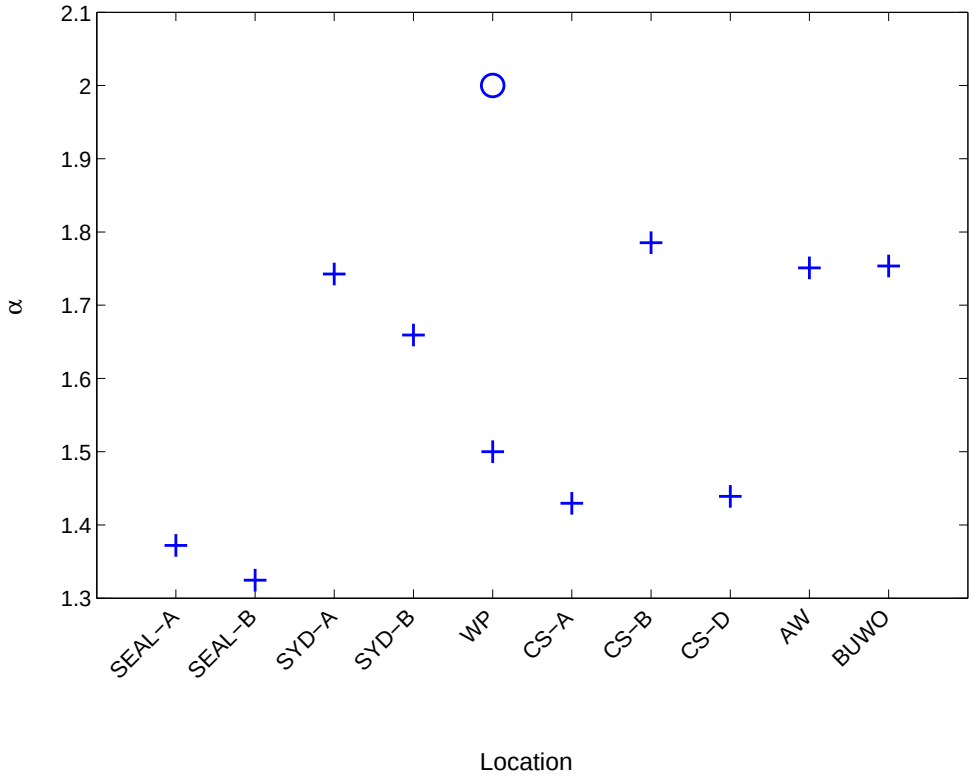

Figure 3.4: SαS parameter α estimated for shrimp noise from various locations around Australian shores. At these locations the value of α was between 1.3 and 1.8. The value $\alpha = 2$ (circle marker) is an outlier caused by poor parameter estimation using the Nornalup-Walpole Estuary data.

obtain an analytic expression for a pdf that can be related to shrimp noise. The model focuses on the distribution of amplitudes that would be received at a hydrophone, but does not include other ambient noise. To arrive at a full ambient noise model the new model (given the name Garnele: a German word for shrimp) is later combined with a background Gaussian using the ϵ-contamination framework. The model has a physical-statistical basis and physically meaningful parameters have been maintained where possible.

The Garnele model derivation differs fundamentally from the α-stable derivation in three ways: the sources are assumed to be uniformly distributed within a circle on the seabed (the α-stable assumes a Poisson spatial distribution of sources (Nikias &

Shao 1995)), the distribution of source pressures (source amplitudes) are defined only for positive values (the α-stable assumes a distribution of source amplitudes that are symmetric about zero (Nikias & Shao 1995)), and propagation from the source to the receiver includes a direct path and a surface reflected path (the α-stable assumes a direct path only; a "cone" from the source to the receiver (Nikias & Shao 1995)). Under the Garnele assumptions, negative amplitudes are a result of surface reflected snaps only: no negative impulse amplitudes are generated at the source. The assumptions were chosen to allow an analytic solution. Many of the assumptions could be adjusted to produce a more physically realistic distribution; however they are likely to require a numerical solution.

Density function transformations are used throughout the derivation, rather than characteristic function transformations. The reason for using density function transformations is that the source level distribution is assumed to be Gaussian, so that the corresponding pressure amplitudes are lognormally distributed. The lognormal distribution does not have a simple exact characteristic function (although various series representations can be found (Leipnik 1991, Beaulieu 2006)) excluding the (practical) use of characteristic function transformations for the derivation. A consequence of using density function transformations is that the Garnele distribution is defined by its probability density function, rather than its characteristic function. An advantage of using density function transformations and assumptions that maintain an analytic solution is that an analytic expression is available for the resulting probability density function of received amplitudes.

3.2.1 Derivation of the density function

A single snap from a shrimp is considered to be an event. If the shrimp snaps are independent in time then the event can be modelled knowing: the location of the shrimp (a single random variable taken from a spatial distribution), the acoustic signal of the shrimp (the source waveform scaled by a single random variable from a source amplitude

distribution), and a relationship that accounts for changes to the source waveform as it travels from the shrimp to a receiving hydrophone. Given this scenario, the distribution of amplitudes arriving at the hydrophone can be found using the following series of random variable transformations:

1. Transform the distribution of source levels into a distribution of source pressure levels
2. Transform the ground range distribution into path range distributions according to the model of propagation
3. When boundaries are encountered there may be (possibly random) phase changes to the propagating signal
4. Source pressure and path range distributions are combined using a propagation function, to give a distribution of received pressure amplitudes.

The series of random variable transformations is quite generic, allowing appropriate choices for the distributions. Motivating factors for distribution choices include: using the most accurate distributions for a specific case, using the most general distributions for a generic case, or making reasonable assumptions to obtain an analytic solution. In the following derivation the motivation has been to obtain an analytic solution, requiring a distribution of source locations that is known not to be true. Despite the over-simplification of source locations and propagation model, the resulting distribution is capable of modelling shrimp noise from a variety of locations around Australian shores and is therefore included as a candidate model of snapping shrimp noise. Following is a list of the distributions and assumptions used in the derivation:

1. Snap source levels (in decibels) are Gaussian distributed about some mean source level
2. The probability density of slant ranges between shrimps and the hydrophone are assumed linear out to some maximum range

3. Sound is assumed to propagate in an iso-velocity, constant depth water column along the direct and surface reflected paths

4. Transmission losses are due to spherical spreading only. Effects such as absorption, scattering and Doppler shift or spread are not included.

In the absence of a known distribution of snap source levels, the Gaussian distribution was chosen. The rationale for choosing a Gaussian was that the central limit theorem would apply to the distribution of snapping shrimp claw sizes. Claw size and snap source level are linearly related (Au & Banks 1998) therefore it was assumed that the central limit theorem would also apply to the snap source levels, leading to the choice of a Gaussian distribution. The assumed distribution of ground ranges between shrimps and the hydrophone can be visualised as a circular shrimp bed, with the shrimp uniformly distributed within the bed and a hydrophone at the centre of the circle. Other geometries and shrimp spatial distributions can be devised that will also give the assumed ground range distribution. Middleton (1977) considers sources Poisson distributed in one, two and three spatial dimensions. The derivation of an α-stable model for impulsive noise using the filtered impulse mechanism (Nikias & Shao 1995) acknowledges the work of Middleton but for simplicity considers a central point of observation and a cone of sources with vertex at the point of observation. The central point of observation and cone of sources used to derive the stable model is similar to the geometry assumed for the Garnele model, except that the Garnele model assumes that the sources are constrained to the base of the cone (the seafloor) and that the sources are uniformly distributed. Bottom reflections are also important for fully describing the received amplitude distribution (Chitre et al. 2003), however to maintain an analytic solution their effect has not been included.

Source level and ground range distributions are respectively transformed into source pressure amplitude and path range distributions using the transformation (Devroye 1986)

$$f_Y(y) = f_X(\mathrm{G}^{-1}) \left| \frac{\mathrm{dG}^{-1}}{\mathrm{d}y} \right| \tag{3.22}$$

where the inverse function G^{-1} maps a realisation of y to a realisation of x.

The peak source levels (SL) are assumed to be Gaussian distributed with probability density function

$$f_{SL}(SL) = \frac{1}{\sqrt{2\pi}\Omega} \exp\left(-\frac{(\mathrm{SL} - \mathrm{SL_o})^2}{2\Omega^2}\right) \tag{3.23}$$

where $\mathrm{SL_o}$ is the mean source level of a shrimp snap, and Ω is the standard deviation of shrimp snap source levels for a field of shrimp. This source level density function is transformed into a source pressure density function using the inverting function

$$\mathrm{G}_{\mathrm{SL}}^{-1} = 20\log_{10}\left(\frac{s}{p_{\mathrm{ref}}}\right) \tag{3.24}$$

where s is the peak source pressure amplitude, and p_{ref} is a reference pressure (typically 1μPa). Substituting Equation 3.23 into Equation 3.22 and using the derivative of Equation 3.24 with respect to s gives

$$f_S(s) = \frac{1}{\sqrt{2\pi}\eta s} \exp\left(-\frac{(20\log_{10}(s/p_{\mathrm{ref}}) - \mathrm{SL_o})^2}{2\Omega^2}\right) \tag{3.25}$$

where

$$\eta = \frac{\Omega \ln(10)}{20}. \tag{3.26}$$

Substituting the mean source level $\mathrm{SL_o}$ with the equivalent expression in terms of p_o gives the distribution of source pressure amplitudes

$$f_S(s) = \begin{cases} \frac{1}{\sqrt{2\pi}\eta s} \exp\left(-\frac{\ln^2(s/p_o)}{2\eta^2}\right), & 0 \le s < \infty \\ 0, & \text{otherwise} \end{cases} \tag{3.27}$$

At this point p_{ref} drops out so that the units of s and p_o are the same (preferably Pascals). The source pressure amplitude distribution is a lognormal distribution with median $p_o > 0$ (Evans et al. 1993). Such lognormal amplitude distributions often arise when logarithmic quantities are assumed to be Gaussian distributed (see for example Fenton 1960).

The next step in the derivation is to define a spatial distribution for shrimp within the shrimp field. Using the spatial visualisation described previously, with central

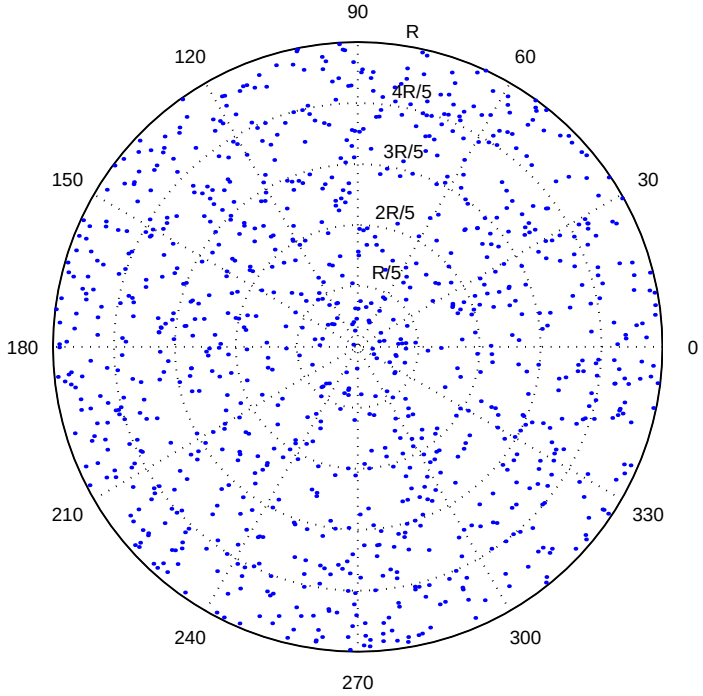

Figure 3.5: Simulated locations of shrimp using a two dimensional (circular) uniform distribution. A uniformly distributed phase component has been included so the shrimp lie within a circle, however this is for the illustration only. The derivation does not required any azimuthal information.

point of observation and shrimp sources constrained to the base of a cone, the shrimp are assumed to be uniformly distributed within a circle on the seafloor as shown in Figure 3.5. What is required is to use this visualisation of source location to obtain the distribution of propagation paths between the sources (the shrimp) and the point of observation (the hydrophone). For clarity, the following notation is used to distinguish between different ranges: r_g is ground range, r_d is the range along a direct propagation path, and r_s is the range along the first surface reflected path. It is assumed that the circular bed of shrimp has a maximum extent R, so that shrimp do not exist at ground ranges r_g greater than R. When this is not physically true, R is assumed to represent the ground range at which shrimp no longer contribute a significant amount to the noise. At large ranges it is assumed that the large number of shrimp contributing very

small amplitude snaps provides the conditions required for the Central Limit Theorem to be applicable, the shrimp noise then becomes part of the Gaussian background. The shrimp ground range distribution function

$$F_{R_g}(r_g) = \begin{cases} \frac{\rho\pi r_g^2}{\rho\pi R^2}, & 0 \leq r_g \leq R \\ 0, & \text{otherwise} \end{cases} \tag{3.28}$$

is the ratio of the number of shrimp in an area defined by r_g to the total number of shrimp in the shrimp bed, where ρ is a shrimp density measure, which is a constant for this derivation. The derivative of the distribution function with respect to r_g gives the ground range density function

$$f_{R_g}(r_g) = \begin{cases} \frac{2r_g}{R^2}, & 0 \leq r_g \leq R \\ 0, & \text{otherwise.} \end{cases} \tag{3.29}$$

The ground range probability density function is required for step two of the transformation process outlined previously. Ground ranges are transformed into slant ranges, as required by the model of sound propagation. A simple ray model assuming constant sound speed and spherical spreading is chosen for simplicity, and only the direct and surface reflected paths are considered; contributions from paths that include a bottom reflection are ignored. An illustration of the assumed propagation is shown in Figure 3.6. The inverting function for the direct and surface reflected paths is

$$\mathrm{G}_{\mathrm{r_g}}^{-1} = \begin{cases} \sqrt{r^2 - (h-d)^2}, & \text{direct} \\ \sqrt{r^2 - (h+d)^2}, & \text{surface reflected} \end{cases} \tag{3.30}$$

where r is the propagation range, h is the depth of the water column and d is the hydrophone depth. The derivative of Equation 3.30 required for the transformation is

$$\frac{\mathrm{dG}_{\mathrm{r_g}}^{-1}}{\mathrm{d}r} = \begin{cases} \frac{r}{\sqrt{r^2-(h-d)^2}}, & \text{direct} \\ \frac{r}{\sqrt{r^2-(h+d)^2}}, & \text{surface reflected.} \end{cases} \tag{3.31}$$

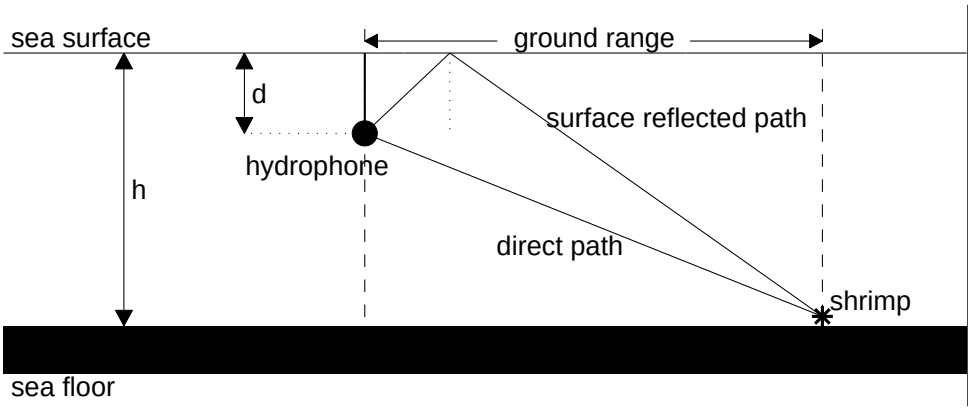

Figure 3.6: The idealised propagation environment assumed for deriving the Garnele distribution. The snap from each shrimp travels through an isovelocity water column from the shrimp to the hydrophone via direct and single surface reflection paths only.

Transformation of ground ranges into propagation ranges, using Equation 3.22, gives a direct path (r_d) solution and a surface reflected (r_s) solution

$$f_{R_d}(r_d) = \begin{cases} \frac{2r_d}{R^2}, & (h-d) \leq r_d \leq \sqrt{R^2+(h-d)^2} \\ 0, & \text{otherwise} \end{cases} \tag{3.32}$$

and

$$f_{R_s}(r_s) = \begin{cases} \frac{2r_s}{R^2}, & (h+d) \leq r_s \leq \sqrt{R^2+(h+d)^2} \\ 0, & \text{otherwise.} \end{cases} \tag{3.33}$$

The final step in deriving the received amplitude distribution due to a field of snapping shrimp is to combine the source amplitude and propagation range density functions, using a propagation relationship, to give the desired received amplitude distribution. When the propagation relationship is simple spherical spreading, a received amplitude random variable $\mathbf{P}$ is related to a source amplitude random variable $\mathbf{S}$, and a range random variable $\mathbf{R}$ by

$$\mathbf{P} = \frac{\mathbf{S}}{\mathbf{R}}. \tag{3.34}$$

The distribution of $\mathbf{S}$ and $\mathbf{R}$ are known, so the distribution of $\mathbf{P}$ can be obtained by transformation of random variables. To conduct this transformation the variates s and

r are mapped to transformed variates p and z using

$$p = \frac{s}{r} \tag{3.35}$$

and

$$z = r. \tag{3.36}$$

The joint distribution of s and r, $f_{SR}(s, r)$, is transformed to a joint distribution of p and z, $f_{PZ}(p, z)$, using

$$f_{PZ}(p, z) = f_{SR}(s = pr, z = r) \left|\bar{J}(p, z)\right| \tag{3.37}$$

where $\bar{J}(p, z)$ is the inverse Jacobian

$$\bar{J}(p, z) = \begin{vmatrix} \frac{\partial s}{\partial p} & \frac{\partial s}{\partial z} \\ \frac{\partial r}{\partial p} & \frac{\partial r}{\partial z} \end{vmatrix}. \tag{3.38}$$

Evaluating the inverse Jacobian, and noting that s and r are independent, gives the joint density function of p and z

$$f_{PZ}(p, z) = f_S(pr) f_R(r) \left|r\right|. \tag{3.39}$$

The probability density function $f_P(p)$ can then be found by back substituting r in place of z, since they are equal from Equation 3.36, and solving for the marginal distribution in p

$$f_P(p) = \int_R f_S(pr) f_R(r) \left|r\right| \, \mathrm{d}r. \tag{3.40}$$

Direct and surface reflected paths are considered separately, since the domain of r is different in each case, and the sign of the pressures in each case will be opposite. The direct path marginal distribution will solve for positive pressures, while the surface reflected path will solve to give negative pressures. As mentioned, the surface is assumed to impart an exact π radian phase shift on the pressure signal. These two distributions will be combined to give an overall pressure distribution. The marginal distribution of (positive) pressure due to direct path arrivals is defined by

$$f_P^+(p) = \int_{r_{\min}}^{r_{\max}} f_S(p\, r_d) f_{R_d}(r_d) \left|r_d\right| \, \mathrm{d}r_d \tag{3.41}$$

which, given the distributions that arise from the assumptions made thus far, expands to give

$$f_P^+(p) = \int_{(h-d)}^{\sqrt{R^2+(h-d)^2}} \frac{1}{\sqrt{2\pi}\eta p\, r_d} \exp\left(-\frac{\ln^2(p\, r_d/p_o)}{2\eta^2}\right) \frac{2r_d}{R^2}\, |r_d|\, \mathrm{d}r_d. \tag{3.42}$$

Solving Equation 3.42 gives the the probability density function of positive received pressures

$$f_P^+(p) = \frac{\exp\left(2\left(m+\eta^2\right)\right)}{|p|^3\, R^2}\left(\mathrm{erf}\left\{\frac{m+(2\eta^2)-\ln(h-d)-\ln(|p|)}{\sqrt{2}\eta}\right\} - \mathrm{erf}\left\{\frac{m+(2\eta^2)-\ln\left(|p|\sqrt{(h-d)^2+R^2}\right)}{\sqrt{2}\eta}\right\}\right) \tag{3.43}$$

where η is given in Equation 3.26, $\mathrm{erf}(\cdot)$ is the error function, $\ln(\cdot)$ is the natural logarithm, and $m = \ln(p_o)$.

A result is obtained for the negative pressures in a similar manner, except that now the propagation function will use the surface reflected range distribution of Equation 3.33. The marginal distribution for the negative pressures is

$$f_P^-(p) = \int_{(h+d)}^{\sqrt{R^2+(h+d)^2}} \frac{1}{\sqrt{2\pi}\eta p\, r_s} \exp\left(-\frac{\ln^2(p\, r_s/p_o)}{2\eta^2}\right) \frac{2r_s}{R^2}\, |r_s|\, \mathrm{d}r_s \tag{3.44}$$

which is identical to Equation 3.43 except that $(h-d)$ is replaced with $(h+d)$ because of the extra path length for the surface reflections. The probability density function for negative pressures is then

$$f_P^-(p) = \frac{\exp\left(2\left(m+\eta^2\right)\right)}{|p|^3\, R^2}\left(\mathrm{erf}\left\{\frac{m+(2\eta^2)-\ln(h+d)-\ln(|p|)}{\sqrt{2}\eta}\right\} - \mathrm{erf}\left\{\frac{m+(2\eta^2)-\ln\left(|p|\sqrt{(h+d)^2+R^2}\right)}{\sqrt{2}\eta}\right\}\right). \tag{3.45}$$

To obtain the received pressure density function over the full range of pressures, the positive and negative distributions are combined with equal probability (because each snap will produce a direct path and surface reflected replica). The result is an overall

pressure distribution with probability density function

$$f_P(p) = \frac{\exp\left(2\left(m+\eta^2\right)\right)}{|p|^3 R^2}\left(\operatorname{erf}\left\{\frac{m+(2\eta^2)-\ln\left(h-\operatorname{sgn}(p)\,d\right)-\ln\left(|p|\right)}{\sqrt{2}\eta}\right\}\right.$$
$$\left.-\operatorname{erf}\left\{\frac{m+(2\eta^2)-\ln\left(|p|\sqrt{(h-\operatorname{sgn}(p)\,d)^2+R^2}\right)}{\sqrt{2}\eta}\right\}\right) \quad (3.46)$$

where $\operatorname{sgn}(\cdot)$ is the sign (or signum) function.

Equation 3.46 is the probability density function of the heuristic Garnele model, with parameters m,η,R,h and d. Parameters h and d (the water depth and hydrophone depth) will often be known in experimental situations. Parameters m and η (related to the distribution of shrimp source levels), and R (the radius of the shrimp bed) will need to be estimated.

3.2.2 Derivation of the distribution function

The distribution function of the heuristic model was also derived analytically. Rather than directly integrating the density function to obtain the distribution function, the distribution function was derived from fundamentals thus giving two independent solution paths for the two results. The integral of the density function could then be used as a consistency check. The distribution function was found by integrating the joint density function of s and r

$$F_P(p) = \iint_{R,S} f_{SR}(s,r)\,\mathrm{d}s\,\mathrm{d}r \quad (3.47)$$

over their respective domains

$$(h-\operatorname{sgn}(p)\,d) \le r \le \sqrt{R^2+\left(h-\operatorname{sgn}(p)\,d\right)^2} \quad (3.48)$$

and

$$0 \le s \le pr. \quad (3.49)$$

The solution of Equation 3.47 gives the distribution function

$$F_P(p) = \frac{1}{2p^2R^2}\Bigg[\exp\left(2\eta^2\right)\exp^2(m)\left(\operatorname{erf}\left\{\frac{2\eta^2+m-\ln\left(p\big(h+\operatorname{sgn}(p)\,d\big)\right)}{\sqrt{2}\eta}\right\}\right.$$
$$\left.-\operatorname{erf}\left\{\frac{2\eta^2+m-\ln\left(p\sqrt{R^2+\left(h+\operatorname{sgn}(p)\,d\right)^2}\right)}{\sqrt{2}\eta}\right\}\right)$$
$$+p^2\left(\left(R^2+\left(h+\operatorname{sgn}(p)\,d\right)^2\right)\operatorname{erfc}\left\{\frac{m-\ln\left(p\sqrt{R^2+\left(h+\operatorname{sgn}(p)\,d\right)^2}\right)}{\sqrt{2}\eta}\right\}\right.$$
$$\left.-\left(h+\operatorname{sgn}(p)\,d\right)^2\operatorname{erfc}\left\{\frac{m-\ln\left(p\big(h+\operatorname{sgn}(p)\,d\big)\right)}{\sqrt{2}\eta}\right\}\right)\Bigg] \quad (3.50)$$

where $\operatorname{erfc}\{\cdot\}$ is the complementary error function. Evaluating Equation 3.50 in the limit $p \to \infty$ gives unity, so that the distribution is properly scaled.

3.3 Ambient noise: a Gaussian-Garnele mixture model

The Garnele distribution is a model of shrimp-only noise. To use this model (or other shrimp-only models) for ambient noise requires another component for other (non-impulsive) background noise; an ambient noise model is created by combining the shrimp model with a background noise model. In this section the Garnele model is extended to an ambient noise model using the ϵ-contamination framework (see for example Vastola 1984). The framework has a first order noise pdf of the form

$$f_\epsilon(x) = (1-\epsilon)\,f_0(x) + \epsilon f_1(x), \qquad 0 \le \epsilon \le 1 \quad (3.51)$$

where f_0 is the pdf of background noise (usually a Gaussian), f_1 is the pdf of the "contaminating" noise (the impulsive shrimp noise), and ϵ defines the relative amount of each of the noise components. When $\epsilon = 0$ there is no contamination and the ambient noise pdf is the background noise pdf, and conversely when $\epsilon = 1$ there is no background and the ambient noise pdf is the impulsive noise pdf.

If the background noise is assumed to be Gaussian distributed, and the impulsive noise Garnele distributed, then the resulting ambient noise model is a Gaussian-Garnele

mixture with density function

$$f(x) = (1-\epsilon)\, N(x:0,\sigma) + \epsilon G(x:m,\eta,h,d,R) \tag{3.52}$$

where N is a zero mean Gaussian pdf with standard deviation σ, and G is a Garnele pdf with parameters m, η, h, d and R.

The ϵ-contamination framework assumes that the noise switches between the two different distributions, rather than being additive. The difference between switching and adding is shown in Figure 3.7. In both of the plot windows the dark blue bars are random variables from the background noise distribution (a Gaussian) and the light green bars are contamination random variables from a Garnele distribution. Additive noise is more physically realistic, the presence of an impulse does not exclude other background noise. When the noise components are additive then the ambient noise pdf is the convolution of the background noise pdf with the impulsive noise pdf. The convolution is most conveniently computed by multiplying the characteristic functions of the two noise pdfs. Unfortunately, the lack of a characteristic function for the Garnele distribution means that the convolution must be computed numerically using the noise pdfs, or the contamination model must be used as an analytic approximation. If a solution for the Garnele characteristic function becomes available then the additive noise model should be used. Issues related to the characteristic function of the Garnele distribution, including investigations using numerical methods, are topics for further research.

3.3.1 Parameter estimation for the Gaussian-Garnele distribution

Due to the physical-statistical derivation used for the Garnele distribution the parameters of the distribution are physical quantities that can be measured or realistically estimated. Parameters such as water depth and hydrophone depth are usually measurable within a reasonable uncertainty. Parameters that are unlikely to be easily measurable are the maximum range of the shrimp bed, the average source level of the shrimp, and the standard deviation of the source level of snaps from the shrimp field.

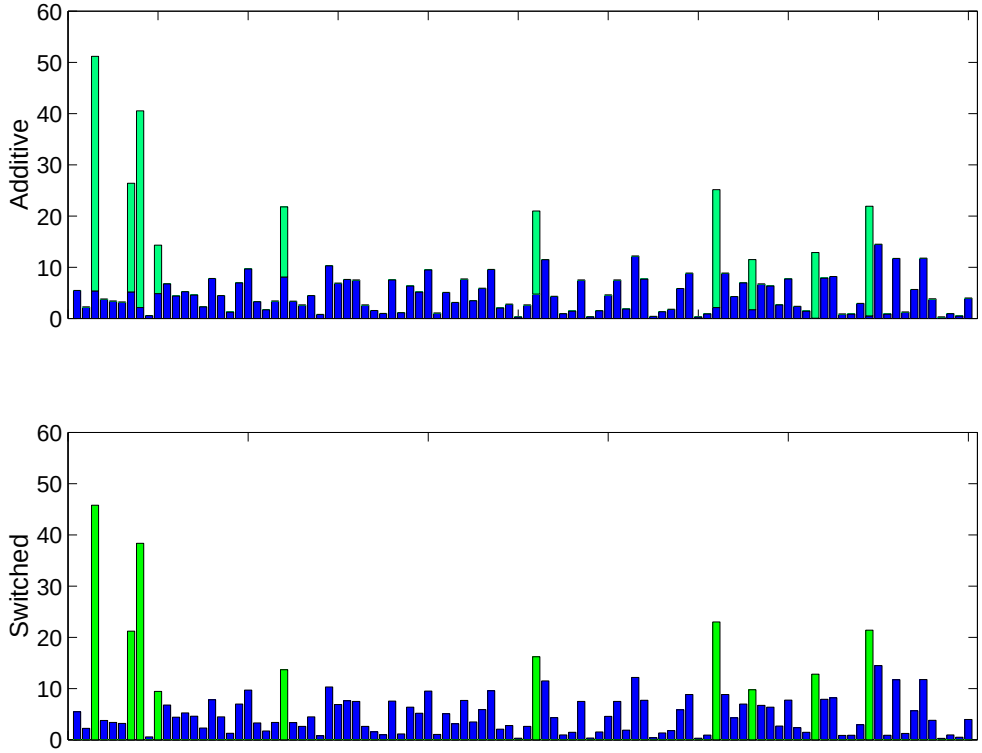

Figure 3.7: A pictorial description of switched and additive combination of random variables. Blue (dark) bars are Gaussian random variables, and green (light) bars are Garnele (impulsive) random variables. The additive method adds the random variables from both distributions together, whereas the switching method uses one or the other but never both.

Sensible values for these parameters can be obtained from observation, or from controlled studies. For example: a sensible estimate for the mean source level of a shrimp snap is 180 dB re 1μPa taken from both tank and *in-situ* measurements (Au & Banks 1998, Beng et al. 2003), and a sensible standard deviation value for the variation of source levels in a field of shrimp is 6 dB (Ferguson & Cleary 2001), the maximum range of shrimp is more likely to be hundreds of metres rather than kilometres and so 100 m is a reasonable estimate of R (see for example Beng et al. 2003). The need for these parameter values motivates further studies of the type conducted by Ferguson & Cleary (2001), and Beng et al. (2003). A reasonable estimate for the standard deviation of the background Gaussian noise is the equivalent standard deviation computed for a

Gaussian-Gaussian mixture (i.e. σ_1 from Equation 3.4).

Initial parameter estimates can be further refined using numerical methods, such as numerical maximum likelihood. The method of maximum likelihood using a non-linear least squares fit (Press et al. 1988) of the logarithm of the probability density functions (theoretical and empirical) performs well and is described here. The method seeks to minimise the χ^2 difference between the observations (y_i) and the model ($y(x_i; a_1 \dots a_M)$)

$$\chi^2 = \sum_{i=1}^{N} \left(\frac{y_i - y(x_i; a_1 \dots a_M)}{\sigma_i} \right)^2 \tag{3.53}$$

where N is the number of observations, M is the number of free model parameters (i.e. parameters that have not been measured and are free to be adjusted to give the best model fit) and σ is a measure of relative uncertainty for each observation. The observations were computed as the base 10 logarithm of the pdf estimates of real shrimp noise. The pdf estimates were computed using a quantization level histogram followed by logarithmic bin smoothing (see Appendix C for details of the smoothing algorithm) with a logarithm base of 1.05. It was assumed that after logarithmic bin smoothing the uncertainty in each observation was equal, and consequently $\sigma_i = \sigma = 1$. Model estimates were computed as the base 10 logarithm of the Gaussian-Garnele mixture density function (Equation 3.52) evaluated using the estimated (and iteratively refined) parameters. Model estimates were computed for each observation at the centre of the smoothing bin used to compute the observation. Smoothed pdf estimates that were equal to zero were eliminated from the optimisation because they are not representative of the Gaussian-Garnele model and produce negative infinite observation values that need not be handled by the computational codes.

Nonlinear least squares fitting was conducted using the "downhill" method of Powell (Press et al. 1988). The more sophisticated Levenburg-Marquardt method suffered from near singular matrices, an indication of correlation between parameters. It is reasonable to expect this correlation between parameters because values such as mean source level and maximum range are related through propagation.

3.4 Comparison of SαS and Gaussian-Garnele models

A comparison of the SαS and Gaussian-Garnele models was conducted using each model's fit to the probability density function of real snapping shrimp noise. Snapping shrimp noise was selected from among the field measurements conducted at the AWharf, Cockburn Sound, Busselton Jetty, and Nornalup-Walpole Estuary sites. An empirical density function was computed from each of the data sets using a quantization level histogram, followed by logarithmic bin smoothing with a logarithm base of 1.05. Parameters were estimated for SαS and Gaussian-Garnele fits using, respectively, the sample fractile and maximum-likelihood by non-linear least squares methods described previously. Probability density functions for each of the models were plotted with the empirical density functions on split-log plots. Relative difference plots were also constructed using the ratio of the difference between the empirical and model results to the value of the empirical results. The relative difference plots show model deviations more readily than the probability density plots.

AWharf results from the HTI-96-MIN hydrophone are shown in Figure 3.8 and Figure 3.9. The deviations are similar for both positive and negative pressure with the exception of larger differences at the negative pressure extreme than for similar extreme positive pressures. At very low pressures ($|x| < 1 \times 10^{-3}$ Pa) both the SαS and Gaussian-Garnele models under-estimate the probability density, with the Gaussian-Garnele rising slightly to join the empirical results near $|x| = 1 \times 10^{-3}$ Pa. In the region $1 \times 10^{-1} < |x| < 1 \times 10^{1}$ both models oscillate about the empirical results by similar amounts. For $|x| > 1 \times 10^{1}$ both models increasingly over-estimate the probability densities at these extreme values. An increase in variability of the relative differences can be seen in the extreme tails. For this data the Garnele model provides comparable or better fit than the SαS model.

Results from Cockburn Sound (CS-B) noise data are shown in Figure 3.10 and Fig-

ure 3.11. The sample rate was 473 kHz, which is the highest of all the results presented. Pressure values approaching $|x| = 1 \times 10^{-1}$ Pa suggest good agreement between both models and the empirical results at very low pressure, however inspection of the density functions in Figure 3.10 shows that there are insufficient empirical estimates to be certain that the asymptote predicted by the models is correct. Oscillation of both models about the empirical results occur in the region $1 \times 10^{-1} < |x| < 1 \times 10^{1}$, both models oscillate about the empirical results by similar amounts. For $|x| > 1 \times 10^{1}$ both models increasingly over-estimate the probability densities at these extreme values. An increase in variability of the relative differences can be seen in the extreme tails. An asymmetry between positive and negative pressure is most obvious for this data, with negative pressure values for the real noise deviating below the levels predicted by the SαS. The Garnele and SαS models have comparable fit through the body of the distribution, however the Garnele model fit is superior at the tails.

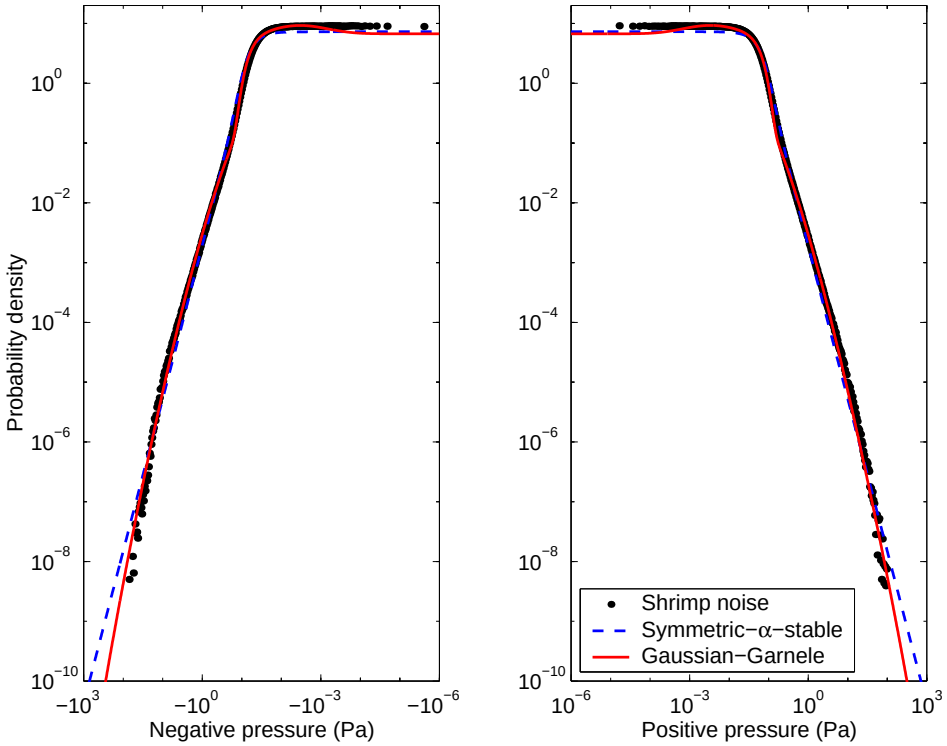

Figure 3.8: A split-log plot of amplitude probability densities derived from AWharf shrimp noise (black dot markers) with SαS (blue dashed line) and Gaussian-Garnele (red solid line) fits.

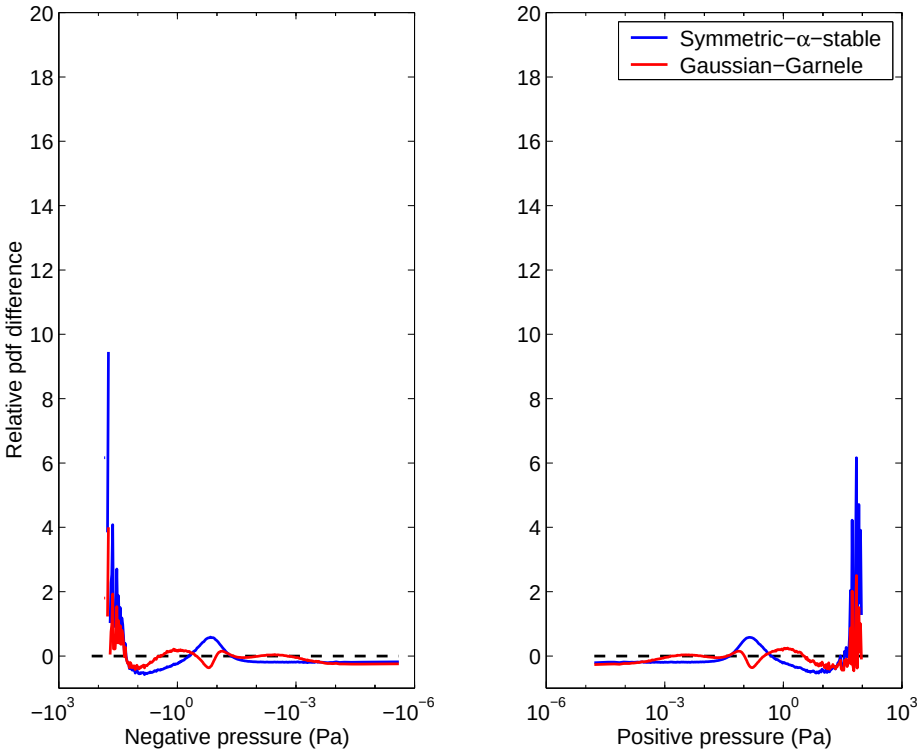

Figure 3.9: Relative difference between SαS (blue solid line) and Gaussian-Garnele (red solid line) models and the amplitude pdf of AWharf noise.

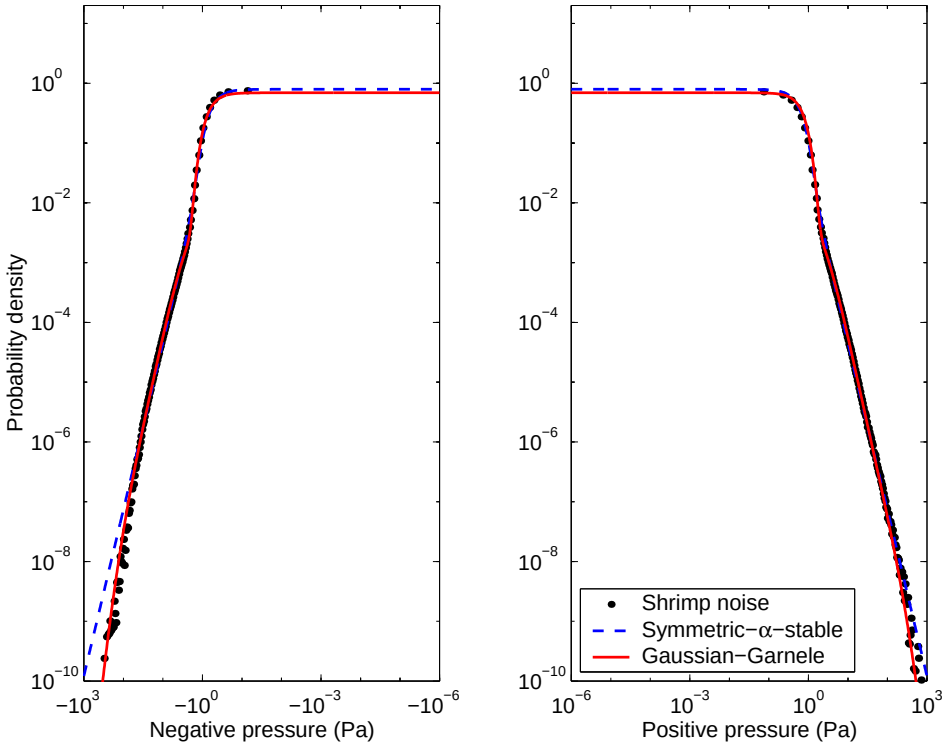

Figure 3.10: A split-log plot of amplitude probability densities derived from Cockburn Sound (CS-B) shrimp noise (black dot markers) with SαS (blue dashed line) and Gaussian-Garnele (red solid line) fits.

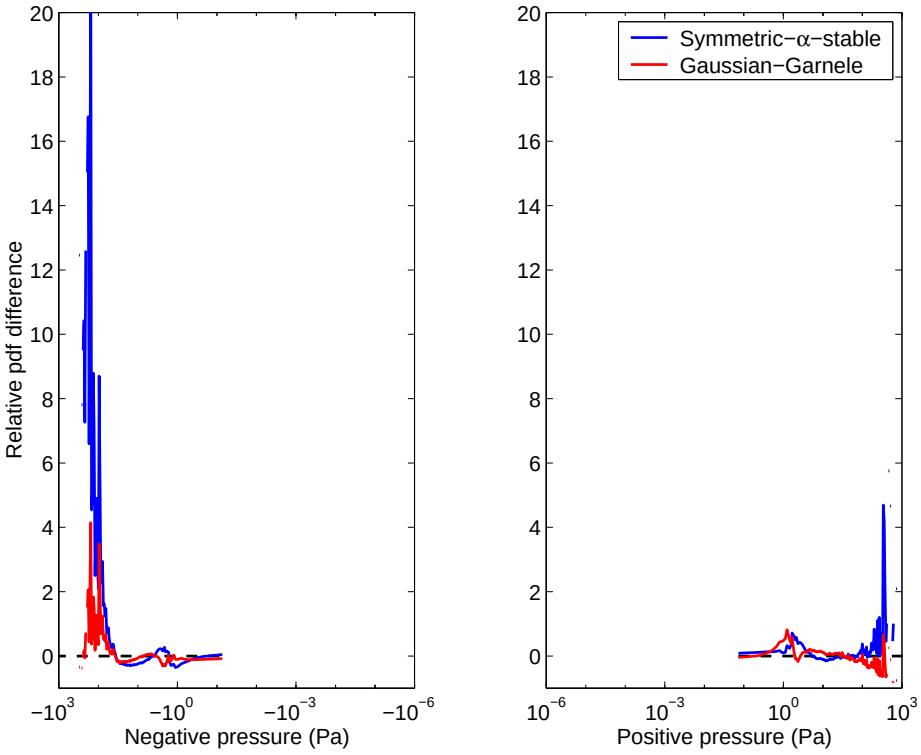

Figure 3.11: Relative difference between SαS (blue solid line) and Gaussian-Garnele (red solid line) models and the amplitude pdf of Cockburn Sound noise.

The Busselton Jetty data used to produce Figure 3.12 and Figure 3.13 were recorded with the same equipment as the AWharf data, and the sample rate was 192 kHz. The model fit to Busselton Jetty data is better at very low pressures than the fit to AWharf data at similar pressures. Some oscillations are evident in the region $1 \times 10^{-1} < |x| < 1 \times 10^{1}$, and this appears to be a recurring feature. Deviations occur in the tails of the distribution and the variability increases as observed in the previous data sets.

Data measured at the Nornalup-Walpole Estuary had a much lower sample rate of 48 kHz. The results for this data are shown in Figure 3.14 and Figure 3.15. At very low pressures (below $|x| = 1 \times 10^{-1}$ Pa) the SαS model fits the real data well, but the Gaussian-Garnele fit is poor. Beyond pressures of $|x| = 1 \times 10^{-1}$ Pa the opposite occurs; the SαS distribution provides a poor fit, while the Gaussian-Garnele oscillates about the real data. Deviations increase for both models in the extreme tails (as observed for all of the data sets) but the asymmetry between positive and negative pressures is not as pronounced as for the other data sets.

Model fits to the above data sets displayed some consistent features. Both the SαS and Gaussian-Garnele models provided a reasonable fit to the real noise pdfs at pressure magnitudes lower than 10 Pa, with both models tending to oscillate about the real data pdfs by similar amounts. The main differences occurred in the tails of the distributions, where the relative pdf difference increased significantly for both models but was consistently less for the Gaussian-Garnele model than for the SαS model. Deviations in the tails of the distribution were consistently larger for negative pressures than for positive pressures, suggesting asymmetry in the tails of the real noise pdfs.

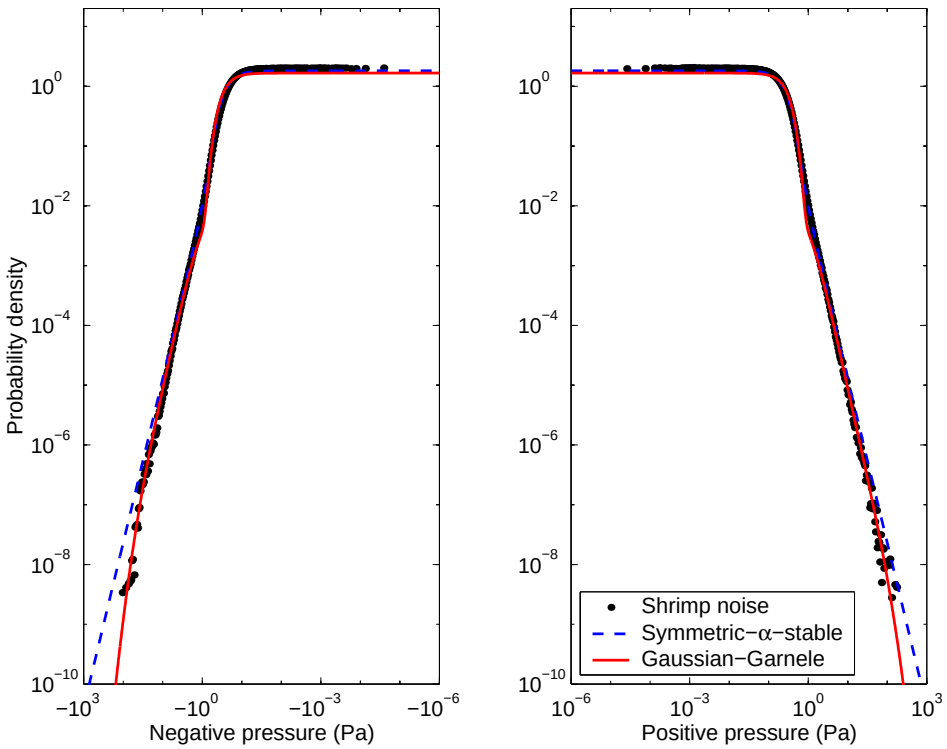

Figure 3.12: A split-log plot of amplitude probability densities derived from Busselton Jetty shrimp noise (black dot markers) with SαS (blue dashed line) and Gaussian-Garnele (red solid line) fits.

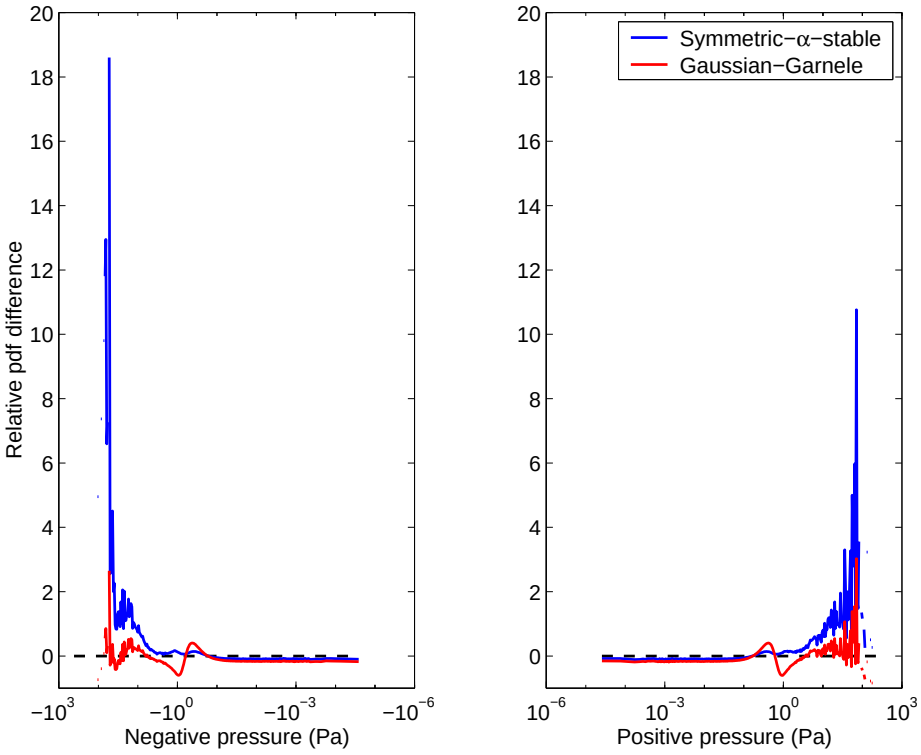

Figure 3.13: Relative difference between SαS (blue solid line) and Gaussian-Garnele (red solid line) models and the amplitude pdf of Busselton Jetty noise.

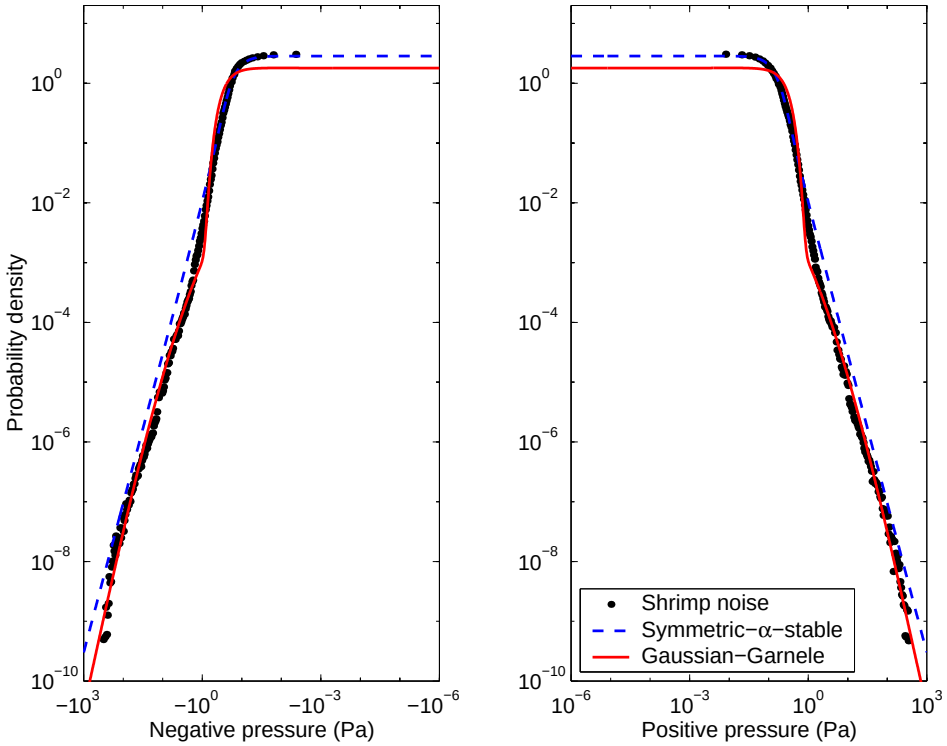

Figure 3.14: A split-log plot of amplitude probability densities derived from Nornalup-Walpole Estuary shrimp noise (black dot markers) with SαS (blue dashed line) and Gaussian-Garnele (red solid line) fits.

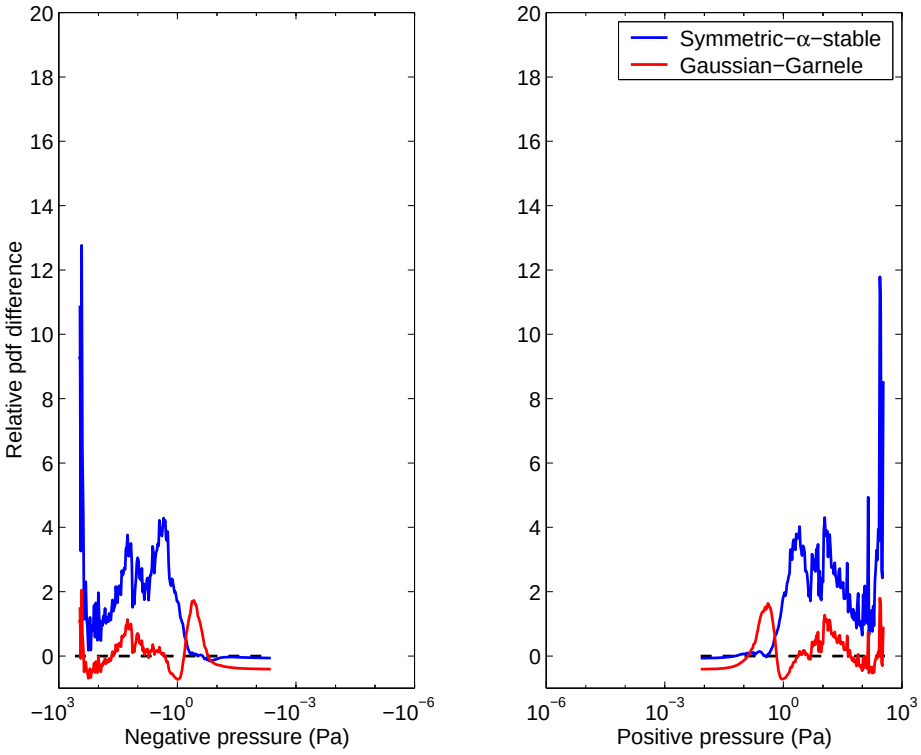

Figure 3.15: Relative difference between SαS (blue solid line) and Gaussian-Garnele (red solid line) models and the amplitude pdf of Nornalup-Walpole Estuary noise.

One important difference between the two models is the number of model parameters, and the associated problem of parameter estimation. Parameter estimation for the SαS model is algorithmically simpler and computationally much more efficient than for the Gaussian-Garnele model. If the pdf fit is most important for pressure magnitudes less than 10 Pa (i.e. through the body and moderate tails of the distribution) then the relative ease of parameter estimation for the SαS model makes it the preferable model. If, however, the extreme tails of the distribution are important then the additional complexity of parameter estimation for the Gaussian-Garnele model may be justified. Computational consideration may also be given to numerical evaluation of the SαS pdf compared with evaluation of the analytic Gaussian-Garnele pdf, noting that the Gaussian-Garnele pdf contains error functions. Evaluation of the SαS pdf using McCulloch's method took (on average) around 50 times longer than the Gaussian-Garnele pdf, using MATLAB®routines on a Pentium M (2.13 GHz) processor. If parameters are to be estimated frequently then the additional cost of numerically evaluating the SαS model may be justified by the cost saving for parameter estimation. Thus, there is a trade-off between the better efficiency of the Gaussian-Garnele model in estimating the pdf when the parameters are already known, and the greater computational cost of parameter estimation.

The comparison of SαS and Gaussian-Garnele pdf results presented suggest two areas warranting further investigation: frequency dependence of model performance, including the effect of receiver bandwidth on real noise observations and the resulting amplitude pdf; and an apparent pdf asymmetry that is observed in real shrimp noise. These are investigated in the following sections.

3.5 Frequency dependence of the pressure amplitude pdf

Frequency dependence of the pressure amplitude pdf for real shrimp noise was investigated using down-sampling. A 10 minute section of real shrimp noise data was selected from Cockburn Sound measurements taken in July 2009. This data set was recorded

using a low-noise, ultra-wide bandwidth RESON 4014 reference hydrophone connected directly into a Fostex FR-2 recorder and sampled at 192 kHz with 24 bit resolution. The frequency response of the FR-2 was measured using an Agilent 33220A function generator configured to output 500 mV (peak-to-peak) white noise over a 20 MHz bandwidth. The FR-2 and hydrophone response curves were then combined and averaged over one-third octaves. One-third octave values were computed by averaging the 1 Hz linear response over each band and then converting back to a logarithmic scale. The last one-third octave value was averaged over the restricted band 37 kHz to 96 kHz, rather than the full band to 112 kHz, due to the sample rate of the data. The averaged receiver response, shown in Figure 3.16, was flat within 3 dB between 100 Hz and 96 kHz. Given the relatively flat response of the receiver, the original receiver response can be removed as a cause of any subsequent down-sampling effects. The down-sampled data can therefore represent a measurement of the same shrimp noise with a receiver that also has a flat acoustic response from 100 Hz to near half of the down-sampled sample frequency, assuming that the response of both systems were similar below 100 Hz.

To investigate the frequency dependence of the pressure amplitude pdf the original 192 kHz sampled data was down-sampled by factors of two from 96 kHz to 750 Hz. Down-sampling was conducted using the *convert sample type* function in CoolEdit Pro version 2. The conversion was conducted using the high-quality (999) mode with pre-filtering and post-filtering enabled. The original 24 bit sample resolution was converted to 32 bit resolution for the down-sampling and subsequently saved data files. The original and down-sampled data were converted to pressure pdfs using a quantization level histogram followed by scaling and logarithmic bin smoothing with a log-base of 1.05. The results are shown in Figure 3.17.

The results show that the shape of the amplitude pdf is not altered significantly for sample frequencies from 192 kHz down to 12 kHz, but the upper limit of observed pressures is reduced as the bandwidth is reduced. For the data set analysed, the shape of the amplitude pdf only changed significantly when the data was down-sampled to 6

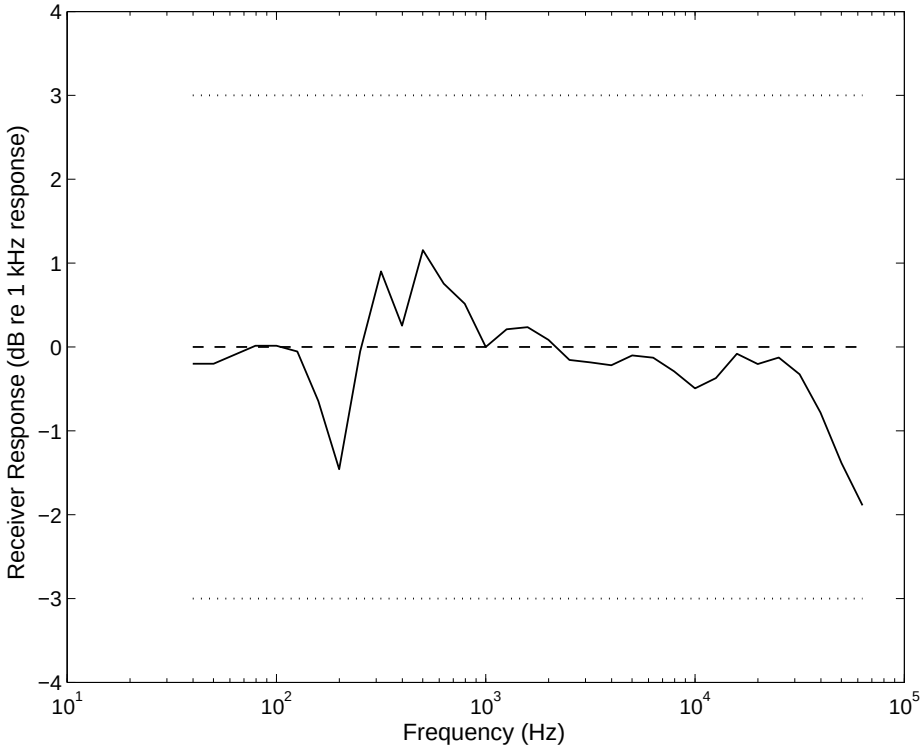

Figure 3.16: Response of the receiver used to measure real shrimp noise for down-sampling analysis as a function of frequency.

kHz and below.

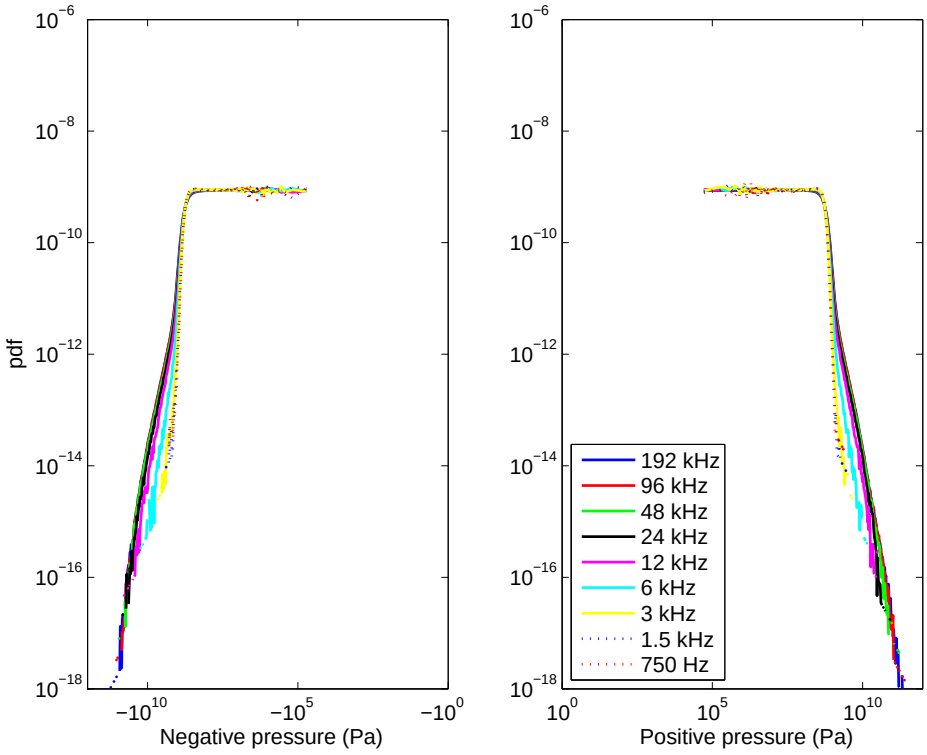

Figure 3.17: Probability density as a function of pressure amplitude for real shrimp noise shown in a split-log format. The original shrimp noise was sampled at 192 kHz (dark blue solid line) and then down-sampled by half to values 96 kHz (red solid line) through 750 Hz (red dotted line).

3.6 Experimental investigation of pdf asymmetry in real shrimp noise

On 10 March 2008 a field experiment was conducted from a set of pontoons in Cockburn Sound, to establish if the asymmetry (between positive and negative instantaneous pressure amplitudes) predicted by the Garnele distribution was observed in real shrimp noise. Asymmetry had been observed in previous single hydrophone shrimp noise measurements, but it was not known if the asymmetry was due to propagation paths taken by the shrimp snaps (as predicted by the Garnele model) or due to deviation from omni-directional hydrophone response caused by the hydrophone cable (which is not considered in the Garnele model). To minimise the effects of hydrophone directivity, two hydrophones were mounted in opposite vertical orientations as shown in Figure 3.18. The two hydrophones were both HTI-96-MIN, with a nominal sensitivity of -164 dB re $1V_{rms}/\mu Pa$ and a usable bandwidth (claimed by the manufacturer) from 2 Hz to 30 kHz. The hydrophones were mounted on a PVC bar that was joined by support ropes to the surface, and the hydrophone cables were cable tied to the ropes. A weight was attached to the bottom of the PVC bar (using support ropes) to help maintain the shape and orientation of the hydrophone mounting while in the water. Bandwidth limited (20 kHz) white noise was used to determine the nominal gains of a two channel FOSTEX FR1 recorder used for the measurements. Weather conditions on the day were realistic (i.e. not ideal), a moderate fetch limited sea had developed due to onshore winds through the previous night and morning. Winds during the measurements were estimated around 10 knots and there was slight vertical movement of the pontoons. Various clunks and noises were caused by the motion of the pontoons against the supporting structures.

A fifteen minute recording of ambient noise was collected. Pressure values from each channel were grouped into quantization level histograms, which were then scaled to give an empirical probability density function (epdf). The epdfs were logarithmically smoothed into 200 bins using a log-base of 1.2. Positive pressure epdf values were

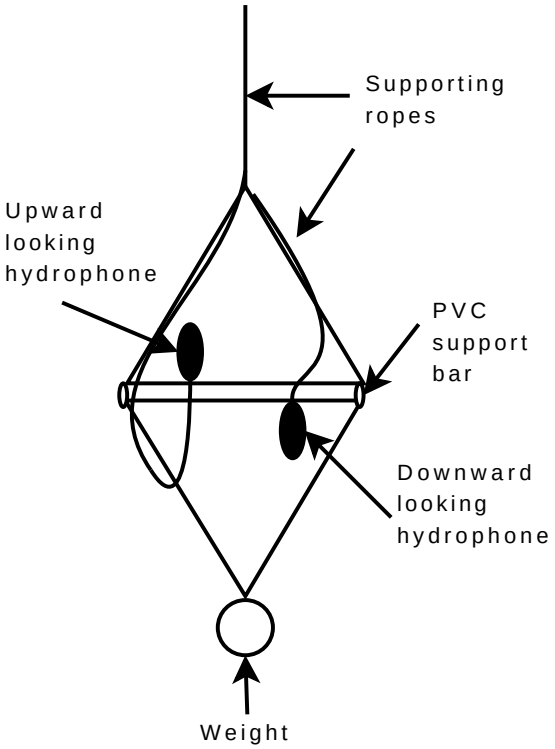

Figure 3.18: Hydrophone setup used for the pdf asymmetry experiment. Two HTI-96-MIN hydrophones were mounted on a PVC bar in opposite orientations. The PVC bar was joined by support ropes to the surface, and to a weight at the bottom.

taken from the downward looking hydrophone, and negative pressure epdf values from the upward looking hydrophone. Combining was conducted using the epdfs from the two hydrophones recorded at the same time. The results are epdf estimates minimally affected by the hydrophone cables, and are simultaneous in time, but with a small spatial separation. Results are shown in Figure 3.19 plotting probability density as a function of the pressure magnitude on a semi-logarithmic scale. Shown in the figures are the real shrimp noise results for positive amplitudes (red cross markers), and negative amplitudes (black square markers). Asymmetry is evident in the real shrimp noise, particularly beyond a magnitude of 50 Pascals. The measurements were repeated with the hydrophones in the opposite orientation to ensure that the observations were not being caused by the response of one of the hydrophones, and the results were in agreement.

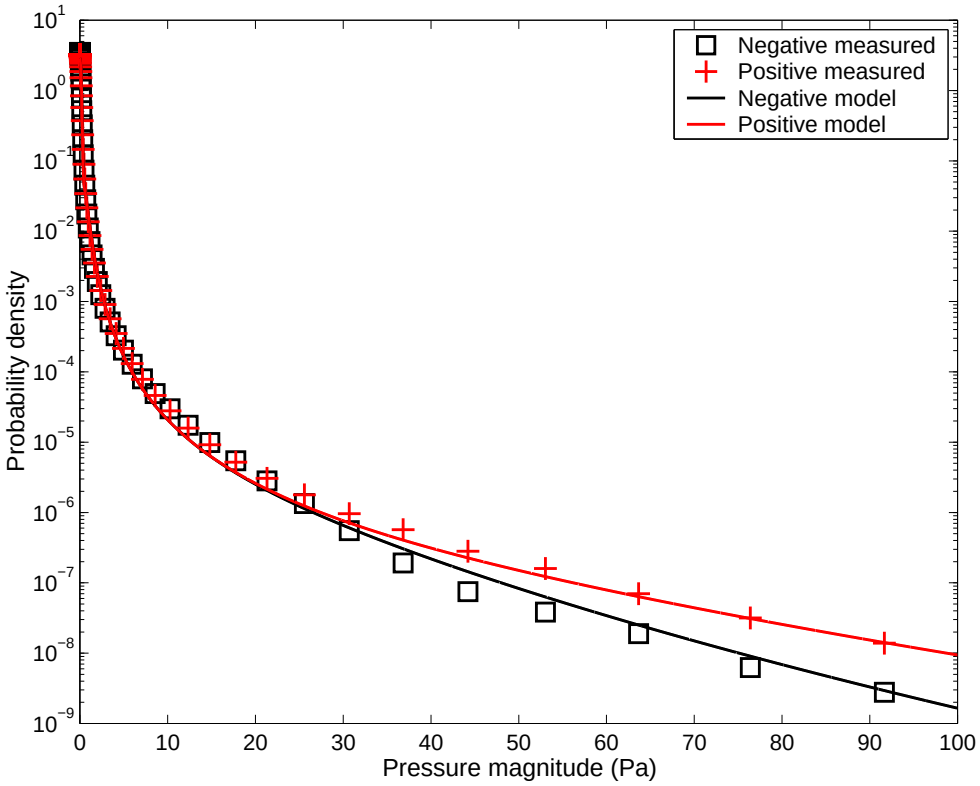

Figure 3.19: Asymmetry between positive pressure (red cross markers) and negative pressure (black square markers) probability densities observed in real shrimp noise. Solid lines show a Gaussian-Garnele fit to the data.

A Gaussian-Garnele model was fit to the epdf data and shown in Figure 3.19 using a solid red line for positive pressure values and a solid black line for negative pressure values. The Gaussian-Garnele model can describe the general behaviour of the real shrimp noise (that the asymmetry is non-zero and positive) but does not describe the detail accurately. The Gaussian-Garnele model depends on both the water depth and hydrophone depth, therefore the measured values of these parameters were used in the computation of the model values. To observe the asymmetry over the full range of pressure values, the difference between pdf values for equivalent positive and negative pressures were computed and scaled by the positive pdf value, to give a relative asymmetry measure

$$\rho(x) = \frac{f(x) - f(-x)}{f(x)}, \qquad x \geq 0. \tag{3.54}$$

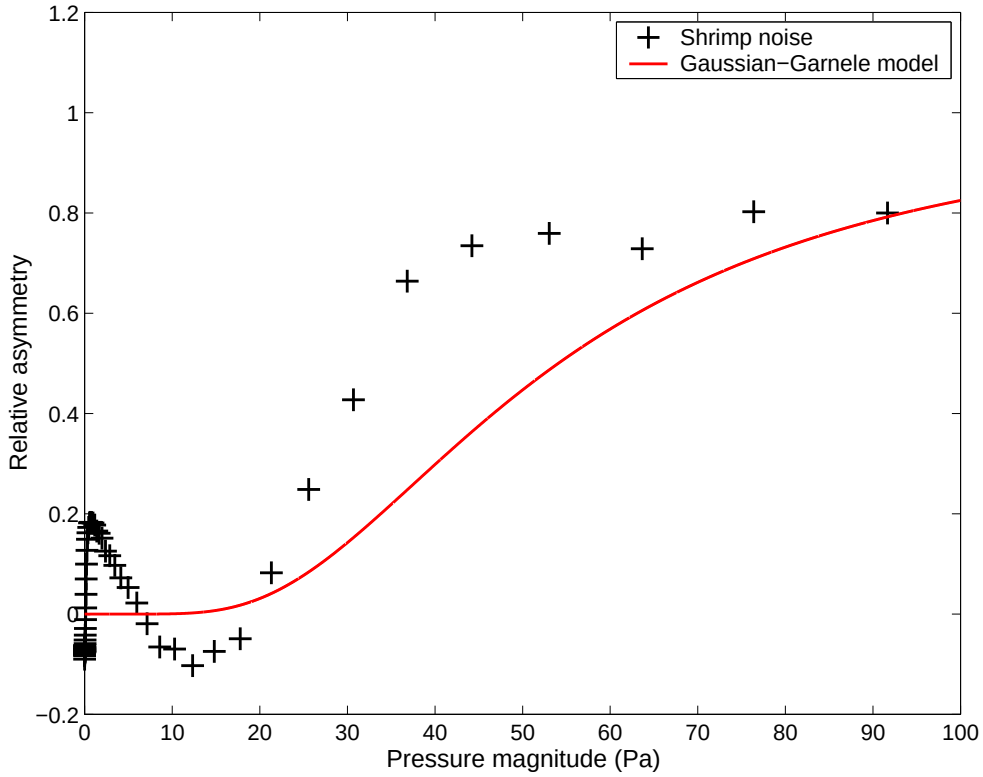

Figure 3.20: Amplitude pdf asymmetry for real shrimp noise (black cross markers) and the equivalent value predicted by the Gaussian-Garnele model (solid red line).

Relative asymmetry measures for real shrimp noise (black cross markers) and the Gaussian-Garnele model (red solid line) were computed from asymmetry trial data and the results shown in Figure 3.20. The real noise contained more asymmetry than anticipated for pressure magnitudes less than 20 Pa, and was more asymmetric than predicted by the Gaussian-Garnele model for all but the very extreme tail.

Two other data sets, recorded from the same location in Cockburn Sound (CS-B) but at a different time, were similarly analysed and the results shown in Figure 3.21 and Figure 3.22. The results shown in Figure 3.21 were recorded with a receiver bandwidth flat within 3 dB to 50 kHz and within 6 dB to 100 kHz (see Appendix A). The resulting relative asymmetry displays a definite relationship with pressure magnitude. A Gaussian-Garnele fit under-estimates the asymmetry through most of the tail but joins with the empirical result in the extreme tail. The results shown in Figure 3.22 were

recorded with a greatly reduced receiver bandwidth (less than 20 kHz). The relative asymmetry does not show the definite relationship with pressure magnitude; the results vary randomly.

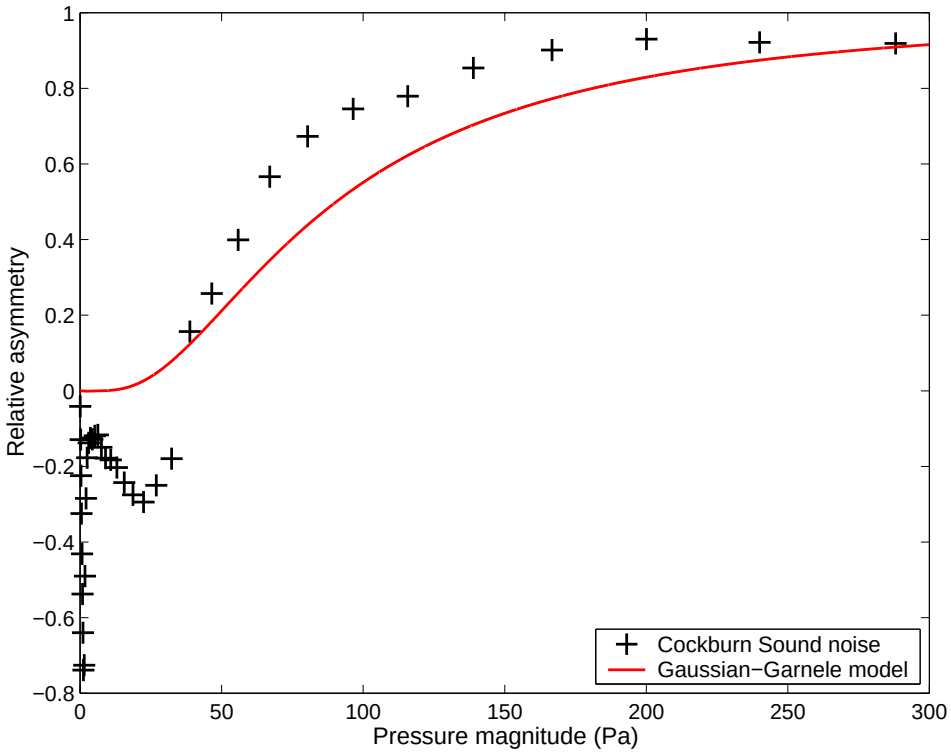

Figure 3.21: Amplitude pdf asymmetry using data from Cockburn Sound (CS-B) measured using a receiver bandwidth exceeding 100 kHz.

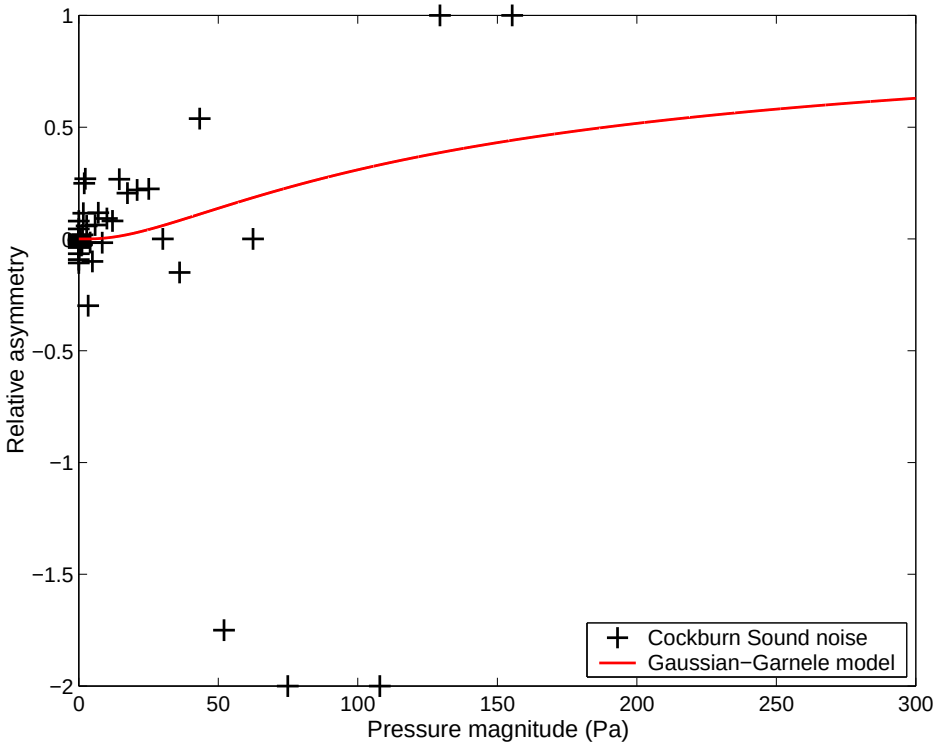

Figure 3.22: Amplitude pdf asymmetry using data from Cockburn Sound measured using a receiver bandwidth less than 20 kHz.

3.7 Summary of amplitude models

Gaussian, Gaussian-Gaussian mixture and SαS models have been discussed as models of shrimp noise. The Cauchy model was also addressed because it is a special case of the SαS distribution. A new candidate model of shrimp noise was derived from first principles and analytic expressions for the density and distribution functions were given. The new model was called the Garnele model. An ambient noise model was produced by combining the Garnele and Gaussian distributions using the ϵ-contamination framework.

Preliminary comparisons of the Gaussian-Garnele and SαS models were conducted using empirical density functions from real shrimp noise. Similar variations of both models about the real data pdf were observed through the body and moderate tails of the density function, while the Gaussian-Garnele showed an improved fit to the extreme tails of the density function. Other differences between the two models were the number of model parameters, the computational efficiency of parameter estimation, and the computational efficiency of evaluating the pdf. Parameter estimation for the SαS model was algorithmically simpler and computationally much more efficient than for the Gaussian-Garnele model, due in part to the large number of parameters in the Gaussian-Garnele model. However, evaluation of the Gaussian-Garnele pdf was more efficient than for the SαS pdf (in an example the difference was a factor of 50). The SαS was the most practical of the two models, and if parameters are to be estimated frequently then the additional cost of numerically evaluating the SαS pdf may be justified by the cost saving for parameter estimation. If the fit of the model through the extreme tails of the pdf is important, especially if pdf asymmetry is evident, then the additional complexity of the Gaussian-Garnele model would be justified.

Asymmetry was observed in the tails of the pdf of real shrimp noise, and the Gaussian-Garnele model was able to describe the general behaviour but not the detail of the asymmetry. An experiment was conducted that eliminated hydrophone directivity, due to the hydrophone cable, as a cause of the pdf asymmetry; further strengthening the

assumption of asymmetry due to path difference used in the derivation of the Garnele distribution. The relative asymmetry of Cockburn Sound shrimp noise was affected by receiver bandwidth, with wide-bandwidth data showing a definite relationship between relative asymmetry and pressure magnitude. When the receiver bandwidth was reduced the definite relationship was not observed.

Chapter 4

Temporal models

The purpose of this chapter is to establish whether the temporal statistics of snaps produced by a group of shrimp, as measured by a hydrophone, are consistent with a homogeneous Poisson process. The homogeneous Poisson assumption is important because it is implicitly assumed by many signal processing algorithms, which are designed to operate optimally under noise conditions that follow such temporal behaviour. Deviation of the real noise conditions from the homogeneous Poisson assumption would be expected to degrade the performance of such signal processing algorithms.

A cross section of temporal analysis techniques were applied to real snapping shrimp noise, drawing mainly on established techniques used in the fields of optics, neurophysics, molecular biology, finance and computer science. Some of the analyses allow formal statistical testing, while others require visual judgements or allow a pseudo-test. First order inter-snap interval histogram and uniform conditional tests were applied to the distribution of times between events. Higher order Fano-factor and k^{th}-order interval techniques were applied respectively to the times between events and the event counts. Each analysis technique revealed slightly different information about the snapping process.

4.1 Random point processes

Random point processes are characterised by highly localised events that occur apparently at random (Snyder and Miller, 1991). Examples of random point processes include emissions from radioactive decay, neuron firings, shot noise in optics, seismic events, and lightning strikes. Shrimp snaps are highly localised events occurring apparently at random within the ambient noise, and therefore display the fundamental characteristics of a random point process.

It is important to distinguish between the temporal statistics of a point process, and other temporal measures such as amplitude variations with time (see for example Ali 1983). A point process is only concerned with the points in time (or space) when highly localised events occur. The time-series detail of each event is ignored; for the case of shrimp noise the acoustic time-series is reduced to a binary time-series where a snap has either occurred or not occurred. This binary time-series is the point process representation of the acoustic time-series.

Statistical analysis is not normally applied to the point process directly. Instead, two processes that arise from a point process are used, they are: the counting process (N), and the interval process (Δ). The counting process looks at the number of events that occur within a given period of time, effectively sectioning the point process into windows and counting the number of events that occur in each window. The interval process uses the amount of time that elapses between events. Often it is the interval between consecutive events that is used, but an interval process can look at the time between every second, third, or nth (positive integer multiple) if desired. An example point process is shown in Figure 4.1. The figure includes an illustration of how the counts and intervals (of the point process) are computed. Fundamentally, the count and interval distributions are related through their complete distributions (Cox & Lewis 1966). The first and second order moments of these distributions may provide different and useful information about the point process. One important difference between the counts and intervals is that the counts retain the same time scale as the point process,

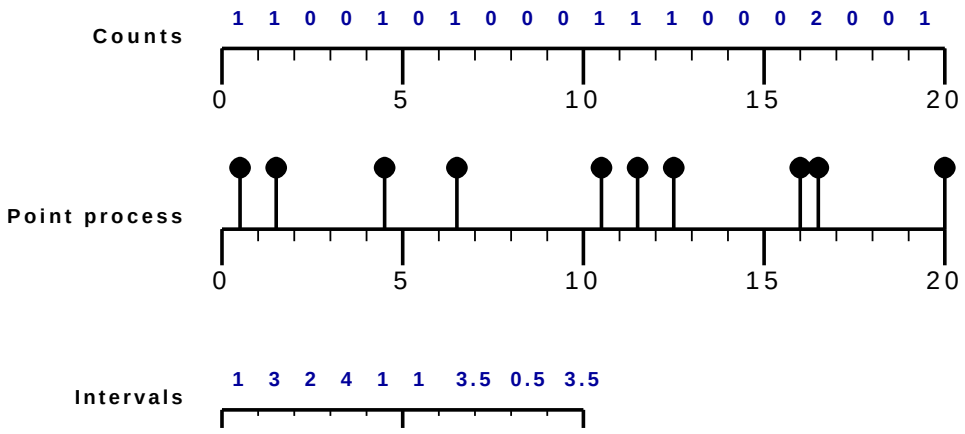

Figure 4.1: An illustrative example of a point process (circle stems) with counts (upper values) and intervals (lower values). The counts are obtained by specifying a window length then counting the number of events in consecutive non-overlapping windows. The intervals are computed as the difference between consecutive events.

whereas the intervals are a function of interval number (an incrementing integer). This makes analysis based on counts attractive because the scales of features observed in the counting process can be directly related back to the point process; the counting process time axis is undistorted (Lowen et al. 2001).

Reference origins (the point in time when the process start is observed) affect the stationarity of the counting and interval processes (Cox & Lewis 1966). The origin can be chosen at either an arbitrary time or an arbitrary event. If the origin is chosen at an arbitrary *event* then the *counting* process will be stationary (but the interval process will not); alternately if the origin is chosen as an arbitrary *time* then the *interval* process will be stationary (but the counting process will not). The elapsed time between an arbitrary time origin and the first event is called the *forward recurrence time* and is the cause of non-stationarity in the counting process with an arbitrary time origin.

In the following sections homogeneous Poisson and doubly-stochastic Poisson models are considered in detail. These models represent respectively the simplest, and slightly more realistic models chosen from a great number of available point process models

that could be used to describe shrimp noise. Selected analysis methods focused on these models are presented, to further understand the nature of snap events arriving at a hydrophone.

4.2 Homogeneous Poisson model

The homogeneous Poisson process is a mathematical concept used to describe a completely random series of events (Cox & Lewis 1966). Defining properties of the process are (for a more mathematical treatment see (Snyder & Miller 1991), (Cox & Lewis 1966) or (Hogg & Craig 1995)):

1. There is no trend in the series
2. Two or more events cannot occur at exactly the same instant of time
3. What happens in one time window is completely independent of what happens in any other non-overlapping time window, irrespective of the window length or the interval of time between them.

For a homogeneous Poisson process the probability density of counts N_t (as a function of time, t) is defined by

$$f(N_t) = \frac{(\lambda t)^{N_t} \exp(-\lambda t)}{N_t!} \tag{4.1}$$

having the characteristic that the mean and variance are equal

$$\langle N_t \rangle = \mathrm{var}(N_t) = \lambda t. \tag{4.2}$$

The name *rate of occurrence* is given to the parameter λ because N_t/t converges in probability to λ in the limit $t \to \infty$ (Cox & Lewis 1966).

For the same homogeneous process, the distribution of intervals Δ is

$$\mathrm{F}(\Delta) = 1 - \exp(-\lambda\Delta) \tag{4.3}$$

and the density function of intervals

$$\mathrm{f}(\Delta) = \frac{\partial \mathrm{F}(\Delta)}{\partial \Delta} = \lambda \exp(-\lambda \Delta). \tag{4.4}$$

The intervals are exponentially distributed with parameter λ.

The rate of occurrence λ is always a constant for a homogeneous Poisson process. The implication for shrimp noise, if it is to follow a homogeneous Poisson process, is that the rate of snapping must be constant; the snapping rate will not vary with time. Long term studies of shrimp noise (Everest et al. 1948) show that the spectrum level from a field of shrimp will typically only vary by a few decibels over the course of a day, with peaks occurring just before dawn and just after dusk. These variations are likely to be caused by an increase in snap rate, rather than a change in the individual snap source levels. If the rate of snapping changes then the process is not a homogeneous Poisson process, but if the changes are over relatively long time scales (a day), then the process may be approximately homogeneous Poisson over short time scales (a few seconds or minutes). It is therefore important to investigate rate changes in real shrimp noise over short and medium time scales, not only to further understand the nature of shrimp snapping, but also to provide important information for signal processing applications.

4.3 Event detection

Point process analysis requires that the measured acoustic time-series be converted into a series of events (an event-series), with each event representing the instant in time that a shrimp snap has been received. Detection of impulsive signal events in poorly defined noise is a challenging problem. Detection of shrimp snaps is made more complicated by the fact that the shrimp snaps do not all have the same or similar amplitude, rather the snap amplitudes are distributed as outlined in the previous chapter on amplitude models. Several detection methods were attempted, including: simple threshold, threshold with dead-time, de-convolution, and a Nuttal power law detector. The threshold with dead-time detector was found to be as reliable as any of the other detectors, with the

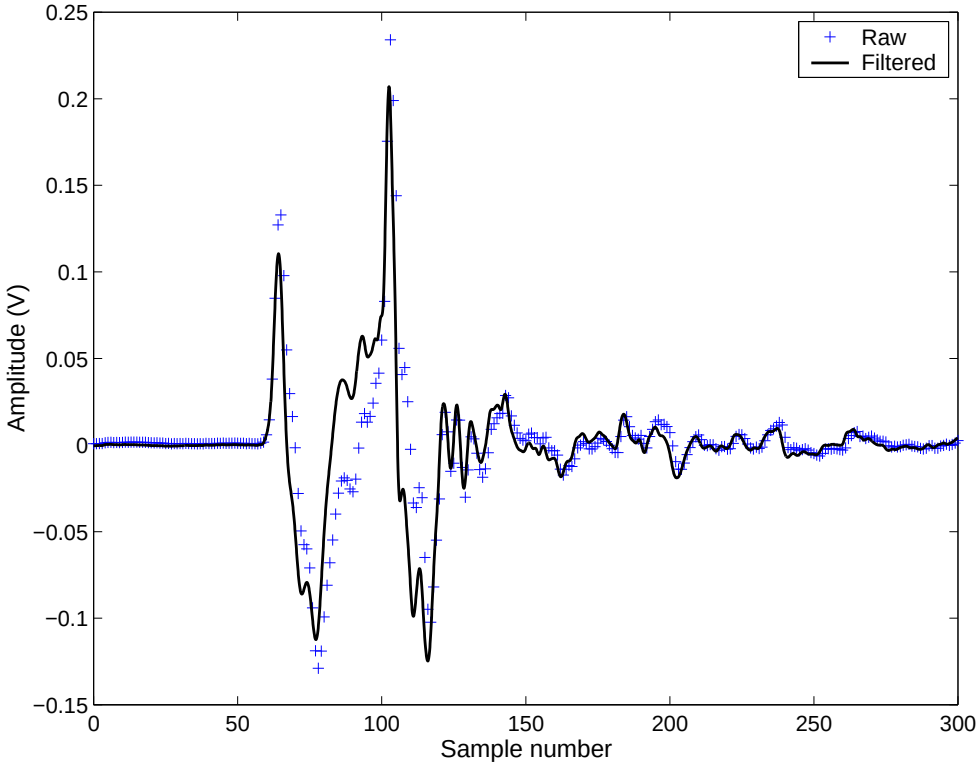

Figure 4.2: Raw (blue cross markers) and filtered (black solid line) time-series showing the effect of the pre-detection filter on a single shrimp snap. Important features of the snap remain unchanged by the filtering operation.

least amount of algorithm complexity, and was the fastest algorithm to execute. For these reasons the threshold with dead-time detector, combined with some pre-filtering, was used to detect the shrimp snaps.

4.3.1 Pre-detection filtering

A 6^{th} order high-pass Bessel filter with cut-off frequency at 1.4 kHz was applied to the data prior to detection, to remove unnecessary low frequency content from the acoustic time-series. A Bessel filter was chosen so that phase distortion introduced by the filtering process was linear. Figure 4.2 shows the difference between raw (blue cross markers) and high pass filtered (black solid line) time-series data for a representative

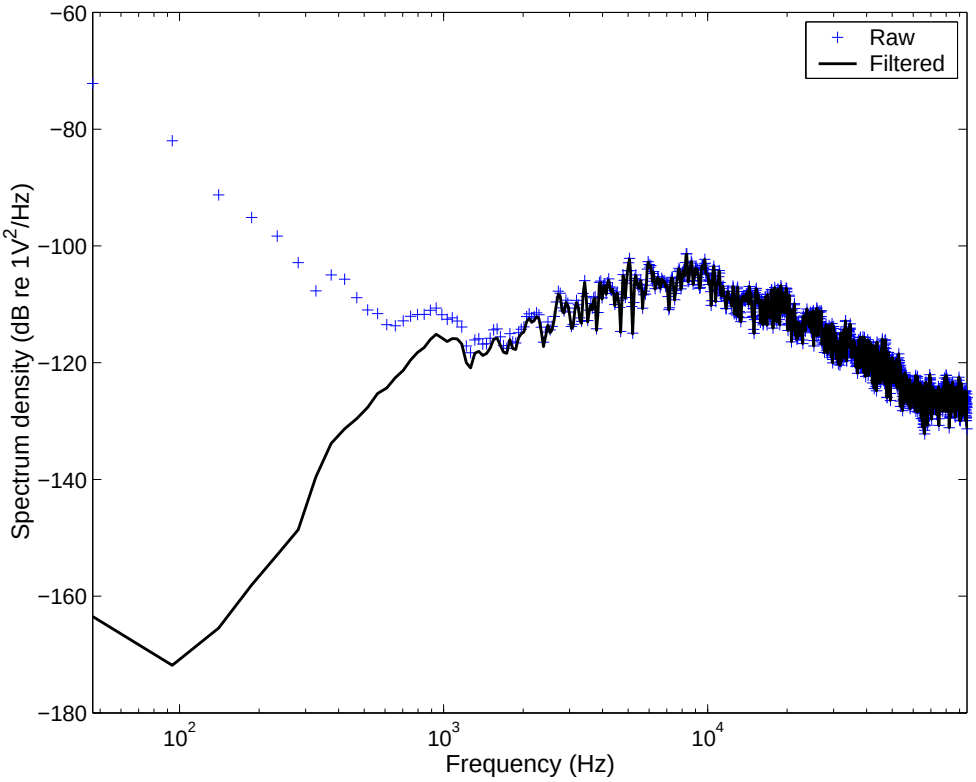

Figure 4.3: Spectrum of shrimp noise before (blue cross markers) and after (black solid line) the pre-detection filter. The filter was designed to attenuate frequencies below 1 kHz.

shrimp snap. The filtering operation reduced the maximum excursion of the precursor and the main peak, but the snap remained largely intact. Figure 4.3 shows a spectral density of shrimp noise, computed before (blue cross markers) and after (black solid line) filtering. Attenuation below 1 kHz is evident, with up to 90 dB difference below 100 Hz. Above 2 kHz the two spectra are almost identical and the pronounced "bump" in the spectrum caused by snapping shrimp is unchanged. The filtering operation substantially attenuated low frequency information, without adversely affecting the important components required for analysis of snapping shrimp noise.

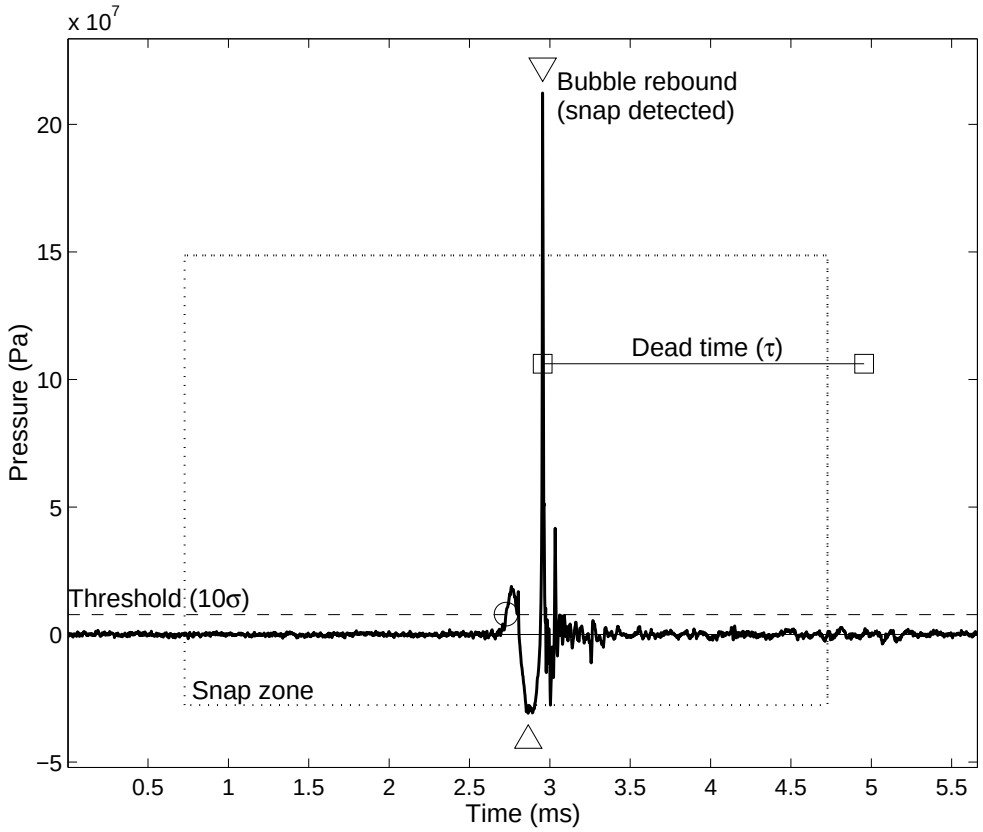

Figure 4.4: A graphical representation of snap detection. The threshold (dashed horizontal line at 10σ), point of threshold exceedance (circle), snap zone (dashed box), detection points (triangles) and dead-time (square ended bar) are shown.

4.3.2 Threshold detection with dead-time

Threshold levels were set at multiples of a standard deviation of the noise (σ). Detections were declared when the amplitude of the time-series exceeded the value of the threshold. The standard deviation σ was estimated using all samples from the first ten seconds of the acoustic time-series.

A representative acoustic time-series of a single snap with a threshold level set at 10 standard deviations above the mean is shown in Figure 4.4. In this case the precursor exceeded the threshold which produced a detection at the wrong time. The snap time was to coincide with the main peak, not the precursor. To choose the correct time, a

snap zone was defined using a fixed number of samples prior-to and after the threshold breach. The snap zone is shown in Figure 4.4 as a dotted box. The maximum value (inverted triangle marker) within the snap zone was considered to be the main peak; the correct snap time.

To reduce the number of false detections on surface reflected replica snaps, the minimum value (triangle marker) in the snap zone was also identified. If the minimum value was larger than the maximum value then the detection was declared a surface reflection, and rejected. Signals from distant shrimp may also contain large negative pressure components, similar to those from surface reflections, due to a low grazing angle bottom reflected signal having a phase shift near π radians (Chitre et al. 2003). When the threshold is sufficiently low, the additional processing used to reject surface reflections may also cause missed detections of distant shrimp.

Following each snap was a short period of time when pressure fluctuations were potentially much larger than the detection threshold. Such fluctuations are evident in Figure 4.4. The fluctuations include a bottom reflected replica (Chitre et al. 2003) and oscillations caused by the propagation environment and the impulse response of the measuring equipment. To avoid false detections during the period of fluctuation a dead-time (shown using a line with square markers at each end) was enforced after each snap. Detections were not declared during the dead-time. The effects of missed detections due to the dead-time are identified for the inter-snap interval and Fano-factor analyses that follow, but are not identified for the Kth order interval analysis. Other modifications to the thresholding technique, such as adaptive noise estimation (see for example Watkins et al. 2004) were not used because they were not expected to provide any benefit additional to the pre-filtering operation. Pre-filtering was preferred due to lower computational costs (complexity, speed and code availability).

4.3.3 Consequences of threshold detection

Threshold detection cannot detect any snap events below the threshold level. Distant shrimp, those with lower received amplitudes, are therefore not included in the event-series. Loosely speaking the threshold relates to a maximum range, beyond which the shrimp events would not be included; the event-series and subsequent analysis is therefore restricted to local shrimp. An alternative argument would be that threshold detection would reduce the detection efficiency. If the missed snap events were similar to Bernoulli random deletion, then the effect would tend to drive the counting distributions toward homogeneous Poisson (Teich & Saleh 1982). Provided the shrimp population within the threshold-defined range did not vary appreciably during the period of observation then the range restriction, or Bernoulli deletion effects, were considered to be acceptable.

Another consequence of threshold detection was modulation of the peak heights by the lower frequency noise. Pre-filtering was designed to minimise the lower frequency noise components but at the same time preserve as much of the snap structure as possible. Filtering techniques are never ideal, and some modulation would always remain. The effect of modulation was to periodically raise some of the peaks (near the threshold) above then below the threshold level. The modulation effects were assumed to be small enough not to appreciably affect the temporal analysis, however the effect was not studied in detail.

4.4 Inter-snap interval histogram analysis

A simple test for the homogeneous Poisson process is to compare the distribution of time intervals between snaps (or events) with a theoretical distribution. The test is referred to as the inter-event interval (IIH) test (see for example Thurner et al. 1997). For a homogeneous Poisson process the intervals are exponentially distributed, with

density function given previously in Equation 4.4. When events are detected using a dead-time then Equation 4.4 must be modified because the probability of observing an interval less than the dead-time is zero (Ricciardi & Esposito 1966). The modified probability density function is

$$f(\Delta) = \lambda \exp(-\lambda(\Delta - \tau)) \tag{4.5}$$

where τ is the dead-time (in seconds), which can be set to zero if dead-time is not used, and λ is the rate of occurrence (the same as that for a homogeneous Poisson process). Variable Δ is the interval length (in seconds). The modified distribution is called the dead-time modified exponential distribution, and it describes the probability density of intervals arising from a process called the Dead Time Modified Poisson (DTMP) point process (Lowen & Teich 1992). Parameter λ can be estimated using

$$\lambda = \frac{1}{\overline{\Delta} - \tau} \tag{4.6}$$

where $\overline{\Delta}$ is the mean interval.

Testing goodness of fit between the empirical and theoretical density function curves was conducted both visually and statistically. For visual comparison the theoretical and empirical density curves were plotted together and any differences noted. To aid comparison a log-log plot was used so that the exponential and dead-time modified exponential density functions would lie on a straight line, as in Liebovitch et al. (1999). Censure corrections (to account for truncation of the observations) were applied when using the empirical probability density function (epdf) method from Waterman & Whiteman (1978). It was observed that the left censure at zero (or the dead-time) was critical for comparing the epdf with theoretical curves. It was also observed that when large numbers of observations were available the scaled histogram density function estimates were less sensitive to both the left and right censures.

Three shrimp noise data sets were chosen as a representative cross section of the available shrimp noise data. These were selected from data measured in the Spencer Gulf (SG), near Seal Island (SEAL-C) and in the Nornalup-Walpole Estuary (WP). The remaining shrimp data sets were reserved for the final summary analysis. A control set

of homogeneous Poisson distributed events was simulated and processed in a similar manner to the real shrimp noise. Inter-snap interval histograms were computed using 150 bins evenly spaced across the range of intervals. A logarithmic smoothing operation was applied to the histogram estimates to improve accuracy in the extreme tail, where count numbers are expected to be low. The smoothing window size was increased with increasing interval duration using a logarithm base of 1.2 (see Appendix C). For each individual data set an estimate of λ was computed using Equation 4.6 and a theoretical curve produced from Equation 4.5. Results are shown in Figure 4.5 by plotting probability density against a normalised interval. Intervals were normalised so that the maximum interval from each data set corresponded with unity. The simulated homogeneous Poisson data lies in a straight line along the theoretical curve, whereas the real shrimp noise deviates at both small (less than 0.2) and large (greater than 0.6) normalised intervals.

Kolmogorov-Smirnov (D), Cramér-von Mises (W^2), and Anderson-Darling (A^2) statistics were computed using methods from D'Agostino & Stephens (1986). Kolmogorov-Smirnov (D) test results can be found in Legg et al. (2005). Anderson-Darling (A^2) results were found to be the most consistent with visual inspection results. The consistency of A^2 was attributed to increased sensitivity to deviations in the tail of the distributions.

The A^2 statistic was computed using

$$A^2 = -n - \frac{1}{n}\left(\sum_{k=1}^{n}\{(2k-1)(\ln(Z_k) + (2n+1-2k)\ln(1-Z_k))\}\right) \tag{4.7}$$

where n is the number of observations, and Z_k are the ordered (ascending) observations transformed using

$$Z_k = 1 - \exp(-\lambda(\Delta_k - \tau)). \tag{4.8}$$

Statistical testing was conducted on all of the real shrimp noise and used to produce Figure 4.6. Each bar in the figure represents an independent data set, from several different locations. Repeated bars at a given location indicates a data set taken at a

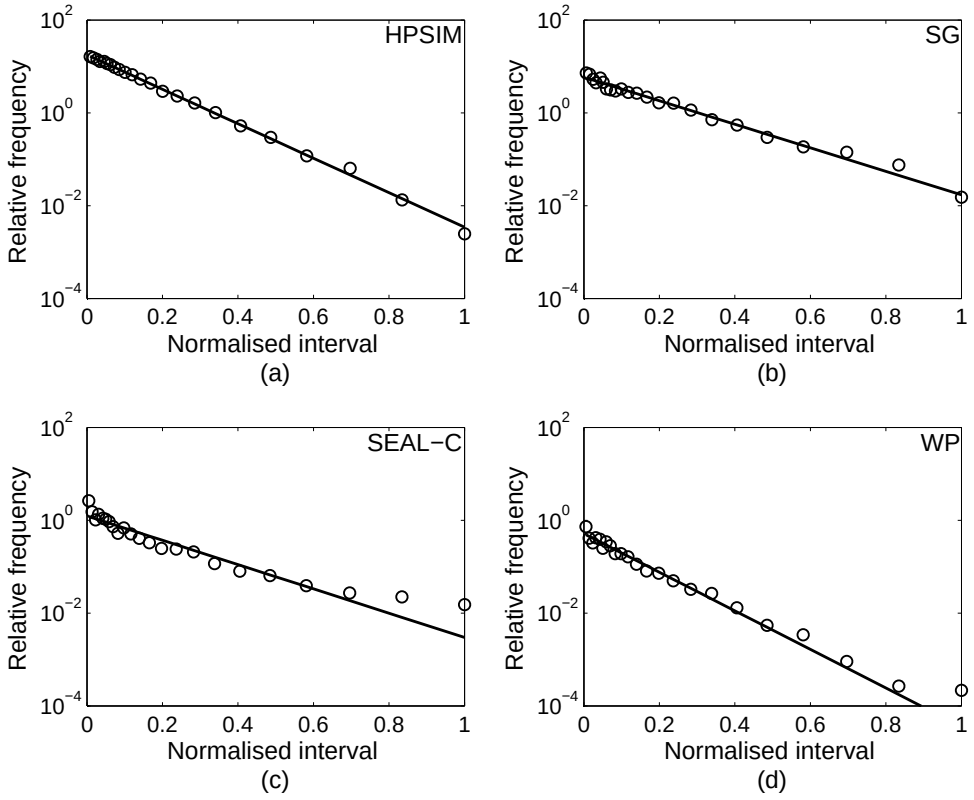

Figure 4.5: Inter-event interval probability density functions shown using a log-log plot so that an exponential curve describes a straight line. The plots show empirical and theoretical curves for simulated homogeneous Poisson data (a), and real shrimp noise from Spencer Gulf (b), Seal Island (c), and Nornalup-Walpole Estuary (d).

significantly different time (at least on a different day). The height of the bar shows the base 10 logarithm of the Anderson-Darling statistic. A horizontal (dashed) line shows the 95% confidence level. Values below this confidence level indicate that the homogeneous Poisson hypothesis was accepted with 95% confidence. As anticipated, the simulated homogeneous Poisson data set lies well within the acceptance region. Of the real data, only the Spencer Gulf (SG) shrimp noise lies within the acceptance region. For all of the other shrimp noise, the homogeneous Poisson hypothesis is rejected. The tests suggest that the homogeneous Poisson model is an inadequate model of snapping shrimp noise.

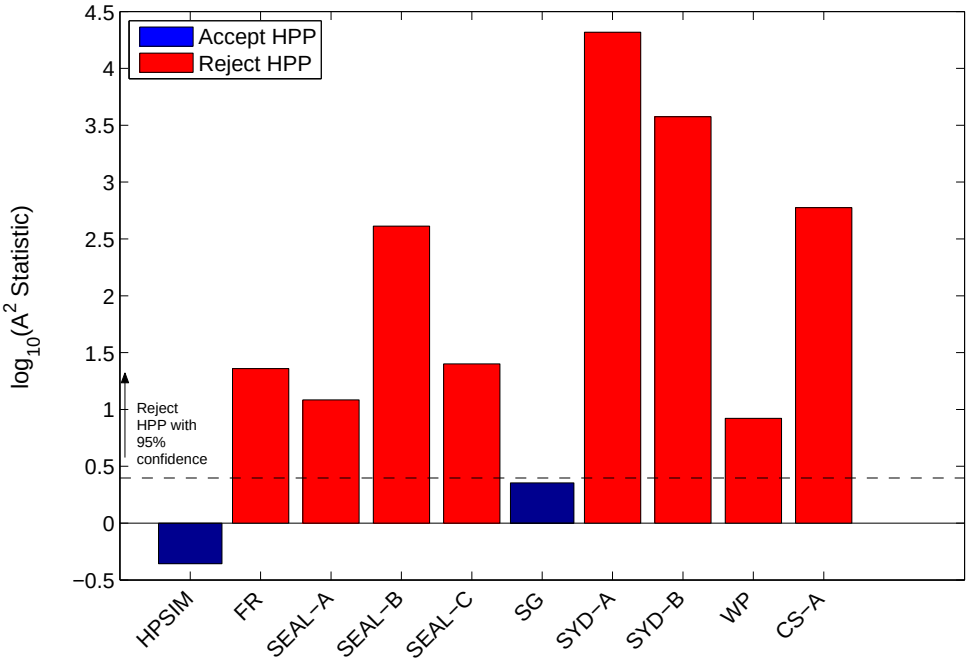

Figure 4.6: A summary of the homogeneous Poisson process (HPP) hypothesis for real shrimp noise using the Anderson-Darling statistic. The control data (HPSIM) accepts the homogeneous Poisson process hypothesis as does the real shrimp noise measured at Spencer Gulf (SG). All other real shrimp noise data reject the hypothesis at the 95% confidence level (horizontal dashed line).

4.4.1 The uniform conditional test

The uniform conditional test for a homogeneous Poisson process (Cox & Lewis 1966) was also applied to the available shrimp noise data. The advantage of the uniform conditional test (over the IIH test) was that it avoided the need to estimate the parameter λ. This is an advantage because it avoids biasing the test by using the same data to estimate the parameter and conduct the test. A disadvantage was that the test was for a homogeneous rather than dead-time modified homogeneous Poisson process. The effect of dead-time would slightly regularise the process and make rejection more likely. Durbin's transformation (described in Cox & Lewis 1966) was used on the event times to give a set of transformed order statistics Z_k. For a homogeneous Poisson distribu-

tion the Z_k are uniformly distributed between 0 and 1, and testing for this case can be conducted using one of the empirical distribution tests.

The two-sided Kolmogorov-Smirnov (D) statistic was chosen for the tests of real shrimp noise. The statistic was computed using the expression (D'Agostino & Stephens 1986)

$$D = \max\left\{D^+, D_-\right\}\left(\sqrt{n} + 0.12 + \left(\frac{0.11}{\sqrt{n}}\right)\right) \tag{4.9}$$

where

$$D^+ = \max\left\{\left(\frac{k}{n}\right) - Z_k\right\} \tag{4.10}$$

and

$$D^- = \max\left\{Z_k - \left(\frac{k-1}{n}\right)\right\} \tag{4.11}$$

are respectively the upper and lower one-sided Kolmogorov-Smirnov statistics. Parameter n is the number of observations and k is the set of integers from 1 to n. Equation 4.9 includes corrections for a single-sample test against a completely specified distribution.

The uniform conditional test, as specified above, was applied to all shrimp noise data and a summary of results shown in Figure 4.7. The figure shows the base 10 logarithm of the D statistic for each location, with some locations repeated at different times. The control data (HPSIM), Spencer Gulf (SG), Seal Island (SEAL-A) and Feather Reef (FR) data sets accepted the homogeneous Poisson hypothesis, all other data sets rejected the hypothesis. This was a curious result because the effect of dead-time was expected to increase the likelihood of rejection of the hypothesis but instead the opposite occurred.

Inconsistencies between the inter-snap interval histogram and uniform conditional tests suggest that these methods are not adequate for testing the homogeneous Poisson process hypothesis for snapping shrimp noise. Alternative methods are investigated in the following sections.

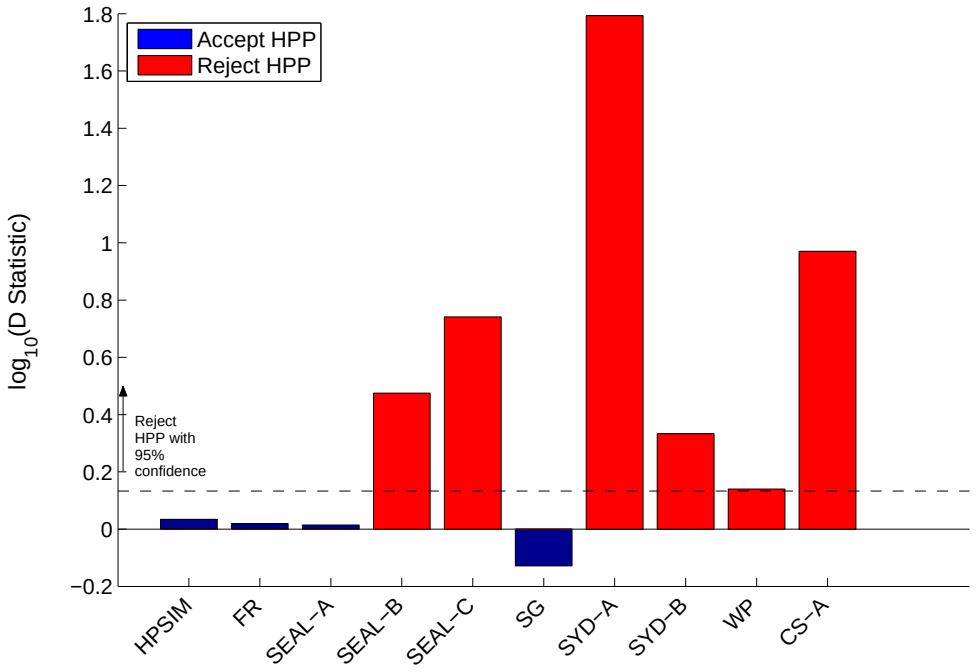

Figure 4.7: A summary of the uniform conditional test for a homogeneous Poisson process (HPP) applied to real shrimp noise. The control data (HPSIM) accepts the homogeneous Poisson process hypothesis as do the Spencer Gulf (SG), Seal Island (SEAL-A) and Feather Reef (FR) data sets. All other real shrimp noise data reject the hypothesis at the 95% confidence level (horizontal dashed line).

4.5 K^{th} order interval analysis

The inter-snap interval histogram analysis presented previously investigated the distribution of time intervals between successive snaps; these were the consecutive first-order intervals of the snaps (Perkel et al. 1967). The second-order intervals are the times between each snap and the one-after-next, and is therefore the sum of two of the consecutive first-order intervals following each snap. A k^{th}-order interval is the sum of k first-order consecutive intervals and therefore passes over $k-1$ snaps between the reference snap and the terminating snap.

For a homogeneous Poisson process the distribution of the k^{th}-order intervals (T_k) is

known; the $2\lambda T_k$ are χ^2 distributed with $2k$ degrees of freedom (Cox & Lewis 1966). A test for a homogeneous Poisson process can be based on the goodness of fit of empirical k^{th}-order interval distributions computed from real data against the expected χ^2 distribution. Results from this formal test were not consistent with observation, despite the agreement between empirical and theoretical probability density functions being visually acceptable. Possible reasons for the inconsistencies were the doubly censured data corrections (for the dead-time to the left and the time-series duration to the right), and the need to estimate the value of λ from the test data. A visual alternative to a formal statistical test was devised using transformed k^{th}-order intervals plotted as a function of a normalised ordering number (defined later) and k. K^{th}-order intervals were computed for incrementing k as outlined previously. For each k the observed intervals $\{X_1, X_2, X_3, ..., X_n\}$ were sorted (ascending) to give the ordering intervals ($\hat{T}_k$). Parameter λ was then estimated using the inverse of the mean value of the observed intervals, $\overline{\lambda} = 1/\langle\hat{T}_k\rangle$. The values $2\lambda\hat{T}_k$ were then transformed using the probability integral transformation for a χ^2 distribution with $2k$ degrees of freedom, giving transformed values Z_i, where $i = 1, 2, 3, ..., n$. These steps were identical to the first steps used for case-0 empirical distribution function tests (D'Agostino & Stephens 1986). For a homogeneous Poisson process the values of Z_i should lie on the line $y = i/n$ for all values of k; the Z are monotonically increasing values between 0 and 1, with slope $1/n$. The order statistics were scaled by the maximum order statistic to give a *normalised ordering number* ($\hat{T}/\hat{T}_{\max}$) so that the slope of the curve Z as a function of normalised ordering number is unity (for a homogeneous Poisson process). Results from simulated homogeneous Poisson control data are shown in Figure 4.8. A colour-bar was used to show the value of Z. For all values of k the Z values increase monotonically between 0 and 1 as expected, with small fluctuations indicative of normal variability for a homogeneous Poisson process. Deviations from the homogeneous Poisson baseline of Figure 4.8 indicate that the process generating the events is not a homogeneous Poisson process.

Rudimentary interpretation of the transformed k^{th}-order interval distributions can be achieved by comparison with the expected result for a homogeneous Poisson process. Statements such as "there are more large intervals between every 5^{th} snap than would

be expected for a homogeneous Poisson process" are possible. Relating these interpretations back to the original point process is still problematic because the intervals lie on a deformed time reference (with respect to the original point process). The average interval between consecutive snaps may be used as a transformation reference time, so if the average time is 0.2 s then the large intervals between every 5^{th} snap, for example, could be interpreted as correlation on a time scale of 1 s. This is, however, not a rigorous treatment of the issue.

Transformed k^{th}-order interval distributions for real shrimp noise are shown in figures 4.9 through 4.13. The plots can be interpreted by choosing a k value of interest, then inspecting the change in Z as a function of the normalised ordering number. If the value of Z increases linearly with normalised ordering number (i.e. follows the same gradient as the Z colour bar) then the behaviour at that k is consistent with a homogeneous Poisson process. For example, the Spencer Gulf results (Figure 4.9) show that for very low k the intervals are consistent with a homogeneous Poisson process, but deviation from a homogeneous Poisson process occurs rapidly as k increases (e.g. when looking at the intervals between every 10^{th} snap there are a higher than expected number of relatively short time intervals). The Spencer Gulf example is particularly important because the process was accepted as homogeneous Poisson using the IIH test, which is consistent because the IIH test is a test based on $k = 1$ intervals. What the k^{th}-order interval analysis shows is that while the process is consistent with a homogeneous Poisson process for $k = 1$ the entire process is definitely not consistent with a homogeneous Poisson process.

Cockburn Sound (CS-A) results in Figure 4.10 are consistent with a homogeneous Poisson process for low values of k, but as k increases there is an increasing number of longer time intervals. The Nornalup-Walpole results (Figure 4.11) are consistent with a homogeneous Poisson process for both low and high values of k with deviations occurring for k between 400 and 800, where there are a higher than expected number of large intervals. The Seal Island Cave (SEAL-A) result shown in Figure 4.12 contains a lot of structure, with some oscillation between consistency with a homogeneous Poisson

process near $k = 200$ and $k = 500$, and higher numbers of small time intervals. For k greater than 600 there are consistently higher than expected numbers of small to medium time intervals. The Feather Reef results in Figure 4.13 are consistent with a homogeneous Poisson process for small k followed by a slight transition to higher numbers of large time intervals and then progressively increasing numbers of both small and large time intervals, displaying a symmetry that is not observed at the other locations. All of the real shrimp noise results show significant structure as a function of k; none of the shrimp noise results display the characteristics expected for a homogeneous Poisson process.

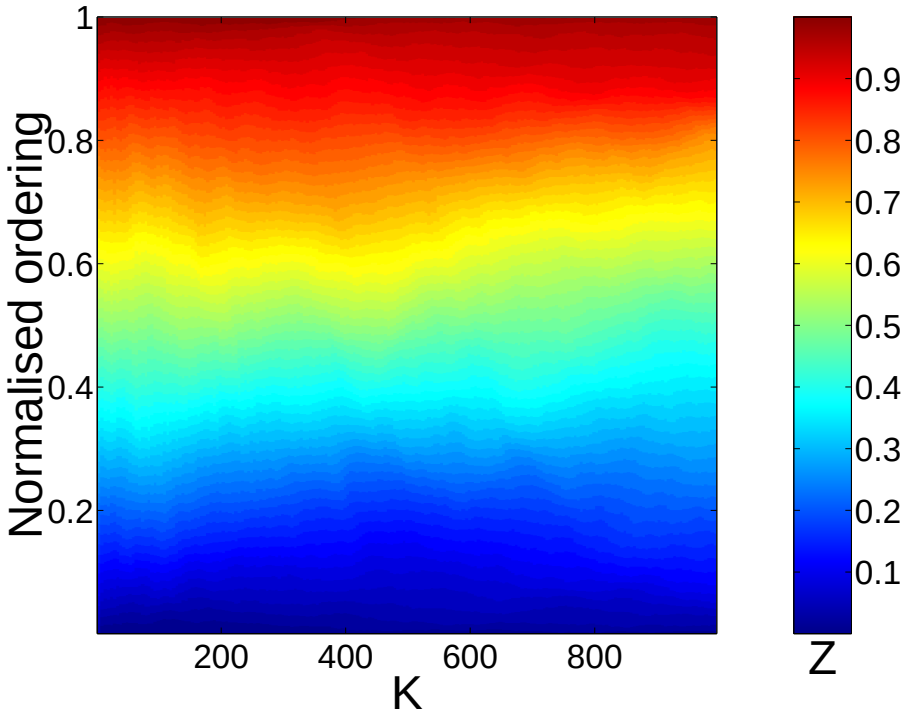

Figure 4.8: A waterfall plot of the k^{th}-order interval distributions for simulated homogeneous Poisson control data.

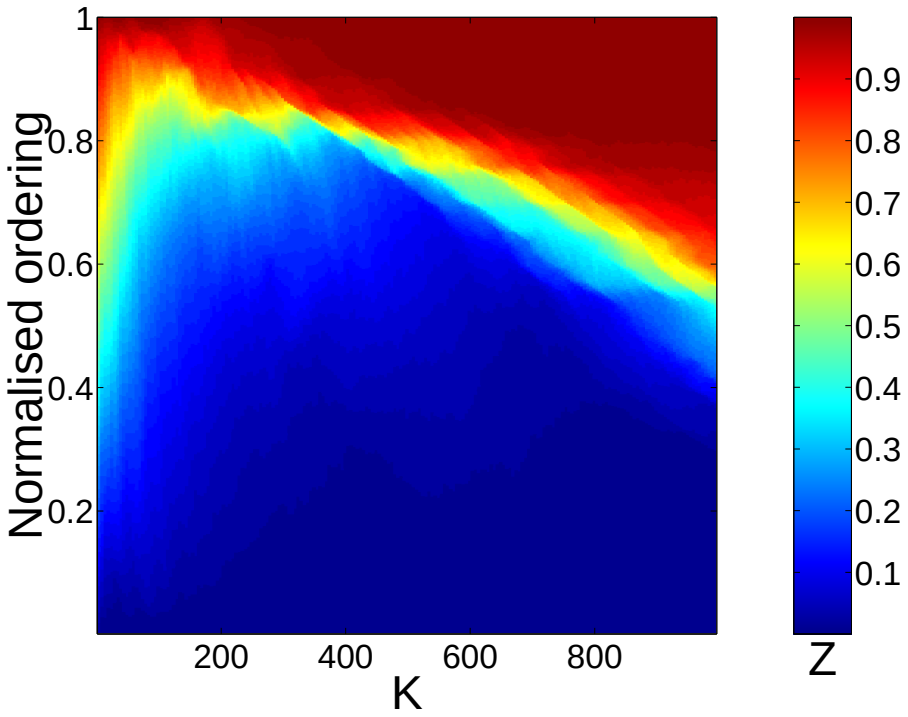

Figure 4.9: A waterfall plot of the k^{th}-order interval distributions from Spencer Gulf.

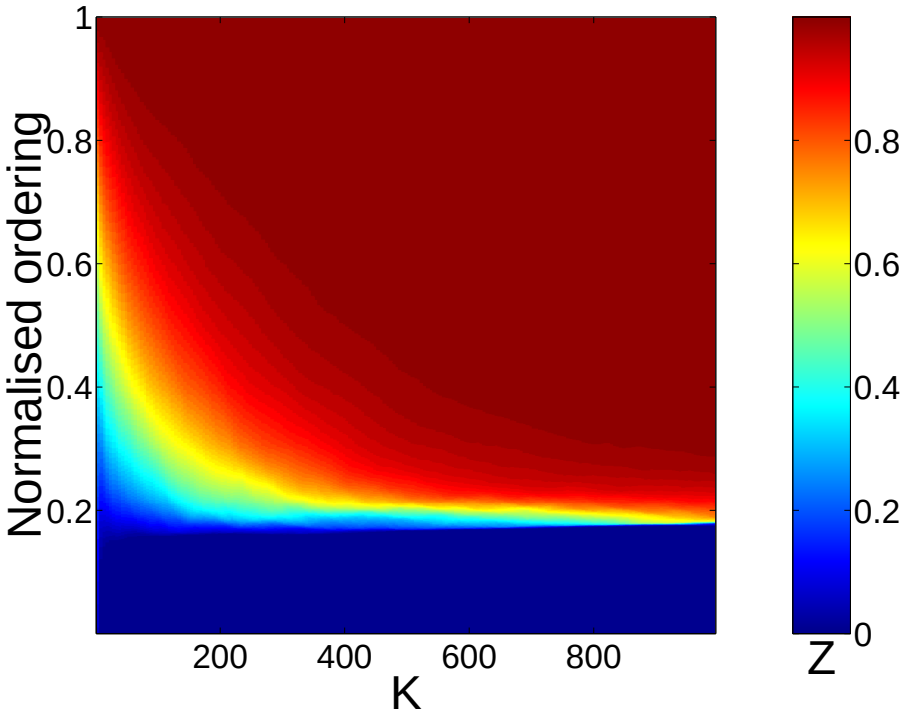

Figure 4.10: A waterfall plot of the k^{th}-order interval distributions from Cockburn Sound (CS-A).

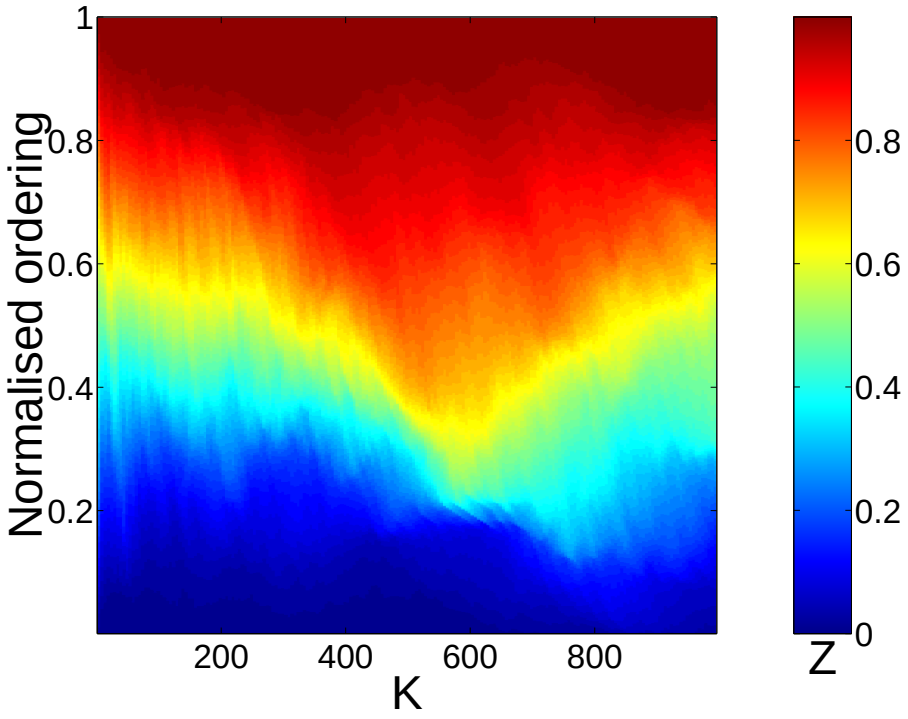

Figure 4.11: A waterfall plot of the k^{th}-order interval distributions from the Nornalup-Walpole Estuary.

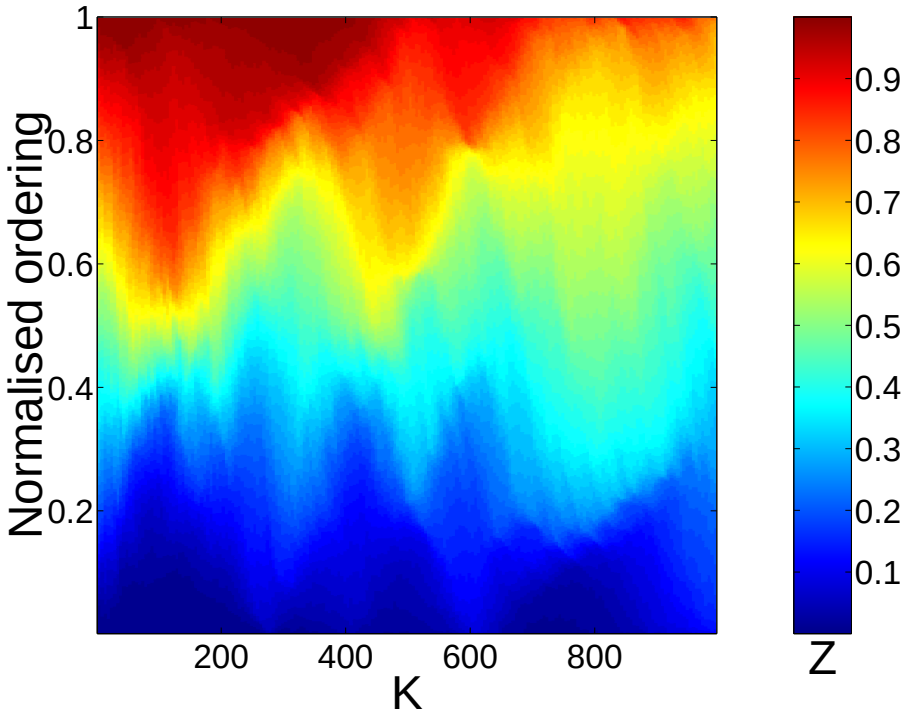

Figure 4.12: A waterfall plot of the k^{th}-order interval distributions from the Seal Island cave (SEAL-A).

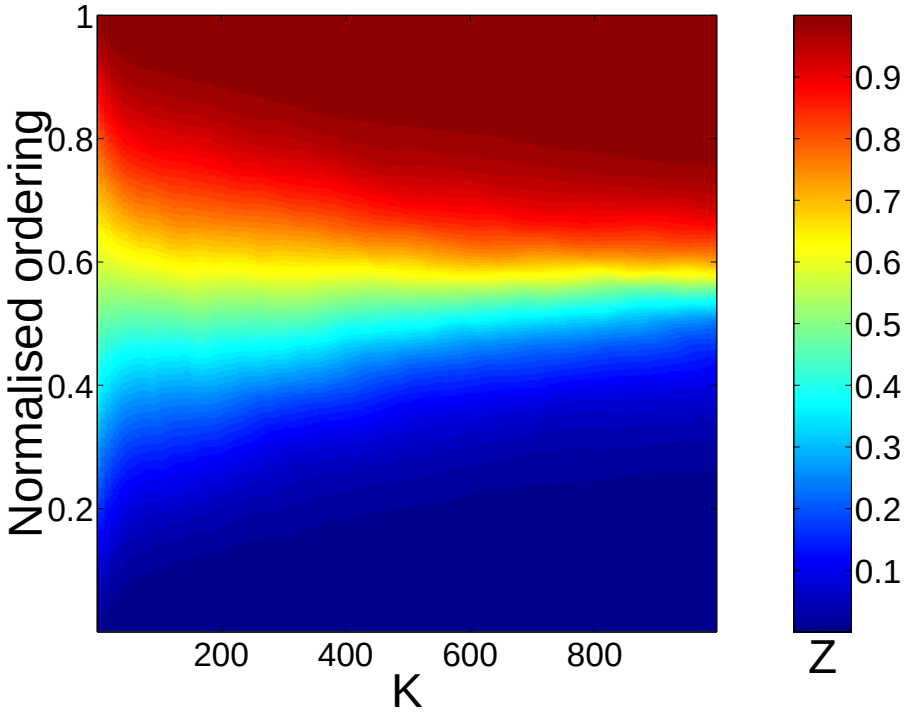

Figure 4.13: A waterfall plot of the k^{th}-order interval distributions from Feather Reef.

4.6 Intensity function analysis

Alternative Poisson models arise when the constant intensity constraint of the homogeneous model is relaxed. For temporal models the intensity is allowed to vary as a function of time. Relaxing the constant intensity constraint on shrimp noise is not a difficult step to take, since the spectrum level of shrimp noise has been observed to vary over the period of one day (Everest et al. 1948) most likely caused by an increase in snapping activity. Empirical time varying intensity functions, $\hat{\Lambda}(t)$, were estimated using a minimum-mean-square filter as a predictor. Assuming that the estimator is a linear function of the data, the estimator has the form (Snyder & Miller 1991)

$$\hat{\Lambda}(t) = a(t) + \int_{t_o}^{t} h(t,u)\,\mathrm{d}N(u) \tag{4.12}$$

where $a(t)$ is a deterministic function of time, and $h(t,u)$ is the impulse response of the linear filter estimator. If $a(t)$ is set to zero, and the impulse response is of the form

$$h_o(t,u) = \begin{cases} \frac{1}{\varpi}, & t-\varpi \le u < t \\ 0, & \text{otherwise} \end{cases} \tag{4.13}$$

then the filter reduces to a simple moving-average histogram estimator, using window size ϖ (Snyder & Miller 1991). When computing $\hat{\Lambda}(t)$ using window-based estimation, the time duration of the window (ϖ) becomes important. The window needs to be concurrently large enough to allow reasonable estimates of rate, and small enough to capture important variations with time. Optimum window estimators can be formed if the autocorrelation function ($\rho(u)$) of the intensity process is known (Virtamo et al. 1996, Snyder & Miller 1991), which is similar to the "rate meter" approach suggested by Perkel et al. (1967). If the autocorrelation function is not known then a histogram estimator can be used (Snyder & Miller 1991).

Empirical intensity functions were computed using a histogram estimator with window length $\varpi = 3$ seconds, moved across the data in 0.1 second increments. A 3 second window was chosen to ensure a reasonable number of events from which to compute the average, given the relatively low average snap intensity of most of the data sets.

A histogram estimator was used because nothing was known of the autocorrelation function (of the intensity process) of real shrimp noise. Results for the control (HPSIM) and representative sets of real shrimp noise from Cockburn Sound (CS-A), Spencer Gulf (SG), Seal Island (SEAL-C) and Nornalup-Walpole Estuary (WP) are shown in Figure 4.14. The control simulation had a snap rate of 17 snap s^{-1}, similar to that of Cockburn Sound which was around 20 snap s^{-1}. The average intensities from other locations are much lower than in Cockburn Sound, most less than 10 snap s^{-1}. In each plot the y-axis (intensity) limits are set at plus 10, and minus 5, standard deviations beyond the mean. Interesting features are the rapid change of rate in the Seal Island data near 300 seconds, and the quantized appearance of the Nornalup-Walpole data due to very low snap intensity. Intensity estimates for the Spencer Gulf data terminate before 200 seconds due to the length of the time-series.

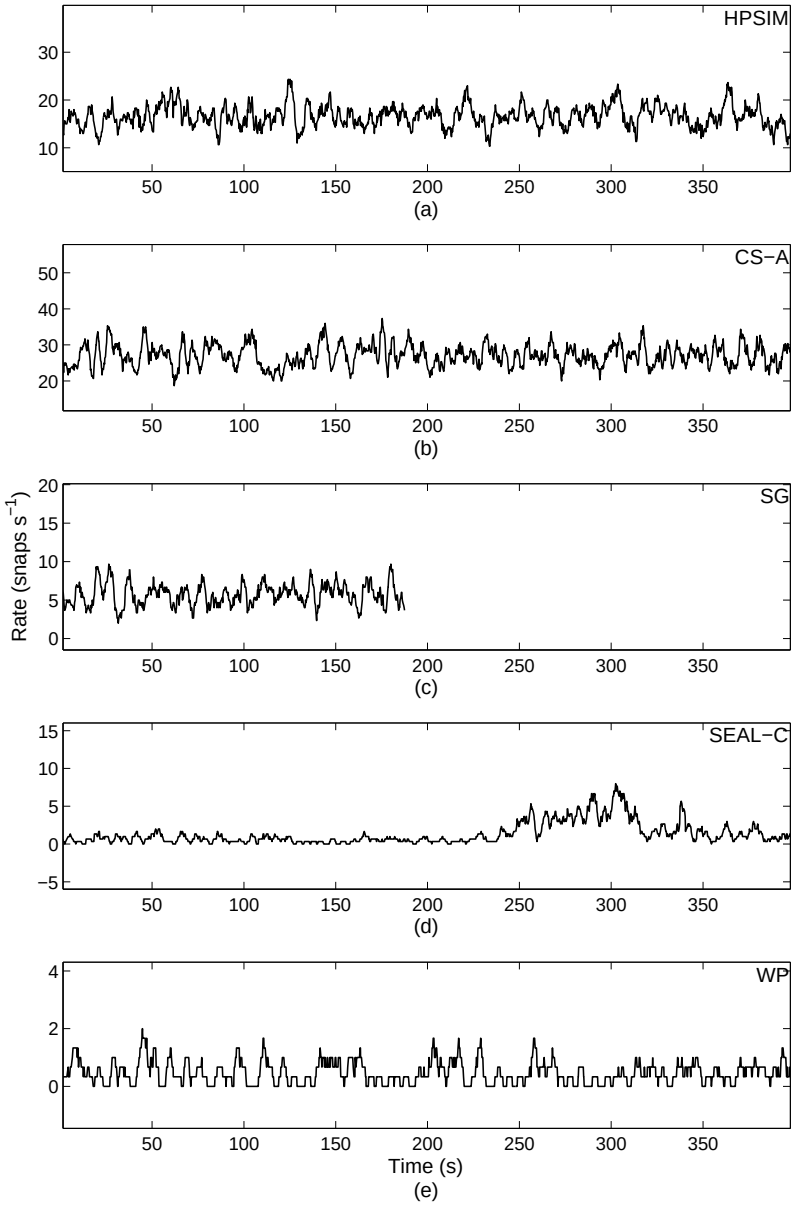

Figure 4.14: Snapping intensity as function of time for control and real shrimp noise data. A homogeneous Poisson control result is shown (a) along with real shrimp noise from Cockburn Sound (b), Spencer Gulf (c), Seal Island (d) and Nornalup-Walpole Estuary (e). Intensities were computed using a histogram estimator with a 3 second window.

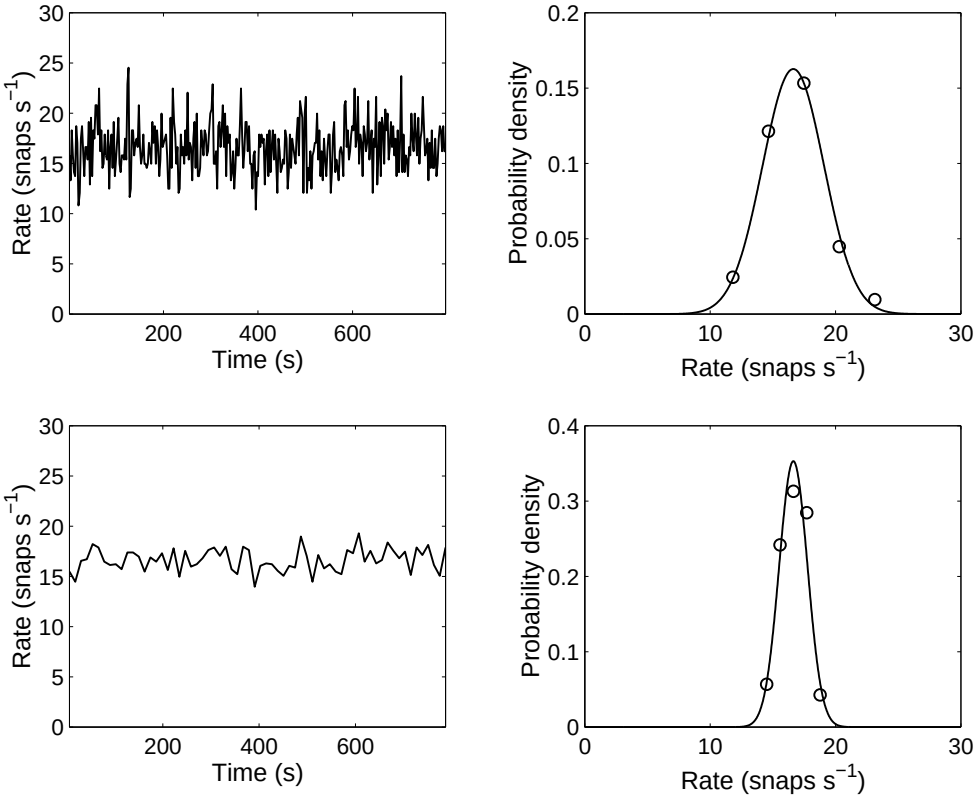

Figure 4.15: Event intensity estimated using 1 second (a) and 10 second (c) windows. The snaps were simulated from a homogeneous Poisson process with constant rate $\lambda = 17$ snap s^{-1}.

Results obtained for the intensity function depend on the window size. To illustrate, Figure 4.15 shows intensity estimates from simulated homogeneous Poisson data (the rate is actually a constant) for a 1 second window (a) and a 10 second window (c). Also shown in Figure 4.15 are empirical probability density functions (circle markers) of the intensities for a 1 second window (b) and a 10 second window (d) as well as a Gaussian fit (solid line). The variance of intensity given a 1 second window was 26, and for a 10 second window was 1.7; the variance reduces as the window size is increased.

Gaussian fits to the same data, using windows of size 1,2,3,5 and 10 seconds, are shown in Figure 4.16. Change in intensity variance as a function of window size was shown using a log-log plot on Figure 4.17. The intensity variances (solid line) describe a

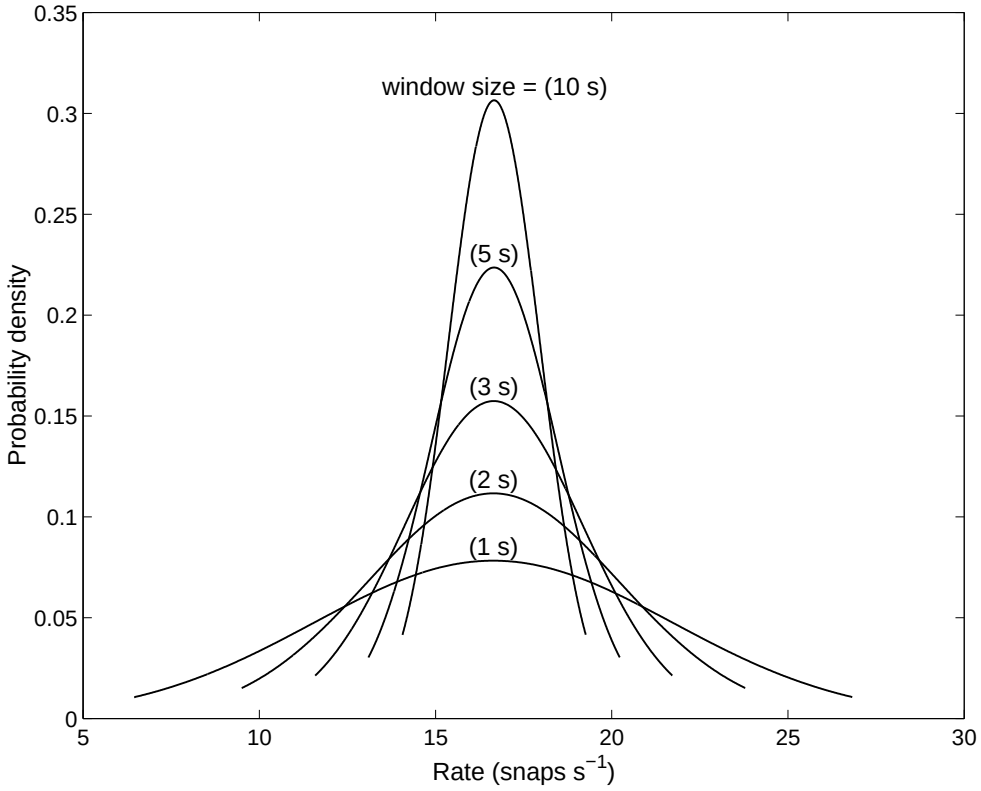

Figure 4.16: Snapping intensity distributions using window sizes ϖ =1,2,3,5 and 10 seconds. The window time is shown on top of each curve near the mean value. A Gaussian representation has been used for illustration purposes only.

decreasing straight line on the log-log plot, indicating an inverse relationship between intensity variance and window size. The mean intensity divided by the window size (square markers) describes the same line because variance and mean are equal for a homogeneous Poisson process. This provides an important bench mark, showing the amount of variability expected for a homogeneous Poisson process.

Normalised intensity variance as a function of window size, using real shrimp noise from selected locations, are plotted in Figure 4.18. The results include simulated homogeneous Poisson events as a control. The homogeneous Poisson control curve lies lower than the real shrimp noise, although at low window sizes the results tend toward a similar value. Of the shrimp noise data sets the Seal Island data has the most obvious deviation from the homogeneous Poisson control. Meaningful rate results for

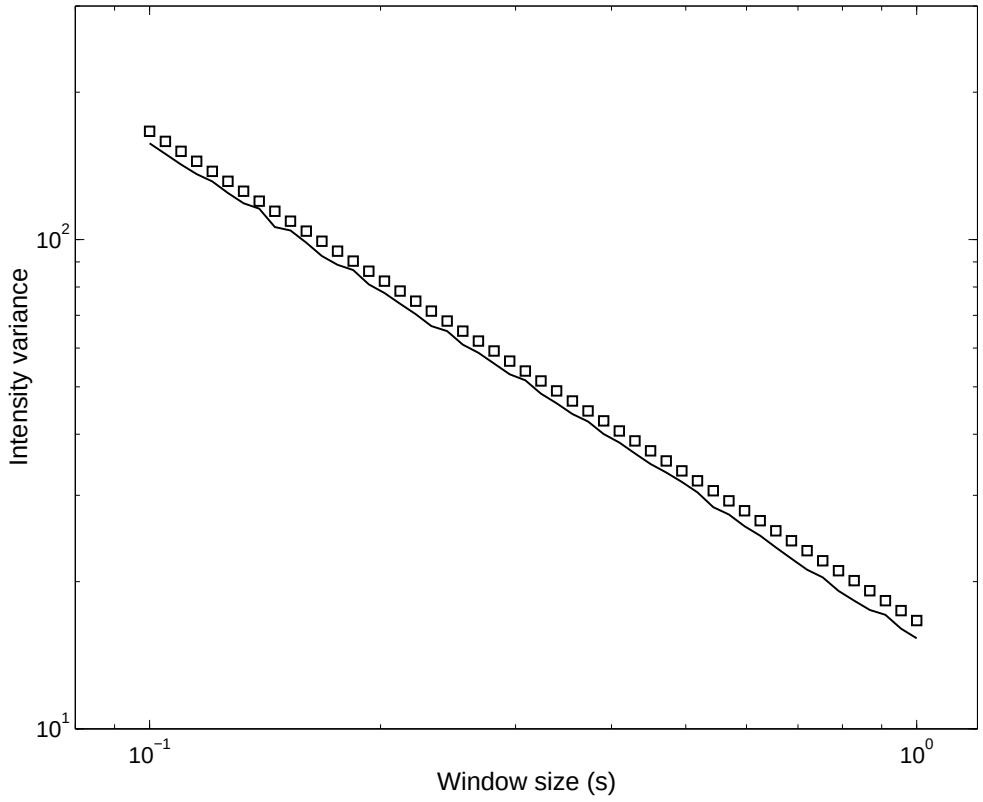

Figure 4.17: Snapping intensity variance as a function of window size shown on log-log scales. Also shown is a scaled mean approximation (square markers) for a homogeneous Poisson process. The variance curve is slightly lower than the scaled mean approximation because of dead-time.

non-homogeneous processes would need to show either different shape or different variability than the homogeneous Poisson bench mark. The rate versus window size curves can be normalised by dividing each variance curve by the mean rate. This normalisation of variance by the mean rate can be described as comparing the variance versus counting time curve with that for a homogeneous Poisson process, and is the basis for the Fano-factor analysis presented in the following section.

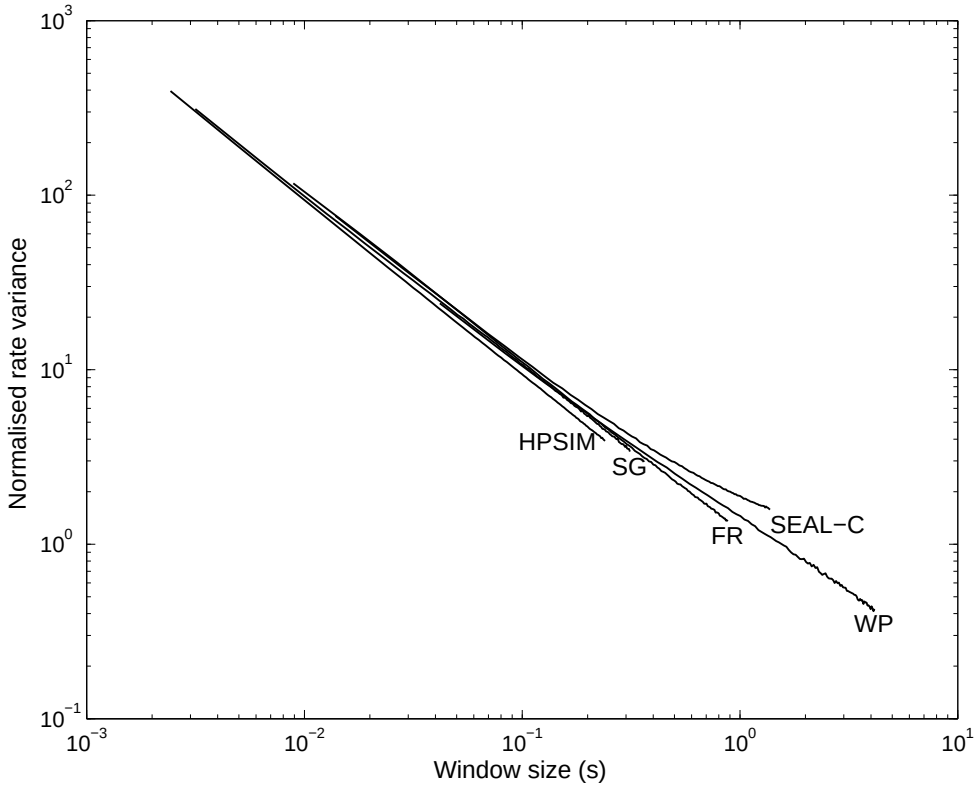

Figure 4.18: Normalised intensity variance as a function of window size for real shrimp noise at selected locations, and a homogeneous Poisson control.

4.7 Fano-factor analysis

The Fano-factor (or Index of Dispersion of Counts) is defined as the variance to mean ratio of the counting process, N (Teich et al. 1996, Fano 1947)

$$FF = \frac{\mathrm{var}(N)}{\langle N \rangle}. \tag{4.14}$$

The significance of this factor arises from its value for a homogeneous Poisson process. A homogeneous Poisson variate is uniquely characterised by having equal mean and variance (Evans et al. 1993), so that the Fano-factor of a homogeneous Poisson process is always unity

$$FF_{hpp} = \frac{\mathrm{var}(N)}{\mathrm{E}[N]} = 1. \tag{4.15}$$

Deviations of the Fano-factor from unity correspond with deviation from a homogeneous Poisson process. The Fano-factor therefore provides an alternative method investigating deviation from a homogeneous Poisson process. The importance of the Fano-factor alternative was demonstrated by Lowen & Teich (1992) who observed long term correlations in auditory-nerve spike trains using Fano-factor versus time curves, even though the inter-event intervals displayed exponential character consistent with a homogeneous Poisson process. However, similar comparison of Fano-factor and inter-snap interval results using snapping shrimp noise showed consistency between the two techniques (Legg et al. 2007).

In general the Fano-factor varies as a function of counting time so the counting process becomes $N(\varpi)$, where ϖ is the counting time. The mean and variance of the counts for different counting times then give the counting time dependent Fano-factor as

$$FF(\varpi) = \frac{\mathrm{var}(N(\varpi))}{\langle N(\varpi) \rangle}. \tag{4.16}$$

The counting time dependent Fano-factor of a homogeneous Poisson process remains unity for all counting times. An equivalent definition for the Fano-factor is the ratio of the variance-time function to its value for a homogeneous Poisson process (Cox & Lewis 1966)

$$FF(\varpi) = \frac{V(\varpi)}{\lambda \varpi} \tag{4.17}$$

where $V(\varpi)$ is the variance of the counting process as a function of counting time. The variance-time curve definition of the Fano-factor allows theoretical expressions to be derived for alternatives to the homogeneous Poisson process.

Empirical Fano-factor estimates can be computed using a windowing scheme, considering equally spaced instants equal to the counting time (ϖ) (Gusella 1991). To compute an estimate of the Fano-factor (for one counting time) all of the available event time-series data is partitioned into equally sized windows. For reasons of independence the windows must be consecutive and must not overlap. The number of events in each window form the values c_k and these values are used to compute the Fano-factor for that particular counting time. The computation is the ratio of the variance of c_k values divided by the mean c_k, thus

$$FF(\varpi) = \frac{\mathrm{var}(\{c_1, c_2, \ldots, c_n\}_\varpi)}{\mathrm{E}[\{c_1, c_2, \ldots, c_n\}_\varpi]} \tag{4.18}$$

where there are a unique set of $c_k = \{c_1, c_2, \ldots, c_n\}$ values for each counting time, indicated using the subscript ϖ at the end of the set. It is important to note that for each Fano-factor estimate the entire event time-series is partitioned into counting-time length windows. To compute the Fano-factor using another counting time, the entire event time-series must be repartitioned into windows that are the size of the new counting time. Figure 4.19 shows the method used to compute Fano-factors at different counting times. This windowing method is not the same as the moving average histogram method used to estimate the intensity function. The moving average histogram method used a sliding window where the start of each new window was incremented by some small value (that was less than a window size), whereas the Fano-factor method required that the start of each window be placed exactly at the end of the previous window.

Dead time detection methods affect the Fano-factor result. Including a dead-time introduces some regularity into the event series, reducing the variance of counts. For a homogeneous Poisson process the effect of dead-time reduces the Fano-factor to a value less than unity. A theoretical expression for a dead-time modified homogeneous Poisson process is obtained from the probability density function for a dead-time modified

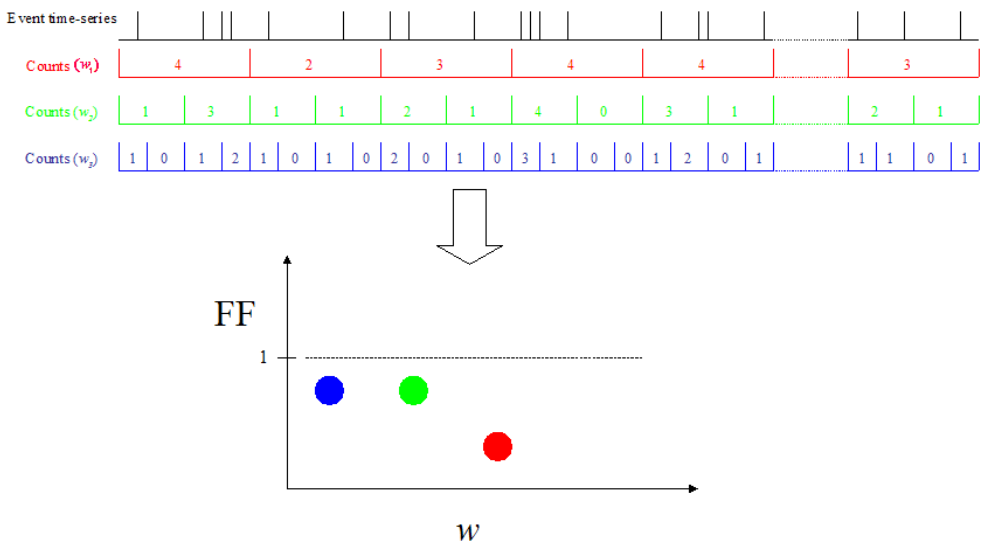

Figure 4.19: Fano-factors are computed by partitioning the event time-series into consecutive non-overlapping windows. The Fano-factor is the ratio of variance and mean of the counts in these windows. For each counting time the event times-series is repartitioned using the corresponding window size.

(homogeneous) Poisson distribution (Cantor & Teich 1975)

$$\begin{aligned} p(\varpi) = &\sum_{k=0}^{N} \frac{\lambda^k(\varpi - N\tau)^k}{k!} \exp\left(-\lambda(\varpi - N\tau)\right) \\ &- \sum_{k=0}^{N-1} \frac{\lambda^k(\varpi - (N-1)\tau)^k}{k!} \exp\left(-\lambda(\varpi - (N-1)\tau)\right) \end{aligned} \tag{4.19}$$

where λ is the rate, ϖ is the counting time, and τ is the dead-time. Expressions for the mean and variance of the dead-time modified homogeneous Poisson distribution are respectively

$$\mu = \frac{\lambda\varpi}{(1+\lambda\tau)} + \frac{\lambda^2\tau^2}{2(1+\lambda\tau)^2} \tag{4.20}$$

and

$$\sigma^2 = \frac{\lambda\varpi}{(1+\lambda\tau)^3}. \tag{4.21}$$

The Fano-factor for a dead-time modified (homogeneous) Poisson process is therefore

$$FF_{\mathrm{DTMP}} = \frac{2\lambda\varpi}{(1+\lambda\tau)[2(\lambda\varpi)(1+\lambda\tau) + \lambda^2\tau^2]} \tag{4.22}$$

which differs from the simple result of Equation 4.15 and importantly is now a function of counting time ϖ as well as the dead-time, τ.

Another effect that alters the value of the Fano-factor at very short counting times is caused by regularity. Middleton et al. (2003) showed that at very short counting times the discrete nature of the point process becomes significant; at very short counting times the intensity appears quite regular. When counting times are short enough that the intensity is approximately constant, then the process tends to behave like a homogeneous Poisson process. For a counting time of length ϖ, the number of events that are expected to occur within the counting time are

$$k = \lambda\varpi \tag{4.23}$$

where λ is the intensity (the instantaneous rate of occurrence of events), and is assumed to be approximately constant over the time ϖ . If k is restricted to be an integer, then there will normally be some small difference (ϵ) between k/λ and ϖ such that

$$\epsilon = \varpi - \frac{k}{\lambda}. \tag{4.24}$$

If the probability of getting k or $k+1$ events in ϖ is

$$p(i) = \begin{cases} 1 - \epsilon\lambda, & i = k \\ \epsilon\lambda, & i = k+1 \\ 0, & \text{otherwise} \end{cases} \tag{4.25}$$

then the mean and variance will be respectively

$$\mu = \varpi\lambda \tag{4.26}$$

and

$$\sigma^2 = \epsilon\lambda\left(1 - \epsilon\lambda\right). \tag{4.27}$$

As the event statistics tend to Equation 4.25, the Fano-factor tends to

$$FF_{short}(\varpi) = \frac{\epsilon}{\varpi}\left(1 - \epsilon\lambda\right). \tag{4.28}$$

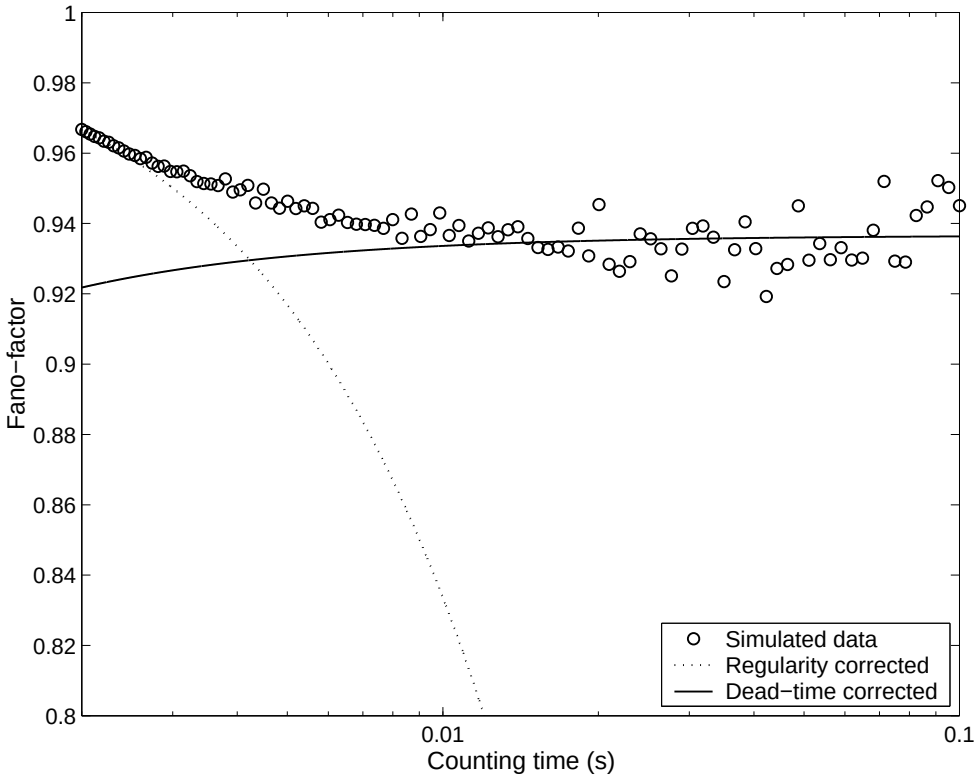

Figure 4.20: Fano-factor versus counting time for simulated dead-time modified homogeneous Poisson events (circles). Theoretical curves for dead-time correction (solid line) and the regularity correction (dotted line) are shown.

Figure 4.20 contains a plot of Fano-factor versus counting time for simulated dead-time modified homogeneous Poisson events (circle markers). Theoretical Fano-factor curves are plotted for a dead-time corrected homogeneous Poisson process (solid line) and the regularity correction (dotted line). For counting times less than 3×10^{-3} s the simulated results agree with the regularity correction curve, and for counting times greater than 1×10^{-2} s the simulation results agree with the dead-time corrected curve. For counting times between 3×10^{-3} s and 1×10^{-2} s the simulated results deviate above both theoretical curves, instead making a smooth transition from the regularity correction curve to the dead-time corrected curve.

Methods of combining the short and long time Fano-factor expressions, to give a theoretical expression valid for all counting times, seem to work well only for specific

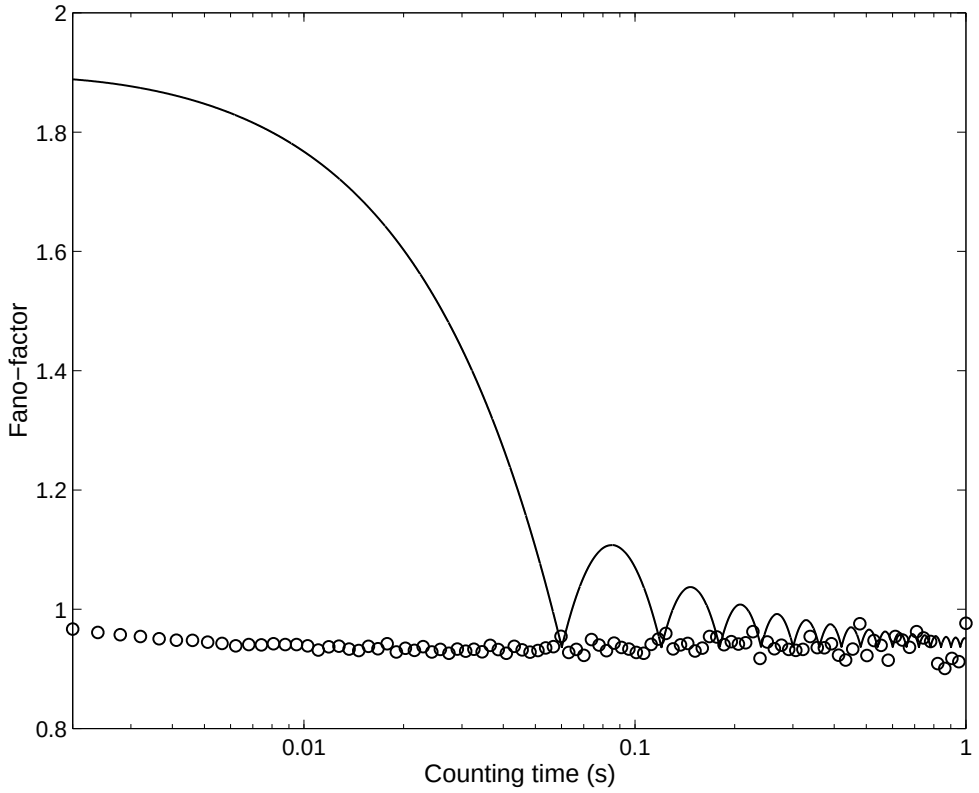

Figure 4.21: Fano-factor versus counting time for simulated dead-time modified homogeneous Poisson events (circles). Additive combination of the dead-time and regularity corrected theoretical curve (solid line) shows that the method used by Middleton for modelling a doubly-stochastic process cannot be applied to the dead-time corrected Poisson process.

applications. Middleton's method of adding the short-time and long-time approximations together, gives good agreement with their proposed model (a doubly-stochastic model). When using this same addition approach for dead-time modified Poisson events the result did not give good agreement, as shown in Figure 4.21, except toward higher counting times. Due to these inconsistencies the regularity correction was not applied directly to empirical results, instead the regularity curve from Equation 4.28 was plotted against any empirical results that may be affected by regularity.

Statistical fluctuations exist in Fano-factor estimates that increase (become more variable) with increasing counting time. The increase in variability is a direct consequence

of truncation of the event time-series, and is present for all empirical results, including the homogeneous Poisson result. Significance levels cannot be computed for the Fano-factor because its distribution is not known exactly (Cox & Lewis 1966). Instead, guide levels are computed by shuffling (randomly permuting) the order of intervals (Lowen & Teich 1992). The shuffling technique destroys any correlation arising from the event order, but at the same time preserves the distribution of inter-snap intervals. By conducting a number of shuffles of the data and recomputing the Fano-factors the mean and standard deviation of the shuffled data can be used as a guide for normal fluctuation. Figure 4.22 shows Fano-factor versus counting time for simulated homogeneous Poisson data including dead-time (circle markers) and guide levels (solid lines) set at ± 2 standard deviations beyond the shuffled mean. Guide levels were produced using 100 shuffles of the data. In this ideal case 198 of the 201 Fano-factor values (98.5%) are contained by the guide levels. Guide levels can also vary with the data, rather than following a predefined expected result. Shuffling the data removes any significance in the order of the intervals but does not change the distribution of intervals. If Fano-factor variations exist due to the distribution of intervals then the shuffling will not change the result, and the guides will follow the variations (Lowen & Teich 1996). Deviations above the upper guide level indicate clustering of the events, referred to as super-Poisson; conversely deviations below the lower guide level indicate anti-clustering (or increased orderliness) and are referred to as sub-Poisson. Deviations of both the empirical Fano-factors and the guide levels indicate changes in the inter-event intervals, rather than in the ordering of the events.

Empirical Fano-factor curves were computed as a function of counting time using Equation 4.18. The minimum counting time was set equal to the dead-time, which was 0.001 s in all cases. The maximum counting time was set at 1/10 the duration of the time-series to ensure that the computation of variance and mean had at least 10 sample points. Counting times were logarithmically spaced between the minimum and maximum values using a log base of 1.05. To distinguish different counting time regions the term *short time* was assigned to times less than a second, the term *medium time* assigned to times between 1 and 60 seconds, and *long time* for times greater than 60

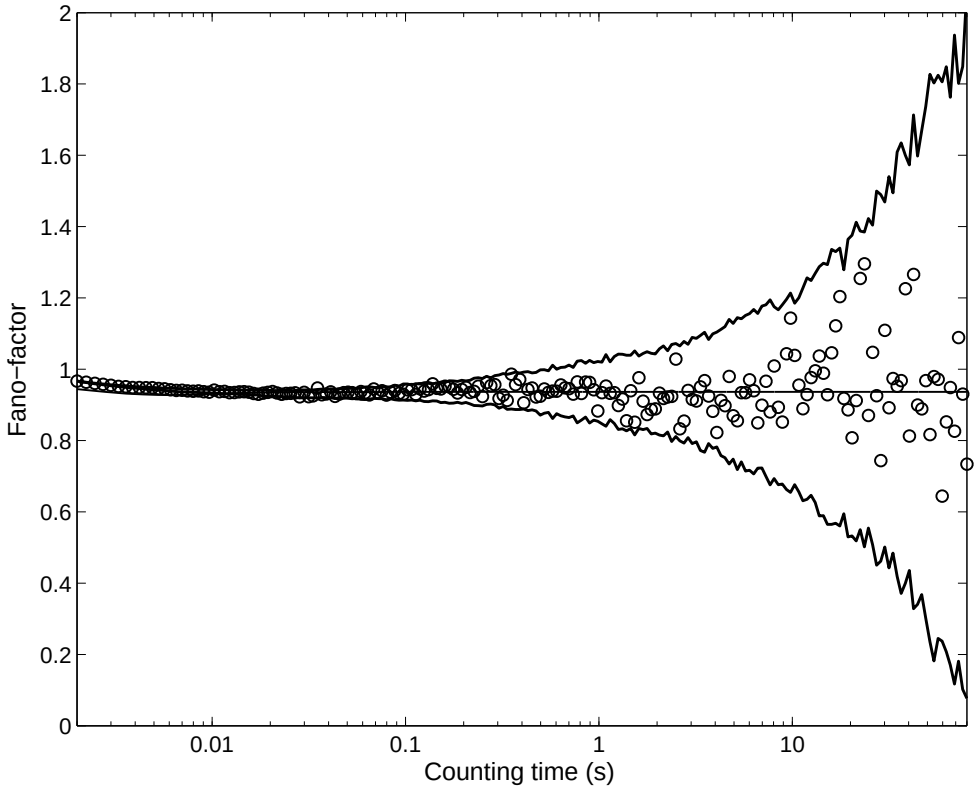

Figure 4.22: Fano-factor versus counting time for simulated homogeneous Poisson events (circles), with positive and negative guide levels (solid lines).

seconds.

Figures 4.23 through 4.28 show Fano-factor versus counting time for selected shrimp noise data. The selection contains data from Spencer Gulf (SG), Cockburn Sound (CS-A), Nornalup-Walpole Estuary (WP), the Seal Island Cave (SEAL-A), and Feather Reef (FR), and includes the results for simulated dead-time modified homogeneous Poisson (HPSIM) as a control. In each figure cross markers were used for empirical Fano-factor results from the real or simulated data, dashed lines show the guide levels set at 2 standard deviations beyond the mean, the mean of the shuffled data is shown using small circles, and a solid line shows both the short and long time theoretical curves for a dead-time modified Poisson process. The relatively large Fano-factor values in Figure 4.25 suggest that the snap events were significantly more clustered at the time of measurement than what is normal.

A null hypothesis that snapping shrimp noise follows a homogeneous Poisson process was pseudo-tested using Fano-factor analysis. The pseudo-test was conducted using guide levels set at 2 standard deviations beyond the mean, with allowances for deviations at short counting times consistent with (our) current understanding of the regularity effects and constraints regarding the joining of Fano-factor results between short and long time approximations. Testing used the percentage of Fano-factor points lying within the guide levels, with guidance set at 95%. If 95% of the Fano-factor points were contained by the guide levels then the process was accepted as a homogeneous Poisson process. Important caveats to the test were, that the dead-time be smaller than the smallest counting time and that the largest counting time be at least 10 seconds. Testing was conducted on all of the available shrimp data sets and on the homogeneous Poisson control. Test results are shown in Figure 4.29 plotting the base 10 logarithm of the percentage of uncontained Fano-factor points for each location. Uncontained values were used in the plot so that rejection of the hypothesis coincided with the higher values (red bars), and conversely acceptance of the hypothesis for lower values (blue bars). A line of guidance corresponding to 95% containment was also shown. According to this test the dead-time modified homogeneous Poisson hypothesis is rejected for the Cockburn Sound, Nornalup-Walpole, Seal Island and Feather Reef data. The test is conditionally accepted for the Spencer Gulf data, and is accepted for the simulated control data. Test results gave the same conclusion as the test for a dead-time modified homogeneous Poisson process using the first order distribution of intervals (the inter-snap interval histogram analysis).

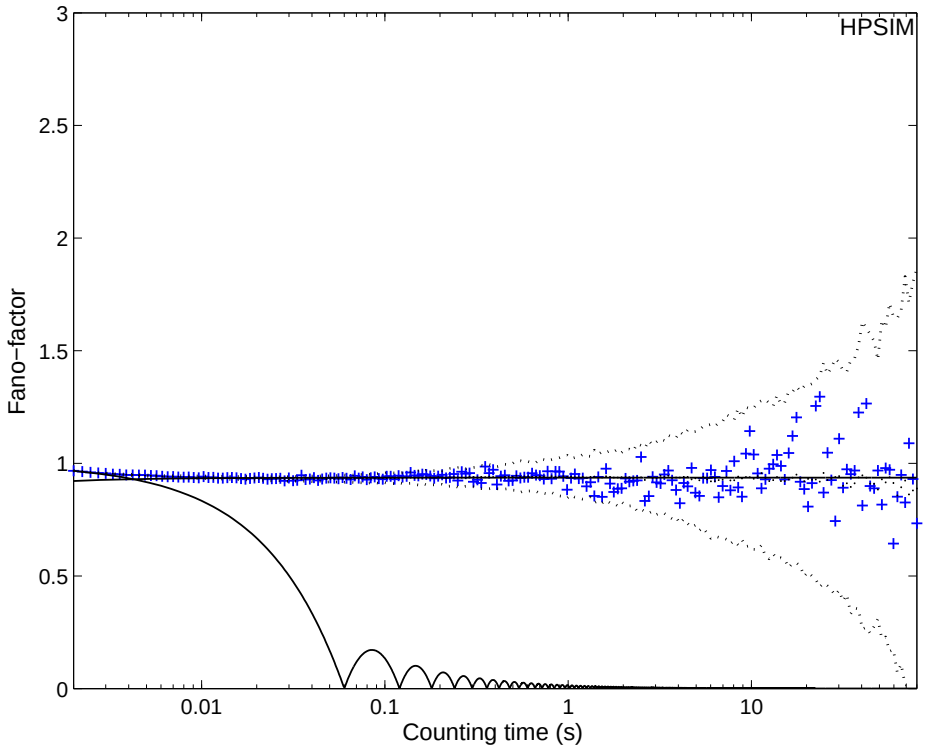

Figure 4.23: Fano-factor versus counting time for homogeneous Poisson control data.

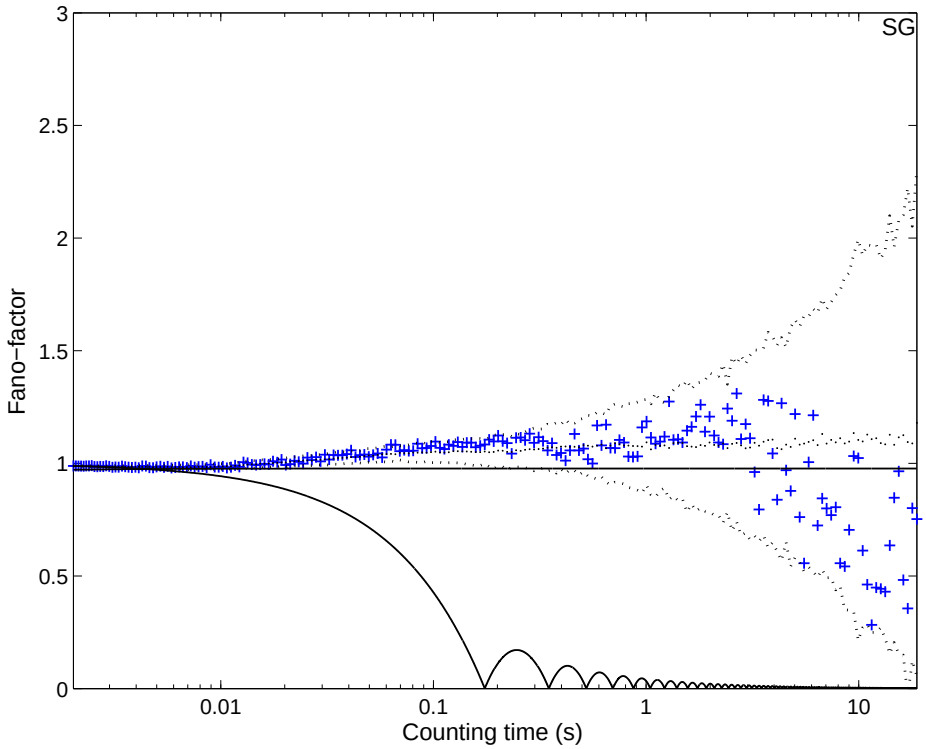

Figure 4.24: Fano-factor versus counting time for Spencer Gulf data.

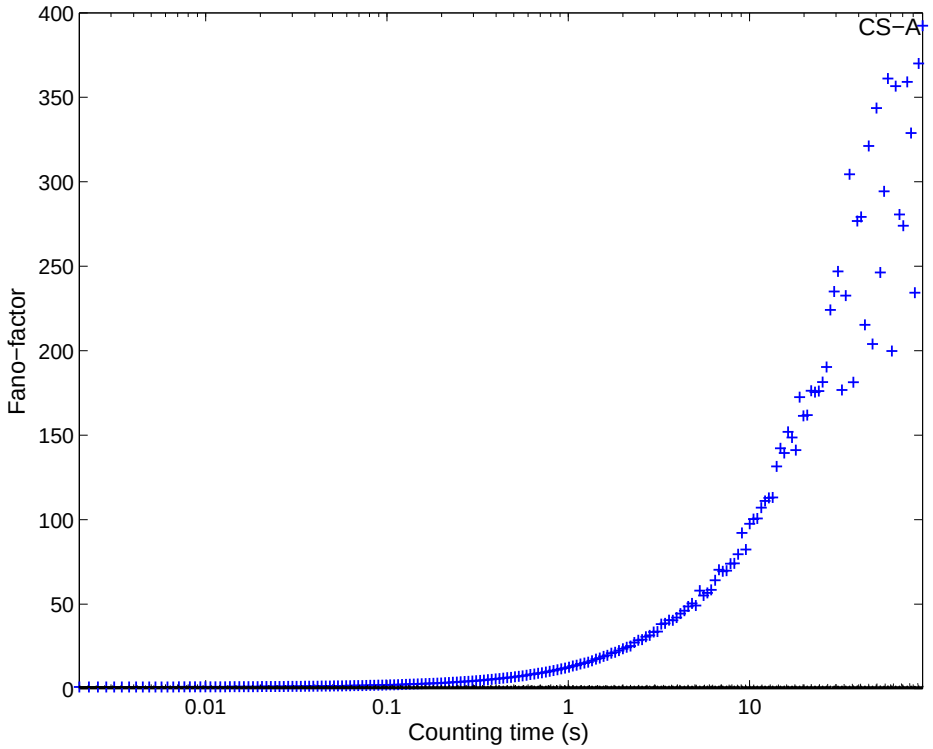

Figure 4.25: Fano-factor versus counting time for Cockburn Sound data.

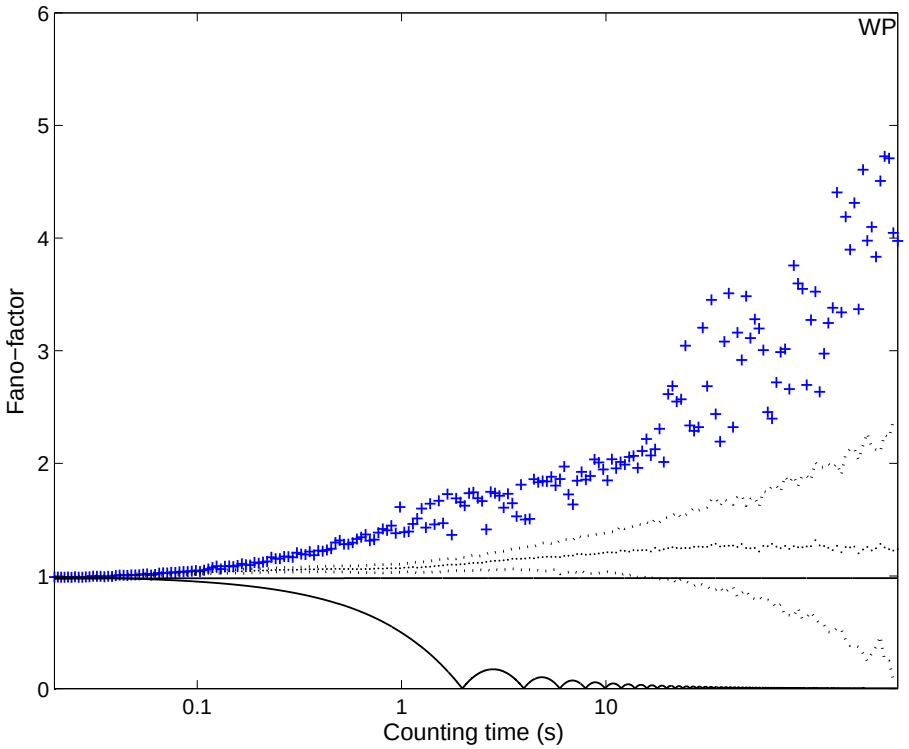

Figure 4.26: Fano-factor versus counting time for Nornalup-Walpole Estuary data.

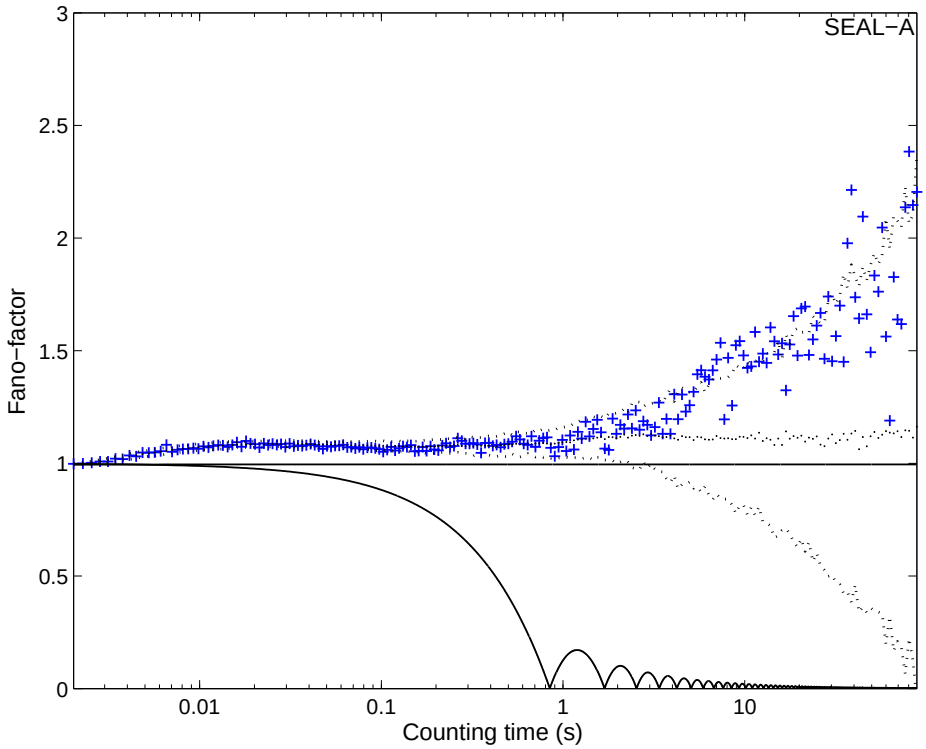

Figure 4.27: Fano-factor versus counting time for Seal Island cave data.

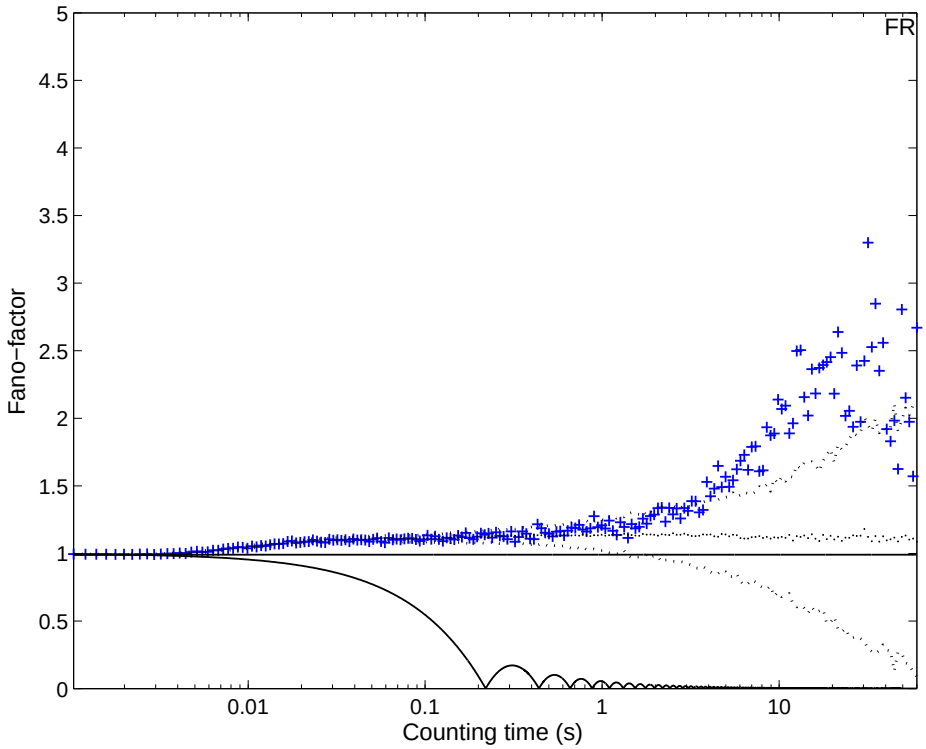

Figure 4.28: Fano-factor versus counting time for Feather Reef data.

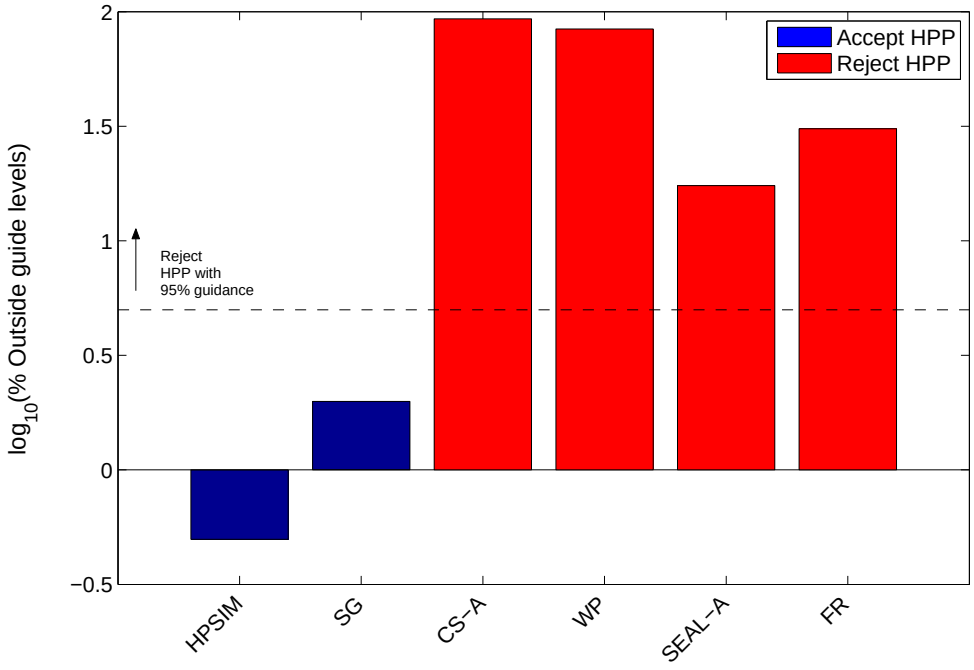

Figure 4.29: Percentage of Fano-factor values outside the guide levels.

Three distinct features in the Fano-factor versus time curves for shrimp noise are shown in Figure 4.30 and Figure 4.31. These two plots are for the same data set, which is a 24 hour recording made at the AWharf site specifically to investigate long counting time effects (see Appendix A). A short-time rise and plateau for counting times less than a second is shown in Figure 4.30. The short time effects are evident in both the original and shuffled results. A medium-time rise and plateau for counting times between one and two hundred seconds is shown in Figure 4.31, followed by a long-time rise for counting times greater than two hundred seconds. The medium and long time effects are evident only in the original shrimp noise data; the shuffled data tends to agree with a dead-time modified homogeneous Poisson curve at these longer counting times. The following sections investigate these features.

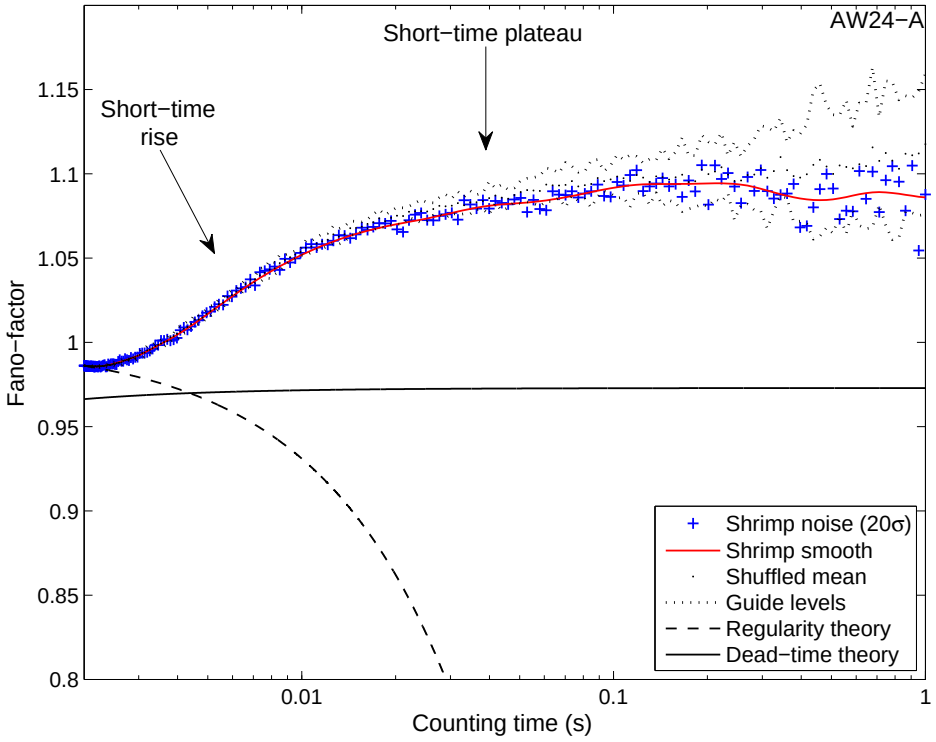

Figure 4.30: Fano-factor versus counting time for short counting times (less than one second).

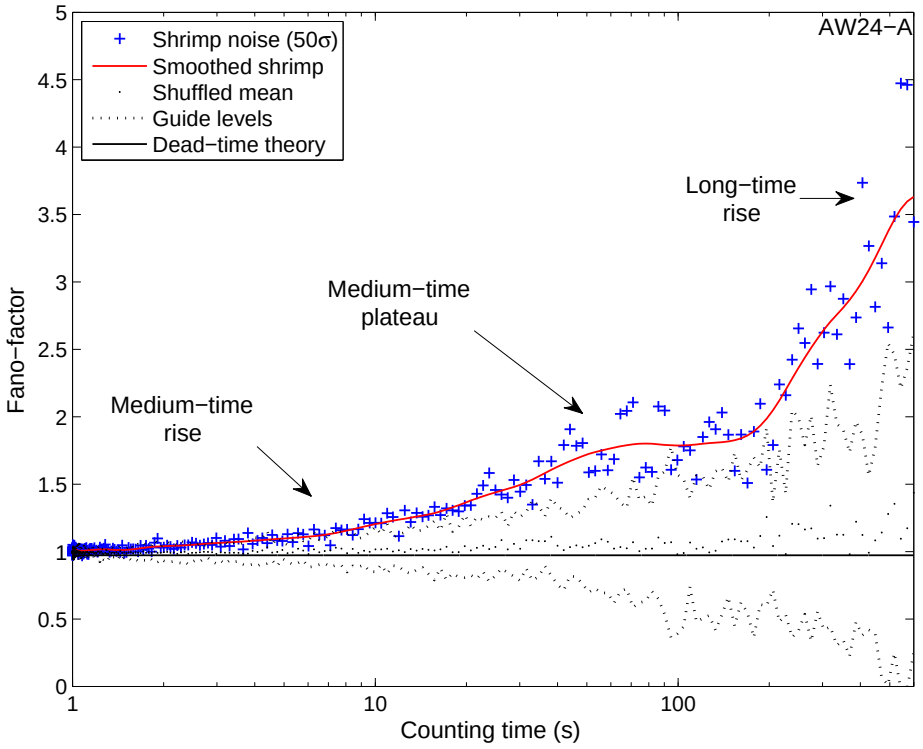

Figure 4.31: Fano-factor versus counting time for medium (1 to 200 seconds) and long (greater than 200 seconds) counting times.

4.8 The cause of short time effects

One of the Fano-factor features observed in real shrimp noise was a rise and plateau for short counting times (less than a second). Figure 4.32 shows this feature in empirical Fano-factor results computed from the Cockburn Sound (CS-B) data and has similar characteristics to Figure 4.30. Cross markers show the Fano-factor of the shrimp noise when detected using an automatic (threshold) detector. Also shown are the shuffled mean (black dotted line) and the shuffled mean of homogeneous Poisson control data (red solid line). The first observation made about the result was that the rise and plateau deviations were not explained by regularity or dead-time, since these tend to reduce (rather than increase) the value of the Fano-factor. The second observation was that the shuffled data followed the rise and plateau, indicating that the effect was caused by an unexpected number of intervals at these counting times, rather than unexpected ordering of the events.

To investigate further, the automatically detected events were inspected visually. Visual inspection revealed that some surface reflected replicas of the shrimp snaps were being detected as events and included in the analysis. The surface reflected replicas were removed manually and a new Fano-factor curve computed as shown in Figure 4.33. The shuffled mean from the original automatically detected Fano-factor result was also shown so that the change made by removing the surface reflection replicas was clear. The result was duplicated using simulated data; when surface reflection events were included in the analysis the short time rise and plateau appeared in the Fano-factor results (the simulation results are not shown because they provide no additional information). It was concluded that the short time rise and plateau were caused by surface reflected snap replicas being included as events in the process.

The short time rise and plateau also has the effect of translating the medium time results up the Fano-factor axis. The medium time effect is not masked by the short time effect and the shape of the medium time effect is unaltered. If the short time effect is small (i.e. a small number of surface reflection detections remain after automatic detection)

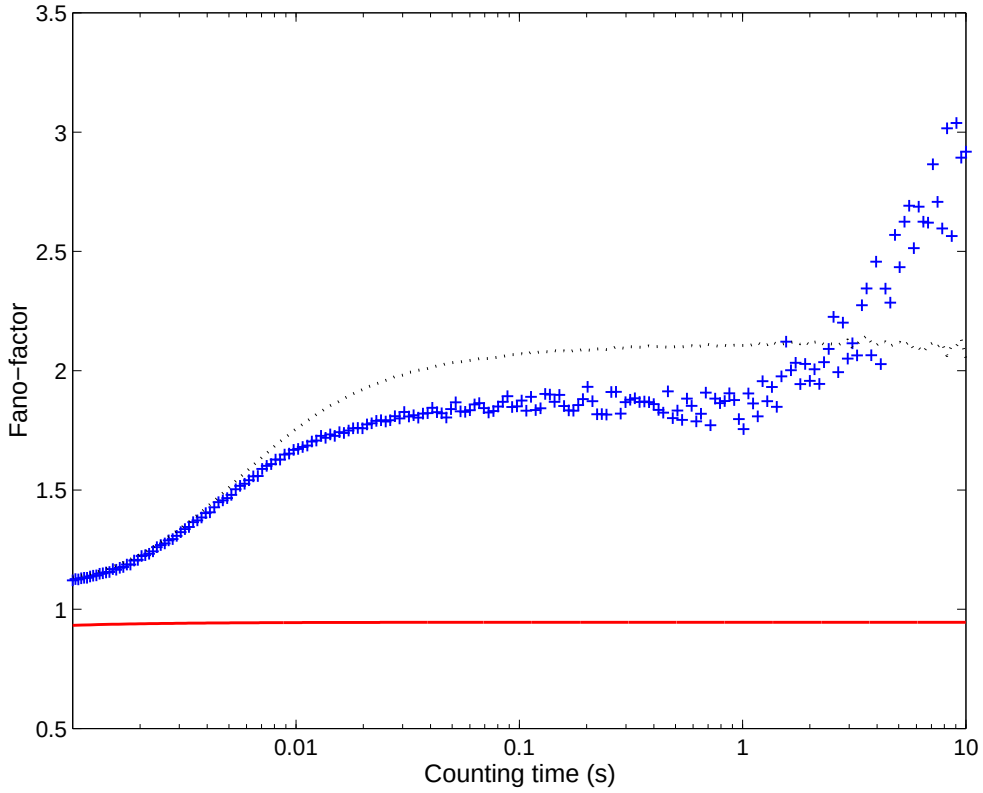

Figure 4.32: Fano-factor as a function of counting time for Cockburn Sound (CS-B) data (blue cross markers) including the mean of shuffled data for the same Cockburn Sound data (black dotted line), and the shuffled mean of homogeneous Poisson control data (red solid line).

then the effect on the medium time results should be negligible.

4.9 Modelling medium and long time effects

Fano-factor analysis showed a rise and possible plateau for medium and long counting times. These features are characteristic of doubly-stochastic Poisson processes driven by Brownian type intensity processes (Middleton et al. 2003). In the following sections these models are applied to shrimp noise and some fundamental properties, such as correlation times, are inferred from the model fits.

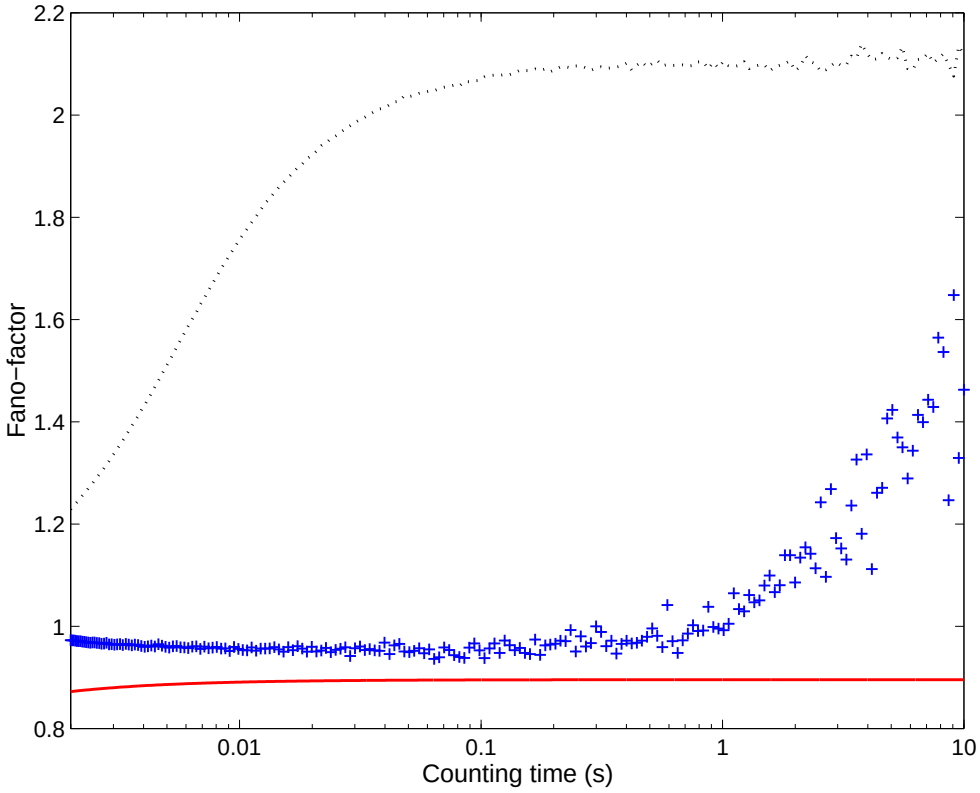

Figure 4.33: Fano-factor as a function of counting time for Cockburn Sound (CS-B) data, with surface reflection events removed manually (blue cross markers). Short time effects with the reflections removed are greatly reduced compared with the shuffled mean of the original data (black dotted line), but do not reduce entirely to a homogeneous Poisson process (red solid line).

4.9.1 Doubly-stochastic Poisson models

Doubly-stochastic processes have proved useful models of real world processes in the fields of optics (Teich & Cantor 1978), particle physics (Fano 1947), neuro-physics (Middleton et al. 2003, Teich et al. 1996), computer science (Gusella 1991, Slimane & Le-Ngoc 1995) and finance (Lepage et al. 2006). A doubly-stochastic Poisson process can be described as a Poisson process whose intensity is modulated by a second stochastic process (Manton et al. 1999). The following strict definition of a doubly-stochastic Poisson process from Snyder & Miller (1991) (page 341) is quoted here to

put the preceding description into proper context

> *$N(t) : t \geq t_o$ is a doubly stochastic Poisson-process with intensity process $\lambda(t, \mathbf{x}(t)) : t \geq t_o$ if for almost every path of the process $\mathbf{x}(t) : t \geq t_o$, $N(\cdot)$ is a Poisson process with intensity function $\lambda(t, \mathbf{x}(t)) : t \geq t_o$. In other words, $N(t) : t \geq t_o$ is conditionally a Poisson process with intensity function $\lambda(t, \mathbf{x}(t)) : t \geq t_o$ given $\mathbf{x}(t) : t \geq t_o$.*

Doubly-stochastic Poisson processes allow the intensity $\lambda(t)$ to vary as a realisation of a stationary, time varying stochastic process $\{\Lambda(t)\}$ (Cox & Lewis 1966). An important characteristic of a doubly-stochastic Poisson process is that the intensity process is influenced by factors external to the point process. Processes with intensity influenced by internal factors are referred to as self-exciting processes, and are not considered here (for further reference see (Snyder & Miller 1991)). The variance (V) of a doubly-stochastic Poisson process varies with counting time (ϖ) according to

$$V(\varpi) = \overline{\lambda}\varpi + 2\overline{\sigma}^2 \int_0^{\varpi} (\varpi - u)\rho(u)\,\mathrm{d}u \tag{4.29}$$

where $\overline{\lambda}$, $\overline{\sigma}^2$ and $\rho(u)$ are respectively the mean, variance and autocorrelation function of the stochastic intensity process $\{\Lambda(t)\}$. The Fano-factor for a doubly-stochastic Poisson process can then be defined in terms of the variance-time function

$$FF_{dspp}(\varpi) = \frac{V(\varpi)}{\overline{\lambda}\varpi} = 1 + \frac{2\overline{\sigma}^2}{\overline{\lambda}\varpi} \int_0^{\varpi} (\varpi - u)\rho(u)\,\mathrm{d}u. \tag{4.30}$$

Setting $\overline{\sigma}$ to zero in Equation 4.29 reduces the expression to that of a homogeneous Poisson process, which in turn reduces the Fano-factor to unity. Some common diffusion intensity models are the Ornstein-Uhlenbeck (OU), Cox-Ingersoll-Ross (CIR) and Lognormal models. Of these models the OU and CIR are the simplest ergodic diffusions with closed form density function expressions, and for this reason they are chosen for further investigation.

4.9.2 The Ornstein-Uhlenbeck model

The Ornstein-Uhlenbeck (OU) doubly-stochastic Poisson process is defined by the stochastic differential equation

$$\mathrm{d}X_t = -a(X_t - \mu)\,\mathrm{d}t + \sigma\,\mathrm{d}W_t \tag{4.31}$$

where X_t is the (time dependent) stochastic variable; a, μ and σ are parameters, and $\mathrm{d}W_t$ is the differential Weiner process (Higham 2001). Notation follows a slight modification of that used by Picchini (2007), but the explanations and solutions draw mainly from Gillespie (1996) and Lepage et al. (2006). The solution to Equation 4.31 is a Gaussian with time dependent mean and variance (Lepage et al. 2006)

$$\mu(t) = \mu(1 - \exp(-at)) + x_o \exp(-at) \tag{4.32}$$

and

$$\sigma^2(t) = \frac{\sigma^2}{2a}(1 - \exp(-2at)). \tag{4.33}$$

Stationary solutions are obtained by evaluating the mean and variance in the limit of infinite time giving respectively

$$\mu_\infty = \mu \tag{4.34}$$

and

$$\mathrm{var}_\infty = \frac{\sigma^2}{2a}. \tag{4.35}$$

The autocovariance function of the process is

$$\mathrm{cov}(X_o, X_t) = \frac{\sigma^2}{2a}\exp(-at) \tag{4.36}$$

which is an exponential decay with correlation time a^{-1}, scaled by the stationary variance. Figure 4.34(a) shows a sample of OU noise time-series (black line) simulated using the Euler-Maruyama scheme (Higham 2001) with parameters $a = 0.1$, $\sigma = 0.6$, and $dt = 0.001$. Also shown is a series of zero mean Gaussian variates with variance equal to var_∞, to illustrate the difference between the time dependent and stationary (infinite time limit) distributions. In Figure 4.34(b) the spectral densities of the two time-series are shown along with a curve proportional to af^{-1}, where f is the frequency.

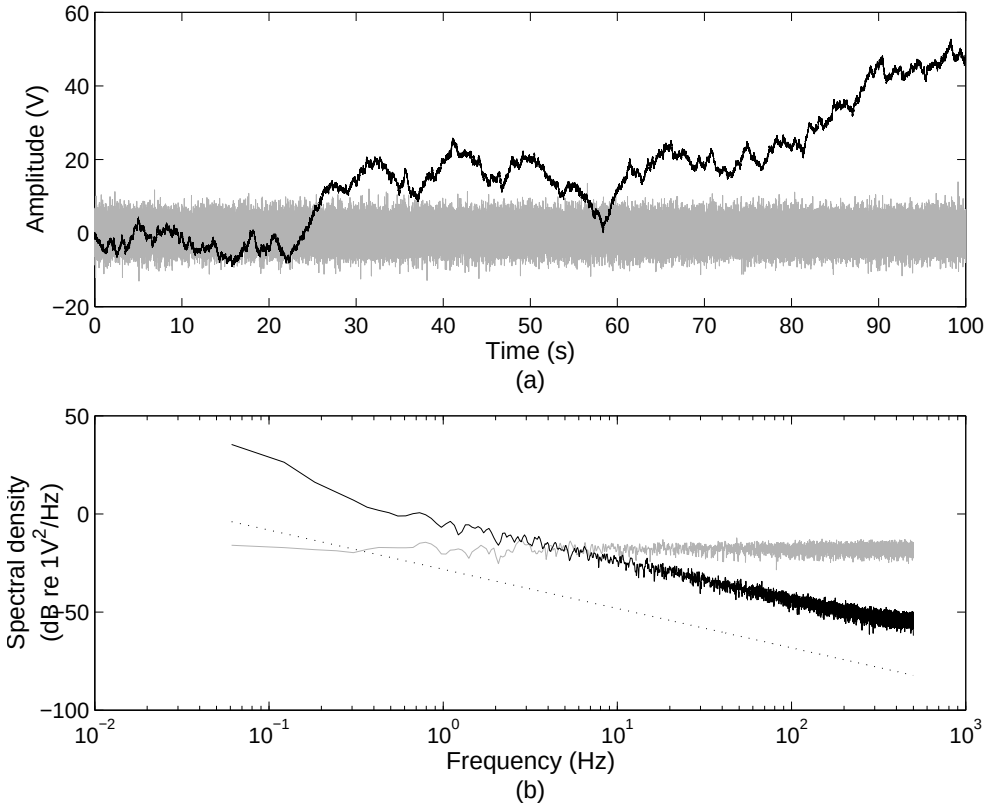

Figure 4.34: A sample of zero mean Ornstein-Uhlenbeck noise (black solid line) simulated using parameters $a = 0.1$, $\sigma = 0.6$, and $dt = 0.001$. Zero mean "white" Gaussian noise with variance equal to var_∞ is also shown to illustrate the stationary limit. In (b) the power spectral density of both types of noise are shown. The "white" Gaussian noise (grey line) has a flat spectrum whereas the Ornstein-Uhlenbeck noise (black solid line) has an af^{-1} relationship (black dashed line).

The af^{-1} curve describes a straight line due to logarithmic spacings used on both axes (intrinsic to the y-values because the spectral density is shown using decibels). The OU spectrum was plotted using a black line, and the stationary Gaussian spectrum using a grey line. The stationary Gaussian was white (i.e had constant spectral density with frequency), whereas the OU spectrum followed an af^{-1} relationship.

To use the OU process as an intensity model that drives a doubly-stochastic Poisson model of shrimp noise requires that the stable intensity of shrimp snapping be Gaussian

distributed. A Gaussian distribution was considered a reasonable first choice model because the factors affecting the snaps were most likely external, numerous and unknown. To investigate, empirical intensity distributions were compared with a Gaussian fit using visual inspection of probability density functions. Results for several real shrimp noise data sets are shown in Figure 4.35.

Empirical probability density functions of shrimp noise (circle markers) were estimated using a scaled histogram with 10 evenly spaced bins. Intensities were estimated using the moving average histogram method with a 3 second window and 0.3 second step sizes. Gaussian fits (solid lines) used the mean and variance of the estimated intensities. Simulated homogeneous Poisson (a) and shrimp noise from Sydney Harbour (h), and Cockburn Sound (j,k & l) all had average intensities greater than 10 snaps per second, and showed acceptable agreement with the Gaussian model. Results for real shrimp noise with average intensity lower than 10 snaps per second showed progressively worse fit of the Gaussian model as the average intensity tended toward zero. In particular the Seal Island (e) and Nornalup-Walpole Estuary (i) show poor agreement with the model. The underlying reason for this problem was that the Gaussian model allows negative intensity. Negative intensity does not have any physical meaning, and cannot be observed in real shrimp noise. When the average intensity of snapping is high, with respect to the variance, then the probability of negative values according to the Gaussian model is relatively low, so the model is reasonable. However, when the average intensity reduces toward zero the probability of negative values becomes unrealistically high and so the model is no longer appropriate. To avoid the possibility of modelling negative rates the Cox-Ingersoll-Ross process was investigated.

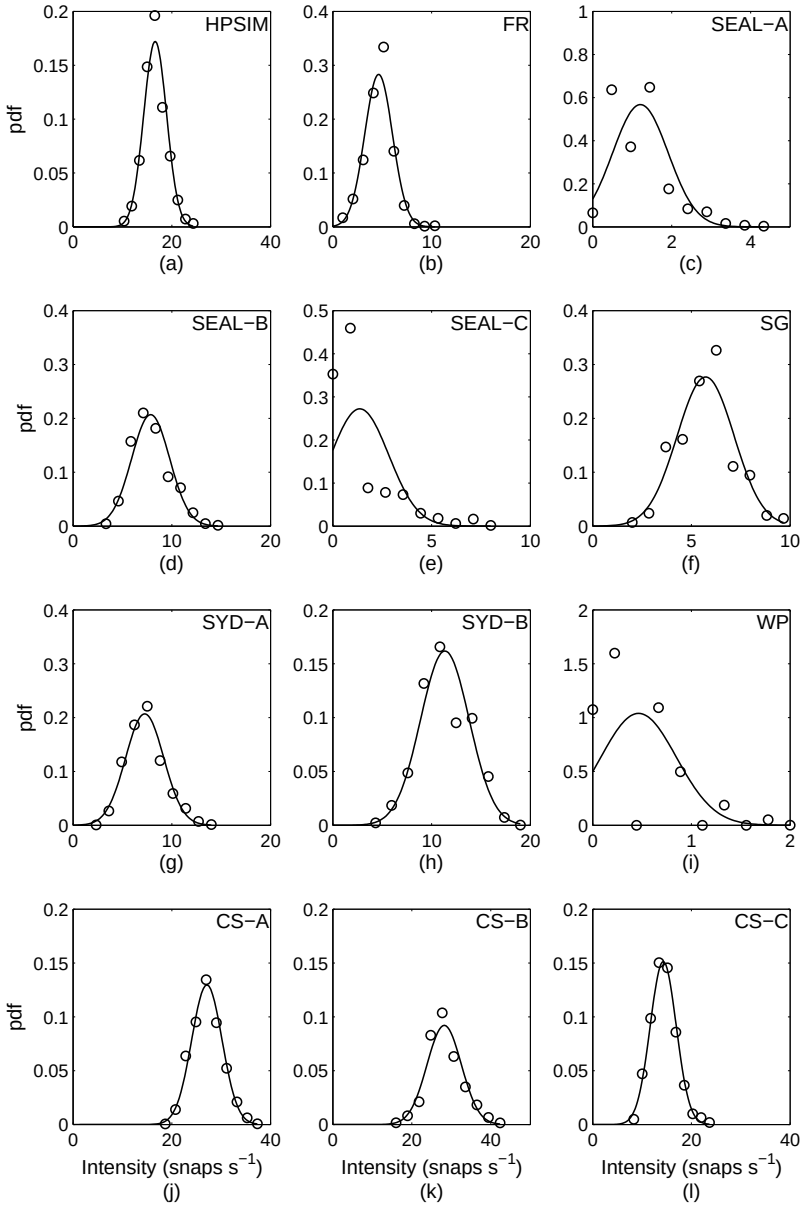

Figure 4.35: Probability density of intensity of real shrimp snaps (circle markers) compared with the Gaussian distribution (solid lines) assumed by the OU model. The model fit was acceptable when the average intensity was high. Low intensity results particularly Seal Island (e) and Nornalup-Walpole Estuary (i) show poor agreement with the model.

4.9.3 The Cox-Ingersoll-Ross model

The Cox-Ingersoll-Ross (CIR) model is a generalisation of the squared Ornstein-Uhlenbeck process (Lepage et al. 2006). The model is defined by the stochastic differential equation

$$\mathrm{d}X_t = a(b - X_t)\,\mathrm{d}t + \sigma\sqrt{X_t}\,\mathrm{d}W_t \tag{4.37}$$

which contains an additional (and important) $\sqrt{X_t}$ in the second term. Derivations here follow those given in Lepage et al. (2006), but for consistency notation follows (exactly) the generic Itô calculus forms given in Picchini (2007). The solution to Equation 4.37 is a non-central χ^2 distribution with degree-of-freedom and non-centrality parameters respectively

$$\varphi(t) = \frac{4ab}{\sigma^2} \tag{4.38}$$

and

$$\zeta(t) = \frac{4ax_o \exp(-at)}{\sigma^2(1 - \exp(-at))}. \tag{4.39}$$

For infinite counting times the expressions reduce to

$$\varphi_\infty = \frac{4ab}{\sigma^2} \tag{4.40}$$

and

$$\zeta_\infty = 0. \tag{4.41}$$

The covariance of the stationary process is

$$\rho(t) = \frac{b\sigma^2}{2a}\exp(-at). \tag{4.42}$$

When $\zeta = 0$ the non-central χ^2 distribution is equivalently a gamma distribution with parameters

$$B_{\text{scale}} = \frac{\sigma^2}{2a} \tag{4.43}$$

and

$$C_{\text{shape}} = \frac{2ab}{\sigma^2}. \tag{4.44}$$

Both the non-central χ^2 and gamma distributions are defined only for positive values; negative values do not occur. The CIR model is therefore a more physically realistic model of intensity.

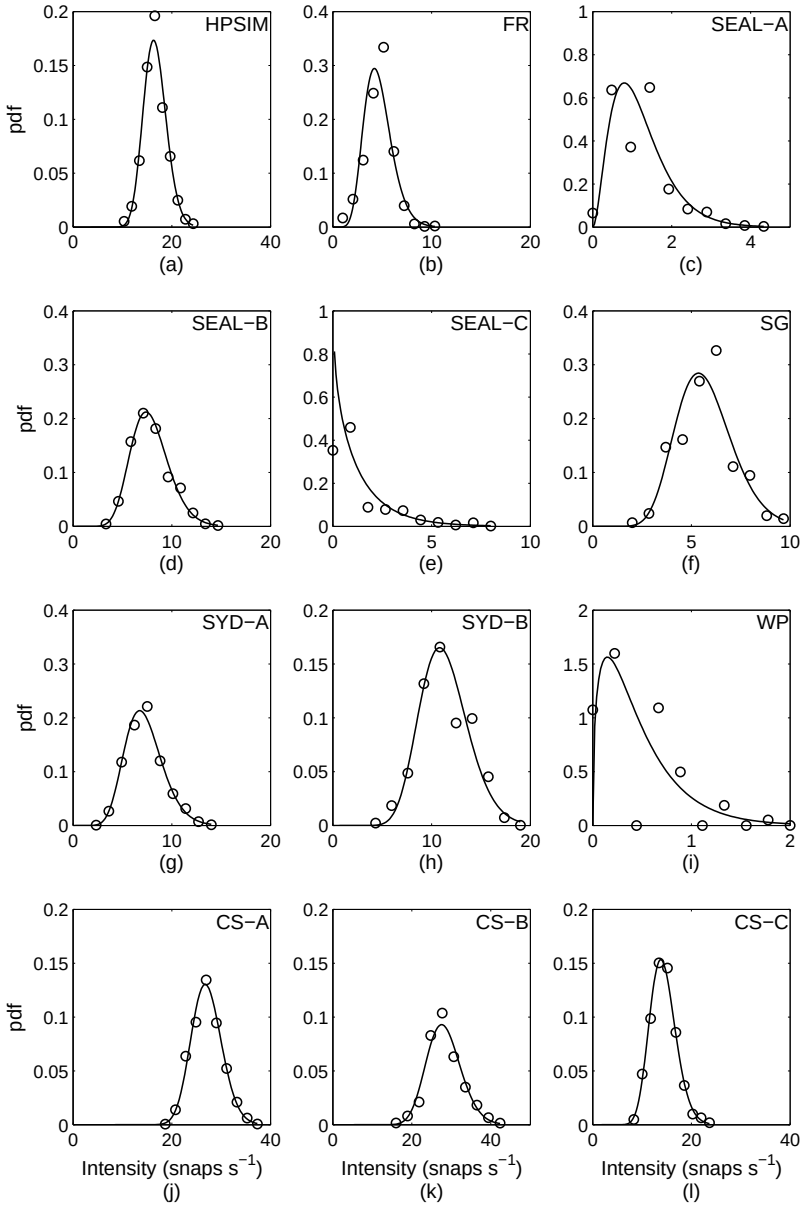

Figure 4.36: Probability density of intensity of real shrimp snaps (circle markers) compared with the gamma distribution fit (solid lines) assumed by the CIR model. Model fit was good for all locations except the Nornalup-Walpole Estuary (i).

Intensity distributions of real shrimp noise were compared with a gamma distribution. Empirical estimates of the intensity probability density function were computed using at least 3 minutes of data to ensure a reasonable estimate, because correlations in the real shrimp noise were expected to only exist for a few seconds. Parameters for the gamma fit were estimated using moment estimators from Evans et al. (1993). Figure 4.36 shows empirical probability density functions (circle markers) of the intensity functions for 12 different data sets, and a gamma fit (solid line). Homogeneous Poisson control data (a) showed good agreement between the empirical and theoretical results although there was a higher than expected number of average intensities. Real shrimp noise results from Feather Reef (b), Spencer Gulf (f), Sydney Harbour (g & h), and Cockburn Sound (j,k & l) showed good agreement with the gamma distribution. Results for one of the Seal Island (c), and the Nornalup-Walpole Estuary (i) data were not as good but may be explained as having outliers that were affecting the fit. The Seal Island (c) data may have an outlier near 1.5 snap s^{-1} and the Nornalup-Walpole Estuary result has three or four zero counts due to the very low snap rate. Perhaps the most important result was that the low snap rate Seal Island data (e) showed good agreement with the gamma fit.

The Fano-factor for a CIR driven doubly-stochastic Poisson process has the analytic expression (Lepage et al. 2006)

$$FF_{CIR}(t) = 1 + \frac{\sigma^2}{a^3 t}(\exp(-at) + at - 1) \tag{4.45}$$

where parameters a and σ are from Equation 4.37, and t is counting time. In the limit of infinite counting time the Fano-factor has an asymptote at

$$FF_{CIR}(\infty) = 1 + \frac{\sigma^2}{a^2}. \tag{4.46}$$

Taking the limit as $\sigma \to 0$ reduces the Fano-factor to unity; that of a homogeneous Poisson process.

Figure 4.37 shows the Fano-factor as a function of counting time for simulated CIR driven doubly-stochastic Poisson noise, and a theoretical curve. Parameter values used for the simulation were $a = 0.5$, $b = 5$, $\sigma = 0.5$. Each simulated time-series was

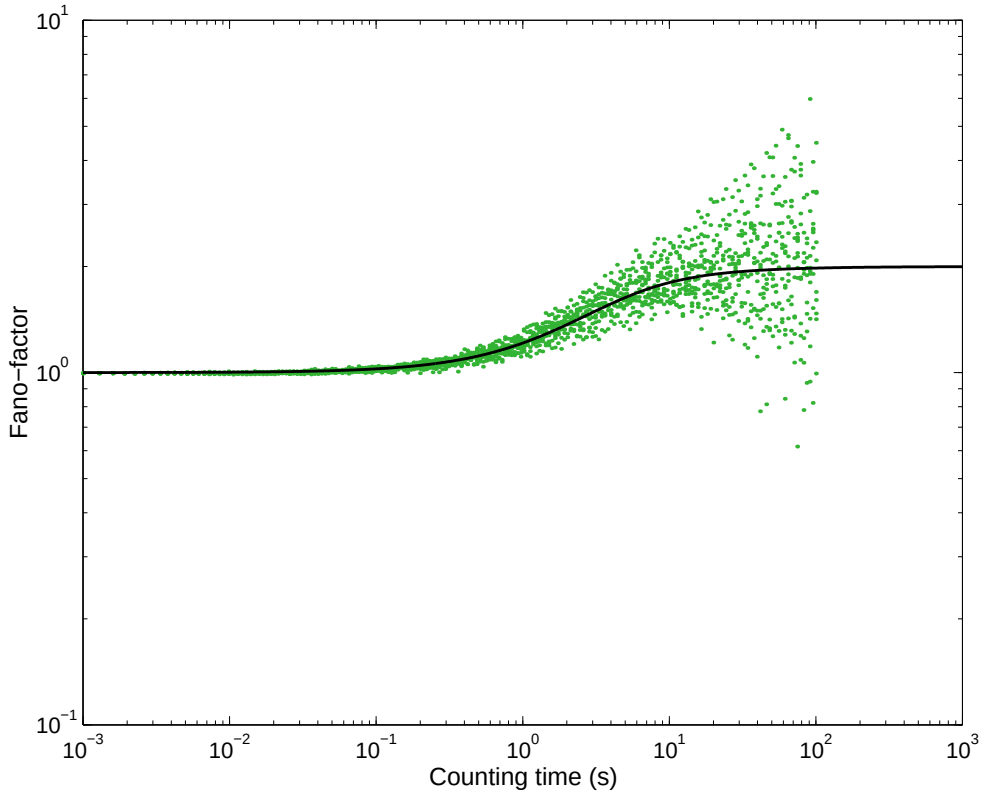

Figure 4.37: Fano-factor variability of simulated CIR doubly-stochastic Poisson data.

1000 s in duration with time increments of 0.001 s. Simulations were repeated 10 times to show the spread of simulated results about the theoretical curve. The spread of results was larger than anticipated, and illustrates the potential for error if used to infer parameters of the generating process from a single observation. Parameter estimates computed from each trial are shown in Table 4.1, and a summary of the parameter estimation statistics shown in Table 4.2. Mean estimates of b and a were respectively 4.94 and 1.42, which were within 1 standard deviation of their true values $b = 5$ and $a = 0.5$. The standard deviation of a estimates was 1.49, which was larger than the mean value of 1.42. Estimates of σ were poor with the mean value of 0.70 lying 10 standard deviations from the true value $\sigma = 0.5$. These results showed that the method used to estimate the parameters of a CIR driven doubly-stochastic Poisson process was problematic. Alternative methods were not found in the literature.

Table 4.1: Estimated parameters from 10 separate simulations of a CIR driven doubly-stochastic Poisson process.

Variable	*Run*									
	1	2	3	4	5	6	7	8	9	10
b	4.64	4.88	5.16	4.99	4.91	5.01	4.92	4.99	4.98	4.85
a	0.83	0.44	2.32	1.57	1.02	0.47	5.33	0.59	0.82	0.75
σ	0.67	0.74	0.66	0.68	0.70	0.72	0.70	0.68	0.71	0.72

Fano-factor versus counting time curves were computed from several real shrimp noise data sets and compared with that of a CIR driven doubly-stochastic Poisson model. Counting times were logarithmically spaced with a base of 1.05 between the dead-time and 100 seconds. Parameter estimates for the model fit were computed using moment estimators of the stationary intensity and an estimate of the anticipated asymptotic value of the Fano-factor for large counting times, as outlined in Lepage et al. (2006). An estimate of the asymptote was computed using the 90^{th} percentile value of the Fano-factor; the value of the 9/10th highest Fano-factor. Parameter estimates were then computed using

$$b = \langle \hat{\Lambda} \rangle, \tag{4.47}$$

$$a = \frac{2b\text{var}\{\hat{\Lambda}\}}{\hat{FF}(\infty) - 1} \tag{4.48}$$

and

$$\sigma^2 = \frac{2a\text{var}\{\hat{\Lambda}\}}{b} \tag{4.49}$$

where $\hat{\Lambda}$ was the empirically computed intensity process, $\langle \cdot \rangle$ the expectation operator, and var$\{\cdot\}$ the variance. Results are shown in Figure 4.38. The model curve (solid line) appears to give a reasonable fit to the empirical Fano-factors (blue cross markers), although the finite asymptote does not seem to apply in many cases. The unusually large values from Sydney Harbour (g) were thought to be suspicious, perhaps resulting from another source of large impulse transients and not the snapping shrimp. Short time effects in the Cockburn Sound results (k & l) were due to an excessive number of surface

Table 4.2: Summary statistics of parameter estimation for a CIR driven doubly-stochastic Poisson process from 10 independent simulated data sets. Mean estimates of b and a were within 1 standard deviation of the true value, with large variability between the a estimates. The mean estimate of σ differed from the true value by 10 standard deviations.

Variable	*True value*	*Mean value*	*Median value*	*Standard deviation*
b	5	4.94	4.95	0.13
a	0.5	1.42	0.82	1.49
σ	0.5	0.70	0.71	0.02

reflections being included in the analysis (as discussed in Section 4.8), suggesting that the detection method used was not ideal for these data sets. Estimates of the correlation time were computed and are shown in Table 4.3. Excluding the Sydney Harbour (g) result with correlation time 16.1 s as an outlier, the mean correlation time was 2.88 s and the standard deviation of correlation times was 3.68 s.

Table 4.3: Correlation times of real shrimp noise assuming a CIR doubly-stochastic Poisson model. Results marked with an asterisk are likely to have been affected by the short time effect.

Location	*Tag*	*Sub-figure*	*Corr. time (s)*
Homogeneous Poisson	(HPSIM)	(a)	0.068
Feather Reef	(FR)	(b)	1.5
Seal Island (Cave)	(SEAL-A)	(c)	0.85
Seal Island	(SEAL-B)	(d)	2.39
Seal Island	(SEAL-C)	(e)	10.9
Spencer Gulf	(SG)	(f)	0.19
Sydney Harbour	(SYD-A)	(g)	16.1
Sydney Harbour	(SYD-B)	(h)	2.8
Nornalup-Walpole Estuary	(WP)	(i)	1.5
Cockburn Sound	(CS-A)	(j)	9.3
Cockburn Sound	(CS-B)	(k)	1.3^{*}
Cockburn Sound	(CS-C)	(l)	0.89^{*}

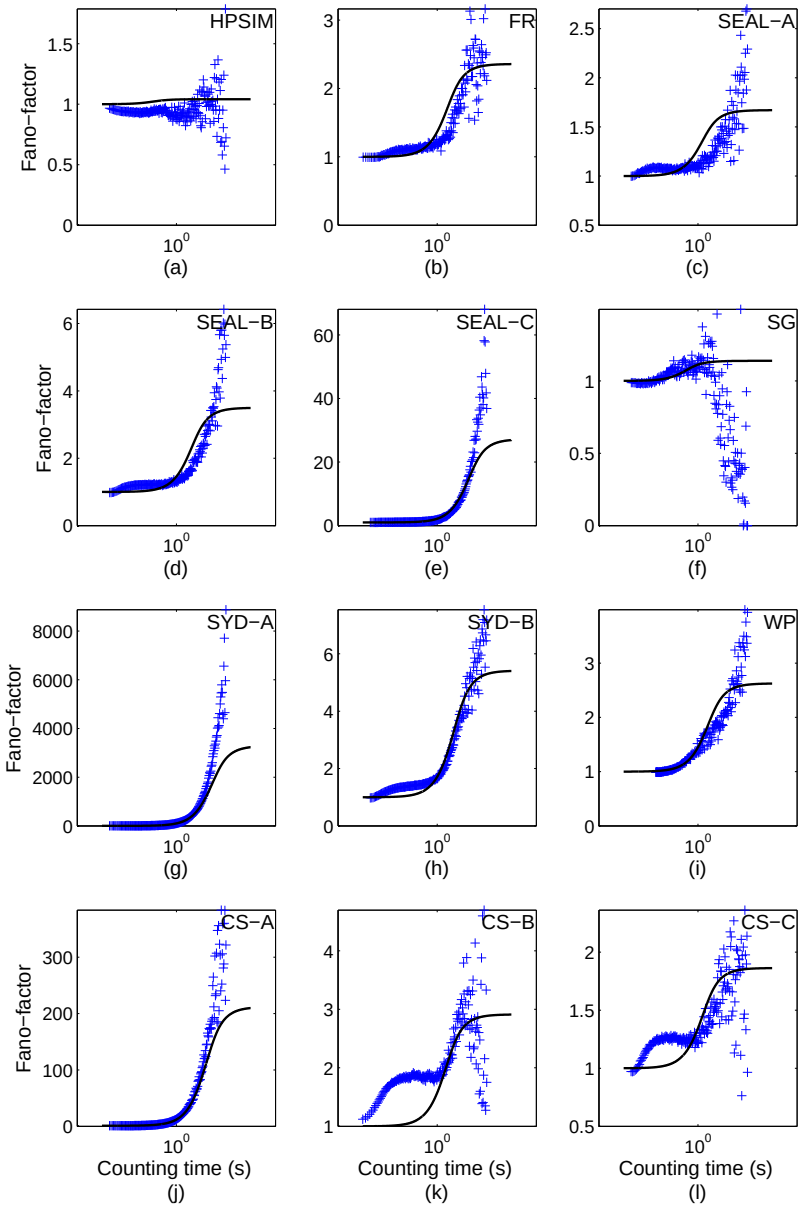

Figure 4.38: Fano-factor versus counting time for real shrimp noise (blue cross markers) from selected locations, and a CIR model fit (black solid line). Drop-off at high counting time for Spencer Gulf (f) and Cockburn Sound (k & l) was due to insufficient data. Surface reflections were not removed.

4.9.4 Asymptote for infinite counting time

An important feature predicted by the CIR doubly-stochastic model was the finite Fano-factor asymptote for infinite counting time. This feature was significant because it means the process is not a fractal process, which has a Fano-factor curve with power law behaviour (Thurner et al. 1997). There was, however, a fundamental difficulty verifying the finite asymptote; given a finite time-series, the number of values available for estimating the mean and standard deviation decreases with increasing counting time. When counting times become large with respect to the duration of the time-series then the uncertainty in the Fano-factor increases substantially. Some evidence for a finite asymptote was observed in the Fano-factor plots, including the Feather Reef, and Cockburn Sound results shown in Figure 4.38. The apparent asymptotes could also have been caused by truncation effects, giving a false impression of an asymptote. To resolve the issue a continuous data set was collected over 24 hours.

4.9.5 A 24 hour time-series

A continuous 24 hour time-series measurement was recorded from the 18th to the 19th of December 2008 at the AWharf site for the purpose of investigating long counting time effects. Weather conditions at the start of the measurement were fine, with clear skies and a wind speed of just over 4 ms^{-1}. The sea state was 1 with a very light swell. Several small boats were visible from the measurement site but most were at a distance greater than 1 km. During the night a tanker transited the area. At the end of measurements the wind had increased to over 7 ms^{-1} and the sea state had increased to 2. A single HTI 96-MIN hydrophone was suspended at a depth of 5 m from a measurement platform near the end of the jetty. The water depth at the start of measurements was 12.0 m. A portable battery power supply was used to power both the hydrophone and the field recorder to minimise 50 Hz interference. Details of the field measurement can be found in Appendix A.

Data pre-processing and detection

An Edirol R-4 Pro field recorder was used for the measurement, configured to save Broadcast Wave Format (BWF) wave files onto a FAT32 filesystem. The filesize limitation of FAT32 is handled by the R-4 by creating multiple files in real-time as the recording progresses. Included in each BWF wave file is a time reference field that contains the number of samples between the previous midnight and the first sample of the recording (BWF 2001). By combining the time reference with the sample number of each file an absolute sample number could be used to reference every sample taken over the full day, noting that at midnight an additional full day of samples needed adding to the time reference. The time reference of the start of recording was then subtracted from each sample to give samples expired since the start of recording. In total 16,337,910,583 samples were recorded, which required the use of a 64 bit integer variable for recording sample indexing numbers. The analysis was conducted in MATLAB version R2008b, which does not allow 64 bit integer mathematical operations. To overcome this problem the embedded java.math.BigInteger was used. Prior to snap detection each individual file was passed through a 1.4 kHz 6^{th} order Bessel high-pass filter. Snaps were detected using a threshold at 20 standard deviations beyond the mean of the nominal background noise, and a dead-time of 0.002 s (384 samples). Threshold levels were computed using the first data file and then fixed for all subsequent files. Detection was performed on each individual data file and the sample number of each detection converted to a 64 bit value (including the file offset) and saved.

Snap rates and the Fano-factor

The data set provided 23 hours, 38 minutes and 13 seconds time separation between the first and last snaps detected at a 20 standard deviation threshold. The data was sufficiently long to allow Fano-factor estimates for counting times up to 8509 seconds, and to observe changes in snap rate over most of a full day. The data was subjected to rate and Fano-factor analysis and the results interpreted for medium and long counting

times. The original computation codes were re-written to allow processing of 64 bit sample numbers using the java.math.BigInteger object. Rate analysis was conducted by computing the number of counts in consecutive non-overlapping one second windows. Snap rates as a function of time for the entire 24 hour period are shown in Figure 4.39. A lower average snap rate was observed during the day, followed by a peak just after sunset and a higher average snap rate through the night. Another peak occurred just before sunrise after which the snap rate reduced to a similar level to the previous morning. The observed pattern is consistent with snap level observations at other locations (Everest et al. 1948), and confirms that the increased snap levels just after sunset and just before sunrise are caused by increases in snap rates (referred to as shrimp activity by Everest et al. (1948)). The probability density function of rates was computed along with a gamma fit and the results shown in Figure 4.40. Small deviations between the observation and the model occur due to the two snap rate peaks and the higher sustained snap rate during the night.

Using the java.math.BigInteger object for detection sample numbers meant that most MATLAB routines (such as the histogram function) could no longer be accessed. For this reason a slightly different algorithm was used to compute the Fano-factor as a function of counting time. Counts were computed using a window based on the minimum counting time of interest. All subsequent counting times were then chosen as multiples of the base counting time to allow for some computational efficiency. In this analysis the minimum counting time was chosen as one second because the focus was on medium and long counting times. Fano-factors were estimated using the slope of the variance versus mean count curve (Gabbiani & Koch 1998) for varying count windows. Slopes were estimated using a linear least squares fit. This Fano-factor algorithm was applied to the entire 24 hour timeseries and the results shown in Figure 4.41. Inspection of the Fano-factor results (dot markers) for medium counting times (greater than 1 second) showed a rise and plateau consistent with previous observations. However, for counting times greater than 400 seconds the Fano-factor curve shows another rise.

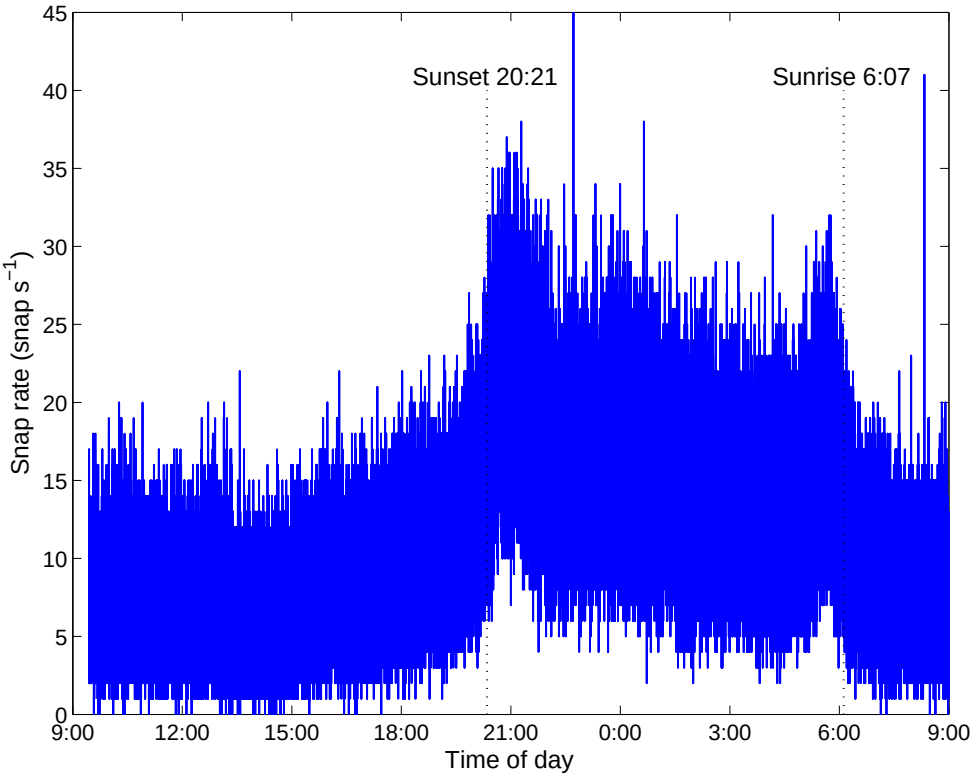

Figure 4.39: Snap rates as a function of time for the 24 hour data. Lower snap rates were observed during the day than at night.

Implications for the CIR doubly-stochastic Poisson model

A finite asymptote was not observed in the data measured over the period of a day, rather a plateau was observed for medium counting times between 1 s and 400 s. The results show that the CIR driven doubly-stochastic Poisson model cannot fully describe the temporal behaviour of shrimp noise over all time-scales but can be used as a model for medium counting times. Averaging times used in underwater acoustic signal processing are often within the time period defined by the medium counting time. The CIR driven doubly-stochastic Poisson model of shrimp impulse times would be applicable for such algorithms.

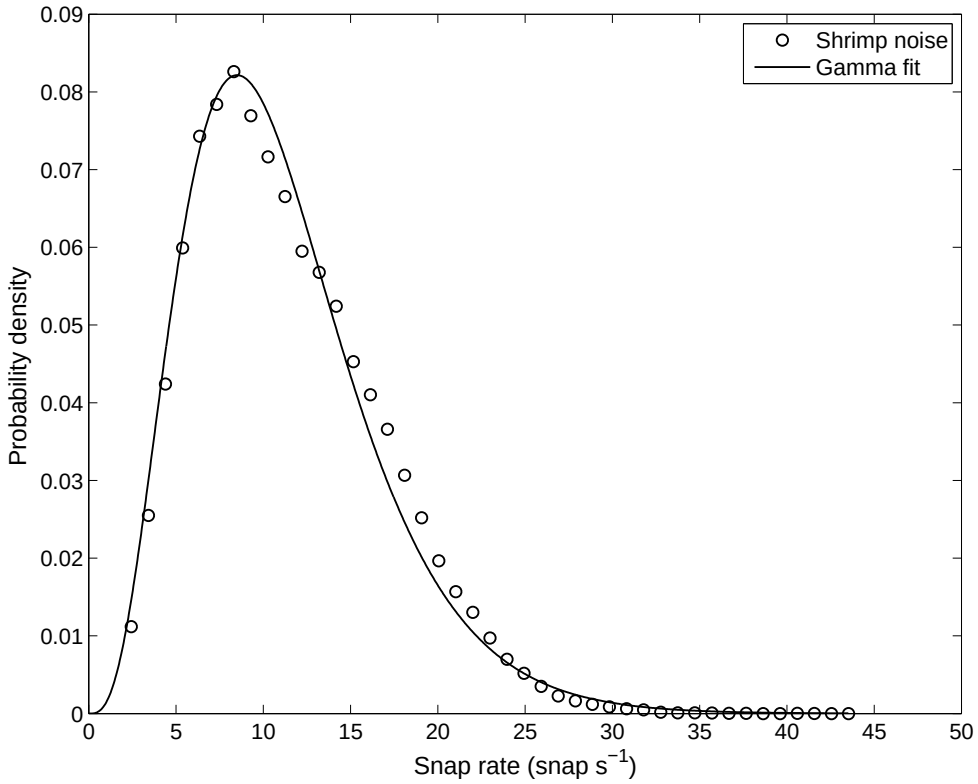

Figure 4.40: Snap rate probability density function and a gamma fit to the 24 hour data. Slight deviations occur due to the variation in snapping rate between day and night.

4.10 Summary of temporal models

A cross section of temporal analysis techniques have been applied to real snapping shrimp noise. Inter-snap interval histogram and uniform conditional tests showed that out of nine different shrimp data sets only one, from Spencer Gulf, was consistent to first order with a homogeneous Poisson process. This was an important result that contradicted initial expectations. Higher order analysis based on k^{th}-order intervals showed that none of the data sets analysed, including the Spencer Gulf data, was consistent with a homogeneous Poisson process at higher orders. Results from this analysis showed structure beyond that expected for a homogeneous Poisson process in the higher order intervals for all of the shrimp noise. Structure in the higher order

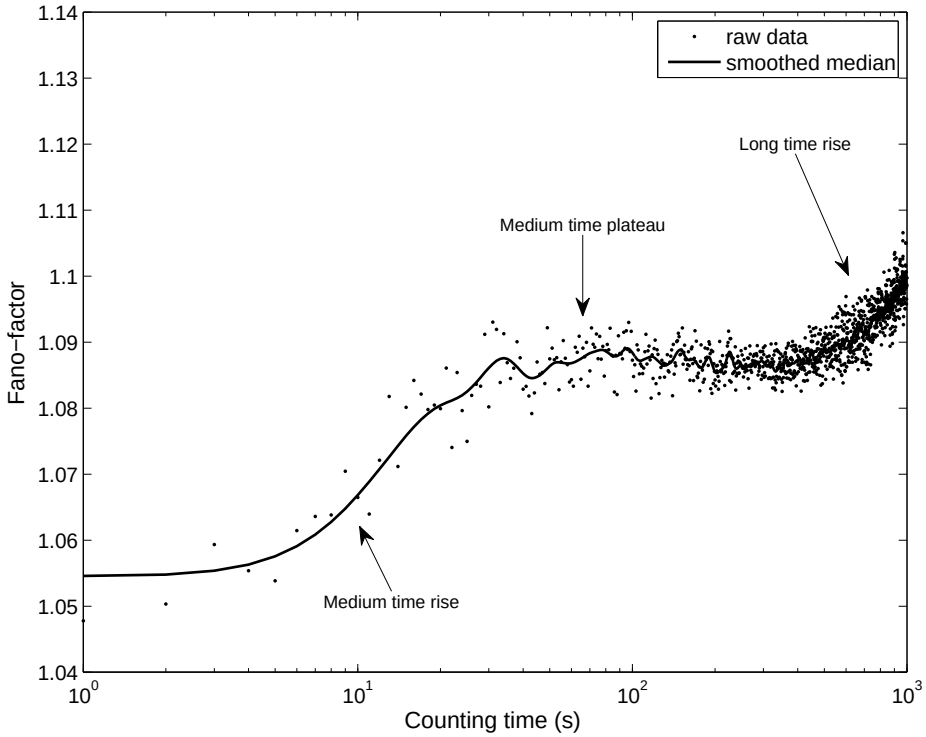

Figure 4.41: Fano-factor as a function of counting time for the 24 hour data. A medium time rise and plateau is evident between 1 s and 400 s, followed by another rise beyond 400 s.

intervals differed between data sets, with the Seal Island Cave data showing the most variability. A summary of test results is given in Table 4.4. When the test results from low order tests were conclusive then higher order tests were not conducted and are shown using dash marks in the table. It was concluded that snapping shrimp noise was not consistent with a homogeneous Poisson process, but under some circumstances may behave like a homogeneous Poisson process to first order.

Intensity function and Fano-factor analysis supported the rejection of the homogeneous Poisson process at higher orders, and provided more information about time scales of non-homogeneous Poisson behaviour. Fano-factors as a function of counting time showed a rise to a plateau for counting times less than a second (short times), followed by another rise and plateau for medium counting times. Short time effects were

Table 4.4: A summary of test results for a homogeneous Poisson process applied to snapping shrimp noise. Tick marks indicate that the test passed with 95% confidence (or visual judgement), cross marks indicate that the test failed, and a dash indicates that the data was not tested.

Location	*Tag*	*IIH*	*Uniform conditional*	K^{th}*-order (visual-test)*	*Fano-factor* (pseudo-test)
Homogeneous Poisson	(HPSIM)	✓	✓	✓	✓
Feather Reef	(FR)	✗	✓	✗	✗
Seal Island (Cave)	(SEAL-A)	✗	✓	✗	✗
Seal Island	(SEAL-B)	✗	✗	–	–
Seal Island	(SEAL-C)	✗	✗	–	–
Spencer Gulf	(SG)	✓	✓	✗	✓
Sydney Harbour	(SYD-A)	✗	✗	–	–
Sydney Harbour	(SYD-B)	✗	✗	–	–
Nornalup-Walpole	(WP)	✗	✗	✗	✗
Cockburn Sound	(CS-A)	✗	✗	✗	✗

identified as surface reflected replicas being included in the event process. Ornstein-Uhlenbeck (OU) and Cox-Ingersoll-Ross (CIR) processes were used as models of the snapping intensity. The (stable) Gaussian distribution of intensity assumed by the Ornstein-Uhlenbeck process did not agree well with empirical intensity results from real shrimp noise, particularly when the average snapping intensity was low. The Ornstein-Uhlenbeck process was, however, a useful process for modelling a coloured noise process, with the spectral shape showing a definite a/f relationship. A (stable) gamma distribution assumed by the Cox-Ingersoll-Ross process provided a much better fit to the empirical intensity results from real shrimp noise and was chosen as the driving distribution for a doubly-stochastic Poisson model of shrimp noise. CIR driven doubly-stochastic noise models were fit to real shrimp noise using curves of Fano-factor versus counting time. The model showed reasonable, but not entirely convincing, agreement with results from real shrimp noise. A finite asymptote predicted by the CIR driven doubly-stochastic Poisson model was investigated using a long-time data set. The finite asymptote was not observed but a plateau was observed for medium counting times between 1 s and 400 s. The results show that the CIR driven doubly-stochastic Poisson model cannot fully describe the temporal behaviour of shrimp noise over all time-scales but can be used as a model for medium counting times. This analysis provides evidence for correlation between shrimp snap events on long time scales.

Chapter 5

Application to simulation and detection

This chapter demonstrates two practical applications of the statistical models developed in this thesis: simulation of semi-realistic ocean acoustic noise, and locally optimum detection of narrow-band signals in real snapping shrimp noise.

5.1 Simulated ocean ambient noise

Semi-realistic ocean acoustic noise was simulated using only random number generators derived from the statistical information provided in previous chapters. The simulation contained the following components:

- Ornstein-Uhlenbeck noise used to simulate very low frequency background noise
- Ornstein-Uhlenbeck noise used to simulate distant shipping noise
- Ornstein-Uhlenbeck noise used to simulate wind noise

- Garnele distributed shrimp snap amplitudes
- CIR driven doubly-stochastic Poisson shrimp snap events.

A time-series was simulated using a sample rate of 192 kHz. Ornstein-Uhlenbeck random variables were generated using the Euler-Maruyama method. Seismic noise was generated with parameters $a = 0.1$ and $\sigma = 1$, shipping with parameters $a = 10$ and $\sigma = 2$, and wind with parameters $a = 1000$ and $\sigma = 20$. For these random variables σ is related to noise power (not bandwidth corrected) and a is the inverse correlation time. Seismic noise had the longest correlation time (about 10 seconds) and wind the shortest (one thousandth of a second). Values for σ were chosen to give an overall noise spectrum similar to real ocean noise. Shrimp noise was generated using Garnele random numbers representing a shrimp field 100 m in diameter, with a hydrophone placed at 5 m depth in a 10 m deep water column. Individual shrimp snaps had a mean source level of 180 dB re 1μPa (at 1 m) and a spread of 6 dB. Shrimp noise was zero except when a snap event was declared. Snap event times were computed using intervals from a CIR driven doubly-stochastic Poisson process using parameters $a = 0.5$, $b = 20$ and $\sigma = 3$. The ocean noise time-series was computed by summing all of the individual components together, and is shown in Figure 5.1.

A set of analysis techniques were selected from the thesis and applied to the simulated ocean noise. A 16384 point power spectral density was computed using the Welch method using a Bartlett (triangle) window and produced the result shown in Figure 5.2. Also shown in Figure 5.2 is a spectrum of the simulated data passed through a 6^{th} order high-pass Bessel filter with cut-off frequency at 1.4 kHz. Spectral density units of the simulation were artificially scaled to give values typical of underwater noise. The simulated noise had a slope of 9 dB per octave for frequencies below 10 Hz, a flat response between 10 Hz and 100 Hz, then a 5 dB per octave slope between 100 Hz and 2 kHz and a flat response beyond 5 kHz. The contribution from the simulated shrimp noise (beyond a few kHz) is flat because the snaps were modelled as single sample "delta functions". Delta functions were used for this example so that the amplitude statistics

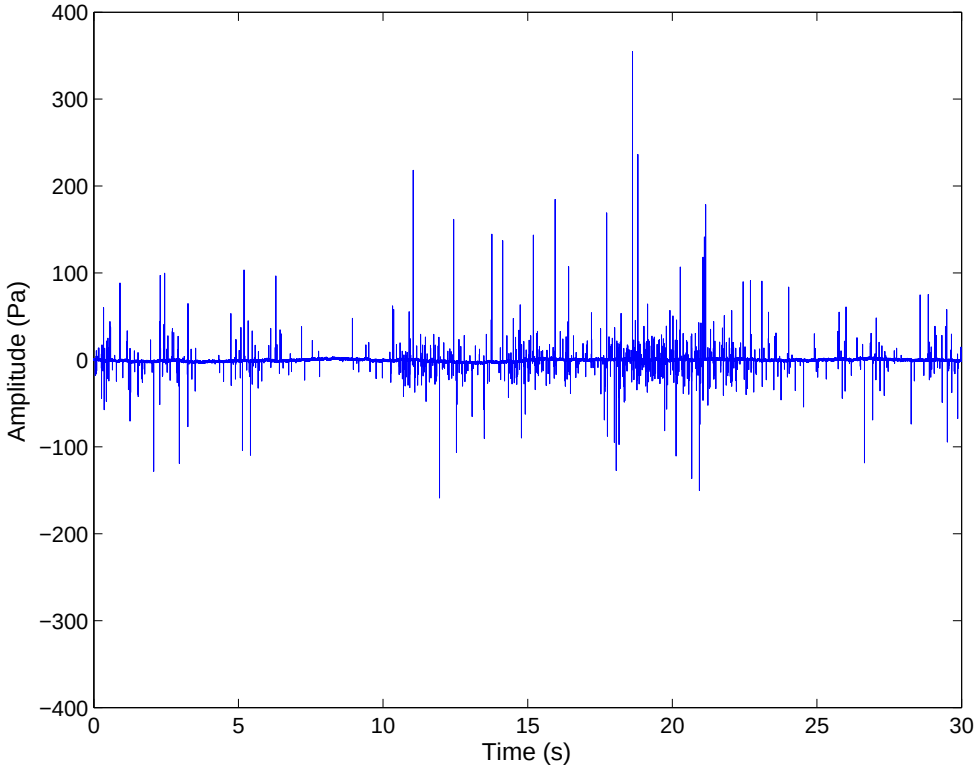

Figure 5.1: A section of ocean ambient noise time-series simulated using only random number generators. Correlated background noise was produced using Ornstein-Uhlenbeck random variables and the shrimp noise using Gaussian-Garnele random variables. The time-series was simulated with a sample rate of 192 kHz.

were known exactly. To simulate more realistic ocean noise the delta functions could be convolved with a representative shrimp snap, such as that shown in Figure 2.3.

The first order probability density function of amplitudes was computed and the result shown in Figure 5.3. SαS and Gaussian-Garnele fits are also shown. The parameters used for the Gaussian-Garnele fit were the values used in the simulation, and the resulting fit shows that the model is consistent when used in the simulation (including being combined with correlated Gaussian background noise). The SαS fit was obtained with a manually adjusted value of $\alpha = 1.98$, an indication that the tails of the distribution were not very heavy in this case. A relative difference plot shown in Figure 5.4 shows that both the SαS and Gaussian-Garnele models over estimate the probability

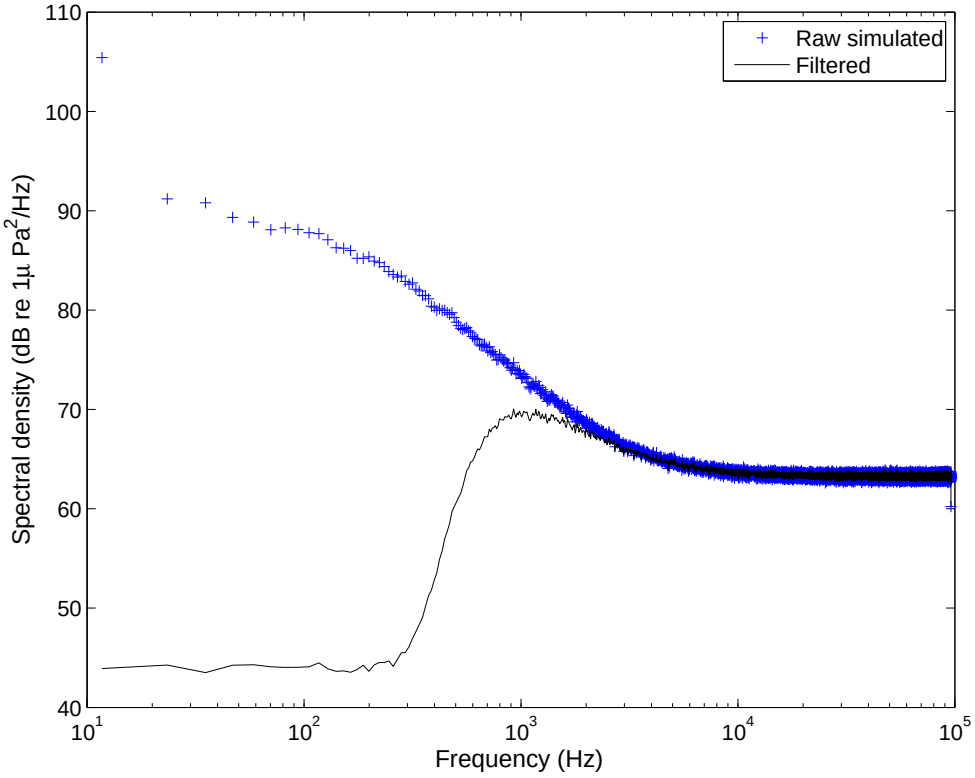

Figure 5.2: Spectral density of the simulated ocean ambient noise as a function of frequency. Slopes in the spectrum were similar to those observed in real ocean noise, although the contribution from the simulated shrimp noise (beyond a few kHz) is flat because the snaps were modelled as single sample "delta functions".

of pressure magnitudes greater than 1 Pa, but then come back into agreement in the tails of the distribution. The SαS model deviates in the extreme tails.

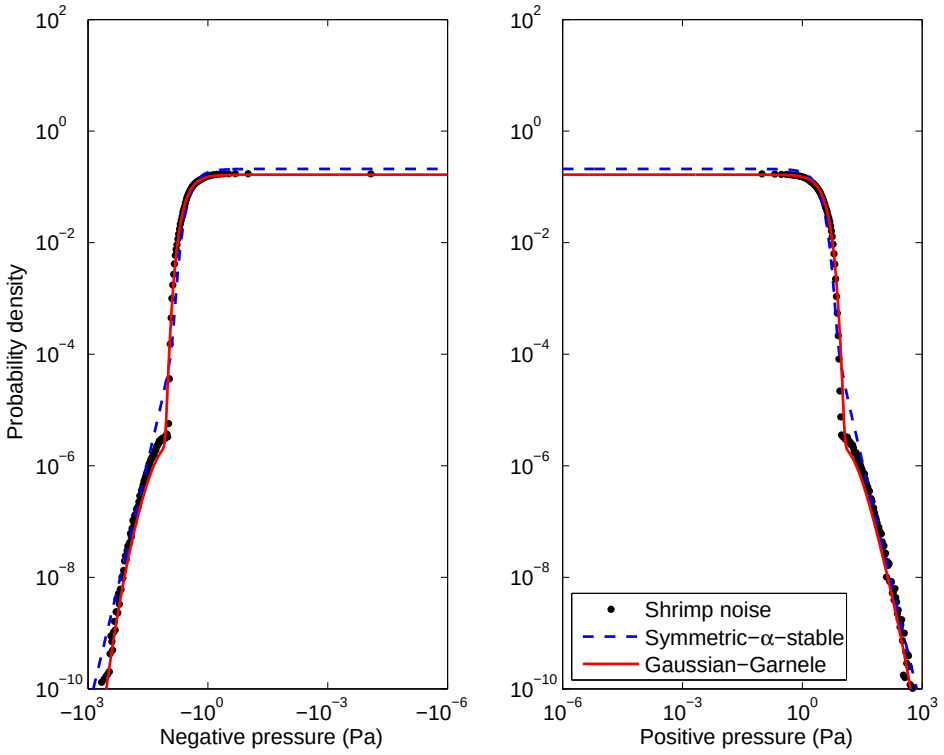

Figure 5.3: Probability density function of simulated ocean ambient noise (black dot markers). Symmetric-α-stable (blue dashed line) and Gaussian-Garnele (red solid line) models are also shown. The Gaussian-Garnele fit parameters were identical to those used in the simulation.

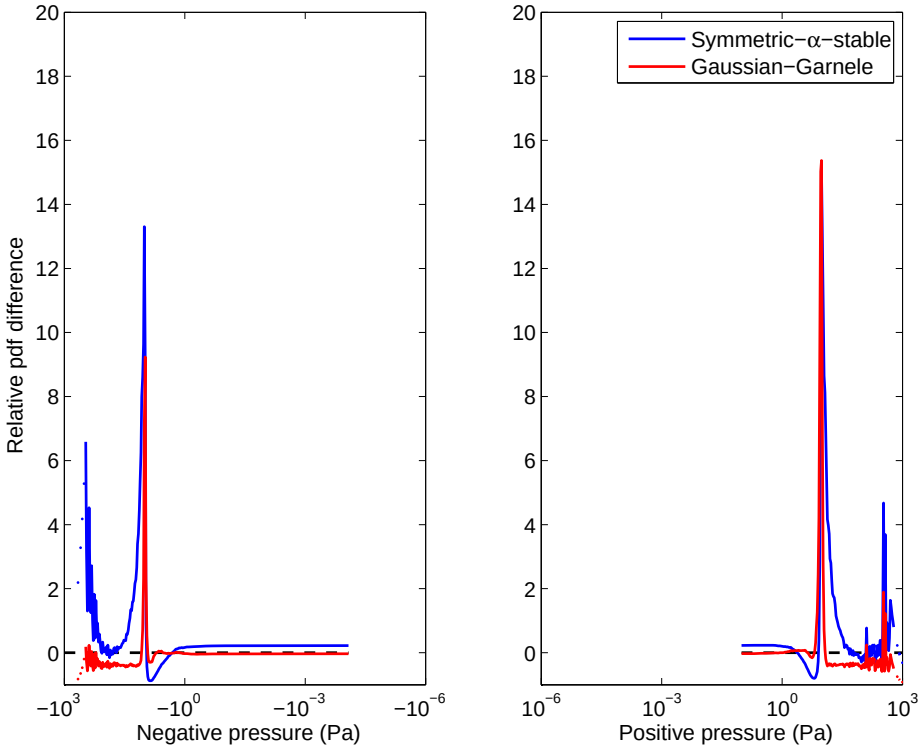

Figure 5.4: Relative difference between SαS (blue solid line) and Gaussian-Garnele (red solid line) models for simulated ocean ambient noise.

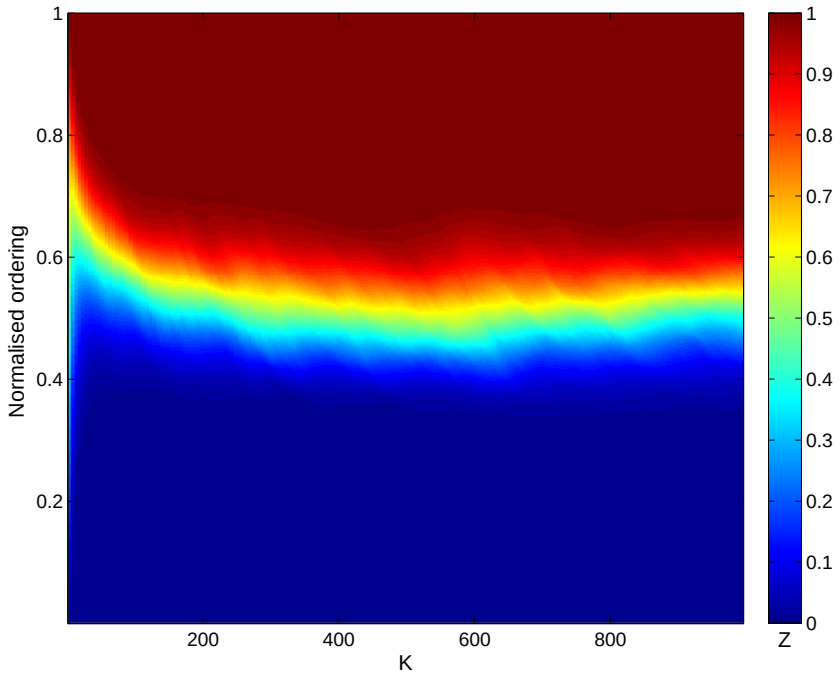

Figure 5.5: K^{th}-order intervals of simulated ocean ambient noise. The result is similar to those obtained from Cockburn Sound (CS-A), with skew in the deviation from a homogeneous Poisson process evident within the first 100 k^{th}-orders.

K^{th}-order interval analysis was conducted on the simulated noise and the results are shown in Figure 5.5. Skew in the deviations from homogeneous Poisson were evident within the first 100 k^{th}-orders similar to those seen in the Cockburn Sound (CS-A) data.

Fano-factor analysis of the simulated noise showed a medium time rise and no evidence for surface reflected (short time) correlations. This is the expected result because there was (deliberately) no causal relationship between positive and negative shrimp impulses. Medium time correlations were seen in the simulated data, and the results were consistent with the original CIR process.

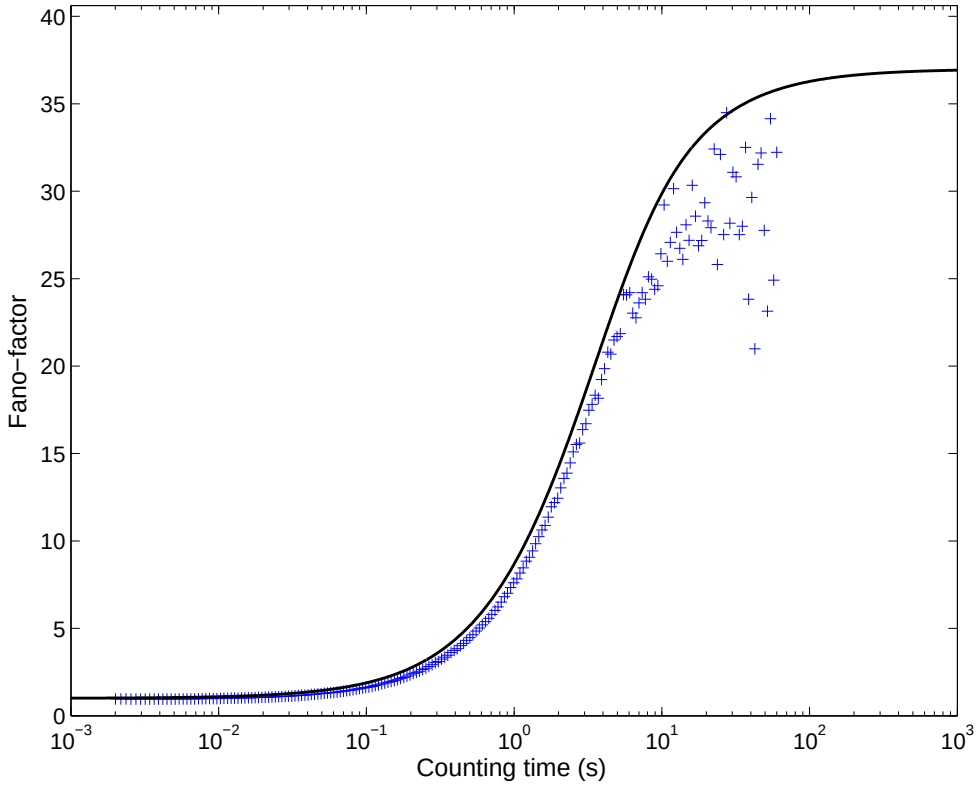

Figure 5.6: CIR driven doubly-stochastic Poisson fit (black solid line) to the Fano-factor as a function of counting time for the simulated noise (blue cross markers).

5.2 Detection in snapping shrimp noise

Receiver Operating Characteristic (ROC) curves were produced for a range of detectors using real shrimp noise. The curves were produced by inserting synthetic signals into real noise. This method of inserting synthetic signals into real noise for the purpose of examining detector performance in underwater noise has also been used by Nielsen & Thomas (1990) and Bertilone & Killeen (2001). Locally optimum detectors were derived from Gaussian-Gaussian mixture, SαS, and Gaussian-Garnele noise models, and compared with a benchmark periodogram detector (Kay 1998). Decision thresholds were empirically estimated using the entire noise-only data. Noise density estimates at the frequency of interest were sorted in ascending order (to give noise density order statistics) and a decision threshold set at the value of the $N(1-\mathrm{P_{fa}})$ 'th order statistic, where N was the number of noise density estimates and $\mathrm{P_{fa}}$ was the probability of false alarm.

Synthetic 10 kHz narrow-band (pure cosine) signals were added to the real shrimp noise at the desired signal to noise ratio (SNR). The SNR was defined as

$$SNR = 10\log_{10}\left(\frac{A^2}{E_{\mathrm{bw}}\,\eta_f}\right) \tag{5.1}$$

where A was the root-mean-squared (RMS) amplitude of the signal sinusoid, η_f was an ensemble noise power spectral density (at the frequency of interest) estimated using the Welch method (Welch 1967) over the entire noise data, and E_{bw} was the effective noise bandwidth. The effective noise bandwidth was computed using (Heinzel et al. 2002)

$$E_{\mathrm{bw}} = \frac{F_s \sum_{k=1}^{N} \omega^2(k)}{\left[\sum_{k=1}^{N} \omega(k)\right]^2} \tag{5.2}$$

where F_s was the data sample rate, and ω the N point windowing function used to shade the periodograms (in this case a Bartlett window with $N = 4096$). The synthetic signal was produced in 4096 point sections to correspond with the number of points

used for a periodogram estimate. The phase of the signal was randomised (uniformly) between 0 and 2π radians at the start of each 4096 point section, then held constant throughout the section. The signal was added to the noise then periodogram estimates were produced for the signal plus noise noise using the Welch method with a 4096 point Bartlett window. Probability of detection was computed using the ratio of the number of estimates exceeding the decision threshold to the total number of estimates.

Locally optimum detectors were implemented by applying a non-linear transformation to the sample data prior to periodogram detection. Non-linear transformation functions ($g(x)$) were obtained using the amplitude pdf (see for example Kassam 1988)

$$g(x) = \frac{-f'(x)}{f(x)} \tag{5.3}$$

where $f(x)$ is the amplitude pdf and dash notation is used to indicate the derivative. Analytic expressions for $g(x)$ were obtained for the Gaussian-Gaussian mixture and Gaussian-Garnele models, and a numerical value obtained for the SαS model. The numerical value for the SαS model was computed by evaluating the pdf using McCulloch's method at point x, then computing a naïve derivative using small increments above and below x thus

$$g_{S\alpha S}(x) = \frac{-(f(x+\epsilon) - f(x-\epsilon))}{2\epsilon f(x)} \tag{5.4}$$

where ϵ was computed using one fourth of the smallest increment of x.

Parameters for the locally optimum detectors were estimated on a per-detector basis using an appropriate amplitude pdf fitting technique. Gaussian-Gaussian mixture parameters were estimated using the method of moments, SαS using the sample fractile method, and Gaussian-Garnele using maximum likelihood (by nonlinear least squares) with careful selection of initial conditions required in this case.

An ambient plus shrimp noise data set was selected from among the Cockburn Sound field data. The sample rate of the acoustic time-series was 473 kHz and the duration was slightly less than 600 seconds. Each periodogram was computed using a 4096 point FFT, resulting in 68104 periodograms in total. Probability of false alarm was

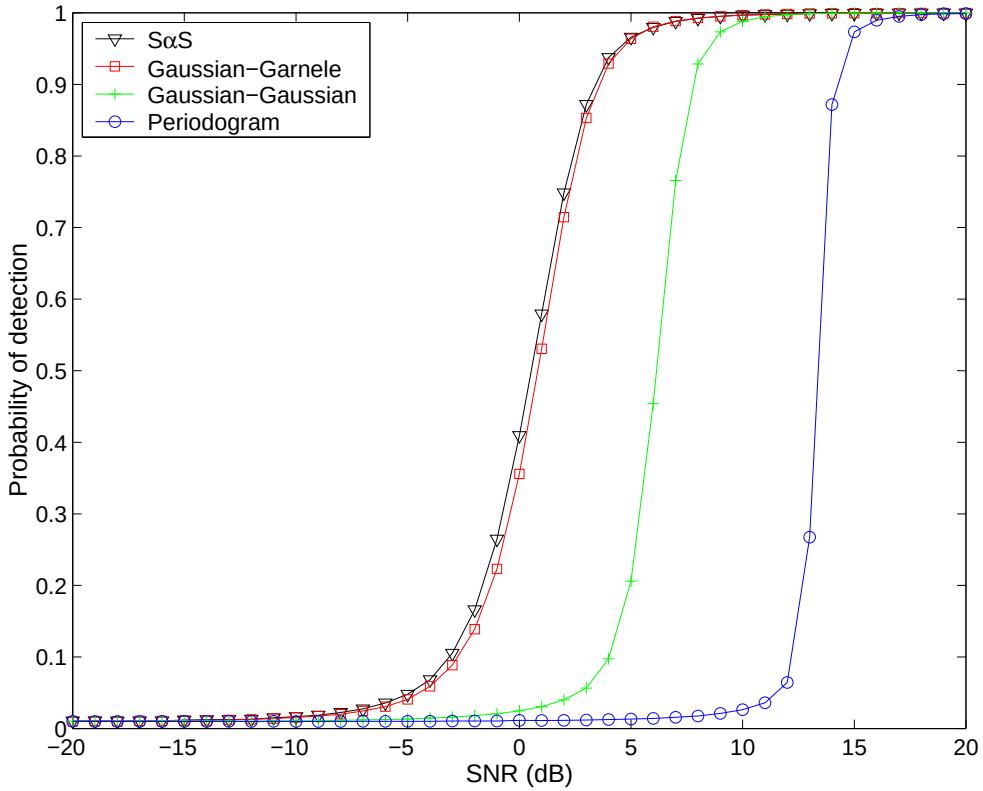

Figure 5.7: ROC curves for SαS, Gaussian-Garnele, Gaussian-Gaussian mixture and Periodogram detectors. Probability of false alarm was 1×10^{-2}.

set at 1×10^{-2}. ROC curves were computed for each detector and the results are shown on Figure 5.7. The SαS detector was superior to all of the other detectors, with a detection threshold (the SNR at $P_{\mathrm{d}} = 0.5$) of 0.53 dB. The Gaussian-Garnele and Gaussian-Gaussian mixture detectors followed with detection thresholds of 0.82 dB and 6.15 dB respectively. The periodogram detector was the worst performing detector with a detection threshold of 13.38 dB, which was the expected result because of the impulsive non-Gaussian nature of the noise. The results are consistent with Bertilone & Killeen (2001) in the sense that all of the locally optimum detectors based on suitable non-Gaussian models gave much better performance than the periodogram detector (which is optimal for Gaussian noise). The superiority of the SαS detector is consistent with results obtained by Chitre (2006).

The superiority of the SαS detector over the Gaussian-Garnele detector was an unex-

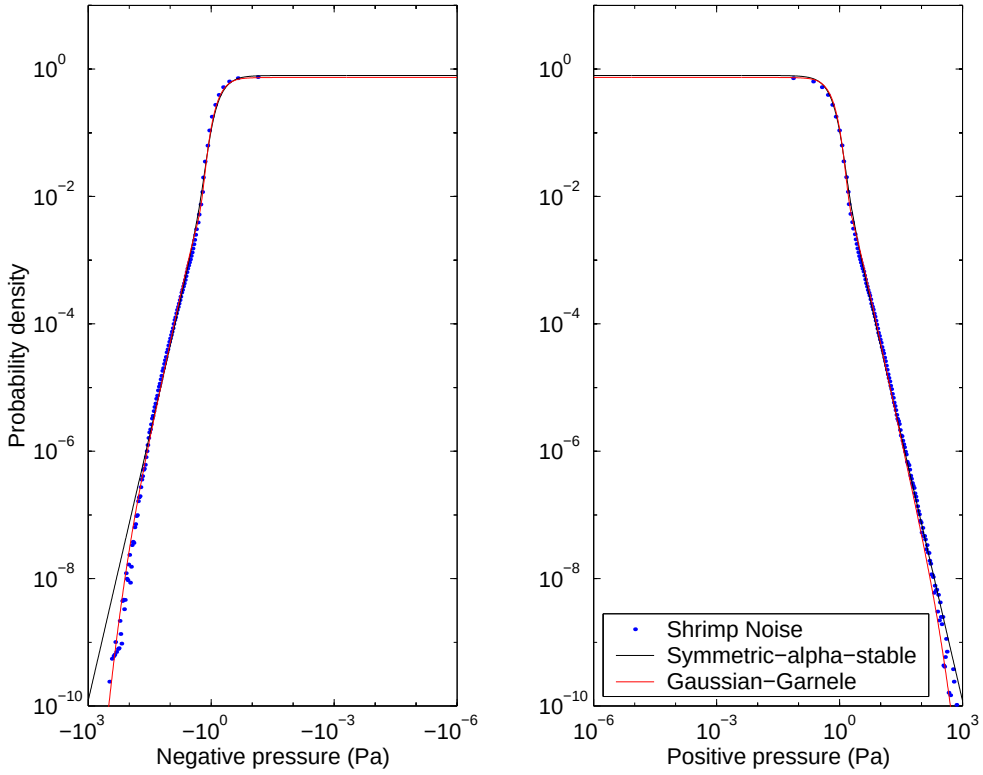

Figure 5.8: Probability density function of shrimp noise amplitudes with SαS and Gaussian-Garnele model fits. The Gaussian-Garnele model appears to provide a better fit to the real shrimp noise over a greater range of pressures.

pected result, because the Gaussian-Garnele model appears to give a slightly better overall fit to the amplitude pdf. Amplitude pdfs for the real shrimp noise, and SαS and Gaussian-Garnele model fits are shown in Figure 5.8. The Gaussian-Garnele model provides a better fit to the real data than the SαS model, so another factor (other than goodness of pdf fit) was contributing to the performance of the SαS detector. Similar inconsistencies have been observed when using locally optimum detectors based on the Cauchy model (a special case of the SαS model) (D Bertilone 2008, per. Comm.). Possible reasons for these inconsistencies include: the ability of the detector to accommodate certain non-stationarities in the shrimp noise data (with respect to the first order amplitude pdf), artificial inflation of detection performance due to over-estimating noise probabilities over certain amplitude regions, or as a consequence of the approximations inherent in the locally optimum detector structure.

5.3 Summary of applications

Ocean acoustic noise was simulated using a series of random number generators and analysed using the spectral density, amplitude probability density, k^{th}-order interval and Fano-factor techniques presented previously. The results show that some of the higher order statistical amplitude and temporal properties of real ocean acoustic noise could be reproduced by the simulation.

Detection of narrow-band signals in real shrimp noise was investigated using locally optimum detectors derived from SαS, Gaussian-Garnele and Gaussian-Gaussian mixture models. All of these non-Gaussian detectors showed performance improvement over a periodogram detector. The SαS detector was the best performing detector, with a detection threshold improvement of 12.85 dB over the periodogram detector. The Gaussian-Garnele detector had a detection threshold only 0.29 dB higher than the SαS detector, resulting in a 12.56 dB performance improvement over the periodogram detector. The results presented are very near the maximum performance that can be expected from locally optimum detectors derived from (first order) amplitude models of snapping shrimp noise.

Chapter 6

Discussion

The purpose of this chapter is to discuss some selected aspects of the amplitude and temporal models relating to their use in practical applications. Methods and assumptions used to derive the Gaussian-Garnele model are discussed including the consistency of parameters when used in simulation, difficulties related to parameter estimation when using the model in detection algorithms, and some cautionary remarks on using the model to infer the physical characteristics of the shrimp field. Temporal models and analysis techniques are discussed and promising techniques are identified. Implications for sonar detection and communication are discussed, and some processing methods that could benefit from the contributions in this thesis are identified.

Two important results regarding the statistics of snapping shrimp noise are confirmed by the results in this thesis. Non-Gaussian models are known to provide a better fit to the amplitude pdf than the Gaussian model. The first result is that sophisticated non-Gaussian amplitude models, such as the SαS model, are better models of snapping shrimp noise than the simpler Gaussian-Gaussian mixture model. The additional complexity associated with the use of sophisticated non-Gaussian models in detection algorithms is justified because meaningful gains in detection performance can be obtained. This is discussed further in Section 6.1 and Section 6.3. The second result is

that short time correlations observed in snapping shrimp noise are caused by surface reflections, this is discussed further in Section 6.2.

6.1 Discussion of amplitude probability density function models

The SαS model is relatively mature: numerous techniques exist for parameter estimation and numerical evaluation of the pdf, and many examples of application to detection problems are available (Nikias & Shao 1995). However, application of the SαS model to shrimp noise is a recent accomplishment and consequently there are a limited number of studies (to date) on this topic. Most of the available studies use shrimp noise from Singapore waters (see for example Chitre et al. 2006).

Garnele and Gaussian-Garnele models were derived to provide a physically realistic model of shrimp noise, with an analytic amplitude pdf. The desire for an analytic amplitude pdf was driven primarily by the practical usefulness of an analytic non-linearity transformation function for locally optimum detection. Throughout the derivation assumptions were chosen to maintain the analytic pdf solution and in some cases these assumptions were not physically realistic. The assumption of a (two-dimensional circular) uniform spatial distribution of the shrimp sources may not be as generally applicable as the Poisson spatial distribution (assumed by the SαS model). An alternative model may combine the source and propagation methods from the Garnele derivation with the general derivation method used for the SαS model.

The Gaussian-Garnele model may also be attractive for estimating the physical characteristics of a field of shrimp, for example estimating the mean and standard deviation of snap sound pressure levels at the source. There are several cautions for use of the Gaussian-Garnele model for this purpose. First, there are parameter correlations. For example, it appears that the mean sound pressure level and maximum extent of the

shrimp field are correlated. One of these parameters would need to be accurately measured if the other is to be inferred through model fitting. Another issue is that the Gaussian-Garnele model is based on the ϵ-framework rather than an additive noise framework. The ϵ-framework provides analytical convenience but is physically unrealistic. Consequences of the ϵ-framework for estimating the parameters of a shrimp field in the presence of additive Gaussian noise requires investigation prior to this type of use.

Parameter estimation was an issue for the Gaussian-Garnele model because the parameters are both useful and the cause of some estimation difficulty. The parameters are physical values that have a certain familiarity (snap source levels, water depth, and hydrophone depth) rather than mathematically derived quantities such as location and scale parameters. In situations where many of the physical parameters can be either measured or reliably estimated using (independent) methods, the Gaussian-Garnele model allows a direct comparison between theory and experiment that does not require parameter estimation from the experimental results. However, the model has a total of 7 parameters and although most can be either directly measured or sensibly estimated, refinement of the parameters requires a non-linear least squares fit. In signal processing applications the cost of estimating the 7 parameters using non-linear least squares could be prohibitive.

An additional result is that the SαS and Gaussian-Garnele models are significantly better models of snapping shrimp noise than the Gaussian-Gaussian mixture model. The Gaussian-Gaussian mixture model is a commonly used non-Gaussian noise model because it is mathematically simple. This study has shown, however, that the performance of the Gaussian-Gaussian mixture model is quite inferior to the SαS and Gaussian-Garnele models. Narrow-band detection results showed that the Gaussian-Gaussian mixture detector only achieved around half of the detection threshold improvement (compared with a periodogram detector) that was realised by the SαS and Gaussian-Garnele detectors. This result is consistent with the conclusions of Willett (1987) who used shrimp noise from the United States. Willett considered the John-

son distribution as an alternative, which gave good agreement out to tail weights of 1×10^{-4} (amplitudes were given in normalised units) but beyond this point the real shrimp noise became progressively heavier tailed than the Johnson prediction. In light of the performance superiority of the SαS detector, despite showing worse agreement in the extreme tails of the pdf than the Gaussian-Garnele detector, a Johnson detector may perform better than anticipated. The Johnson detector should therefore be included in further work to understand the relationship between model pdf fit (to real shrimp noise) and the performance of model based locally optimum detectors.

6.2 Emerging knowledge of the temporal nature of snapping shrimp noise

Many studies of the temporal nature of snapping shrimp noise have investigated the change in intensity (i.e. changes in spectrum level) over long time durations, or have indirectly considered the temporal statistics through tests of stationarity of the amplitude statistics. However, few (to date) have considered the snap events directly as a point process in time. Temporal analysis of snapping shrimp impulses as a point process is currently at a very early stage of development. The temporal analysis presented in this thesis is therefore exploratory, but based on a sound foundation of point process analysis techniques used in other fields. On reflection, the inter-snap interval histogram analysis and related uniform conditional test were useful only as indicators that the process may not be homogeneous Poisson. Their usefulness was found in justifying the more sophisticated Fano-factor and k^{th}-order interval analyses. Due to the current immature status of this type of analysis, there are many issues for discussion.

Of the attempted techniques, only the higher order Fano-factor and k^{th}-order interval analyses were able to reveal the true nature of the shrimp snapping. Fano-factor results were easier to interpret than the k^{th}-order interval results because the k^{th}-order intervals distort the time axis (with respect to the original point process). However, the k^{th}-

order interval results appear to be more "rich" with information than the Fano-factor results. Further study of interpreting the k^{th}-order interval results is likely to provide information additional to what is available from Fano-factor analysis.

The k^{th}-order interval analysis provided the strongest evidence that all of the real shrimp data sets were not homogeneous Poisson distributed, and therefore contributed the most important conclusion for the thesis. The results also showed the greatest amount of variation between the different data sets, and so was the most revealing of the analysis techniques. Unfortunately, the interpretation of k^{th}-order interval results is difficult. Some progress was made to help understand these results by devising a transformation, based on part of a statistical test, and applying the transformation to the interval lengths prior to plotting. The transformed values could then be compared with what would be expected for a homogeneous Poisson process. Interpretation could then proceed by first choosing a k^{th}-order of interest, and by looking at the progression of the order statistics make a judgment relative to a homogeneous Poisson process. Statements such as "there are more large intervals between every 5^{th} snap than would be expected for a homogeneous Poisson process" are possible using this method. Relating these interpretations back to the original point process is still problematic because the intervals lie on a deformed time reference (with respect to the original point process). The average interval between consecutive snaps may be used as a transformation reference time, so if the average time is 0.2 s then the large intervals between every 5^{th} snap from the above statement could be interpreted as correlation on a time scale of 1 s. It is the author's opinion that this is not a rigorous enough treatment of the issue, and that the potential of k^{th}-order interval analysis will only be realised through more careful interpretation.

Fano-factor analysis revealed three time-scales on which the snap events were correlated. Short time correlation (less than a second) was attributed to the arrival of surface reflected replicas of the snaps, and provided the second important conclusion for the thesis. The cause of medium time (greater than one second) correlations was not identified. Some candidate mechanisms for the correlation include the shrimp responding to

the acoustic background noise (possibly consistent with one of the methods outlined in Herz et al. (2004)), modulation of the sources above and below the threshold level due to fluctuating propagation conditions, movement of the shrimp's food sources through the shrimp field, or interactions between the shrimp (for example a shrimp may be more likely to snap if another shrimp has snapped nearby). In the absence of an identified mechanism for the medium term correlations, the snapping process was modelled mathematically as a doubly-stochastic Poisson process. Ornstein-Uhlenbeck (OU) and Cox-Ingersoll-Ross (CIR) processes were investigated as models of the intensity process driving the doubly-stochastic Poisson process. An investigation of snapping rate distributions showed that the OU process did not correctly model the shrimp noise when the snapping rate was low. This problem was solved by using the CIR process. Theoretical curves for the Fano-factor, as a function of counting time, were available for both of these processes allowing a comparison of empirical Fano-factor results with a theoretical curve. The results showed that the CIR driven doubly-stochastic Poisson process was able to model the medium time effects observed in the empirical Fano-factor results. Analysis of a long time-series (a full day) showed that a plateau exists in the Fano-factor at medium counting times and also shows evidence of correlation between snaps on longer time scales. For the data analysed the long time scale correlations were for times greater than 400 seconds.

The CIR driven doubly-stochastic Poisson process was therefore chosen as the snap event time model to use for simulating ocean noise. An empirical Fano-factor curve was produced from the simulated data and compared with a theoretical Fano-factor curve generated using the parameters from the simulation. The results were in agreement.

The temporal analysis presented in this thesis is approaching the stage where spatial considerations can no longer be ignored. It has been shown conclusively that the snapping from fields of shrimp does not conform with a homogeneous Poisson process, and therefore the time and location of the shrimp snaps (the spatio-temporal nature of the shrimp noise) becomes important. The conclusions of this thesis confirm that spatio-temporal analysis of snapping shrimp noise is warranted, and is a topic that follows

naturally from this thesis. A possibility for analysing the spatio-temporal nature of snapping from a shrimp field, that continues from the temporal techniques presented in this thesis, would be to apply k^{th}-order interval analysis to snap events measured by a hydrophone array. By improving the relatively immature understanding of temporal statistics, and combining with existing knowledge of the amplitude and spatial statistics, an overall picture of the true nature of snapping from fields of shrimp can be developed and links between amplitude, spatial and temporal statistics can be understood.

6.3 Implications for sonar detection and communications

Significant improvements in the detection of weak narrow-band signals can be realised using locally optimum detectors based on non-Gaussian noise models. Of the available models, the SαS model appears to provide the greatest performance gains when used for narrow-band detection. This study confirms the superior performance of the SαS detector for narrow-band detection using real shrimp noise from (independent) locations around Australian shores, measured using different equipment and independent measurement methods.

One of the original intentions of this study was to explore methods for exploiting new statistical knowledge of snapping shrimp noise to improve the performance of sonar detection and underwater communication systems. During the course of the study it became apparent that more work was needed developing an understanding of temporal statistics, and so the original aims were revised. This section provides a brief discussion of the original intentions and identifies some signal processing algorithms that may benefit from the results of this thesis.

Recalling Middleton's general rule (Middleton 1995):

...the more relevant information regarding both the signal and noise that is

properly used, the better the performance.

Two important aspects of the general rule are: that the information is relevant, and that it is properly used. Models of the amplitude, temporal and spatial statistics of a noise source constitutes relevant information. Proper use of amplitude models, such as the Symmetric-α-stable model, in (memoryless) locally optimum detectors gives near optimum results. It remains, therefore, to use the spatial and temporal models of snapping shrimp noise to obtain improvements in detection performance.

Some signal processing algorithms that make use of temporal information are the auto-regressive (AR), moving average (MA), auto-regressive moving average (ARMA), and Quasi-equivalent (QE) models. However, these models are primarily concerned with sample level correlations and are less likely to benefit from information relating to the snapping point process. Detectors that do benefit from knowledge of the point process statistics are the CFAR processors (Himonas 1994, Doukovska 2007). CFAR detector performance depends on the parameters of randomly occurring impulse events, even if the events have a low probability of appearance (Doukovska & Kabakchiev 2006). Investigation of the effect of CIR driven doubly-stochastic Poisson noise on CFAR processing may provide a way forward for improved detection in snapping shrimp noise.

Chapter 7

Conclusions

7.1 Thesis conclusions

There are many contributions that result from the work presented in this thesis. Most of the contributions are modest, often confirming existing knowledge using independent methods. However, there are two important contributions regarding the temporal nature of snapping shrimp noise that are substantial in their own right, and have been studied to the point of being conclusive. They are:

- Snap events from a field of snapping shrimp (received by a hydrophone) are not consistent with a homogeneous Poisson process;
- Short time correlation of the snap event process is caused by surface reflected replicas.

In Chapter 4 it was shown using Fano-factor analysis that the shrimp (snap) point process is correlated over two distinctly different time scales. Short time correlations, less than a second, were shown to be caused by surface reflected replicas. Medium time correlations, between 1 and 60 seconds, were modelled using a Cox-Ingersoll-Ross

driven doubly-stochastic Poisson process. In support of the model for medium time effects, the distribution of rates was compared with the required gamma distribution and the results were in excellent agreement. A full day recording was analysed and showed that a Fano-factor plateau existed for medium counting times and that further correlation is evident between the snap events on long time scales.

K^{th}-order interval analysis conducted in Chapter 4 provided the strongest evidence that all of the real shrimp data sets were not homogeneous Poisson distributed, and therefore contributed the most important conclusion for the thesis. The results also showed the greatest amount of variation between the different data sets, and so was the most revealing of the analysis techniques. Interpretation of k^{th}-order interval results is complicated because the time scales are distorted with respect to the original point process. A method was devised to assist interpretation of the k^{th}-order interval results by using part of a statistical test to transform the results prior to plotting, allowing interpretation to be made with respect to a homogeneous Poisson process.

The Gaussian-Garnele model derived in Chapter 3 contributes a dedicated model of snapping shrimp noise that has an analytic probability density function. While the contribution to improved narrow-band detection made by the new Gaussian-Garnele model is yet to be fully understood, there are aspects of the model that are useful for the study of snapping shrimp noise. For example, a representation of source levels from the shrimp field could be estimated given the water depth, hydrophone depth, shrimp field extent, and background noise power were known. The issues of parameter correlation and definition for the shrimp field extent also arise in this context, motivating further study. Investigation into asymmetry in the extreme tails of the amplitude probability density function was motivated by the fact that it is both predicted by the Gaussian-Garnele model and observed in real shrimp noise. Consequently, an experimental investigation of the phenomenon was initiated, rather than ignoring the effect as an artifact, or attributing it to insufficient statistics. The experimental investigation contributed further by eliminating hydrophone directivity as a possible cause for the effect, strengthening the possibility that the effect is indeed due to the source and

propagation models used by the Garnele model. Comparison of the Gaussian-Garnele model with the Symmetric-α-stable model revealed similar levels of variability from both models about real shrimp noise pdfs, with the exception of the extreme tails. In the extreme tails the Gaussian-Garnele model provided a superior fit to the real shrimp noise pdf.

Results from Chapter 5 confirm that narrow-band detection using locally optimum detection based on the Symmetric-α-stable noise model is near optimum in the presence of snapping shrimp noise. The Symmetric-α-stable detector was superior to all of the detectors considered. A locally optimum detector based on the Gaussian-Garnele model performed only marginally worse than the Symmetric-α-stable detector, and was clearly superior to the Gaussian-Gaussian mixture and periodogram detectors. Detector performance was conducted using real shrimp noise collected from a location in Australia, thus providing independent confirmation of similar results obtained for shrimp noise in Singapore waters. Additional conclusions from the narrow-band detection study include the sub-optimal performance of the Gaussian-Gaussian mixture model of snapping shrimp noise, which was consistent with similar studies on shrimp noise from the United States. In these studies using data from the United States, the Johnson distribution was used to model the shrimp noise

7.2 Recommendations for further work

Topics that have been identified for further work can be grouped into the following: refining key statistical distributions, interpretation of temporal statistics and transition to understanding a full spatio-temporal picture, and understanding relationships between goodness-of-fit and system performance in practical applications.

The development of dedicated models of snapping shrimp amplitude statistics relies on two fundamental distributions: the distribution of shrimp snap source levels (the source distribution), and the distribution of ranges to the shrimp and the times at which

the snaps occur (the spatio-temporal distribution). Refinement of these fundamental distributions will result in better shrimp noise models which can be used to better understand the shrimp and to improve signal processing in shrimp noise.

K^{th}-order interval analysis was the most promising of the temporal analysis techniques used in this thesis. Further work is required to enable accurate interpretation of this analysis and more data needs to be analysed to find consistent features that are characteristic of snapping shrimp noise.

A wealth of further research ideas arise from the detection of narrow-band signals in snapping shrimp noise. Issues for narrow-band detection include, understanding how the pdf fit of the model affects the performance of locally optimum detectors, and how deviations of the model above and below the empirical results affect detection performance. Models that should be considered for this study are the Symmetric-α-stable, Cauchy, Gaussian-Garnele, Johnson, and Gaussian-Gaussian mixture models. The detection threshold of detectors derived from these models should also be computed as a function of signal frequency and compared with the periodogram detector. The issue of broadband detection and spread-spectrum communication performance should be considered after the narrow-band results are fully understood. There are a number of detection algorithms that may benefit from improvements in temporal models, such as the CFAR processing algorithms. The greatest gain, however, is most likely to be obtained through spatio-temporal (space-time) processing.

Appendix A

Field Measurements

Several field measurements were conducted to provide data for this thesis. A summary of these measurement activities is presented for each of the measurement locations. Multiple measurements were taken at each of the sites using a variety of different equipment and measurement methods. Measurements were often taken in conjunction with other field work unrelated to this thesis, indicated as other duties.

A.1 AWharf (AW)

The AWharf is a jetty located near 32°10′36.3″S, 115°40′42.7″E, in Western Australia. Only one of the data sets collected at the A-Wharf was used in this thesis. The data was collected at midday on 31 August 2007. Weather conditions on the day were completely overcast, and the temperature measured at 15.6°C. The sea state was relatively calm with no swell, and a light breeze was blowing.

The following people contributed to the measurement:

- Matthew Legg (design; recording equipment setup, calibration and operation;

note taking; other duties)

- Dr. Dave Matthews (rigging; other duties)
- Damien Killeen (observation; other duties)
- Dr. Rod MacLeod (rigging; observation; other duties)

The following equipment was used:

- Hydrophone: HTI-96-MIN S/N 554003

  Sensitivity: -164 dB re 1V per μPa

  Nominal bandwidth: 2 Hz to 30 kHz

  Horizontal directivity: omni-directional

  Vertical directivity: unknown

- Recorder: FOSTEX FR1

  Sample Rate: 192 kHz

  Resolution: 24 bit

  Calibration: 20 kHz white noise at -34 dBV and -78 dBV from a Neutrik Minirator

The hydrophone was mounted on a single piece of PVC tubing, horizontally separated from another hydrophone by a few centimeters. The hydrophones were suspended from a rigid steel super-structure using a counter-weighted rope suspension system. The hydrophones were held at a depth of 4 m in a 13 m water column. The ambient noise measurement commenced at 12:28 pm (local time), recording continuously for 10 minutes. Hydrophone sensitivity and recorder response curves are shown in Figure A.1.

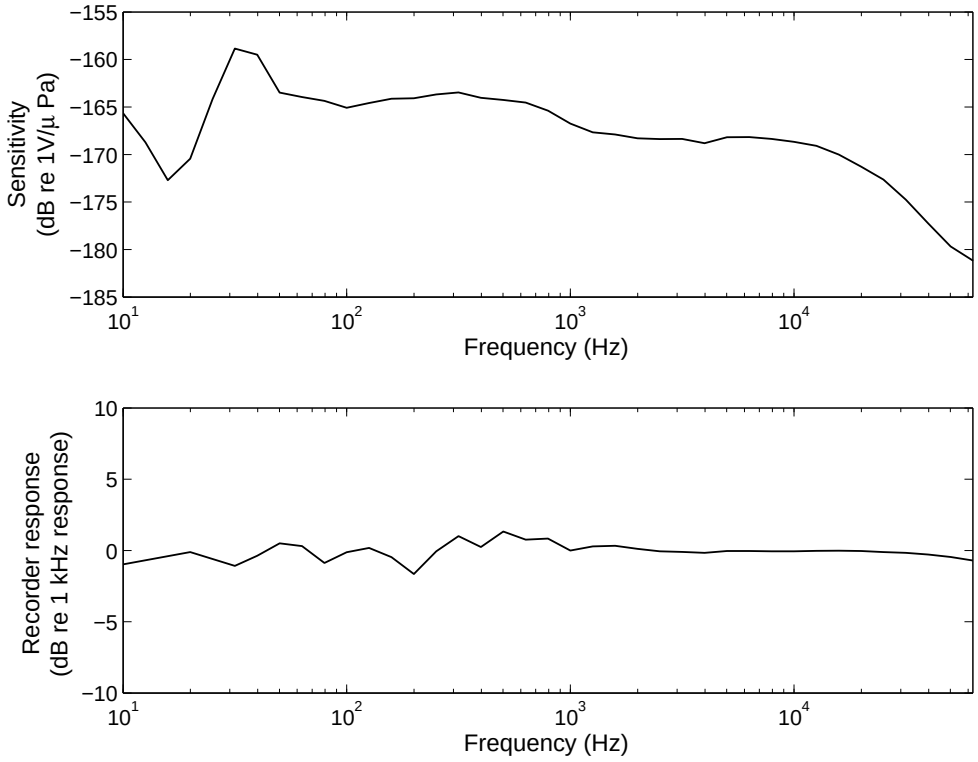

Figure A.1: Hydrophone sensitivity and recorder response used to measure the AW data. The response is shown relative to the response at 1 kHz.

A.2 Busselton Jetty (BUWO)

Busselton Jetty is located in Geographe Bay, Western Australia. The jetty projects 1.8 km from the shore into the bay and is one of the longest jetties in the southern hemisphere. At the end of the jetty is an underwater observatory, a cylindrical structure of approximately 5 m radius that extends from the jetty surface to the seafloor. The observatory allows public viewing of the underwater environment in the bay, and is therefore air filled. A series of acoustic measurements were conducted on the 10^{th} and 11^{th} of September 2007, however only data recorded on the 10^{th} was used in this thesis. Weather on the day was overcast and a moderate sea had developed from moderate to strong winds the previous night. At the time of recording the winds had eased slightly to 3.3 ms^{-1} from the north.

The following people contributed to the measurement:

- Matthew Legg (design; recording equipment setup, calibration and operation; observation; note taking)
- Dr. Dave Matthews (hydrophone deployment; other duties)
- Damien Killeen (rigging; other duties)
- Dr. Rod MacLeod (rigging; other duties)

The following equipment was used:

- Hydrophone: HTI-96-MIN S/N 554011

  Sensitivity: -164 dB re 1V per μPa

  Nominal bandwidth: 2 Hz to 30 kHz

  Horizontal directivity: omni-directional

  Vertical directivity: unknown

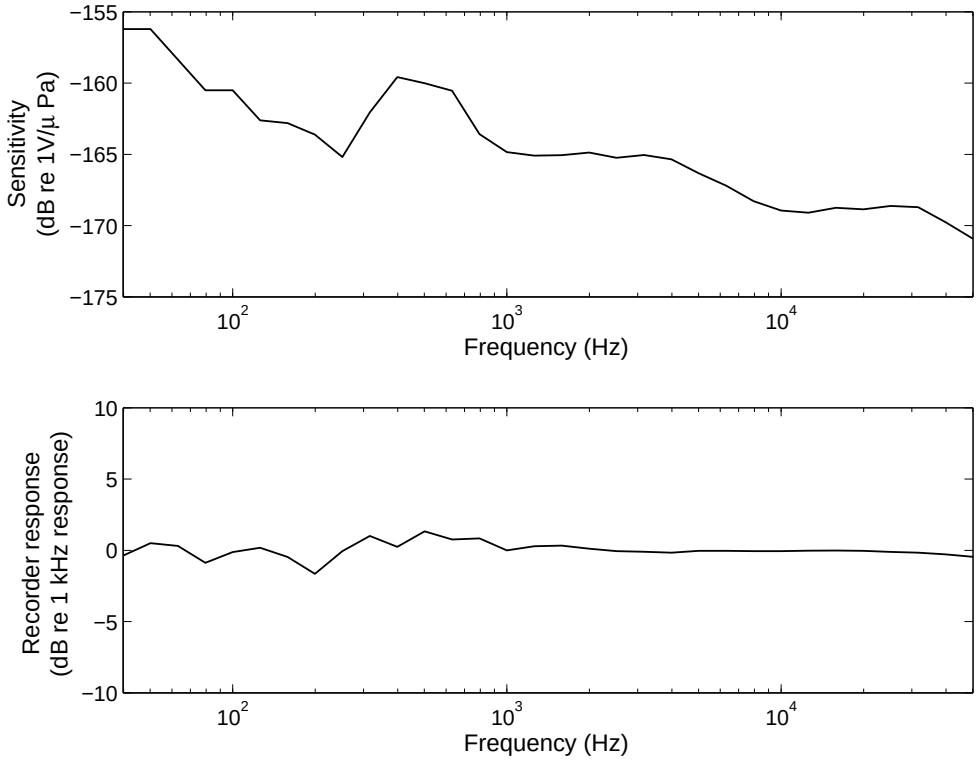

Figure A.2: Hydrophone sensitivity and recorder response used to measure the BUWO data. The response is shown relative to the response at 1 kHz.

- Recorder: FOSTEX FR1

  Sample Rate: 192 kHz

  Resolution: 24 bit

  Calibration: 20 kHz white noise at -34 dBV from a Neutrik Minirator

Two hydrophones were placed either side of the underwater observatory, each mounted on a PVC pipe and suspended using a counterweighted rope suspension system from the top platform. Only one of the hydrophones (on the left side of the observatory) was used for the ambient noise recording. The measurement commenced at 16:03 pm (local time) and recorded continuously for 50 minutes.

Hydrophone sensitivity and recorder response curves are shown in Figure A.2.

A.3 Cockburn Sound measurements

The following measurements were conducted from a set of pontoons located in Cockburn Sound, Western Australia. The measurements were conducted at times when the weather was fine and sea states as low as possible. Commercial shipping and small boat activity was common during measurements, and at times dolphins came within 100 m of the hydrophone.

A.3.1 10 March 2008 (CS-A,CS-D)

As part of the field experiment to investigate the apparent amplitude pdf asymmetry of real shrimp noise, ambient noise was recorded. Weather conditions were fine with some cloud, the temperature was estimated as 20°C and a moderate wind of approximately 8-10 knots was blowing from an east-south-easterly direction. The sea state was higher than desired, and there was a reasonable amount of movement of the pontoons.

The following people contributed to the measurement:

- Matthew Legg (design; recording equipment setup, calibration and operation; observation; note taking)
- Dr. Dave Matthews (rigging; hydrophone deployment; other duties)
- Dr. Rod MacLeod (observation; other duties)
- Paul Moses (observation; other duties)

The following equipment was used:

- Hydrophones: HTI-96-MIN S/N 544002

  Sensitivity: -164 dB re 1V per μPa

Nominal bandwidth: 2 Hz to 30 kHz

Horizontal directivity: omni-directional

Vertical directivity: unknown

- Recorder: FOSTEX FR1

  Sample Rate: 192 kHz

  Resolution: 24 bit

  Calibration: 20 kHz white noise at -40 dBV from a Neutrik Minirator

The hydrophone was mounted on a PVC pipe and suspended at a depth of 5 m. The water depth was not measured at the time of the recordings but was estimated to be between 9 m and 12 m.

Hydrophone sensitivity and receiver response are shown in Figure A.3.

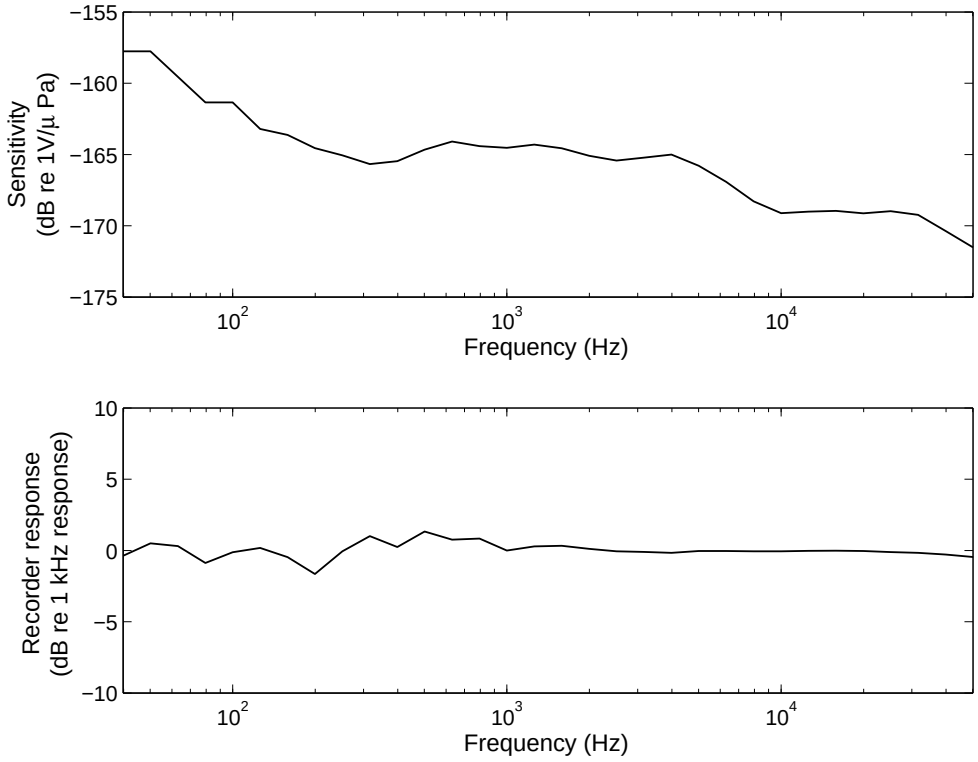

Figure A.3: Hydrophone sensitivity and recorder response used to measure the CS-A and CS-D data. The response is shown relative to the response at 1 kHz.

A.3.2 1 December 2005 (CS-B)

The purpose of this measurement was to measure snapping shrimp noise using a wide-bandwidth recording system. The measurement site was on the near side of the pontoons, to the north just past the on-ramp. Weather conditions were fine and winds were calm. There was slight movement of the pontoons and some rubbing against a support post.

The following people contributed to the measurement:

- Matthew Legg (design; recording equipment setup, calibration and operation; observation; note taking)
- Dr. Dave Matthews (rigging)
- Dr. Rod MacLeod (observation)

The following equipment was used:

- Hydrophones: RESON 4034 S/N 1405010

  Sensitivity: -225 dB re 1V per μPa plus 50 dB gain

- Recorder: Data Translation DT9834

  Sample Rate: 473 kHz

  Resolution: 16 bit

  Calibration: 20 kHz white noise at -34 dBV from a Neutrik Minirator

A single hydrophone was placed mid-water (exact hydrophone depth was not recorded), suspended from the hydrophone cable fixed to the pontoon. A water depth of 9.9 m was measured using a Hondex PS-7 hand-held depth sounder. The ambient noise

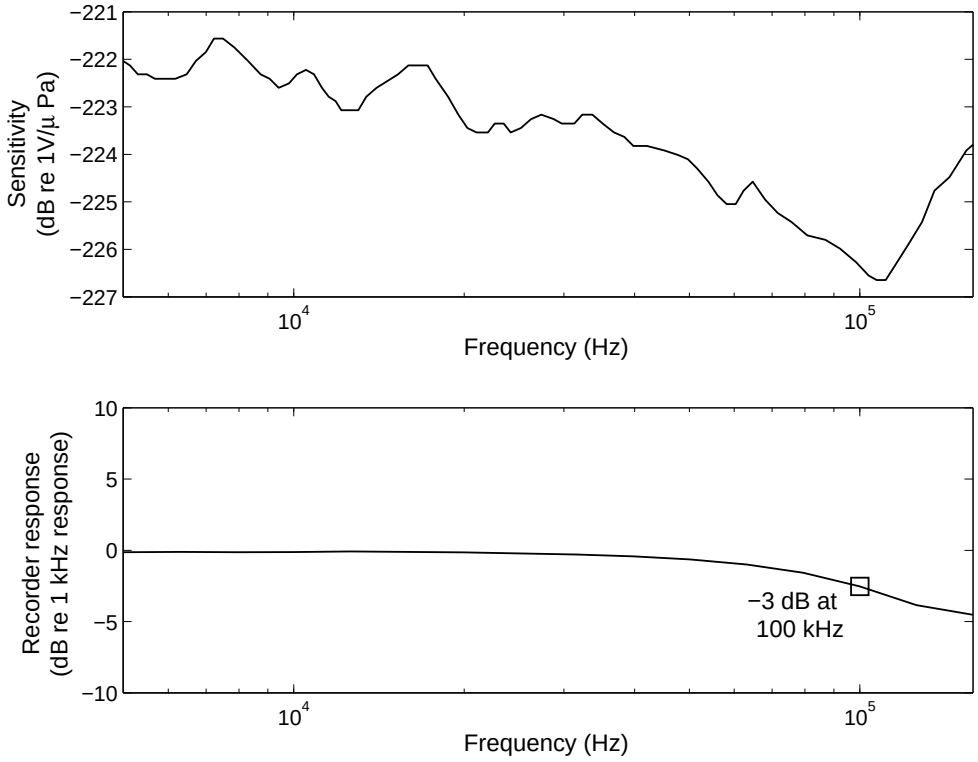

Figure A.4: Hydrophone sensitivity and recorder response used to measure the CS-B data. The recorder response is shown relative to the response at 1 kHz.

measurement commenced at 9:40 am (local time) and a continuous 30 minute recording was obtained.

A receiver response curve for the recording system used for the measurements is shown in Figure A.4. Vertical and horizontal directivities at 100 kHz are shown in Figure A.5. The hydrophone was omnidirectional in both the horizontal and vertical planes with the exception of those angles in the vertical that coincide with the hydrophone cable.

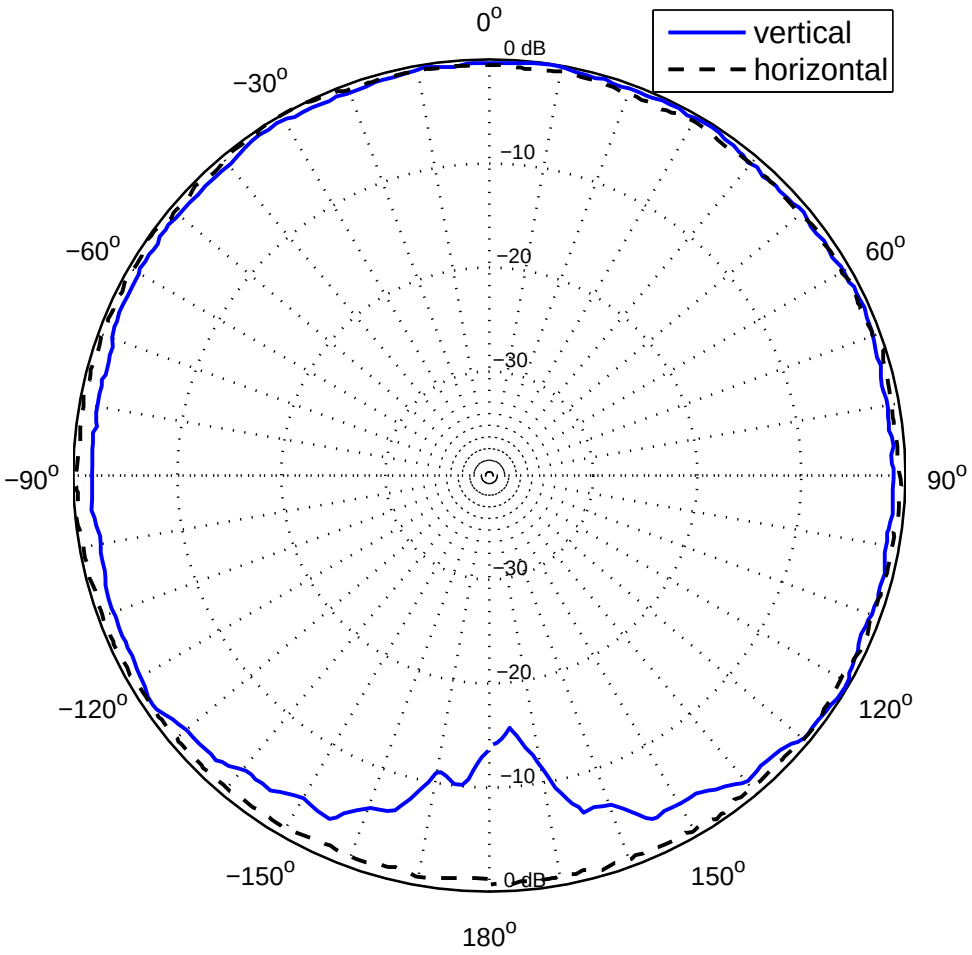

Figure A.5: Vertical and horizontal hydrophone directivity at 100 kHz.

A.3.3 25 November 2005 (CS-C)

The purpose of this measurement was to measure snapping shrimp noise using a wide-bandwidth recording system. The measurement site was on the near side of the pontoons, to the north just past the on-ramp. Weather conditions were fine with a light wind of approximately 2-5 knots from the south-east. A light swell caused some slight movement of the pontoons.

The following people contributed to the measurement:

- Matthew Legg (design; recording equipment setup, calibration and operation; observation; note taking)
- Dr. Dave Matthews (rigging; observation)
- Dr. Rod MacLeod (observation)

The following equipment was used:

- Hydrophones: RESON 4034 S/N 1405010

  Sensitivity: -225 dB re 1V per μPa plus 60 dB gain

- Recorder: Data Translation DT9834

  Sample Rate: 473 kHz

  Resolution: 16 bit

  Calibration: 20 kHz white noise at -34 dBV from a Neutrik Minirator

A single hydrophone was placed at 5 m depth, suspended from the hydrophone cable fixed to the pontoon. A water depth of 9.9 m was measured using a Hondex PS-7 hand-held depth sounder. A continuous 10 minute recording of the ambient noise was obtained.

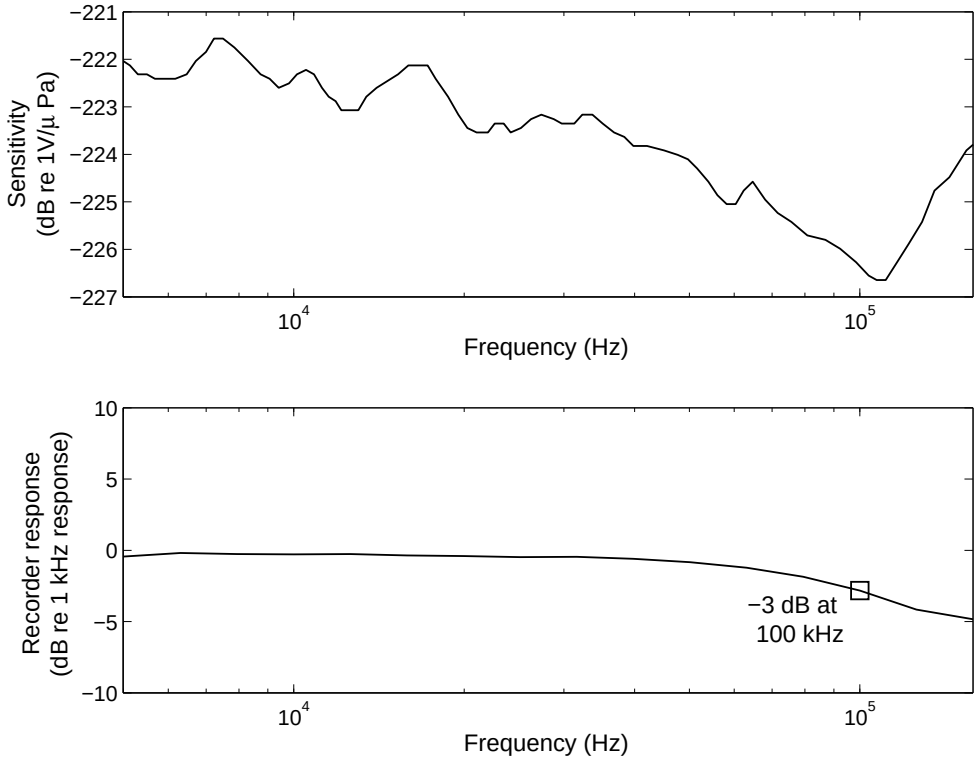

Figure A.6: Combined hydrophone and recorder response used to measure the CS-C data. The response is shown on a semilogarithmic scale and is relative to the response at 1 kHz.

A receiver response curve for the recording system used for the measurements is shown in Figure A.6.

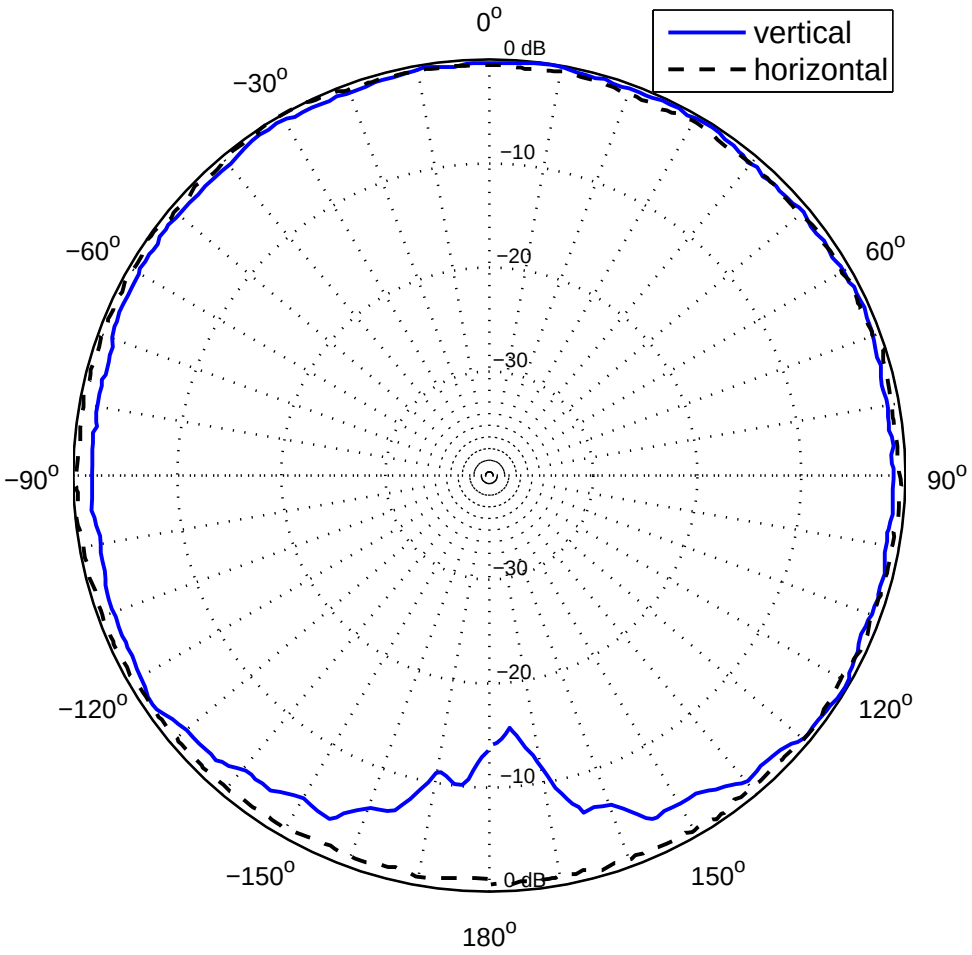

Figure A.7: Vertical and horizontal hydrophone directivity at 100 kHz.

A.4 Nornalup-Walpole Estuary (WP)

Exploratory measurements were conducted in the Nornalup-Walpole Estuary from the Rest Point jetty located at 34°59′18″S, 116°43′18″E, on the southern coast of Western Australia. The jetty extends approximately 25 m over the water near a channel that joins the Walpole and Nornalup Inlets. Snapping shrimp were not expected in these waters, but it appears that they do inhabit the estuary system in reasonable numbers.

The following people contributed to the measurement:

- Matthew Legg (design; recording equipment setup, calibration and operation; rigging and deployment; observation; note taking)
- Damien Killeen (rigging and deployment; observation)

The following equipment was used:

- Hydrophone: HTI-96-MIN S/N 306001

  Sensitivity: -164 dB re 1V per μPa

  Nominal bandwidth: 2 Hz to 30 kHz

  Horizontal directivity: omni-directional

  Vertical directivity: unknown

- Recorder: SONY DAT

  Sample Rate: 48 kHz

  Resolution: 16 bit

  Calibration: 20 kHz white noise at -20 dBV from a Neutrik Minirator

The hydrophone was secured from the south eastern corner of the jetty at a depth of 0.5 m, and recording commenced. A single continuous recording was made over a

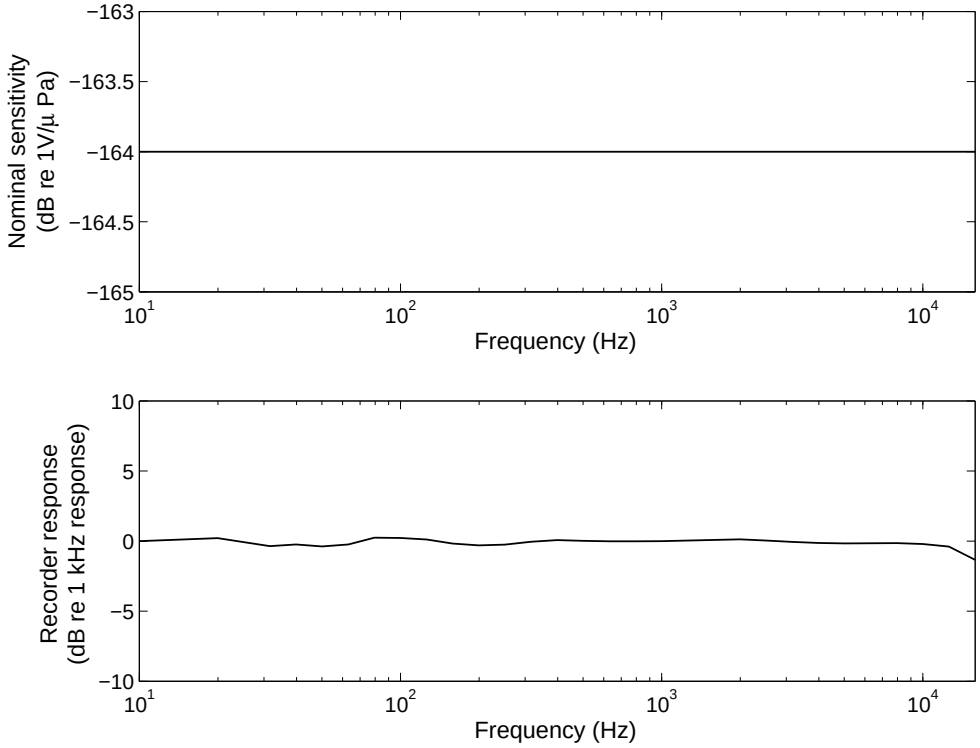

Figure A.8: Nominal hydrophone sensitivity and recorder response used to measure the WP data. The response is shown relative to the response at 1 kHz.

period of 42 minutes, during which a number of scraping sounds can be heard. The scraping sounds were thought to be caused by stingrays coming into contact with the hydrophone cable, although this could not be confirmed visually. During the recording several people visited the jetty, and some of the visitors commenced fishing. Various transient signals can be heard as a result, including the sound of a fish being caught. A water depth of 1.2 m was measured by lowering the hydrophone until it lightly touched the estuary floor.

Nominal hydrophone sensitivity and recorder response curves are shown in Figure A.8.

A.5 24 hour recording at the AWharf (AW24)

A 24 hour measurement was recorded from the 18th to the 19th of December 2008 at the AWharf site for the purpose of investigating long counting time effects. Weather conditions at the start of the measurement were fine, with clear skies and a wind speed of just over 4 ms^{-1}. The sea state was 1 with a very light swell. Several small boats were visible from the measurement site but most were at a distance greater than 1 km. During the night a tanker transited the area. At the end of measurements the water depth was 12.1 m, the wind had increased to over 7 ms^{-1} and the sea state had increased to 2.

The following people contributed to the measurement:

- Matthew Legg (design; recording equipment setup, calibration and operation; rigging and deployment; observation; note taking)
- Dr. Dave Matthews (rigging and deployment; observation)
- Paul Moses (power supply setup)

The following equipment was used:

- Hydrophone: HTI-96-MIN S/N 554003

  Sensitivity: -164 dB re 1V per μPa

  Nominal bandwidth: 2 Hz to 30 kHz

  Horizontal directivity: omni-directional

  Vertical directivity: unknown

- Recorder: Edirol R-4 pro

  Sample Rate: 192 kHz

  Resolution: 24 bit

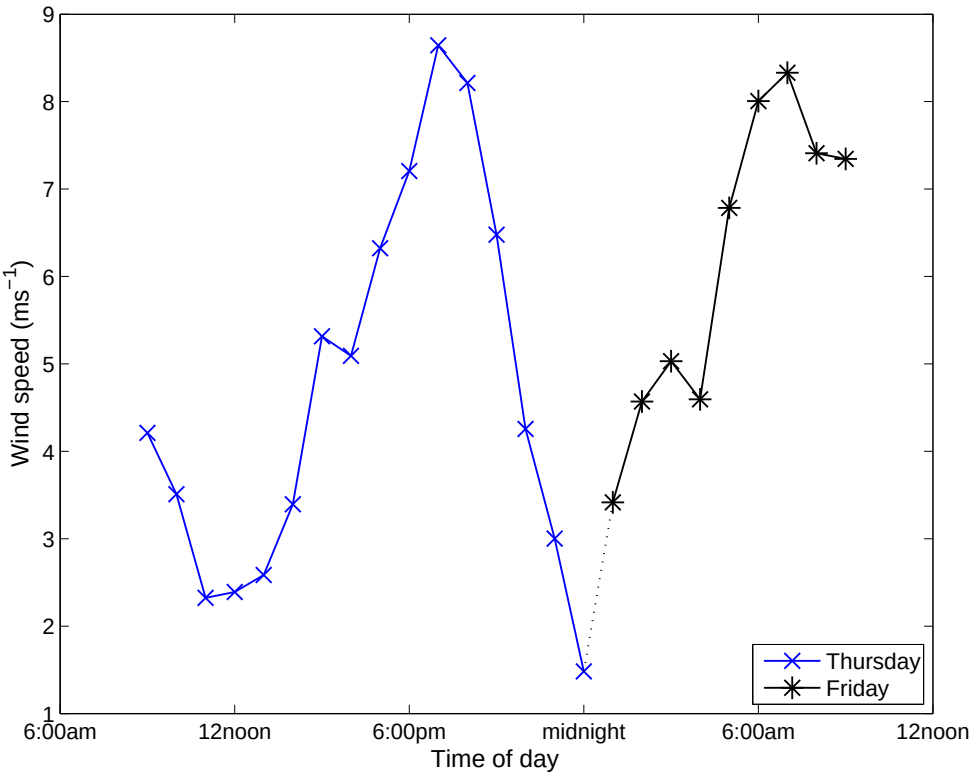

Figure A.9: Local wind record for the Garden Island region over the same time period as the 24 hour measurement (wind data from www.seabreeze.com).

Calibration: 20 kHz white noise at -34 dBV from a Neutrik Minirator

A single HTI 96-MIN hydrophone was suspended from a measurement platform near the end of the jetty using rigging shown in Figure A.10. The water depth at the start of measurements was 12.0 m and the hydrophone was placed at a depth of 5 m. Output from the hydrophone was connected directly into the line input of an Edirol R-4 field recorder configured to sample at 192 kHz with 24 bit resolution. The combined response of the hydrophone and recorder is shown in Figure A.11. A portable battery power supply was used to power both the hydrophone and the field recorder to minimise 50 Hz interference.

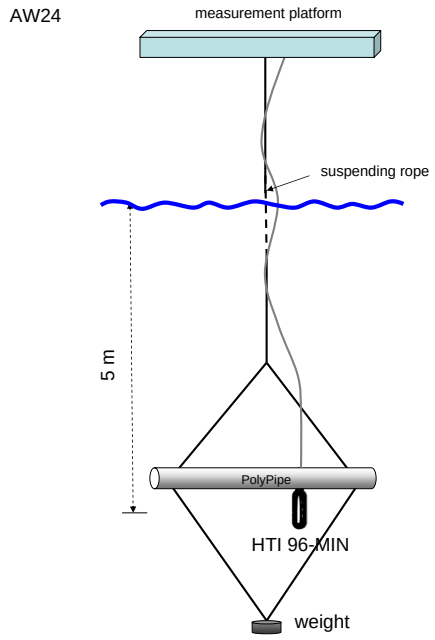

Figure A.10: A single hydrophone was mounted on a PVC weighted rig and suspended from a measurement platform. The hydrophone was located at a depth of 5 m.

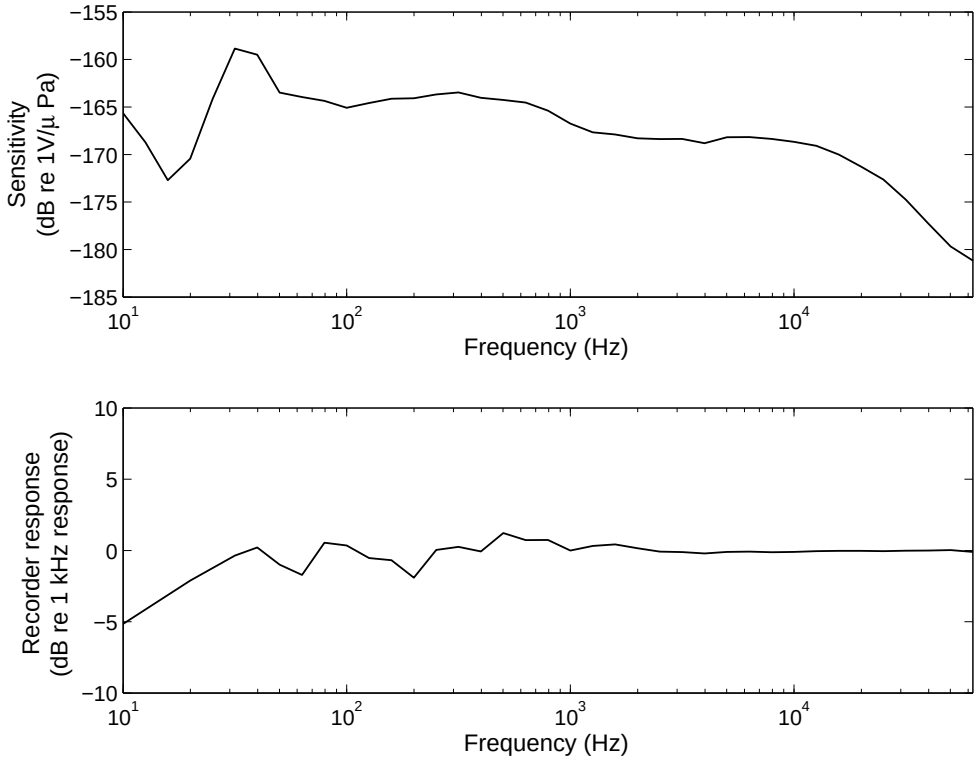

Figure A.11: Hydrophone sensitivity and recorder response used to measure the 24 hour data. The recorder response is shown relative to the response at 1 kHz.

Appendix B

Field data sets

Following are details of the data obtained from field trials conducted by other people.

B.1 Seal Island

Data from Seal Island was provided by Dr Dave Matthews.

Seal Island is located amongst a group of Islands off Shoalwater Bay in Western Australia at position 32°17′33.8″S, 115°41′23.5″E. This recording was made to investigate the difference between shrimp snaps inside an underwater cave and in nearby open water.

B.1.1 Seal Island Cave (SEAL-A and SEAL-B)

Two measurements were conducted during this field work, one set of measurements were taken inside an underwater cave (SEAL-A) immediately followed by other in nearby open water (SEAL-B). The water depth at both locations was 5 m and the hydrophone

was mounted on the seafloor. Weather on the day was fine with a 5-10 knot breeze from the NE. There was no swell and the sea state was 1.

The following equipment was used:

- Hydrophone: HTI-96-MIN S/N 306001

  Nominal sensitivity: -164 dB re 1V per μPa

  Nominal bandwidth: 2 Hz to 30 kHz

  Horizontal directivity: omni-directional

  Vertical directivity: unknown

- Recorder: SONY DAT

  Sample Rate: 48 kHz

  Resolution: 16 bit

  Calibration: 20 kHz white noise from a Neutrik Minirator

Manufacturers hydrophone response curves were not available for this hydrophone. White noise was recorded from a Neutrik Minirator onto the DAT tape. A response curve for the DAT tape is shown in Figure B.1.

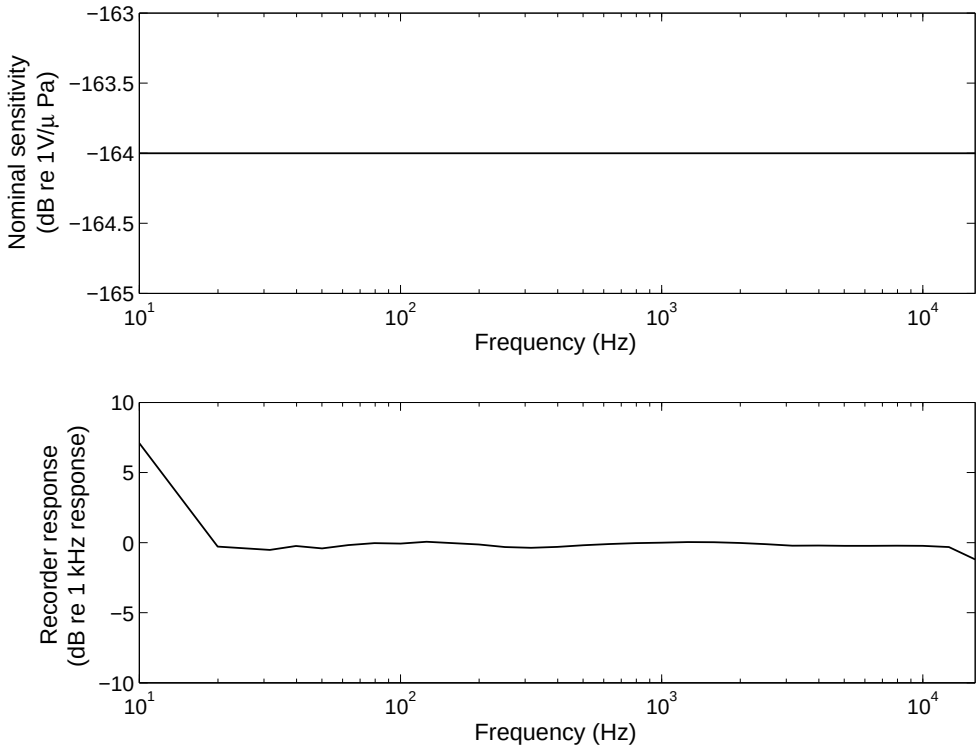

Figure B.1: Nominal hydrophone sensitivity and recorder response used to measure the SEAL-A and SEAL-B data. The recorder response is relative to the response at 1 kHz.

B.1.2 Seal Island (SEAL-C)

The Seal Island data was recorded using a hydrophone near the surface in a very shallow water column of between 3 and 5 metres, near to a set of reefs. The sea state was very low and winds calm.

The following equipment was used:

- Hydrophone: HTI-96-MIN

  Nominal sensitivity: -164 dB re 1V per μPa

  Nominal bandwidth: 2 Hz to 30 kHz

  Horizontal directivity: omni-directional

  Vertical directivity: unknown

- Recorder: SONY DAT (short play mode)

  Sample Rate: 41 kHz

  Resolution: 16 bit

  Calibration: Unavailable

Calibration information for this data set was unavailable, however the equipment used was similar to that used for SEAL-A and SEAL-B therefore the response of the system is likely to to be very similar.

B.2 Feather Reef (FR)

Data from Feather Reef was provided by Dr Rob McCauley

Feather Reef is located at position 17°31′4.4″S, 146°23′12.2″E off the coast of Queens-

land, Australia. The Feather Reef data was recorded using a bottom mounted hydrophone in 24 metres of water. The hydrophone was placed near a set of reefs.

The following equipment was used:

- Hydrophone: MASSA TR1025C

  Nominal sensitivity: -196 dB re 1V per μPa

  Nominal bandwidth: 10 Hz to 20 kHz

  Horizontal directivity: omni-directional

  Vertical directivity: 20 deg. toroidal at -3 dB total angle (25 kHz)

- Recorder: DAT (long play mode)

  Sample Rate: 32 kHz

  Resolution: 16 bit

  Calibration: White noise at -130 dB re $1V^2$/Hz

The manufacturers nominal hydrophone response was available for this hydrophone. White noise at -130 dB re $1V^2$/Hz was recorded onto the DAT tape. A response curve for the DAT tape is shown in Figure B.2.

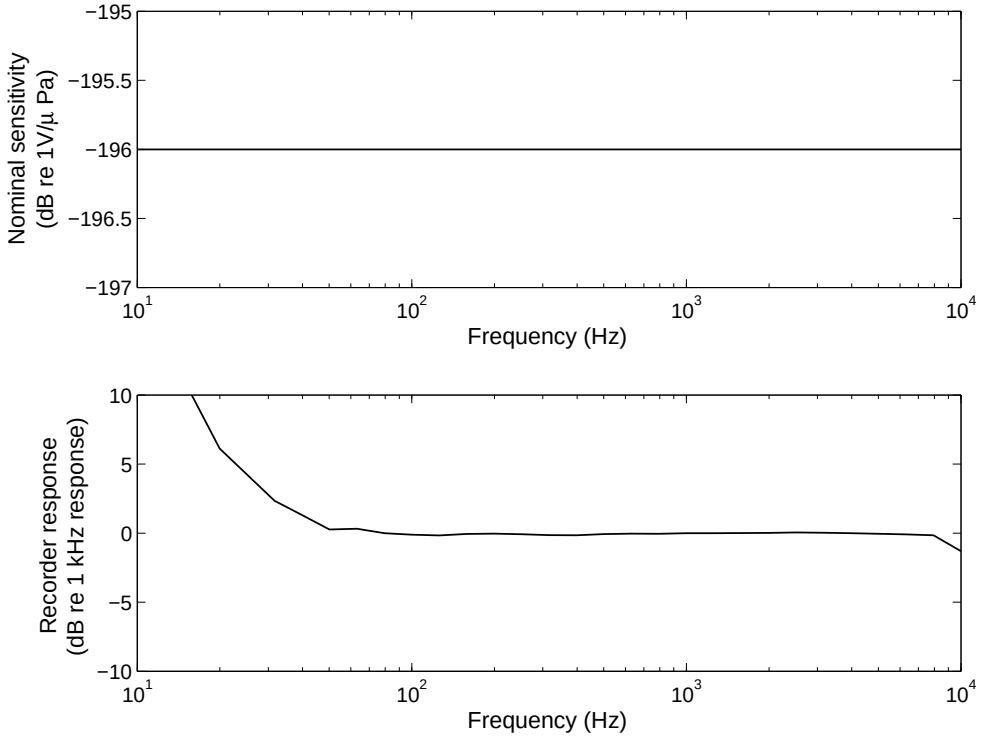

Figure B.2: Nominal hydrophone sensitivity and recorder response used to measure the FR. The recorder response is relative to the response at 1 kHz.

B.3 Spencer Gulf (SG)

Data from Spencer Gulf was provided by Dr Doug Cato

The Spencer Gulf data was recorded using a hydrophone placed mid-water in the water column.

The following equipment was used:

- Hydrophone: ITC-1032

  Nominal sensitivity (representative mid-band OCV): -194 dB re 1V per μPa

  Nominal bandwidth: 10 Hz to 50 kHz

  Horizontal directivity: omni-directional

  Vertical directivity: Unknown

- Recorder: SONY DAT TCD-D8 (long play mode)

  Sample Rate: Usable upper frequency limit 14 kHz

  Resolution: 16 bit

  Calibration: 3 dB per octave pink noise at -110 dB re $1V^2$/Hz at 1 kHz

Hydrophone sensitivity and recorder response curves are shown in Figure B.3.

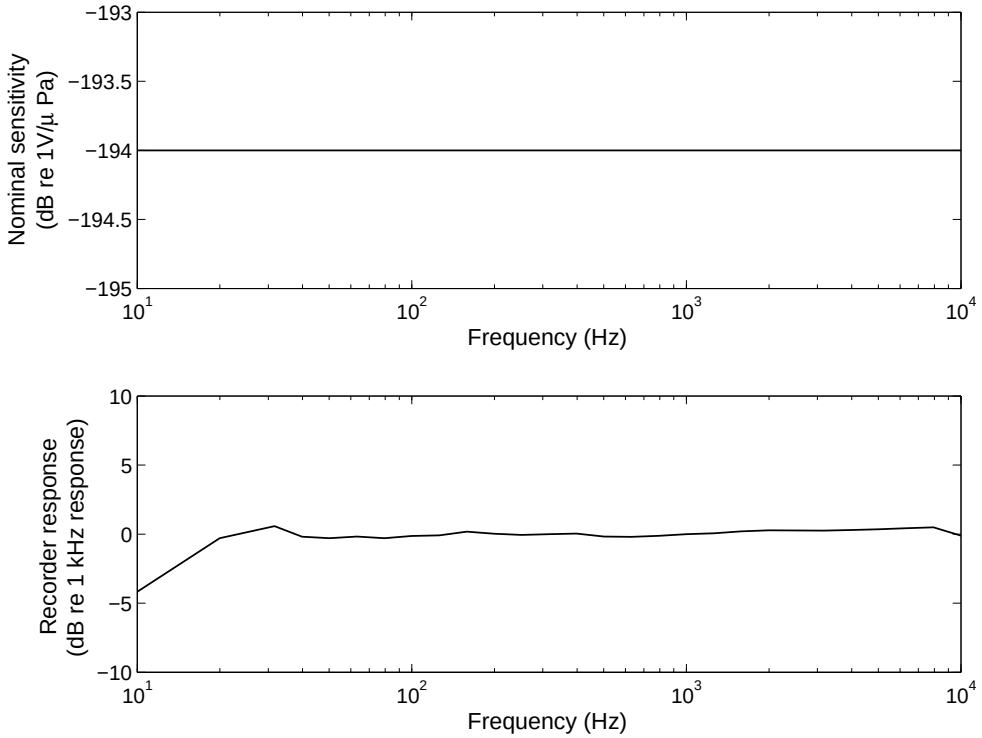

Figure B.3: Nominal hydrophone sensitivity and recorder response used to measure the Spencer Gulf data. The recorder response is relative to the response at 1 kHz.

B.4 Sydney Harbour (SYD-A and SYD-B)

Data from Sydney Harbour was provided by Dr Dave Matthews

Sydney Harbour data was recorded at position 33°51′52.1″S, 151°11′43.6″E on 4th of October 2007. The hydrophone was suspended from a wharf at a depth of 4 m in a 10.6 m water column. Winds were 15 to 20 knots from the NE and small boat activity was regular.

The following equipment was used:

- Hydrophone: HTI-96-MIN 554003

  Nominal sensitivity: -164 dB re 1V per μPa

  Nominal bandwidth: 2 Hz to 30 kHz

  Horizontal directivity: omni-directional

  Vertical directivity: unknown

- Recorder: FOSTEX FR-2

  Sample Rate: 192 kHz

  Resolution: 24 bit

  Calibration: 20 kHz white noise from a Neutrik Minirator

Hydrophone sensitivity and recorder response curves are shown in Figure B.4.

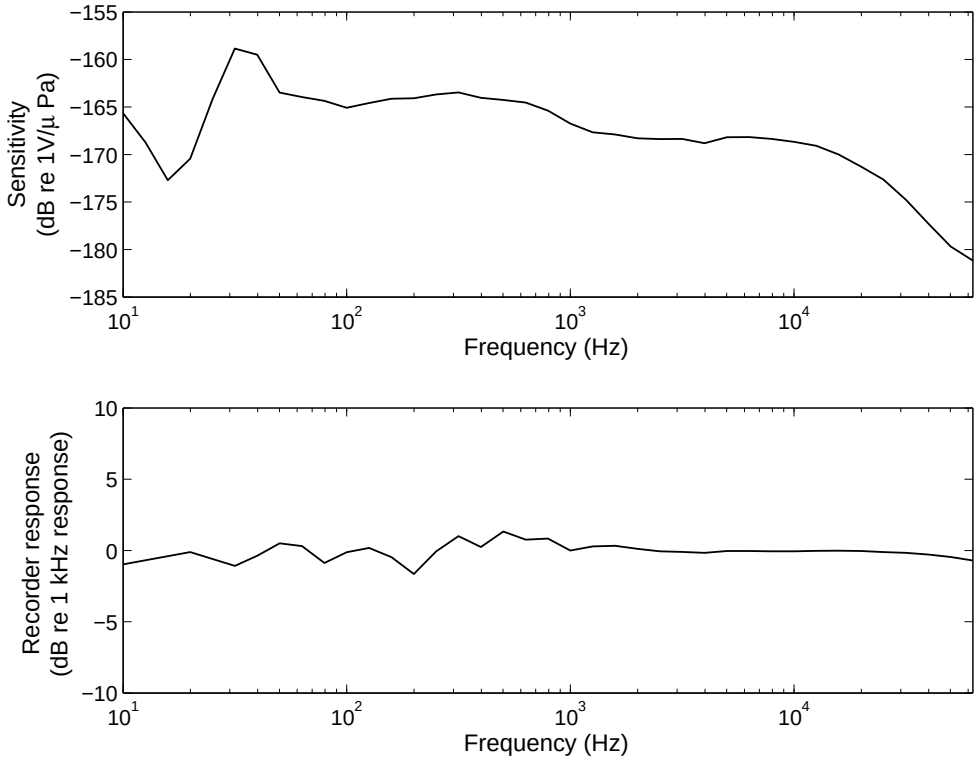

Figure B.4: Hydrophone sensitivity and recorder response used to measure the SYD-A and SYD-B data. The recorder response is relative to the response at 1 kHz.

Appendix C

Logarithmic smoothing algorithm

Logarithmic smoothing (logsmooth) was conducted by specifying the edges of consecutive, non-overlapping windows with size increasing by a specified logarithm base to the power of the distance of the window from the origin. Window sizes were always specified in the positive sense, from an origin of zero. Orientation and shift operations to accommodate negative directions and provide offset origins were handled by codes outside of the logsmooth algorithm.

Window sizes were computed using

$$\delta_n = \beta^n \tag{C.1}$$

where β is the specified logarithm base, and n is the integer number of windows from the origin to the window of interest. Window edges were computed using the sum of the preceding window sizes

$$\omega = \sum_{k=0}^{n-1} \delta_k \tag{C.2}$$

The representative window location was the center of the window, ω plus half of δ. The value assigned to the window was computed as the mean value of the window contents. The following MATLAB®code is representative of the algorithm used for logarithmic smoothing operations in this thesis.

```
function [YY,XX] = logsmooth(X,Y,NumBins,LOGBASE)
% smooth data in logarithmically spaced bins
MaxVal = max(X);
MinVal = min(X);
MaxAbs = max(abs(X));
MinAbs = min(abs(X));
Range = MaxAbs-MinAbs;
MinInc = Range./sum(LOGBASE.^[0:1:NumBins-1]);
% compute the bin edges
BinIncrements = [0,MinInc.*(LOGBASE.^[0:1:NumBins-1])];
BinEdges = MinAbs+cumsum(BinIncrements);
Edges = sign(MinVal).*BinEdges;
% sort so they are ordered from lowest to highest (ascending)
Edges = sort(Edges);
% remove any edges that are out of bounds
Edges = Edges(find(Edges>=MinVal & Edges<=MaxVal));
% bin centres provide the XX return values
Centres = Edges(1:end-1)+(diff(Edges)./2);
XX = Centres;
YY = repmat(nan,size(Centres));
% mean value in the window provides the YY return value
for k=1:1:length(Centres)
    WinData = Y(find(X>=Edges(k) & X<Edges(k+1)));
    if ~isempty(WinData)
        YY(k) = mean(WinData);
    end
end
% Done
```

Bibliography

Aazhang B & Poor HV 1987, 'Performance of DS/SSMA communications in impulsive channels - Part I: Linear correlation receivers', *IEEE Trans. Commun.*, vol. COM-35, no. 11, pp. 1179–1188.

Aazhang B & Poor HV 1988, 'Performance of DS/SSMA communications in impulsive channels - Part II: Hard-limiting correlation receivers', *IEEE Trans. Commun.*, vol. 36, no. 1, pp. 88–96.

Ali HB 1983, 'Spatial and temporal variabilities in underwater acoustic transmission: an analytical review', Tech. Rep. SM-166, SACLANT ASW Research Centre, La Spezia, Italy.

Arase T & Arase EM 1968, 'Deep-sea ambient-noise statistics', *J. Acoust. Soc. Am.*, vol. 44, no. 6, pp. 1679–1684.

Au WWL & Banks K 1998, 'The acoustics of the snapping shrimp *Synalpheus parneomeris* in Kaneohe Bay', *J. Acoust. Soc. Am.*, vol. 103, no. 1, pp. 41–47.

Bardyshev VI 2007, 'Underwater ambient noise in shallow-water areas of the Indian Ocean within the tropical zone', *Acoustical Physics (Akusticheskĭ Zhurnal)*, vol. 53, no. 2, pp. 167–171.

Beaulieu NC 2006, 'A simple integral form of lognormal characteristic functions convenient for numerical computation', in *IEEE GLOBECOM 2006*, IEEE, San Francisco, CA, USA, pp. 1–3.

Beng KT, Teck TE, Chitre M & Potter JR 2003, 'Estimating the spatial and temporal distribution of snapping shrimp using a portable, broadband 3-dimensional acoustic array', in *OCEANS 2003 Marine Technology and Ocean Science Conference (MTS/IEEE)*, IEEE, San Diego, USA, pp. 2706–2713.

Bertilone DC & Killeen DS 2000, 'Adaptive non-Gaussian processing for enhanced sonar detection in biological noise interference', in T McMinn & G Yates (eds.) *Proceedings of Acoustics 2000*, Australian Acoustical Society, Joondalup, Australia, pp. 35–40.

Bertilone DC & Killeen DS 2001, 'Statistics of biological noise and performance of generalized energy detectors for passive detection', *IEEE J. Oceanic Eng.*, vol. 26, no. 2, pp. 285–294.

Blum RS, Zhang Y, Sadler BM & Kozick RJ 1999, 'On the approximation of correlated non-Gaussian noise pdfs using Gaussian mixture models', in *1st Conference on the Applications of Heavy Tailed Distributions in Economics, Engineering and Statistics*, American University, Washington DC.

Buckingham MJ, Berkhout BV & Glegg SA 1992, 'Imaging the ocean with ambient noise', *Nature*, vol. 356, pp. 327–329.

BWF 2001, 'BWF - a format for audio data files in broadcasting', Tech. Rep. TECH-3285, European Broadcasting Union.

Cantor BI & Teich MC 1975, 'Dead-time-corrected photocounting distributions for laser radiation', *J. Opt. Soc. Am.*, vol. 65, no. 7, pp. 786–791.

Cato DH 1980, 'Some unusual sounds of apparent biological origin responsible for sustained background noise in the Timor Sea', *J. Acoust. Soc. Am.*, vol. 68, no. 4, pp. 1056–1060.

Cato DH & Bell MJ 1992, 'Ultrasonic ambient noise in Australian shallow waters at frequencies up to 200 kHz', MRL Technical Report MRL-TR-91-23, Materials Research Laboratory, Australia.

Chen F, Lambert D & Pinheiro JC 2000, 'Incremental quantile estimation for massive tracking', in R Ramakrishnan & S Stolfo (eds.) *Proceedings of the Sixth International Conference on Knowledge Discovery and Data Mining*, Association for Computing Machinery, New York, pp. 516–522.

Chitre M 2006, *Underwater Acoustic Communications in Warm Shallow Water Channels*, Ph.D. thesis, Electrical and Computer Engineering, National University of Singapore.

Chitre M 2007, 'A high-frequency warm shallow water acoustic communications channel model and measurements', *J. Acoust. Soc. Am.*, vol. 122, no. 5, pp. 2580–2586.

Chitre M, Beng KT & Potter JR 2003, 'Origins of directionality in snapping shrimp sounds and its potential applications', in *OCEANS 2003 Marine Technology and Ocean Science Conference (MTS/IEEE)*, IEEE, San Diego, USA, pp. 889–896.

Chitre MA, Potter JR & Ong SH 2006, 'Optimal and near-optimal signal detection in snapping shrimp dominated ambient noise', *IEEE J. Oceanic Eng.*, vol. 31, no. 2, pp. 497–503.

Chitre MA, Shahabudeen S & Stojanovic M 2008, 'Underwater acoustic communications & networking: Recent advances and future challenges', *Marine Technology Society Journal*, vol. 42, no. 1, pp. 103–116.

Coates RF 1990, *Underwater Acoustic Systems*, Macmillan New Electronics Series, Macmillan Education Ltd, London.

Cox DR & Lewis PAW 1966, *The statistical analysis of series of events*, Methuen's Monographs on Applied Probability and Statistics, Methuen & Co, Ltd, London.

D'Agostino RB & Stephens MA (eds.) 1986, *Goodness of fit techniques*, vol. 68 of *Statistics, textbooks and monographs*, Marcel Dekker, Inc., New York.

Devroye L 1986, *Non-Uniform Random Variate Generation*, Springer-Verlag, New York, NY.

Doukovska L 2007, 'Moving traget Hough detector in randomly arriving impulse interference', *Cybernetics and Information Technologies*, vol. 7, no. 3, pp. 55–72.

Doukovska L & Kabakchiev C 2006, 'Performance of Hough detectors in presence of randomly arriving impulse interference', in K Kulpa & M Piotrkowski (eds.) *International Radar Symposium, IRS 2006*, IEEE, Krakow, Poland, pp. 473–476.

Evans M, Hastings N & Peacock B 1993, *Statistical Distributions*, 2nd edn., John Wiley & Sons, Inc.

Everest FA, Young RW & Johnson MW 1948, 'Acoustical characteristics of noise produced by snapping shrimp', *J. Acoust. Soc. Am.*, vol. 20, no. 2, pp. 137–142.

Fano U 1947, 'Ionization yield of radiations. ii. The fluctuations of the number of ions', *Physical Review*, vol. 72, no. 1, pp. 26–29.

Fenton LF 1960, 'The sum of log-normal probability distributions in scatter transmission systems', *IRE Transactions on Communications Systems*, vol. CS-8, pp. 57–67.

Ferguson BG & Cleary JL 2001, '*In situ* source level and source position estimates of biological transient signals produced by snapping shrimp in an underwater environment', *J. Acoust. Soc. Am.*, vol. 109, no. 6, pp. 3031–3037.

Gabbiani F & Koch C 1998, 'Principles of spike train analysis', in C Kock & I Segev (eds.) *Methods in Neuronal Modeling: From Ions to Networks*, 2nd edn., MIT Press, Cambridge, MA, pp. 313–360.

Gillespie DT 1996, 'Exact numerical simulation of the Ornstein-Uhlenbeck process and its integral', *Physical Review E*, vol. 54, no. 2, pp. 2084–2091.

Gusella R 1991, 'Characterizing the variability of arrival processes with indexes of dispersion', *IEEE Journal on Selected Areas in Communications*, vol. 9, no. 2, pp. 203–211.

Heinzel G, Rüdiger A & Schilling R 2002, 'Spectrum and spectral density estimation by the discrete Fourier transform (DFT), including a comprehensive list of window

functions and some new flat-top windows', Tech. Rep. 395068, Max-Plank-Institut für Gravitationsphysik (Albert-Einstein-Institut), Hannover.

Herberholz J & Schmitz B 1998, 'Role of mechanosensory stimuli in intraspecific agonistic encounters of the snapping shrimp (*Alpheus heterochaelis*)', *Biol. Bull.*, vol. 195, pp. 156–167.

Herz A, Benda J, Gollisch T, Machens C, Schaette R, Schütze H & Stemmler M 2004, *Methods in Insect Sensory Neuroscience*, chap. 5, Frontiers in Neuroscience, CRC Press, pp. 129–158.

Higham DJ 2001, 'An algorithmic introduction to numerical simulation of stochastic differential equations', *SIAM Review*, vol. 43, no. 3, pp. 525–546.

Himonas SD 1994, 'CFAR integration processors in randomly arriving impulse interference', *IEEE Transactions on Aerospace and Electronic Systems*, vol. 30, no. 3, pp. 809–817.

Hogg RV & Craig AT 1995, *Introduction to mathematical statistics*, 5th edn., Prentice Hall, New Jersey.

Hulbert EO 1943, 'An underwater sound of natural origin', *J. Acoust. Soc. Am.*, vol. 14, no. 3, pp. 173–174.

Inman DL 2003, 'Scripps in the 1940s: The Sverdrup Era', *Oceanography*, vol. 16, no. 3, pp. 20–28.

Kassam SA 1988, *Signal Detection in Non-Gaussian Noise*, Springer-Verlag, New York.

Kay SM 1998, *Fundamentals of statistical signal processing : detection theory*, Prentice-Hall.

Legg MW, Duncan AJ, Zaknich A & Greening MV 2005, 'An exploratory analysis of non-Poisson temporal behaviour in snapping shrimp noise', in T McMinn (ed.) *Proceedings of ACOUSTICS 2005*, Australian Acoustical Society, Busselton, Australia, pp. 399–403.

Legg MW, Zaknich A, Duncan AJ & Greening MV 2007, 'Analysis of impulsive biological noise due to snapping shrimp as a point process in time', in *Proceedings of OCEANS'07*, IEEE, Aberdeen, Scotland.

Leipnik RB 1991, 'On lognormal random variables: I-The characteristic function', *J. Austral. Math. Soc. Ser. B*, vol. 32, pp. 327–347.

Lepage T, Lawi S, Tupper P & Bryant D 2006, 'Continuous and tractable models for the variation of evolutionary rates', *Mathematical Biosciences*, vol. 199, no. 2, pp. 216–233.

Liebovitch LS, Todorov AT, Zochowski M, Scheurle D, Colgin L, Wood MA, Ellenbogen KA, Herre JM & Bernstein RC 1999, 'Nonlinear properties of cardiac rhythm abnormalities', *Physical Review E*, vol. 59, no. 3, pp. 3312–3319.

Lowen SB, Ozaki T, Kaplan E, Saleh BEA & Teich MC 2001, 'Fractal features of dark, maintained, and driven neural discharges in the cat visual system', *Methods*, vol. 24, pp. 377–394.

Lowen SB & Teich MC 1992, 'Auditory-nerve action potentials form a nonrenewal point process over short as well as long time scales', *J. Acoust. Soc. Am.*, vol. 92, no. 2, pp. 803–806.

Lowen SB & Teich MC 1996, 'The periodogram and Allan variance reveal fractal exponents greater than unity in auditory-nerve spike trains', *J. Acoust. Soc. Am.*, vol. 99, no. 6, pp. 3585–3591.

Manton JH, Krishnamurthy V & Elliott RJ 1999, 'Discrete time filters for doubly stochastic Poisson processes and other exponential noise models', *Int. J. Adapt. Control Signal Process.*, vol. 13, pp. 393–416.

Martin RD & Thomson DJ 1982, 'Robust-resistant spectrum estimation', *Proceedings of the IEEE*, vol. 70, no. 9, pp. 1097–1115.

McCulloch JH 1998, 'Numerical approximation of the symmetric stable distribution and density', in RJ Adler, RE Feldman & MS Taqqu (eds.) *A Practical Guide to Heavy Tails: Statistical Techniques and Applications*, Birkhäuser, Boston, pp. 489–499.

McDonough RN & Whalen AD 1995, *Detection of signals in noise*, 2nd edn., Academic Press, San Diego, CA.

Middleton D 1977, 'Statistical-physical models of electromagnetic interference', *IEEE Transactions on Electromagnetic Compatibility*, vol. EMC-19, no. 3, pp. 106–127.

Middleton D 1995, 'Threshold detection in correlated non-Gaussian noise fields', *IEEE Transactions on Information Theory*, vol. 41, no. 4, pp. 976–1000.

Middleton D 1999, 'Non-gaussian noise models in signal processing for telecommunications: New methods and results for Class A and Class B noise models', *IEEE Transactions on Information Theory*, vol. 45, no. 4, pp. 1129–1149.

Middleton J, Chacron M, Lindner B & Longtin A 2003, 'Firing statistics of a neuron model driven by long-range correlated noise', *Physical Review E*, vol. 68, no. 2, pp. 21920–8.

Newman M 2005, 'Power laws, Pareto distributions and Zipf's law', *Contemporary Physics*, vol. 46, no. 5, pp. 323–351.

Neyman J & Scott EL 1952, 'A theory of the spatial distribution of galaxies', *Astrophysical Journal*, vol. 116, pp. 144–163.

Nielsen PA & Thomas JB 1990, 'A comparison of parametric and nonparametric detector performance levels in underwater noise', *J. Acoust. Soc. Am.*, vol. 87, no. 1, pp. 225–236.

Nikias CL & Shao M 1995, *Signal Processing with Alpha-Stable Distributions and Applications*, John Wiley & Sons, New York, NY.

Perkel DH, Gerstein GL & Moore GP 1967, 'Neuronal spike trains and stochastic point processes 1: The single spike train', *Biophysical Journal*, vol. 7, pp. 391–418.

Picchini U 2007, *SDE Toolbox: Simulation and Estimation of Stochastic Differential Equations with MATLAB*, URL http://sdetoolbox.sourceforge.net.

Poor HV & Tanda M 2002, 'Multiuser detection in flat fading non-gaussian channels', *IEEE Trans. Commun.*, vol. 50, no. 11, pp. 1769–1777.

Potter JR & Koay TB 2000, 'Do snapping shrimp chorus in time or cluster in space? Temporal-spatial studies of high-frequency ambient noise in Singapore waters', in P Cheveret & M Zakharia (eds.) *Proceedings of the Fifth European Conference on Underwater Acoustics*, ECUA, Lyon, France.

Potter JR, Lim TW & Chitre M 1997a, 'Ambient noise environments in shallow tropical seas and the implications for acoustic sensing', in *Proceedings of Oceanology International '97*, vol. 1, Singapore, pp. 191–199.

Potter JR, Lim TW & Chitre M 1997b, 'High-frequency ambient noise in warm shallow waters', in T Leighton (ed.) *Proceedings of the Fourth International Conference on Natural Physical Processes Associated with Sea Surface Sound*, Chilworth Manor, England, pp. 45–54.

Press WH, Flannery BP, Teukolsky SA & Vetterling WT 1988, *Numerical recipes in C: The art of scientific computing*, Cambridge University Press, Cambridge.

Readhead M 1994, 'The distribution of snapping shrimp noise near Gladstone, Queensland', Technical Report DSTO-TR-0047, DSTO Aeronautical and Maritime Research Laboratory, Melbourne, Victoria.

Readhead ML 1997, 'Snapping shrimp noise near Gladstone, Queensland', *J. Acoust. Soc. Am.*, vol. 101, no. 3, pp. 1718–1722.

Ricciardi L & Esposito F 1966, 'On some distribution functions for non-linear switching elements with finite dead time', *Kybernetic*, vol. 3, pp. 148–152.

Slimane S & Le-Ngoc T 1995, 'A doubly stochastic poisson model for self-similar traffic', in *IEEE International Conference on Communications*, vol. 1, pp. 456–460.

Snyder DL & Miller MI 1991, *Random point processes in time and space*, 2nd edn., Springer Texts in Electrical Engineering, Springer, New York.

Teich MC & Cantor BI 1978, 'Information, error, and imaging in deadtime-perturbed doubly stochastic Poisson counting systems', *IEEE Journal of Quantum Electronics*, vol. QE-14, no. 12, pp. 993–1003.

Teich MC & Saleh BE 1982, 'Effects of random deletion and additive noise on bunched and antibunched photon-counting statistics', *Optics Letters*, vol. 7, no. 8, pp. 365–367.

Teich MC, Turcott RG & Siegel RM 1996, 'Temporal correlation in cat striate-cortex neural spike trains', *IEEE Engineering in Medicine and Biology*, vol. 15, no. 5, pp. 79–87.

Thurner S, Lowen SB, Feurstein MC, Heneghan C, Feichtinger HG & Teich MC 1997, 'Analysis, synthesis, and estimation of fractal-rate stochastic point processes', *Fractals*, vol. 5, no. 4, pp. 565–595.

University of California Division of War Research 1946, 'Underwater noise caused by snapping shrimp', Tech. Rep. U337, Scripps Institution of Oceanography Library, University of California, San Diego.

Urick RJ 1986, *Ambient noise in the sea*, Peninsula Publishing.

Vastola KS 1984, 'Threshold detection in narrow-band non-Gaussian noise', *IEEE Transactions on Communications*, vol. COM-32, no. 2, pp. 134–139.

Venugopalan P, Chitre M, Teck TE, Potter JR, Beng KT, Ruiz SB & Tan SP 2003, 'Ambient noise imaging - first deployments of romanis and preliminary data analysis', in *OCEANS 2003 Marine Technology and Ocean Science Conference (MTS/IEEE)*, San Diego, USA, pp. 882–888.

Versluis M, Schmitz B, von der Heydt A & Lohse D 2000, 'How snapping shrimp snap: through cavitating bubbles', *Science*, vol. 289, pp. 2114–2117.

Virtamo J, Aalto S & Down D 1996, 'Window based estimation of the intensity of a doubly stochastic Poisson process', in *Proceedings of the International IFIP-IEEE Conference on Broadband Communications*, IEEE, pp. 294–305.

Waterman MS & Whiteman DE 1978, 'Estimation of probability densities by empirical density functions', *Int. J. Math. Educ. Sci. Technol.*, vol. 9, no. 2, pp. 127–137.

Watkins PT, Santhanam G, Shenoy KV & R HR 2004, 'Validation of adaptive threshold spike detector for neural recording', in *Proceedings of the 26th Annual International Conference of the IEEE EMBS*, IEEE, San Fransisco, California, pp. 4097–4082.

Welch PD 1967, 'The use of fast fourier transform for the estimation of power spectra: A method based on time averaging over short, modified periodograms', *IEEE Transactions on Audio and Electroacoustics*, vol. AU-15, no. 2, pp. 70–72.

Wenz GM 1962, 'Acoustic ambient noise in the ocean: Spectra and sources', *J. Acoust. Soc. Am.*, vol. 34, no. 12, pp. 1936–1956.

Widener MW 1967, 'Ambient-noise levels in selected shallow water off Miami, Florida', *J. Acoust. Soc. Am.*, vol. 42, no. 4, pp. 904–905.

Willett PK 1987, *Density representations with applications to signal detection*, Ph.D. thesis, Department of Electrical Engineering, Princeton University.